

MODELS OF COCHLEAR IMPLANT STIMULATION

BIOPHYSICAL AND PHENOMENOLOGICAL MODELS OF COCHLEAR IMPLANT STIMULATION

By
JASON BOULET, B.A.Sc., M.Sc.

A Thesis Submitted to the School of Graduate Studies
in Partial Fulfillment of the Requirements for the Degree
Doctor of Philosophy

McMaster University © Copyright by Jason Boulet, September 2016

McMaster University
Hamilton, Ontario

DOCTOR OF PHILOSOPHY (2016)
(Neuroscience)

TITLE: Biophysical and Phenomenological Models of
Cochlear Implant Stimulation

AUTHOR: Jason Boulet, B.A.Sc. (University of Ottawa),
M.Sc. (University of Ottawa)

SUPERVISOR: Ian C. Bruce, Ph.D.

NUMBER OF PAGES: xvi, 152

LAY ABSTRACT

Cochlear implants (CI) attempt to restore hearing to individuals with severe to profound hearing deficits by stimulating the auditory nerve with a series of electrical pulses. Recent CI stimulation strategies have attempted to improve speech perception by stimulating at high pulse rates. However, studies have shown that speech perception performance does not necessarily improve with pulse rate increases, leading to speculation of possible causes. Certain ion channels located in auditory nerve fibers may contribute to driving the nerve to reduce its excitability in response to CI stimulation. In some cases, those channels could force nerve fibers to cease responding to stimulation, causing a breakdown in communication from the CI to the auditory nervous system. Our simulation studies of the auditory nerve containing certain types of channels showed that the effective rate of communication to the brain is reduced when stimulated at high rates due to the presence of these channels.

ABSTRACT

Numerous studies showed that cochlear implant (CI) users generally prefer individualized stimulation rates in order to maximize their speech understanding. The underlying reasons for the reported variation in speech perception performance as a function of CI stimulation rate is unknown. However, multiple interacting electrophysiological processes influence the auditory nerve (AN) in response to high-rate CI stimulation. Experiments studying electrical pulse train stimulation of cat AN fibers (ANFs) have demonstrated that spike rates slowly decrease over time relative to onset stimulation and is often attributed to spike rate (spike-triggered) adaptation in addition to refractoriness. Interestingly, this decay tends to adapt more rapidly to higher stimulation rates. This suggests that subthreshold adaptation (accommodation) plays a critical role in reducing neural excitability.

Using biophysical computational models of cat ANF including ion channel types such as hyperpolarization-activated cyclic nucleotide-gated (HCN) and low threshold potassium (KLT) channels, we measured the strength of adaptation in response to pulse train stimulation for a range of current amplitudes and pulse rates. We also tested these stimuli using a phenomenological computational ANF model capable of applying any combination of refractoriness, facilitation, accommodation, and/or spike rate adaptation.

The simulation results show that HCN and KLT channels contribute to reducing model ANF excitability on the order of 1 to 100 ms. These channels contribute to both spike rate adaptation and accommodation. Using our phenomenological model ANF we have also shown that accommodation alone can produce a slow decay in ANF spike rates responding to ongoing stimulation.

The CI users that do not benefit from relatively high stimulation rates may be due to ANF accommodation effects. It may be possible to use electrically evoked compound action potentials (ECAP) recordings to identify CI users exhibiting strong effects of accommodation, i.e., the increasing strength of adaptation as a function of increasing stimulation rate.

ACKNOWLEDGEMENTS

My doctoral experience was akin to being immersed in virtual reality only because I was facing a liquid crystal display for most of the time. Occasionally, people would manage to get me back to reality and for that, I am very thankful. Of all of these people, my doctoral advisor Ian C. Bruce has provided me with unbounded support and mentorship. We did not necessarily stick to regular supervisory meeting times, so I appreciate that Ian was always willing to oblige my surprise office pop-in appearances that always ended with me getting back on track. He has exposed me to numerous international conferences where I had the opportunity to present my work and gain critical feedback. By the end, I had no trouble spelling his name on posters. Of course, there are many dimensions to an excellent advisor, but one particular aspect of Ian's supervision was executed so immaculately that I have not noticed it until recently. It is that his suggestions were so subtle that they made me think that they were my ideas. Because of this, it felt as though I was challenging myself and advancing at just the right pace—understanding what I needed to understand and leaving enough room to push forward and try new approaches on my own. Ian introduced me to his wonderful family and over time his official status as my doctoral advisor has in the very best meaning of the term, eroded to a colleague and good friend.

Ian also brought world class collaborators to my attention. My initial one month interaction with Sonia Tabibi boiled over into what is now my third chapter. I would also like to thank her for her careful eye throughout that process. My collaboration with Mark White has developed over five years resulting in chapters two and three. Constantly working at a computer sometimes makes one lose sight of the bigger picture, but Mark has always given his unwavering encouragement and enthusiasm, claiming that our work was indispensable to the cochlear implant research community. I am grateful to my learned friends Stephanie Cheung, Larissa Taylor, Spencer Chambers, and Dana Swarbrick, as current and previous members of the Auditory Engineering Laboratory they always kept a playful atmosphere during our lab meetings. In my humble opinion, that should be the prevailing attitude in a research environment. I would also like to thank Michael Wirtzfeld, my companion doctoral student in our lab. Having to face many of the same challenges in tandem certainly reduced the burdens on our way to the finish line. Members of my thesis committee Daniel Goldreich and Hubert de Bruin have kept me on track and given me the broader neuroscience perspectives. I would also like to thank committee members of my comprehensive exam Alexander Ball and Michael Noseworthy for setting me straight at least once during my tenure at McMaster. The computing resources of Department of Electrical and Computer Engineering, affectionately known as the 'The GRID', or as I like to think of it as a byzantine collection of servants always waiting to realize any of my concoctions, was an invaluable resource—one which without it would have been impossible to carry out the countless simulations that made its way to this thesis. I would also like to thank Dan Manolescu for keeping The GRID obedient.

As I set out to start doctoral training at McMaster, only moments elapsed before I felt

settled into my new Hamilton surroundings. That was in large part due to a rather sizable and tight-knit group of individuals who eventually became my very close friends. Those that know who they are kept me level headed as we explored the local delights, pursuing more than the mere graduate student experience. I also want to express my gratitude for my family's patience and support during my extended *adult-in-training* phase. Finally, my wife Justine Spencer knows all-too-well what it takes to get it done. She has been a never-ending source of inspiration, positivity, spirited encouragement, love, and knowing when to keep her distance—which will be ending momentarily. Her support goes far beyond the game—thank you.

TABLE OF CONTENTS

1	General Introduction and Overview	1
1.1	Brief Introduction	2
1.2	Overview of the Thesis Chapters	3
1.2.1	Chapter 2	3
1.2.2	Chapter 3	3
1.2.3	Chapter 4	3
1.2.4	Chapter 5	4
1.2.5	Chapter 6	4
2	Temporal Considerations for Stimulating Spiral Ganglion Neurons with Cochlear Implants	6
2.1	Introduction	7
2.2	Stimulus-Response Phenomena	12
2.2.1	Refractoriness	12
2.2.2	Facilitation and Accommodation	13
2.2.3	Spike Rate Adaptation and Interacting Phenomena	17
2.3	Mechanisms and Models	19
2.3.1	Refractoriness	21
2.3.2	Facilitation	22
2.3.3	Accommodation	24
2.3.4	Spike Rate Adaptation	24
2.4	Spatial Effects of CI Stimulation Related to Temporal Interactions	25
2.5	Conclusions	27
3	Phenomenological Model of Auditory Nerve Fiber Responses to Cochlear Implant Stimulation: Subthreshold and Suprathreshold Influences	37
3.1	Introduction	38
3.1.1	Single Pulse or Resting Response	41
3.1.2	Refractoriness	43
3.1.3	Spike Rate Adaptation	44
3.1.4	Facilitation and Accommodation	45
3.2	Methods	48
3.2.1	Dynamic Threshold Potential Model	48
3.2.2	Model Simulation	57
3.2.3	Stimuli	57
3.2.4	Data analysis	59
3.3	Results	61

3.3.1	Single Pulse Response	61
3.3.2	Paired Pulse Response	62
3.3.3	Pulse Train Response	65
3.4	Discussion	68
3.5	Conclusions	70
4	Predictions of the Contribution of Hyperpolarization-Activated Cyclic Nucleotide-Gated Cation Half-Maximal Activation Potential Heterogeneity to Variability in Intrinsic Adaptation of Spiral Ganglion Neurons	74
4.1	Introduction	75
4.2	Methods	77
4.2.1	Membrane Model	77
4.2.2	Modifications to Kinetic HCN Channel Models	79
4.2.3	Stimuli	80
4.2.4	Analysis	81
4.2.5	Spike Detection	83
4.3	Results	85
4.3.1	Single Pulse	85
4.3.2	Adaptation	86
4.3.3	Recovery from Masker Train	91
4.3.4	Refractoriness	95
4.4	Discussion	97
4.5	Conclusions	99
4.6	Appendix	99
4.6.1	HCN(r) Channel Model	100
4.6.2	HCN(q,s) Channel Model	100
4.6.3	Neuron-Specific Channel Modifications	101
5	Spike Initiation at Different Nodes of Ranvier in Spiral Ganglion Neurons: Spatio-Temporal Responses to Cochlear Implant Stimulation	107
5.1	Introduction	109
5.2	Methods	110
5.2.1	Multicompartmental SGN Model	110
5.2.2	Stimuli	112
5.2.3	Computer Simulation and Analysis	114
5.3	Results	118
5.3.1	Single Pulse Response	118
5.3.2	Refractory Paired Pulse Response	122
5.3.3	Subthreshold Paired Pulse Response (Facilitation and Accommodation)	126
5.3.4	Pulse Train Response	128
5.3.5	Masker-Probe Train Response	134
5.4	Discussion	137
5.5	Conclusions and Future Directions	138

5.6	Appendix	139
5.6.1	Multicompartmental SGN Model	139
5.6.2	Transmembrane Potential	140
5.6.3	Ionic Currents and Channel Distribution	142
6	Conclusions and Future Directions	148
6.1	Summary of Conclusions	149
6.2	Implications for Cochlear Implant Stimulation Strategies	149
6.3	Future Directions	150

LIST OF FIGURES

2.1	Illustration of effective pulse rates for electrical stimulation of spiral ganglion neurons (SGNs) by a cochlear implant.	8
2.2	Stimulus-response phenomena and their associated mechanisms.	11
2.3	Published data from cat SGN recordings illustrating the four stimulus-response phenomena.	14
2.4	Hyperpolarization-activated cyclic nucleotide-gated (HCN) channel subunit expression in rat cochlea identified on Type I SGN.	20
2.5	Illustration of passive and active contributions to the facilitation (temporal summation) phenomenon, generated with a Hodgkin–Huxley-type SGN membrane model.	22
3.1	Stimulus-response phenomena represented by single-trial traces of the relative membrane potential.	39
3.2	Cat ANF response rate as a function of the time since pulse train onset over a 300 ms interval.	40
3.3	Single pulse or resting firing efficiency (FE) as a function of the injected current.	42
3.4	Refractory threshold and RS ratio as a function of the interval between masker and probe pulses from cat ANF	44
3.5	Contributions of passive and active facilitation.	46
3.6	Data from cat ANF recordings illustrating the combined effects of facilitation and accommodation on the threshold and RS ratio.	47
3.7	Diagram of phenomenological stimulus-response model.	49
3.8	Diagram of the dynamic threshold potential model.	50
3.9	Overview of inputs to and phenomenological model system variables.	58
3.10	Single pulse response or resting response represented as the proportion of spiking responses.	61
3.11	Responses of a paired pulse paradigm for the subthreshold conditioner response: facilitation and accommodation, and the suprathreshold conditioner response: refractoriness.	63
3.12	Zoomed-in sections of Fig. 3.11A.	64
3.13	Response rates of four different phenomenological model versions to pulse train stimulation.	65
3.14	Final response rate as a function of the number of RS_{SP} away from θ_{SP}	66
3.15	NSRD versus onset rate in response to pulse train stimulation.	68
4.1	HCN kinetic characterization.	80

4.2	Determination of a spiking threshold based on the sodium conductance duration.	84
4.3	Monophasic and biphasic single pulse sodium conductance duration threshold, AP threshold current, and relative spread.	85
4.4	Feline SGN response rate as a function of the time since pulse train onset.	87
4.5	PSTH responses to pulse train stimulation.	87
4.6	PSTH or response rate for the strongest-adapting SGN membrane models in response to pulse train.	88
4.7	Summary of the pulse train response statistics.	90
4.8	Feline SGN masker-probe pulse train responses in terms of response probability.	92
4.9	PSTH or response rate for the strongest-adapting SGN membrane models in response to masker-probe train.	93
4.10	Summary of the probe response recovery ratio.	95
4.11	Refractory threshold ratio as a function of the interval between pulses.	96
4.12	Absolute refractory period vs. the HCN $V_{1/2}$ shift parameter c for each of the membrane models	97
5.1	Morphology of the Type I SGN in cat and corresponding circuit model.	111
5.2	Ion channel densities at each node of Ranvier for three model configurations.	112
5.3	Single pulse threshold for each SGN model version as a function of the site of stimulation.	119
5.4	Single pulse relative spread for each SGN model version as a function of the site of stimulation.	120
5.5	Spatial probability of spiking in response to a single pulse.	121
5.6	Correlation between site of stimulation and spike initiation node in response to a single pulse.	121
5.7	Correlation between site of stimulation and spike initiation node in response to a single pulse (zoomed).	122
5.8	Refractory threshold ratio as a function of the interval between pulses.	123
5.9	Absolute refractory period.	124
5.10	Average number of nodes between first and second spike initiation.	125
5.11	Paired pulse response to subthreshold conditioner pulse in terms of the probe threshold ratio.	127
5.12	Response rate to extracellular biphasic pulse train stimulation at p1 and a distance of 2500 μm	129
5.13	Spatial probability of spiking in response to the final 100 ms of a 300 ms biphasic pulse train.	130
5.14	Correlation between site of stimulation and spike initiation node in response to the final 100 ms of a 300 ms biphasic pulse train.	131
5.15	Normalized spike rate decrement as a function of the onset response rate.	132
5.16	Adaptation time constants as a function of the onset response rate.	133

5.17	Response rate to extracellular biphasic masker-probe train stimulation at p1 and a distance of 2500 μm	135
5.18	Probe response recovery ratio as a function of the mean response rate to the masker train.	136

LIST OF TABLES

3.1	Summary of parameters for the phenomenological dynamic threshold potential model.	52
3.2	Parameters and quality of fit of the single pulse response.	62
3.3	Quality of fit of the paired pulse response.	64
4.1	SGN node of Ranvier membrane model parameters.	78
4.2	Refractory recovery function parameter estimates for strongest-adapting model variants.	96
5.1	Multicompartmental model parameters.	141
5.2	SGN node of Ranvier ion channel densities.	141
5.3	SGN node of Ranvier parameters.	143

LIST OF ACRONYMS AND ABBREVIATIONS

a	accommodation
ACE	Advanced Combined Encoder
AN	Auditory Nerve
ANF	Auditory Nerve Fiber
AP	Action Potential
APmax	Action Potential maximum
ARP	Absolute Refractory Period
<i>cn</i>	central node of Ranvier <i>n</i>
CI	Cochlear Implant
CIS	Continuous Interleaved Sampling
DA	Diffusion Approximation
dB	decibel
ECAP	Electrically-evoked Compound Action Potential
f	facilitation
FE	Firing Efficiency
GΩ	gigaohm
HCN	Hyperpolarization-activated Cyclic Nucleotide-gated
HH	Hodgkin-Huxley
IAF	Integrate-and-Fire
IHC	Inner Hair Cell
IPI	Interpulse Interval
kΩ	kiloohm
K ⁺	Potassium ion
KLT	Low-Threshold Potassium
K _v	Voltage-gated potassium ion channel
MΩ	megaohm
μA	microampere
μF	microfarad
μm	micrometer
μs	microsecond
mA	milliampere
ms	millisecond
mV	millivolt

MC	Markov Chain
Na ⁺	Sodium ion
Na _v	Voltage-gated sodium ion channel
NSRD	Normalized Spike Rate Decrement
<i>pn</i>	peripheral node of Ranvier <i>n</i>
pA	picoampere
pF	picofarad
pS	picosiemens
PRRR	Probe Response Recovery Ratio
PSTH	Post-Stimulus Time Histogram or Peri-Stimulus Time Histogram
<i>r</i>	refractoriness
RMP	Resting Membrane Potential
RRP	Relative Refractory Period
RS	Relative Spread
<i>s</i>	second or spike rate adaptation
SGN	Spiral Ganglion Neuron
SP	Single Pulse
S _{Peak}	Spectral Peak
SPT	Single Pulse Threshold
VCN	Ventral Cochlear Nucleus

DECLARATION OF ACADEMIC ACHIEVEMENT

This is a listing of research and content contributions to the thesis from the author and co-authors for each chapter. Note that the format of this thesis is a sandwich thesis and may contain overlap in content, particularly across different introduction, discussion, and conclusion sections.

Chapter 2 was a collaboration between myself, Mark White, and Ian C. Bruce. I was the lead on conceiving the literature review and I wrote the manuscript with Ian C. Bruce. This chapter serves as the introduction and background for the thesis. This chapter was published and is reprinted in this thesis with permission from Springer (license number 3902041402777). It has been reformatted for consistency in this thesis. Below, we provide a citation of the article

Boulet, J., White, M. W., and Bruce, I. C. (2016). Temporal considerations for stimulating spiral ganglion neurons with cochlear implants. *J Assoc Res Otolaryngol*, 17(1):1–17.

Chapter 3 was a collaboration between myself, Sonia Tabibi, Mark White, and Ian C. Bruce. I was the lead on designing the models and simulations, analyzing the data, and I wrote the manuscript with Ian C. Bruce.

Chapter 4 was a collaboration between myself and Ian C. Bruce. I was the lead on designing the models and simulations, analyzing the data, and I wrote the manuscript with Ian C. Bruce. This chapter was accepted at *J Assoc Res Otolaryngol*.

Chapter 5 was a collaboration between myself and Ian C. Bruce. I was the lead on designing the models and simulations, analyzing the data, and writing the manuscript.

CHAPTER **1**

General Introduction and Overview

1.1 Brief Introduction

The cochlear implant (CI) is the seminal computer-brain interface that provides restorative prosthesis-aided hearing for individuals with severe to profound deafness. The CI accomplishes this by first receiving acoustic information from the external environment and at this stage, it is represented by an analog signal. This envelope of this time-varying signal is then extracted and is encoded as a digital signal that is temporally discretized with a train of pulses. This signal is then sent to a linear electrode array placed in the cochlea that electrically stimulates the auditory nerve (AN), which in humans is composed of approximately 30 000 spiral ganglion neurons (SGNs). This form of electrical stimulation bypasses inner hair cells and directly excites SGNs, initiating transmission of non-synaptic auditory information to be sent to higher levels of the nervous system.

Statistics available on the web site of the National Institute on Deafness and Other Communication Disorders (2016) state that since its inception decades ago up until December of 2012, CIs have given approximately 324 200 individuals worldwide a sense that other healthy people normally take for granted. CIs have given those individuals an improved quality of life (Klop et al., 2007; Mo et al., 2005; Orabi et al., 2006). Unfortunately, even those with modern CIs experience difficulties with speech perception in noisy environments and typically show severe deficits in music comprehension (Clark, 2006). Researchers are still plagued by some of the fundamental issues that were faced in the infancy of CI development. Improving on the current state of the art of CI technology will require significant breakthroughs in understanding the electrode-neuron interface, followed by engineering advancements of equal magnitude (Clark, 2006; Macherey and Carlyon, 2014).

The purpose of this thesis is to develop accurate biophysical and phenomenological models of the spiral ganglion neuron response to cochlear implant stimulation. This thesis was motivated by inconsistencies between the current mechanistic understanding of how cat SGNs generate responses to CI stimulation and the actual recorded firing pattern of those cells. Specifically, contemporary models of the SGN either 1) cannot predict certain aspects of the SGN response or 2) if they can, then those responses are modeled by biological elements that are not known to be endogenous to mammalian SGNs. Over all biophysical models of the SGN to date, each may accurately predict a few of the properties: refractoriness, facilitation, adaptation (accommodation and spike rate adaptation), stochasticity, and spike generation and propagation, but none of the models can successfully predict all of them (for a review see O'Brien and Rubinstein, 2016, and references therein). There are many reasons for this, however the most apparent one is that biophysical models require many parameters. Thus, tuning the parameters of those models to simultaneously produce all of the aforementioned response patterns observed in animals, although useful for illuminating mechanisms, has not yet yielded total success. Phenomenological models have been useful in reducing the complexity of biophysical models by instead directly modeling the stimulus-response behaviors of SGNs. These models have typically considered properties such as changes to the neuron's threshold, dynamic range, latency, and jitter, in response to the spiking activity and stimulation, but

have yet to predict accommodation (for a review see Takanen et al., 2016, and references therein).

The first aim is to directly predict the electrical responses of spiral ganglion neurons to stereotypical cochlear implant stimulation in a top-down fashion by using a phenomenological modeling approach. Through the use of voltage-gated ion channels embedded in the membranes of entire spiral ganglion neurons, the second aim is to develop biophysical models that give rise to the various stimulus-response phenomena. Both of these approaches focused on determining what mechanisms cause reduction in excitability on the order of 10s to 100s of milliseconds in response to electrical pulsatile stimulation.

1.2 Overview of the Thesis Chapters

1.2.1 Chapter 2

We present a review of the literature that covers the background and scope of the problems we aim to address in this thesis. Specifically, we survey four stereotypical temporal stimulus-response phenomena that differentially govern changes to the excitability of SGNs and how they may interact. Here, we explore the different stimulation paradigms and analyses that researchers have used to characterize these stimulus-response phenomena. We then consider the likely biophysical models and mechanisms that give rise to these phenomena by focusing on voltage-gated ion channels.

1.2.2 Chapter 3

We develop a predictive phenomenological model of auditory nerve responses to pulsatile electrical stimulation based on recorded stimulus-response characteristics. We build on previous stochastic single-pulse response models to show how by allowing the stimulus-response phenomena to dynamically modulate the SGN firing threshold, the SGN can regulate excitability in response to stimulating pulses and spike history. We show that together accommodation and spike rate adaptation cause the steady state spike rate to drop over time in response to ongoing pulse train stimulation.

1.2.3 Chapter 4

We build computational models of a spiral ganglion neuron node of Ranvier containing different voltage gated-ion channel types. We show how experimentally-supported heterogeneity in the activation characteristics of the hyperpolarization-activated cyclic

nucleotide-gated (HCN) ion channel can predict systematic variability in the strength of adaptation that is observed in animals, whilst occurring on timescales reported in the literature. We suggest that these effects support that the nature of intrinsic adaptation in SGNs is represented by subthreshold and suprathreshold stimulus-response phenomena: accommodation and spike rate adaptation.

1.2.4 Chapter 5

Whereas the previous chapters focused on temporal stimulus-response relationships, in this chapter, we also represent spatial aspects by developing multicompartmental models of extracellular stimulation of the SGN. We show that the nodes of Ranvier at which spikes are initiated are influenced by the distribution of ion channel types along the length of the SGN. We also show that models with HCN channels tend to be more reliable at spiking at a node closer to the electrode than models without the HCN channel.

1.2.5 Chapter 6

We provide our conclusions based on all of the results of the thesis and discuss future directions for research. We focus on how HCN-related reductions in excitability in response to trains of high pulse rate stimulation drive SGNs into non-spiking states which require long periods of recovery in order to return to resting excitability levels. We hypothesize that CI development should focus on increasing the effective spatial resolution of the electrode-neuron interface since increasing the pulse rate generally produces a version of temporally masked stimulation. The advantages may include reduction in power consumption, a return to stimulation in the range of acoustically-driven rates, and improvements to place coding that represents the tonotopic arrangement of the cochlea.

References

- Clark, G. M. (2006). The multiple-channel cochlear implant: the interface between sound and the central nervous system for hearing, speech, and language in deaf people—a personal perspective. *Philos T Roy Soc B*, 361(1469):791–810.
- Klop, W. M. C., Briaire, J. J., Stiggelbout, A. M., and Frijns, J. H. M. (2007). Cochlear implant outcomes and quality of life in adults with prelingual deafness. *Laryngoscope*, 117(11):1982–1987.
- Macherey, O. and Carlyon, R. P. (2014). Cochlear implants. *Curr Biol*, 24(18):R878–R884.

- Mo, B., Lindbaek, M., and Harris, S. (2005). Cochlear implants and quality of life: a prospective study. *Ear Hear*, 26(2):186–194.
- National Institute on Deafness and Other Communication Disorders (2016). Cochlear Implants.
- O’Brien, G. E. and Rubinstein, J. T. (2016). The development of biophysical models of the electrically stimulated auditory nerve: Single-node and cable models. *Network*, pages 1–22.
- Orabi, A. A., Mawman, D., Al-Zoubi, F., Saeed, S. R., and Ramsden, R. T. (2006). Cochlear implant outcomes and quality of life in the elderly: Manchester experience over 13 years. *Clin Otolaryngol*, 31(2):116–122.
- Takanen, M., Bruce, I. C., and Seeber, B. U. (2016). Phenomenological modelling of electrically stimulated auditory nerve fibers: A review. *Network*, pages 1–29.

CHAPTER **2**

Temporal Considerations for Stimulating Spiral Ganglion Neurons
with Cochlear Implants

Abstract

A wealth of knowledge about different types of neural responses to electrical stimulation has been developed over the past 100 years. However, the exact forms of neural response properties can vary across different types of neurons. In this review we survey four stimulus-response phenomena that in recent years are thought to be relevant for cochlear implant stimulation of spiral ganglion neurons (SGNs): refractoriness, facilitation, accommodation, and spike rate adaptation. Of these four, refractoriness is the most widely known, and many perceptual and physiological studies interpret their data in terms of refractoriness without incorporating facilitation, accommodation, or spike rate adaptation. In reality, several or all of these behaviors are likely involved in shaping neural responses, particularly at higher stimulation rates. A better understanding of the individual and combined effects of these phenomena could assist in developing improved cochlear implant stimulation strategies. We review the published physiological data for electrical stimulation of SGNs that explores these four different phenomena, as well as some of the recent studies that might reveal the biophysical bases of these stimulus-response phenomena.

2.1 Introduction

Cochlear implants (CIs) are prosthetic devices that attempt to provide a coherent auditory perception to individuals with severe to profound deafness. The CI's electrode array resides in the cochlea where it communicates with the user's auditory system by sending out a series of short electrical pulses to Type I spiral ganglion neurons (SGN). Figure 2.1A shows an electrode array placed in the scala tympani of the cochlea (drawn as a wireframe) where the colors (blue, green, yellow, red) represent the subpopulations of SGNs targeted by the corresponding stimulating electrodes. Note that the term spiral ganglion neuron or cell sometimes refers just to the cell body or soma. It is also common to refer to the bipolar peripheral and central neurites of the SGN as auditory nerve fibers (ANFs). Unless otherwise specified, the term SGN used in this paper will refer to the whole spiral ganglion neuron. Importantly, SGN firing patterns are different in multiple aspects when comparing acoustic and electrical stimulation (Hartmann et al., 1984; Javel and Viemeister, 2000). Under acoustic stimulation, SGNs have a greater dynamic range, a more variable firing rate, and they undergo weaker phase locking. In the healthy ear, SGNs act as the bridge connecting the peripheral to the central nervous system. More specifically, they receive synaptic input from inner hair cells (IHCs) and output to a variety of cell types in the cochlear nucleus. As such, these neurons act as crucial contributors to the auditory system since they serve as the first layer of auditory neurons encoding afferent spiking information. Inner hair cells release synaptic vesicle packets in a probabilistic nature (Glowatzki and Fuchs, 2002; Heil et al., 2007; Safieddine et al., 2012) which could be responsible for the high variability of SGN firing rates in acoustic stimulation. In contrast, when electrically

stimulated with a cochlear implant, SGNs are directly excited by voltage-gated ion channel activity.

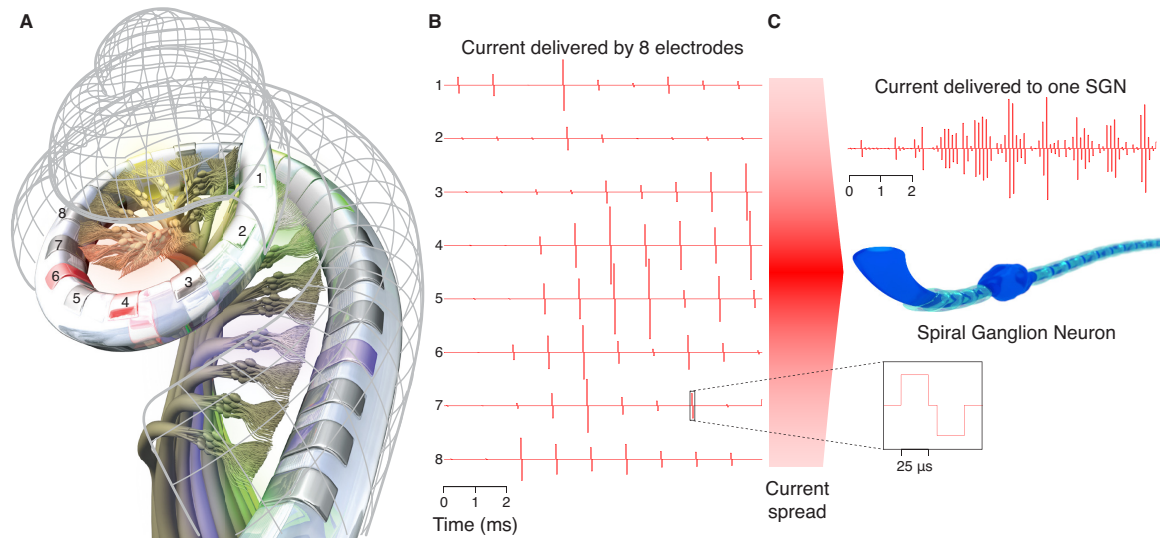


Figure 2.1 Illustration of effective pulse rates for electrical stimulation of spiral ganglion neurons (SGNs) by a cochlear implant. **A** The positioning of an electrode array inserted into the cochlea (drawn as the grey mesh wireframe) relative to the SGNs that form the auditory nerve. It is desirable for stimulating electrical currents from different electrodes or electrode pairs (*highlighted blue, green, yellow, and red*) to maximally stimulate distinct subpopulations of SGNs (also highlighted correspondingly with *blue, green, yellow, and red*), such that the tonotopic arrangement of SGNs is utilized in transmitting information about different sound frequencies. However, in practice there is substantial current spread along the length of the cochlea, such that a single SGN is subjected to a weighted sum of the currents delivered by the nearby electrodes. For example, plotted in **B** are current pulse trains delivered by electrodes 1–8 for a short speech segment encoded at a rate of 900 pulses/s on each electrode. **C** An electrode separation of 1.4 mm and a monopolar stimulation attenuation of 0.5 dB/mm (Merzenich and White, 1977) translate to the current spread profile (*shaded red*) that smears the contribution of all 8 electrodes to an example SGN situated between electrodes 4 and 5. This compound stimulation of an SGN results in an effective pulse rate that is much higher than the single-electrode rate of 900 pulses/s. Each biphasic pulse has a duration of 25 μs/phase and an gap of 8 μs between positive and negative phases. Image in **A** courtesy of Cochlear Americas, © 2015, adapted from Gray’s Anatomy textbook.

With the aim of improving speech perception in individuals with cochlear implants, an early approach was to ascertain whether or not increasing the stimulation pulse rate could improve the information transfer to the SGN (e.g., Wilson et al., 1988). Figure 2.1 shows that due to current spread in the cochlea and by using a single-channel rate of 900 pulses/s, an SGN can be exposed to an effective rate of 7200 pulses/s when stimulation is delivered by 8 electrodes. Some studies have shown that subjects prefer high single-channel stimulation rates in the range of 1700 to 4000 pulses/s (Kiefer et al., 2000; Loizou et al., 2000; Nie et al., 2006; Verschuur, 2005), others demonstrated no benefit (Arora et al., 2009; Friesen et al., 2005; Holden et al., 2002; Plant et al., 2007, 2002; Weber et al., 2007), while other research indicates that low to moderate stimulation rates, i.e., 250 to 500 pulses/s, work best (Balkany et al., 2007; Vandali et al., 2000). Significantly, most of these studies report large variance

between the performance of individuals as a function of the stimulation rate. Cochlear implant researchers currently do not fully understand why this is the case. Therefore, the complex interaction between stimulation rate and the wide range of patient outcomes suggests the need for a more refined comprehension of the neurophysiological mechanisms that modulate the response of spiral ganglion neurons to high stimulation rates. This paper describes several features of neural responses that may help us develop a much better understanding of this behavior.

We have an impoverished understanding of SGN excitability in response to high rates of stimulation chiefly due to the greater occurrence of temporal interactions for short inter-pulse intervals. In actuality, the SGN response will be determined by membrane capacitance and the types of voltage-gated ion channels that reside in its membrane. However, it is beneficial to characterize the resulting effects of these mechanisms in terms of stereotypical stimulus-response phenomena. Four phenomena that have been identified as occurring to varying degrees for the majority of excitable cells are refractoriness, facilitation, accommodation, and spike rate adaptation. These phenomena are also produced in Type I SGN when stimulated by a CI. At high rates of stimulation all of these behaviors are important and are interacting factors that regulate the firing pattern, whereas some are non-factors at low rates.

Figure 2.2 gives a single-trial stimulus-response overview of the phenomena of interest. The voltage traces in Fig. 2.2A–D were generated from an SGN membrane model (Negm and Bruce, 2014) with updated hyperpolarization-activated cyclic nucleotide-gated cation (HCN) kinetics (Liu et al., 2014b). It should be kept in mind throughout that multiple trials are necessary to capture the mean and variance of the response arising from the stochastic nature of action potential generation. Nevertheless, it is useful to visualize a representative membrane potential response to each stimulus pattern. The stimuli used in Fig. 2.2A–C are typically referred to as either masker-probe (first-second) or paired-pulse paradigms, which are commonly employed to investigate refractoriness, facilitation, and accommodation. The purpose of this type of stimulation is to systematically determine how the neuron responds after a pre-conditioning stimulus. The response to the two pulses in Fig. 2.2A is typical of a neuron in a refractory state, i.e., refractoriness, which is defined as a neuron's reluctance to spike twice in rapid succession. In order for refractoriness to be considered possible, the neuron must spike in response to the first pulse. In this example, the second pulse does not elicit an action potential from the neuron even though the second pulse has an amplitude well above the resting threshold current because it is still recovering from the first pulse and thus, is said to be in a refractory state. Facilitation typically occurs, as shown in Fig. 2.2B, when the masker-probe interval is small and both pulses are below the average threshold current. Effectively, this causes the first pulse to not generate a spike, but since the membrane potential remains near threshold long enough, the second pulse can push the membrane potential beyond threshold, resulting in a spike. Sometimes referred to as subthreshold adaptation (Brette and Gerstner, 2005), accommodation also occurs when there is a subthreshold response to the masker pulse, but unlike facilitation, this leads to reduced excitability for the probe pulse response. When the masker-probe

interval is so large as to allow the membrane potential to decay back near or below rest, then in addition to a lack of facilitation, it is sometimes observed that the membrane excitability is suppressed for a short time. This can result in the probe pulse insufficiently exciting the neuron to trigger a spike even though the second pulse amplitude is above the resting threshold current, as shown in Fig. 2.2C. Moving beyond the masker-probe stimulus paradigm, when a neuron is exposed to an ongoing pulse train, spike rate adaptation can occur in some neurons such that the spike rate decreases over time, even more than can be explained by refractoriness. This form of adaptation is distinct from accommodation in that spike rate adaptation is dependent on ongoing spiking (Benda and Herz, 2003; Brette and Gerstner, 2005). Over multiple trials, the spike rate can be determined by averaging the number of spikes occurring within a time interval. Figure 2.2D shows the membrane potential response to one trial in which the neuron progressively loses its ability to spike for every pulse.

The degree of refractoriness, facilitation, and accommodation (or their functions) can be mapped by using a paired-pulse (or masker-probe) paradigm by varying the levels of each pulse and the lag between them. Several experiments have been successful at measuring the refractory function, which shows the recovery in response to the second pulse given a spike in response to the first pulse. Facilitation and accommodation are described by the likelihood of a spike to occur in response to the probe pulse, given a subthreshold response to the masker pulse. Essentially, when the neuron constructively uses both pulses to produce one spike, it is referred to as facilitation, otherwise, when both pulses work to effectively desensitize the neuron, producing no spikes, we call this accommodation. However, the effects of facilitation and accommodation may be greater in response to pulse train stimulation compared to a paired pulse response due to accumulation of the effects over the duration of the pulse train. Finally, spike rate adaptation is the neuron's tendency to lower its excitability in response to its prior spiking activity, i.e., spikes occurring before the immediately preceding spike. Taken together, it is easy to formulate scenarios in which more than one, or all four behaviors simultaneously overlap (see Fig. 2.3E). Data illustrating these phenomena have been available in the literature for more than a decade in some cases (see the following section), yet physiological and perceptual data are often interpreted in light of refractoriness alone, with the other three stimulus-response phenomena not taken properly into consideration. In this review article, we will present the current state of methods which quantify each behavior's contribution to SGN activity and the respective emerging biophysical mechanisms.

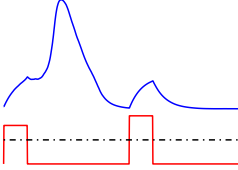
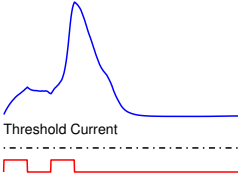
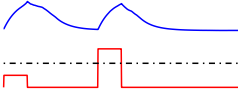
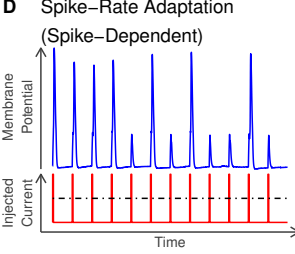
Phenomenon	Mechanisms	Reference
A Refractoriness 	Dominant effects <ul style="list-style-type: none"> - Absolute Refractory Period (ARP): Na channel inactivation, higher conductance of delayed-rectifier K channel - Relative Refractory Period (RRP): Na channel inactivation Secondary effects <ul style="list-style-type: none"> - HCN and KLT channels contribute to extending ARP - KLT channels lengthen the RRP - Rapidly activating, transient K_F current shortens RRP 	Hodgkin and Huxley (1952); Matsuoka et al (2001) Hodgkin and Huxley (1952); Matsuoka et al (2001) Negm and Bruce (2014) Negm and Bruce (2014) Imenov and Rubinstein (2009)
B Facilitation (Temporal Summation) 	Passive effects <ul style="list-style-type: none"> - Capacitive charging of membrane towards threshold potential Active effects <ul style="list-style-type: none"> - Residual Na activation increases excitability to next pulse 	Lapicque (1907) Hodgkin (1938); Hodgkin and Huxley (1952)
C Accommodation (Subthreshold Adaptation) 	General mechanisms <ul style="list-style-type: none"> - Subthreshold adaptive exponential IAF model - Na channel inactivation Ionic channel contributions in SGN <ul style="list-style-type: none"> - HCN channels: fewer open channels with ongoing subthreshold pulse train - HCN channels: hyperpolarization with depolarizing pulses leads to regulation of the RMP - KLT channel activation and extracellular K^+ accumulation 	Brette and Gerstner (2005) Frankenhaeuser and Vallbo (1965) Negm and Bruce (2014) Liu et al (2014) Miller et al (2011)
D Spike-Rate Adaptation (Spike-Dependent) 	General mechanisms <ul style="list-style-type: none"> - Spike-triggered adaptive exponential IAF model - M-type currents: high-threshold K channels - Afterhyperpolarization-type current - Fast Na current: slow recovery from inactivation Ionic channel contributions in SGN <ul style="list-style-type: none"> - HCN channels: accumulating afterhyperpolarization - Extracellular K^+ accumulation 	Benda and Herz (2003) Brette and Gerstner (2005) Brown and Adams (1980) Madison and Nicoll (1984) Fleidervish et al (1996) Negm and Bruce (2014) Baylor and Nicholls (1969); Woo et al (2009a,b,c)

Figure 2.2 Stimulus-response phenomena and their associated mechanisms. The *left column* (Phenomenon) shows sample SGN membrane potentials (*blue*) in response to monophasic current pulses (*red*) representing the different phenomena. These were generated with a Hodgkin–Huxley-type SGN membrane model (Negm and Bruce, 2014). The *horizontal black dot-dashed line* indicates the resting threshold current for the SGN model. Possible responsible mechanisms for each are listed in the *middle column* (Mechanisms), with the source listed in the *right column* (Reference). Note that each panel (**A–D**) represents one trial outcome, and in general, many trials are required to characterize each behavior due to the stochastic nature of the membrane potential and thus the resulting spiking. **A** Refractoriness appears as reduced excitability to the second pulse given a spike in response to the first pulse, whereas at longer inter-pulse intervals, a second spike is more probable.

Figure 2.2 (continued) **B** Facilitation acts as membrane integration of two subthreshold pulses at small inter-pulse intervals to enable an action potential in response to the second pulse, whereas in the case of **C** accommodation, the states of some ion channels are responsible for reducing excitability after a subthreshold masker pulse such that an action potential may not be generated in response to a following pulse above the resting threshold current. **D** In response to ongoing spiking due to pulse train stimulation, spike rate adaptation refers to the diminished spiking activity over longer timescales than refractoriness. *HCN* hyperpolarization-activated cyclic nucleotide-gated, *KLT* low-threshold potassium, *IAF* integrate-and-fire, *RMP* resting membrane potential.

2.2 Stimulus-Response Phenomena

2.2.1 Refractoriness

In healthy SGNs, refractoriness is actually a feature which enhances spike timing precision (Avisar et al., 2013). Yet, even though SGNs have one of the fastest post-spike recoveries (Cartee et al., 2006, 2000; Miller et al., 2001; Rattay et al., 2013), when CIs are involved refractoriness can be perceived as a limitation of the maximum firing rate in response to pulse rates of 2000 pulses/s or higher.

Just over a century has passed since refractoriness was discovered in nervous and cardiac tissue (Tait, 1910). At that point it was described with an operational definition as a period of reduced excitability immediately following an action potential. Figure 2.2A demonstrates this concept by a single trial of a neuron's membrane potential that is unable to spike in response to the second pulse. This operational definition of refractoriness significantly predates the discovery of voltage-gated ion channels and their dynamics that give rise to refractoriness (Hodgkin and Huxley, 1952).

Specifically, the refractory period is broken into an absolute refractory period (ARP) followed by a relative refractory period (RRP). The absolute refractory period is an interval of time which begins immediately following a spike when the neuron has a zero probability of spiking again to a second pulse of any magnitude. Following this 'dead-time', the relative refractory period is the interval of time where the elevated threshold for spiking eventually returns to the single pulse threshold. The effect of this temporary threshold increase and recovery on the response to a stimulus of a fixed current amplitude translates to a spiking probability throughout the course of the RRP that begins at 0, which eventually returns to the single pulse discharge probability.

Due to the stochastic nature of the Type I SGN, multiple trials of spikes responding to pulses must be averaged to characterize the refractory function. Numerous groups have done work to extract the refractory function of the auditory nerve from spike train data in response to an ongoing pulse train (Bi, 1989; June and Young, 1993; Mark and Miller, 1992; Miller, 1985; Miller and Mark, 1992; Prijs et al., 1993). However, this approach had limitations for practical CI stimulation strategies since it failed to take into account the pulse current level by only delivering pulse trains with constant level. In efforts to address

this issue, Dynes (1996), Cartee et al. (2000), and Miller et al. (2001) have used a two-pulse masker-probe paradigm to map out the refractory function. For example, shown in Fig. 2.3A is the result of using a masker-probe stimulus paradigm to uncover the refractory function. Miller et al. (2001) accomplished this by first determining the single pulse threshold (SPT) which, gathered over numerous trials, is the current level at which the neuron fires 50% of the time to a pulse while the neuron is at rest. A measure of the magnitude of the neuron's stochastic activity and dynamic range can also be calculated and is referred to as the relative spread (Bruce et al., 1999; Verveen, 1961). The masker-probe stimuli can then be delivered with a suprathreshold masker pulse and a variable level probe pulse separated by some masker-probe interval. After independently varying both the probe current level and the masker-probe interval for multiple trials each, the refractory function can be expressed as a ratio of the probe threshold to the single pulse threshold.

Data from several single neuron recordings in cats were fit to a function (shown in Fig. 2.3A) to extract the absolute and relative refractory periods. From this data, they found mean values for the ARP of 0.33 ms and the RRP time constant of 0.41 ms. Cartee et al. (2000) produced a value of 0.7 ms for the RRP time constant by pooling data from all cells in their recordings, also in cats. However, this value is confounded with the ARP since compared with the Miller et al. (2001) study, Cartee et al. (2000) did not specify an ARP value in their refractory function fit. Parameter extraction from the refractory function is difficult and the outcome may lead to uncertain results. Parameter estimates are sensitive to the number of data points, the masker-probe interval axis values, the initial guesses for the parameters, and any constraints on the parameters in the fitting procedure.

Although not explicitly stated by Miller et al. (2001), Fig. 2.3A shows a sizable proportion of neurons with relative refractoriness extending from 2 to 4 ms or greater and the refractory function fit undershoots the mean data points in that range. Similarly, in Cartee et al. (2000) the refractory function fit underestimates the mean data points from 2 to 3 ms (see Fig. 7 from Cartee et al., 2000). This longer timescale of relative refractoriness translates to a reduced neural excitability at pulse rates over 250 Hz. Protracted refractory periods have also been found in humans with CIs (Botros and Psarros, 2010; Cohen, 2009) using electrically evoked compound action potential (ECAP) measurements.

2.2.2 Facilitation and Accommodation

To the best of our knowledge, Lucas (1910) introduced the concept of two monophasic subthreshold pulses, separated by a 'summation interval' working to produce an action potential in response to the second pulse. The use of the term summation has persisted in several papers (Cartee et al., 2006, 2000) whereas Dynes (1996) named it sensitization. In this context, summation refers to temporal summation. This is different from spatial summation that describes the addition of numerous postsynaptic potentials (Kandel et al., 2000). To remove the ambiguity between temporal summation and spatial summation in this paper, we will adopt the term facilitation, which has been used previously in the

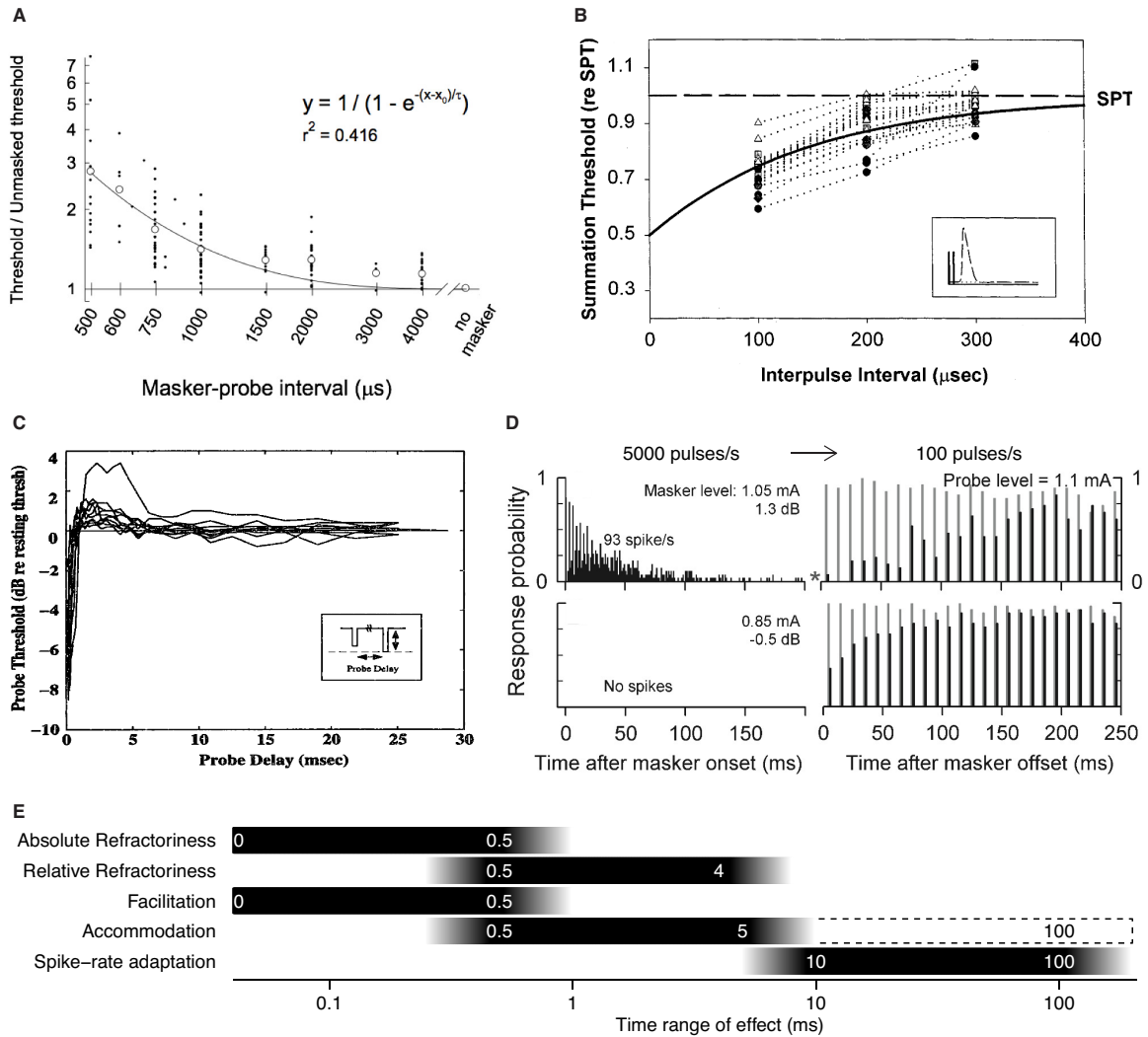


Figure 2.3 Published data from cat SGN recordings illustrating the four stimulus-response phenomena: **A** refractoriness, **B** facilitation, **C** accommodation, and **D** spike rate adaptation, and **E** a summary of the timescale ranges of their operation. Data in panels (A–C) were collected with monophasic pulses, while the data in panel D were in response to biphasic pulses. Data in panels A–C were obtained with masker-probe pairs of pulses at a range of intervals, and the responses were characterized by the ratio of the threshold current for the second (probe) pulse to the single pulse threshold (SPT; also referred to as the unmasked or resting threshold). **A** To determine the absolute and relative refractory behavior, only cases when the masker pulse elicits a spike are considered. Elevated probe pulse thresholds due to refractoriness are shown for multiple SGNs (*solid dots*) and their average (*open circles*) is fitted by the function (*black line*) with the equation given. **B** Reduced probe pulse thresholds due to facilitation are observed in the range of 100 to 300 μs . Data are shown for multiple SGNs and their average is fitted by an exponential function. **C** Both facilitation and accommodation were observed by using a masker-probe stimulation protocol including longer interpulse intervals. The masker pulse is set to levels of 2 to 0.5 dB below the single pulse threshold, while the level of the delayed probe is varied. Accommodation is seen at probe threshold values greater than 0 dB, whereas facilitation occurs below 0 dB. **D** Responses to a masker train (*left panels*, stimulating at a rate of 5000 pulses/s) and following responses to a probe train (*right panels*, stimulating at 100 pulses/s) displayed using normalized post stimulus time histograms. Probe responses (shown in the *right panels*) are displayed as black bars if preconditioned with a masker train, otherwise they are displayed as *gray bars*.

Figure 2.3 (continued) In the *top-left panel*, the masker train is delivered with a constant pulse current level, substantially above the SPT, whereas in the *bottom-left panel*, the masker train is delivered with a subthreshold current level. In all conditions, probe trains are set to a constant current level, close to threshold. Reduced excitability to the start of the probe train is observed for both the suprathreshold masker (*top-right panel*) and the subthreshold masker (*bottom-right panel*) compared to the cases with no masker train. The *bottom-left panel case* is indicative of accommodation while the *top-left panel case* may include the combined effects of spike rate adaptation and accommodation. **E** The time ranges that refractoriness, facilitation, accommodation, and spike-rate adaption operate at are shown as *black bars*. The *black-to-white gradients* indicate the variability in the time ranges. The *white bar outlined by a dashed black line* represents the time range of accumulated accommodation in response to pulse train stimulation shown in panel **D**. Panel **A** reprinted with kind permission of Springer Science & Business Media: Fig. 7 from Miller et al. (2001), © 2001. Panel **B** reprinted with kind permission of Elsevier: Fig. 5 from Cartee et al. (2000), © 2000. Panel **C** is used with permission from Fig. 3-2 of Dynes (1996). © Massachusetts Institute of Technology. Panel **D** adapted with kind permission of Springer Science & Business Media: Fig. 1 from Miller et al. (2011), © 2011.

literature to describe temporal summation (Cohen, 2009; Heffer et al., 2010; White, 1984). The term accommodation was used by Sly et al. (2007) and Heffer (2010) but has also been referred to as desensitization (Dynes, 1996) and inhibition (Cohen, 2009). However, we will persist with the historical nomenclature, namely accommodation which was introduced by Nernst (1908) and later developed further (Hill, 1936; Katz, 1936; Solandt, 1936) to describe how the membrane responds to a slowly changing stimulus current. Some of these earlier studies focused on one ramp stimulus, but in the context of CI stimulation, the issue of multiple pulses and how they precondition future pulses is more appropriate.

Phenomenologically, facilitation and accommodation represent two sides of the same coin when applied to CI stimulation. Following a subthreshold response to a masker pulse, the neuron can build on its depolarized membrane potential in order to facilitate an action potential in combination with the next pulse (Fig. 2.2B). Alternatively, it can accommodate to the masker pulse causing reduced excitability to the probe pulse. The reduced excitability is caused by the state of various ion channels following the response to the masker pulse (Fig. 2.2C). These definitions apply to typical single trial responses of masker-probe stimuli but vary to some extent due to stochastic membrane activity. Similar to the masker-probe stimuli methodology used for establishing the refractory function, multiple trials are necessary for characterizing the facilitation and accommodation functions in terms of threshold ratios.

Facilitation By setting both masker and probe pulses to a current level of 5% below threshold and varying the masker-probe interval, Lucas (1910) found a value of masker-probe interval which facilitated spiking in frog muscle tissue. More recently, Heffer et al. (2010) used biphasic pulse trains with stimulation rates between 200 to 5000 pulses/s at current levels corresponding to low, medium, and high onset spike probabilities to investigate facilitation in the auditory nerve. They could estimate the effect of facilitation as the increase in spiking probability from a single pulse to a pulse train in a 2 ms window, while

capping the spike count at 1. Consistent with the subthreshold notion of facilitation, they found that facilitation occurred predominantly at the low spike onset probabilities and increased as a function of the stimulation rate. As an improvement to the Lucas (1910) study, Cartee et al. (2006, 2000) expanded the experiment by concurrently varying the masker and probe current levels in single neuron recordings of feline Type I SGN. Cartee et al. (2006, 2000) computed the summation (facilitation) threshold relative to the SPT by stimulating with charge-balanced pseudo-monophasic masker-probe pulses in a fashion similar to that employed by Miller et al. (2001) for determining their refractory function. Technically, the only difference between the procedures was that as the pulse levels were varied to extract the threshold for a given masker-probe interval, Cartee et al. (2006, 2000) set both masker and probe pulses to equal current amplitudes. Figure 2.3B shows how this allowed for a functional description of facilitation in the tested range of 100 to 300 μ s. The facilitation model was assumed to be equal to half of the single pulse threshold at a masker-probe interval of 0 μ s, since both pulses would simply add. As the masker-probe interval increased, the effect of facilitation diminished and eventually tended towards the single pulse threshold. A caveat of the Cartee et al. (2000) study was the assumption that both masker and probe pulses were linearly additive in Type I SGNs. Upon closer examination of Fig. 2.3B, since a subset of the SGNs at 300 μ s had thresholds that were greater than the single pulse threshold, this notion is violated. Although Cartee et al. (2000) attributed this anomaly to a SGN threshold shift during the data collection procedure, an alternative explanation is that accommodation is responsible (Dynes, 1996; Sly et al., 2007).

Accommodation For cases of reduced neural excitability at short timescales, instances of accommodation are sparse in the refractory-dominated CI literature despite being well known in neuroscience. In a similar experimental protocol to Cartee et al. (2006, 2000), Dynes (1996) found evidence of the coexistence of facilitation and accommodation by significantly expanding the maximum masker-probe interval out to 25 ms. Figure 2.3C illustrates this point clearly, with data from 10 neurons in 4 different cats and by using a monophasic masker-probe paradigm. Specifically, masker levels were 2 to 0.5 dB lower than the SPT (i.e., where discharge probability = 0.5) and a tracking algorithm was employed to determine the probe threshold at all masker-probe interval values. Facilitation is said to occur when the probe threshold was less than 0 dB with respect to the SPT. In Fig. 2.3C, facilitation is observed below 0.5 to 1 ms, whereas when the masker-probe interval took on values between 1 and 5 to 10 ms accommodation occurred. Here, the mean probe threshold was 1 dB greater than the single pulse threshold. Finally, the return to the SPT at large masker-probe intervals is an indicator that the temporal interactions imposed on the membrane potential by the pulses is no longer in effect and the subthreshold responses may be considered independent. Given that we know the shape of the facilitation function (Cartee et al., 2006, 2000) and the combined effects of facilitation and accommodation (see Fig. 2.3C,E), it may be possible to obtain a separate accommodation function by using a subtractive fitting procedure.

Another instance of what could be interpreted as accommodation was reported for two subjects by Cohen (2009) in human biphasic CI stimulation with ECAP recording. In these two instances, accommodation was observed over the 0 to 6 ms masker-probe interval. Current levels were 20% for the probe pulse and slightly larger for the masker, nevertheless still below the 50% current level (see Figs. S3 and S4 of Cohen, 2009). Using single neuron recordings in deafened guinea pig and stimulating with trains of 200 pulses/s, Sly et al. (2007) also found evidence of accommodation that occurred at all levels of subthreshold current. In the next section, we will also discuss accommodation and how it can be misunderstood as spike rate adaptation.

2.2.3 Spike Rate Adaptation and Interacting Phenomena

Neural adaptation is a widely observed response seen in sensory systems. Its function is thought to remove redundant information and conserve energy. In this context, spike rate adaptation is thought to be one of the possible mechanisms by which neural adaptation occurs. More specifically, spike rate adaptation is a neuron's tendency to lower its excitability in response to ongoing action potentials. This is generally observed across timescales on the order of 10s to 100s of milliseconds (Heffer et al., 2010; Miller et al., 2011; Zhang et al., 2007) or even minutes (Litvak et al., 2003) but typically greater than those for refractoriness, facilitation, and accommodation. For example, one trial of a neuron's response to high-rate stimulation in Fig. 2.2D shows that initially, the neuron fires multiple consecutive action potentials, then later in the pulse train the occurrence of spikes diminishes. Therefore, the neuron is said to be adapting its spike rate. A neuron's spike rate can be quantified simply with a post-stimulus time histogram (PSTH) by counting the number of spikes occurring in a time bin, dividing by the width of that bin, then averaging over multiple trials. A naive assumption is that one can directly estimate the degree of spike rate adaptation from a PSTH. However, as we have seen in previous sections, the neuron's refractoriness, facilitation, and accommodation can also contribute to the shape of the PSTH, especially at small timescales (or high stimulation rates).

Zhang et al. (2007) explored effects on the spike rate by applying pulse trains at various stimulation rates and current levels to cat SGNs. Generally, the shape of the PSTHs across all conditions was described by a decay from an initial maximum spike rate towards a stabilized lower spike rate. The exception to these canonical PSTHs appeared in the case where neurons responded to the 10 000 pulses/s pulse train for a current level lower than the SPT. Beyond some initial spiking activity, the final spike rate reached 0 spikes/s (see the upper-rightmost panel of Fig. 2 of Zhang et al., 2007), which implied an ongoing accommodation to the subthreshold pulse train.

In a follow-up study, Miller et al. (2011) investigated both the build up of and the recovery from adaptation. The stimulation paradigm involved applying a "masker" pulse train to induce adaptation and immediately after the cessation of the masker to switch to a low-rate "probe" pulse train, in order to observe the recovery from adaptation. Figure 2.3D shows

two particularly different cases: illustrating that either suprathreshold or subthreshold masker pulse trains can reduce excitability to future probe pulse trains. In the top-left panel of Fig. 2.3D, a suprathreshold masker pulse train at 5000 pulses/s elicits a slowly decaying spike rate (black bars) over a 200 ms interval, which on the surface, appears to be spike rate adaptation. The top-right panel of Fig. 2.3D shows what happens when the pulse rate subsequently drops to 100 pulses/s for the probe pulse train, which had a near-threshold current level: the spikes rate (black bars) remains near zero for the first two pulses, and then the spike rate gradually increases back towards the unmasked spike rate (shown by the gray bars) over a period of around 200 ms. Thus, the build-up of spike rate adaptation and recovery from that adaptation appear to occur on similar time scales of 10s to 100s of milliseconds. In the bottom panels of Fig. 2.3D this stimulus paradigm is replicated but with the masker pulse train at a subthreshold current level, which leads to generating no action potentials during this interval.

Despite the lack of spikes to the 5000 pulses/s subthreshold masker train (bottom-left panel of Fig. 2.3D), when the pulse rate switches to 100 pulses/s for the probe pulse train the spike rate (black bars in the bottom-right panel of Fig. 2.3D) is again reduced relative to the unmasked spike rate (gray bars) and takes around 100 ms to recover. It thus appears that *accommodation* was accumulating during the 200 ms of the high-rate masker pulse train, and it took the SGN some time to recover from this accommodation once the pulse rate dropped to 100 pulses/s for the probe pulse train. This suggests that such a level of baseline recovery that is attributed to accommodation seen here in the bottom panels of Fig. 2.3D could also be present along with the spike rate adaptation shown in the top panels of Fig. 2.3D. Refractoriness also makes an appearance in the top-left panel of Fig. 2.3D, for times less than 25 ms, in the form of the oscillatory response whereas the spike rate adaptation component of the normalized PSTH is its slowly-decaying envelope.

Studies by Litvak et al. (2001) and Heffer (2010) have reported on accommodation in response to biphasic pulse trains. The results of similar experiments by Zhang et al. (2007) also showed evidence of reduced excitability due to subthreshold responses although it was not explicitly stated by the authors. True spike rate adaptation should only depend on the onset spike rate. However, Zhang et al. (2007) found that greater spike rate decrements occurred for higher pulse rates at equal onset spike rate (see Fig. 5D–I of that article). In fact, all three experimental studies (Heffer, 2010; Litvak et al., 2001; Zhang et al., 2007) showed that the normalized spike rate decrement (or spike reduction ratio) increased concomitantly with stimulus frequency. This indicates that accommodation is contributing to the spike rate decrement in parallel to spike rate adaptation.

Due to the simultaneous interaction of refractoriness, facilitation, accommodation, and spike-rate adaption, several groups have proposed computational methods to disentangle the contributions of a subset of stimulus-response phenomena to the total spike rate. Using similar techniques, Trevino et al. (2010) and Plourde et al. (2011) were able to extract a rudimentary refractory function (i.e., low temporal resolution) from the neuron's spiking history given an acoustic stimulus, but this framework could easily be extended for electrical stimulation. Campbell et al. (2012) were also able to delineate between

the effects of refractoriness and spike rate adaptation using constant and variable pulse train amplitudes. Similar work has been done to predict the effect of facilitation and refractoriness on the spiking pattern (Goldwyn et al., 2012). However, spike rate adaptation was not addressed. Thus, to date there have been several attempts to mathematically separate subsets of the four stimulus-response phenomena, but it remains to develop a mathematical methodology for fully isolating all four phenomena from a set of spike trains. Future methods which attempt to separate the effects of facilitation and/or accommodation from the spike rate must consider the current level of the stimulus pulse train. This is in contrast to refractoriness and spike-rate adaption which can be detected from spiking only.

2.3 Mechanisms and Models

In parallel to the subthreshold and suprathreshold Type I SGN phenomena we have just discussed, insights into the mechanisms responsible for these phenomena have begun to take shape with the help of relatively recent electrophysiology and computational modeling work. Historically, Hodgkin and Huxley (1952) laid the groundwork for mechanisms of action potential depolarization, repolarization, and fast afterhyperpolarization in squid giant axon. In their model, the principle ionic currents were formed by the fast sodium and delayed-rectifier potassium voltage-gated ion channels. To this day, these channels are central to explaining the biophysical underpinnings of neural excitation in the SGN and thus, are used in many computational models (Cartee, 2000, 2006; Chow and White, 1996; Imennov and Rubinstein, 2009; Matsuoka et al., 2001; Miller et al., 2011; Mino et al., 2004; Negm and Bruce, 2008, 2014; Phan et al., 1994; Rattay, 2000; Rattay and Danner, 2014; Rattay et al., 2001, 2013; Rubinstein, 1995; Smit et al., 2008; Woo et al., 2009a,b, 2010). However, the ion channels of the Hodgkin–Huxley model alone cannot explain long relative refractoriness, long-term accommodation, and spike rate adaptation.

Research has begun to address the effect of CI stimulation in mammalian auditory systems by using more biologically-realistic information and models. In doing so, a remarkable diversity of voltage-gated ion channel types have been revealed in Type I SGNs. To follow up on the Hodgkin–Huxley sodium channels, a modern survey of the Type I SGN in mice revealed $\text{Na}_v1.6$ channel subunits located at all nodes of Ranvier with particularly higher densities at the unmyelinated afferent process innervating the IHC layer and the nodes flanking the soma (Hossain et al., 2005). In end-stage postnatal development murine Type I SGN, Adamson et al. (2002) found several potassium channel subunits. Specifically, the high frequency basal neurons were dominated by high threshold fast delayed rectifier $\text{K}_v3.1$, low-threshold $\text{K}_v1.1$, and calcium-activated K^+ subunits, while the low frequency apical neurons showed a majority of inactivating $\text{K}_v4.2$ subunits known for extending the latency of spiking near threshold.

Of particular importance to the SGN response phenomena are the $\text{K}_v1.1$ and $\text{K}_v1.2$ low threshold potassium (KLT) and hyperpolarization-activated cyclic nucleotide-gated cation

(HCN) channel subunits. The kinetics of both channel types operate at slower timescales than the Hodgkin–Huxley channels (Liu et al., 2014b; Rothman and Manis, 2003). KLT channels are responsible for increasing the cell's voltage threshold and hyperpolarizing the resting membrane potential (Liu et al., 2014a). HCN channels are well known for being permeable to Na^+ and K^+ with ratios ranging from 1:3 to 1:5 (Biel et al., 2009). When HCN is activated under membrane hyperpolarization, this generates a dominant inward Na^+ current which helps return the membrane potential back towards rest. HCN channels contribute to stabilizing the resting membrane potential of SGNs (Liu et al., 2014a,b), a function that HCN appears to fulfill in a range of different cell types (Benarroch, 2013; Howells et al., 2012; Robinson and Siegelbaum, 2003). An interesting property of the current produced by HCN channels, known as I_h , is that it can increase the neuron's firing by a rebound excitation which happens towards the end of a hyperpolarizing pulse (Chen, 1997).

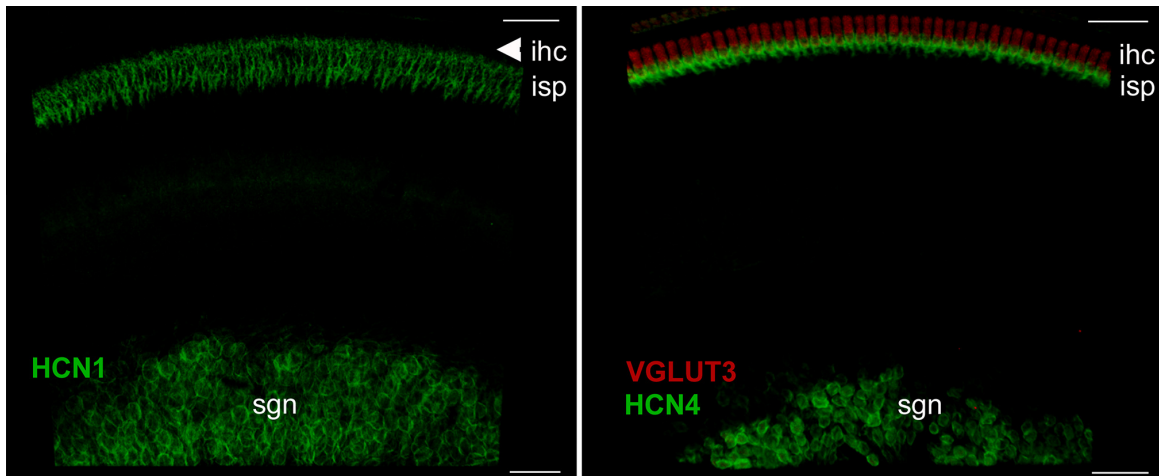


Figure 2.4 Hyperpolarization-activated cyclic nucleotide-gated (HCN) channel subunit expression in rat cochlea identified on Type I SGN. Labelled in green, both HCN1 and HCN4 subunits are localized to the nodes of Ranvier neighboring the cell body and the first peripheral node of Ranvier, or the inner spiral plexus (ISP). Shown in red, vesicular glutamate transporter 3 (VGLUT3) was used to identify inner hair cells (IHCs). Reprinted with kind permission of the American Physiological Society: Fig. 4 from Yi et al. (2010), © 2010.

Recently, Yi et al. (2010) complemented the Hossain et al. (2005) $\text{Na}_v1.6$ subunit localization of HCN subunits in rat Type I SGN. Figure 2.4 shows the HCN1 and HCN4 subunits at nodes surrounding the soma and the first peripheral node. Although it remains unclear where the KLT channels in Type I SGN are located, several studies have shown that they are indeed present. $\text{K}_v1.2$ subunits were found on axons of rat Type I SGNs projecting to the anteroventral cochlear nucleus (Bortone et al., 2006). Mo et al. (2002) found $\text{K}_v1.1$ subunits on cell bodies and axons of Type I SGN in mice. Again in mice, Reid et al. (2004) found differential densities of $\alpha\text{-K}_v1.1$ subunits along the cochlea. Type I SGNs in the basal cochlear region showed a greater expression than those in the apical regions. A better understanding of the localization of KLT channels in other sensory systems may serve as a starting point for investigation in Type I SGNs. For example, in mammalian retinal

ganglion neurons, reviews of voltage-gated ion channels by Rasband and Shrager (2000) and Lai and Jan (2006) unambiguously show that $K_v1.1$ and $K_v1.2$ subunits, responsible for the low-threshold potassium current, cluster on the cell membrane in the region under the myelin sheath but proximal to the node of Ranvier, otherwise known as the juxtaparanode.

2.3.1 Refractoriness

Amongst the various definitions for refractoriness, neuroscience textbooks, e.g., Kandel et al. (2000), often portray the simplistic view that sodium channel inactivation is the cause. However, the SGN has multiple other ion channel types which also shape the cell's refractory properties. Because of this, it becomes infeasible to concisely describe refractoriness in terms of ion channel activity. This is where the first operational description that Tait (1910) offered is attractive. Several computational studies have augmented the Hodgkin–Huxley standard with additional channel types found in SGNs in order to understand their contribution to refractoriness given the results from mammalian CI studies.

Imenov and Rubinstein (2009) used a computational model of cat SGN axon embedded with the fast sodium channels, rapidly activating and transient potassium channels, and delayed rectifier channels. This combination yielded an absolute refractory period 0.75 ms, which is longer than the range reported in Miller et al. (2001). Imenov and Rubinstein (2009) reported a relative refractory period of 5 ms, which is greater than the mean 442 μ s that Miller et al. (2001) produced, yet shows promise in terms of accounting for the long relative refractory period observed in a fraction of the SGNs (recall Fig. 2.3A). With a persistent sodium current added to the temperature-modified Hodgkin–Huxley model of the human Type I SGN, Smit et al. (2010) found similar values for the ARP and RRP time constant of 0.8 ms and 3 ms, respectively. More recently, by using a node of Ranvier model of cat SGN with fast sodium and delayed rectifier channels, Negm and Bruce (2014) iteratively augmented the model with HCN and KLT channels. Even though the model variants could not explain cases of long relative refractoriness, they found ARPs in the same range to that of Miller et al. (2001), with 0.31 ms for the Hodgkin–Huxley channels only, 0.4 ms when both HCN and KLT were added and intermediate values when only one channel type was added, although KLT produced the largest single change.

In general, biophysical neuron models use a bottom-up approach to predict higher-order emergent phenomena. It must be kept in mind that defining a model that can simultaneously predict refractoriness, facilitation, accommodation, and spike rate adaptation is often problematic due to the complexity that stems from a high dimensional parameter space exploration. A rather salient example of this issue is depicted in Fig. 6 of Miller et al. (2011). It shows that even after varying the densities of two unique potassium ion channel types, the model cannot successfully predict one ratio of densities that can simultaneously and accurately quantify refractoriness and spike rate adaptation in electrically stimulated SGNs.

2.3.2 Facilitation

One of the possible mechanisms for facilitation, i.e., the process of stimulating with sequential pulses thus leading to a spiking on the last pulse (see Fig. 2.2B), is through capacitive membrane charging. Conceptually, this can be understood with the venerable integrate-and-fire model (Brunel and van Rossum, 2007; Burkitt, 2006; Knight, 1972; Lapicque, 1907). If depolarizing monophasic pulses are separated by some time which is smaller than the membrane time constant, then the charge accumulated on the membrane from the first pulse will be too great to completely discharge before the membrane begins to integrate the next pulse. This process accumulates until the membrane potential reaches threshold, then fires. One of the caveats of relying solely on membrane charging to account for facilitation is that the charge across the membrane dissipates faster when the neuron is presented with the second hyperpolarizing phase of a biphasic pulse. This would diminish the accumulation of charge that would otherwise augment the effectiveness of the next pulse. However, experiments have shown that facilitation is also present in cases of biphasic pulse stimulation (Cohen, 2009; Heffer et al., 2010) which implies that there is an active agent that can at least partially suppress the hyperpolarizing phase.

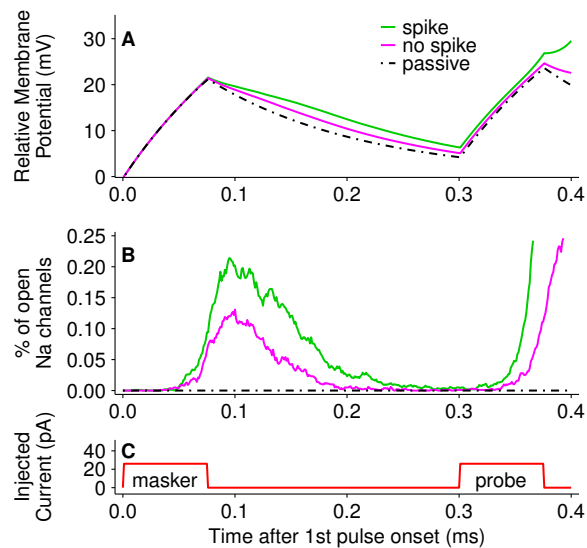


Figure 2.5 Illustration of passive and active contributions to the facilitation (temporal summation) phenomenon, generated with a Hodgkin–Huxley-type SGN membrane model (Negm and Bruce, 2014). **A** Relative membrane potential and **B** % of open Na channels responding to a **C** monophasic masker–probe stimulation paradigm with $75\ \mu\text{s}$ /phase pulse durations. Responses were averaged over 100 simulation trials for the relative membrane potential and % of open Na channels. Panels **A** and **B** show instances when the model SGN spiked (green curve) in response to the probe pulse, when it did not spike (magenta curve) in response to the second pulse, and where the fraction of open ion channels were fixed at their resting values (passive response; black, dot-dashed curve). By comparing the cases of spiking versus no spiking, it is apparent that when the SGN spiked it was caused by an increased number of Na channels flicking open in response to the first pulse, such that the membrane potential decayed back towards rest more slowly than it did for cases where the SGN did not spike. The increased depolarization of the membrane at the time when the second pulse is delivered contributes to greater facilitation than would be produced by the passive response.

A mechanism which could explain facilitation with either monophasic or biphasic stimulation relates to sodium activation near threshold (Hodgkin, 1938). In cases where the membrane potential is near the threshold potential and the neuron does not produce an action potential, “residual” sodium activation can sustain the membrane potential near the threshold potential longer than the duration of the pulse, as illustrated in Fig. 2.5 (see also Figs. 10–11 of Hodgkin, 1938). Figure 2.5A compares membrane potential responses of a mammalian temperature-adjusted Hodgkin–Huxley model (Negm and Bruce, 2014) stimulated by two monophasic pulses (Fig. 2.5C) in three different cases. Each trace shown is the average of 100 simulations for that particular case. The first case is that of a passive membrane response (black dot-dashed curve), for which the numbers of open ion channels are fixed at their resting values. This curve shows the passive charging up and decay of the membrane potential in response to the two pulses. In the second and third cases, the model ion channels were allowed to obey their prescribed voltage-dependent gating dynamics. The magenta curve corresponds to 100 trials in which the model SGN happened to *not* spike in response to the second pulse, whereas the green curve corresponds to 100 trials in which the model *did* spike to the second pulse. In both cases, the decay of the membrane potential back towards rest after the first (masker) pulse is slower than for the passive membrane, because of the action of the Na channels. Figure 2.5B shows the average percentage of open Na channels as a function of time. It can be observed that for the case where the model did spike (green curve), a greater number of sodium channels happened to open up in response to the depolarization from the first (masker) pulse when compared to the case where the model did not spike (magenta curve). The greater number of open Na channels led to a slower decay of the membrane potential during the interpulse interval and a higher residual membrane potential at the time of the second (probe) pulse, thus facilitating a spike. With regards to facilitation in response to trains of biphasic pulses, a Frankenhaeuser–Huxley model of a myelinated neuron mimicked (simulated) facilitation when stimulated with multiple biphasic conditioner pulses (see Fig. 8 of Butikofer and Lawrence, 1979). Although they did not explicitly examine the mechanisms, sodium activation is most likely to be the major active factor responsible for facilitation in the study by Butikofer and Lawrence (1979). The evidence points to the response of the masker pulse lowering the threshold for the response to probe pulse as the pulses move closer together (see Fig. 2.3B) after conducting multiple trials to discern the average behavior of facilitation. Therefore, the effect of sustained subthreshold sodium activation build-up (active facilitation) combined with the capacitive membrane charging (passive facilitation) from multiple pulses makes the mechanism for facilitation easier to understand, although it is likely that sodium channel inactivation will limit the duration over which facilitation can accumulate.

2.3.3 Accommodation

As we have pointed out in § 2.2.2, there is a shortage of CI-related research on accommodation. Yet, as little as one subthreshold pulse can easily precondition responses of future stimuli such that they have elevated thresholds. Despite the subthreshold adaptation exhibited by some generalized mathematical models (Brette and Gerstner, 2005; Izhikevich, 2003), unfortunately biophysical mechanisms for accommodation are less well understood. However, one notable study gave some direction to accommodation in neurons with fast sodium and delayed-rectifier potassium channels (Frankenhaeuser and Vallbo, 1965). They found that out of all parameters in a model of frog neuron, sodium inactivation correlated the highest with rapid accommodation. The involvement of sodium inactivation may have some explanatory power when the neuron spikes infrequently in response to pulse train stimuli due to residual sodium inactivation. However, sodium inactivation in response to a subthreshold masker pulse may not have sufficient strength and duration to fully explain the degree of accommodation experienced by the probe pulse in all cases.

Modern experimental studies have shown that several ion channel types may be implicated in generating currents that could further contribute to accommodation over a range of timescales, particularly beyond the timescale of sodium inactivation. For example, KLT channels show evidence of hyperpolarizing tail currents following subthreshold depolarizing voltage-clamp pulses (see Fig. 8 of Rothman and Manis, 2003) when their inactivation properties are taken into account. Further, a small but non-negligible, hyperpolarizing HCN conductance exists at voltages just above the resting membrane potential (RMP) of Type I SGNs (see Fig. 6 of Liu et al., 2014b). Both of these instances drop the membrane potential below the RMP at the offset of depolarizing pulses and under these conditions, increase the threshold for the next pulse.

In a stochastic Hodgkin–Huxley model augmented with HCN channels, Negm and Bruce (2014) determined that the I_h current was involved in accommodation. The stimulation used was a 20 ms 2000 pulses/s biphasic pulse train at a constant current amplitude corresponding to a single pulse spiking probability of 0.2. When only collecting the 20 ms trials that elicited no spikes, the interpulse membrane potential and the fraction of open HCN channels concomitantly experienced an ongoing drop in response to each successive subthreshold pulse. Over time, this leads to a lowered SGN excitability by distancing the membrane potential from threshold.

2.3.4 Spike Rate Adaptation

An effort to explicitly model spike rate adaptation for CI stimulation was developed in a series of papers by Miller et al. (2011) and Woo et al. (2009a,b, 2010). The idea was that during the repolarization of an action potential, K^+ ion efflux contributed to incrementally increasing the extracellular K^+ ion concentration. This would progressively shift the resting membrane potential to a more positive value, leading to sodium channel inactivation

and thus, reduce the excitability of the cell. Even though the models were successful for predicting spike rate adaptation in response to low and high rates of stimulation, the biophysical mechanism was taken from the leech central nervous system (Baylor and Nicholls, 1969) and the applicability to mammalian auditory physiology remains in question.

One of the key findings on the cause of spike rate adaptation in the auditory system was found in a study by Mo et al. (2002). By injecting a constant current into rapidly-adapting murine Type I SGNs and blocking $K_v1.1$ channels, the neuron significantly increased its excitability. In another auditory neuron, namely the medial nucleus of the trapezoid body, Brew et al. (2003) also demonstrated elevated excitability in $K_v1.1$ subunit deficient mice, compared to the wild-type and heterozygous variants. These findings motivated multiple groups to incorporate the KLT channels in their modeling of CI stimulation (Miller et al., 2011; Negm and Bruce, 2008, 2014). Without using the extracellular potassium mechanism, Negm and Bruce (2008, 2014) simulated spike rate adaptation behavior by adding KLT and HCN channels to their computational node of Ranvier model. It was found that HCN affected the firing rate under stimulation rates ranging from low to high, whereas KLT only became a factor at the high stimulation rates.

Other possible contributors may explain reduced excitability to an ongoing stimulus. Sources include the sodium-potassium pump, which produces a slow afterhyperpolarization (Gulledge et al., 2013), channel mechanisms from different systems (Brown and Adams, 1980; Fleidervish et al., 1996; Madison and Nicoll, 1984), and several general models (Benda and Herz, 2003; Brette and Gerstner, 2005). However, further research is necessary to determine their applicability to Type I SGNs.

2.4 Spatial Effects of CI Stimulation Related to Temporal Interactions

The Type I SGN response to CI stimulation is very different from its response to synaptic input from an IHC. The firing pattern of a single SGN when stimulated by a CI is the combined result of spatial and temporal interactions. Due to current spread, the SGN receives smeared pulse streams originating from multiple independent neighboring electrodes. While the strongest current is from the closest electrode, distal electrodes may impose a subthreshold influence on the SGN which can result in both facilitation and accommodation. The case of current spread illustrated in Fig. 2.1B–C is applicable for cases of moderate-rate stimulation (in this illustration 900 pulses/s on each electrode) with pulse trains coming from nearby electrodes in a monopolar configuration (i.e., with the return electrode outside the cochlea). The types of patterns produced across the electrode array will depend on exactly which coding strategy is implemented in the CI sound processor (for a review of different approaches see Loizou, 1998), the mapping from acoustic frequency

channels to electrodes (which varies from user to user), and the spectrum of the sound. The pattern of pulses in Fig. 2.1B could potentially be produced by a broad spectral peak processed by a peak-based strategy such as the Advanced Combined Encoder or Spectral Peak schemes (ACE, SPeak; Cochlear Corp., Sydney, Australia), or alternatively by the Continuous Interleaved Sampling strategy (CIS; Wilson et al., 1988, 1993) mapped to 8 neighboring electrodes. To reduce the effects of current spread for a CIS strategy, the 8 channels could be mapped to more widely-spaced electrodes on the array. However, for monopolar stimulation the current spread is so broad that the spatial summation is still likely to strongly affect the temporal interactions. Therefore, efforts to reduce current spread have been proposed that could lead to the reduction of subthreshold effects and the targeting of smaller subpopulations of SGNs per channel. Some promising methods are being developed for more accurately steering current towards the intended SGNs, such as using bipolar, tripolar, or even multipolar electrode configurations (van den Honert and Kelsall, 2007).

In addition to the issue of which SGN is stimulated by which current pulse, another concern for stimulation by a CI is the variability in the site of spike initiation, i.e., on which node of Ranvier for a particular SGN the spike is first generated. In the healthy acoustically-driven ear, spikes are initiated at the peripheral terminal aided by a dense population of $\text{Na}_v1.6$ channels (Hossain et al., 2005). The spike timing of the SGN inherits variability from the synaptic transmission process between an IHC that is characterized by probabilistic release of vesicles (Glowatzki and Fuchs, 2002; Heil et al., 2007; Safieddine et al., 2012). However, the spike timing of the SGN is known to have intrinsic variability due to the inherent stochasticity of voltage-gated ion channel fluctuations (Sigworth, 1981; Verveen and Derksen, 1968). While smaller in magnitude than IHC vesicle release variability, the effect of ion channel fluctuations in SGNs is larger than for many other types of neurons since membrane noise is greater at small node of Ranvier diameters (Verveen, 1962). So in the case of cochlear implant stimulation, even with just one extracellular electrode, these same stochastic properties promote multiple locations on the SGN from where an action potential can originate (Miller et al., 2003; Rattay et al., 2001; Sly et al., 2007), in contrast to the reliable spike initiation at the peripheral terminal for synaptic transmission by an IHC. In a stochastic model of an SGN axon, Mino et al. (2004) demonstrated that spike timing variability was maximized near the single pulse threshold current level and the spike initiation node exhibited a wider distribution as the electrode-to-axon distance increased. If the peripheral processes of SGNs begin to deteriorate following IHC loss (e.g., Hardie and Shepherd, 1999; Webster and Webster, 1981), then the nodes of Ranvier flanking the soma may serve as the predominant loci for CI-induced excitability since they also contain a relatively high density of $\text{Na}_v1.6$ subunits (Hossain et al., 2005).

Furthermore, due to the underlying ion channels mechanisms, membrane potential responses are dependent on the polarity and the pulse shape of the stimulation. It is possible for anodic and cathodic pulse phases to cause different patterns of depolarization and hyperpolarization across the nodes of Ranvier in an SGN. For example, in the simplest case, by stimulating with monophasic pulses using computational models of cat and human

SGNs, Rattay et al. (2001) demonstrated that while model cat SGNs were more easily excited with the cathodic polarity, model human nerves displayed greater sensitivity to the anodic pulse. This result was confirmed in humans with biphasic pulses (Macherey et al., 2008). Therefore, care should be taken in generalizing across stimulation pulse type and species with respect to the response properties of refractoriness, facilitation, accommodation, and spike rate adaptation, because the site of action potential initiation or the patterns of subthreshold depolarizations and hyperpolarizations along an axon will be dependent on the exact electrode-neuron geometry and the pulse waveform.

2.5 Conclusions

We are still in the infancy of the Type I SGN characterization of ion channel type and location across different species. As a result, different phenomena have been explored in different classes of SGNs ranging from the base to the apex of the cochlea and from low to high thresholds. More research must be done to determine if all four behaviors: refractoriness, facilitation, accommodation, and spike rate adaptation can, in fact, be generated by a single Type I SGN. Even though biphasic stimulation is clinically relevant, our understanding of the neural response to biphasic stimulation is impoverished compared to the monophasic response. In the interim, computational modeling could be an important way to relate in vivo electrophysiological data to possible ion channel distribution, and determining if monophasic responses generalize to biphasic ones, or understanding the mechanisms, if they are different.

CIs are experiencing an interesting period in their development. Contemporary research is addressing methods of delivering stimulation from the CI to SGNs—all with the goal of improving speech perception in a variety of real-world settings. Many studies focus on how the stimulating paradigms can improve auditory perception. However, a look at SGN neurophysiological data show that there are definite temporal operating limits which should be considered for CI stimulation. Going forward, approaches that are successful at taking into account the temporal characteristics of the stimulus-response phenomena (or the underlying SGN neurophysiology that gives rise to them) may provide the insights necessary for significantly improving the functionality of cochlear prostheses.

References

Adamson, C. L., Reid, M. A., Mo, Z.-L., Bowne-English, J., and Davis, R. L. (2002). Firing features and potassium channel content of murine spiral ganglion neurons vary with cochlear location. *J Comp Neurol*, 447(4):331–350.

- Arora, K., Dawson, P., Dowell, R., and Vandali, A. (2009). Electrical stimulation rate effects on speech perception in cochlear implants. *Int J Audiol*, 48(8):561–567.
- Avissar, M., Wittig, J. H., Saunders, J. C., and Parsons, T. D. (2013). Refractoriness enhances temporal coding by auditory nerve fibers. *J Neurosci*, 33(18):7681–7690.
- Balkany, T., Hodges, A., Menapace, C., Hazard, L., Driscoll, C., Gantz, B., Kelsall, D., Luxford, W., McMenemy, S., Neely, J. G., Peters, B., Pillsbury, H., Roberson, J., Schramm, D., Telian, S., Waltzman, S., Westerberg, B., and Payne, S. (2007). Nucleus Freedom North American clinical trial. *Otolaryngol Head Neck Surg*, 136(5):757–762.
- Baylor, D. A. and Nicholls, J. G. (1969). Changes in extracellular potassium concentration produced by neuronal activity in the central nervous system of the leech. *J Physiol*, 203(3):555–569.
- Benarroch, E. E. (2013). HCN channels: function and clinical implications. *Neurology*, 80(3):304–310.
- Benda, J. and Herz, A. V. M. (2003). A universal model for spike-frequency adaptation. *Neural Comput*, 15(11):2523–2564.
- Bi, Q. (1989). A closed-form solution for removing the dead time effects from the poststimulus time histograms. *J Acoust Soc Am*, 85(6):2504.
- Biel, M., Wahl-Schott, C., Michalakis, S., and Zong, X. (2009). Hyperpolarization-activated cation channels: from genes to function. *Physiol Rev*, 89(3):847–885.
- Bortone, D. S., Mitchell, K., and Manis, P. B. (2006). Developmental time course of potassium channel expression in the rat cochlear nucleus. *Hear Res*, 211(1-2):114–125.
- Botros, A. and Psarros, C. (2010). Neural response telemetry reconsidered: II. the influence of neural population on the ECAP recovery function and refractoriness. *Ear Hear*, 31(3):380–391.
- Brette, R. and Gerstner, W. (2005). Adaptive exponential integrate-and-fire model as an effective description of neuronal activity. *J Neurophysiol*, 94(5):3637–3642.
- Brew, H. M., Hallows, J. L., and Tempel, B. L. (2003). Hyperexcitability and reduced low threshold potassium currents in auditory neurons of mice lacking the channel subunit Kv1.1. *J Physiol*, 548(1):1–20.
- Brown, D. A. and Adams, P. R. (1980). Muscarinic suppression of a novel voltage-sensitive K⁺ current in a vertebrate neuron. *Nature*, 283(5748):673–676.
- Bruce, I. C., White, M. W., Irlicht, L. S., O’Leary, S. J., Dynes, S., Javel, E., and Clark, G. M. (1999). A stochastic model of the electrically stimulated auditory nerve: single-pulse response. *IEEE Trans Biomed Eng*, 46(6):617–629.

- Brunel, N. and van Rossum, M. (2007). Quantitative investigations of electrical nerve excitation treated as polarization. *Biol Cybern*, 97(5-6):341–349.
- Burkitt, A. N. (2006). A review of the integrate-and-fire neuron model: I. homogeneous synaptic input. *Biol Cybern*, 95(1):1–19.
- Butikofer, R. and Lawrence, P. D. (1979). Electrocutaneous nerve stimulation-II: stimulus waveform selection. *IEEE Trans Biomed Eng*, BME-26(2):69–75.
- Campbell, L. J., Sly, D. J., and O’Leary, S. J. (2012). Prediction and control of neural responses to pulsatile electrical stimulation. *J Neural Eng*, 9(2):026023.
- Cartee, L. A. (2000). Evaluation of a model of the cochlear neural membrane. II: comparison of model and physiological measures of membrane properties measured in response to intrameatal electrical stimulation. *Hear Res*, 146(1-2):153–166.
- Cartee, L. A. (2006). Spiral ganglion cell site of excitation II: numerical model analysis. *Hear Res*, 215(1-2):22–30.
- Cartee, L. A., Miller, C. A., and van den Honert, C. (2006). Spiral ganglion cell site of excitation I: comparison of scala tympani and intrameatal electrode responses. *Hear Res*, 215(1-2):10–21.
- Cartee, L. A., van den Honert, C., Finley, C. C., and Miller, R. L. (2000). Evaluation of a model of the cochlear neural membrane. I. physiological measurement of membrane characteristics in response to intrameatal electrical stimulation. *Hear Res*, 146(1-2):143–152.
- Chen, C. (1997). Hyperpolarization-activated current (I_h) in primary auditory neurons. *Hear Res*, 110(1-2):179–190.
- Chow, C. C. and White, J. A. (1996). Spontaneous action potentials due to channel fluctuations. *Biophys J*, 71(6):3013–3021.
- Cohen, L. T. (2009). Practical model description of peripheral neural excitation in cochlear implant recipients: 5. refractory recovery and facilitation. *Hear Res*, 248(1-2):1–14.
- Dynes, S. B. C. (1996). *Discharge characteristics of auditory nerve fibers for pulsatile electrical stimuli*. PhD thesis, Massachusetts Institute of Technology, Cambridge, Massachusetts.
- Fleidervish, I. A., Friedman, A., and Gutnick, M. J. (1996). Slow inactivation of Na^+ current and slow cumulative spike adaptation in mouse and guinea-pig neocortical neurones in slices. *J Physiol (Lond)*, 493(1):83–97.
- Frankenhaeuser, B. and Vallbo, A. B. (1965). Accommodation in myelinated nerve fibres of *Xenopus laevis* as computed on the basis of voltage clamp data. *Acta Physiol. Scand.*, 63(1-2):1–20.

- Friesen, L. M., Shannon, R. V., and Cruz, R. J. (2005). Effects of stimulation rate on speech recognition with cochlear implants. *Audiol. Neurootol.*, 10(3):169–184.
- Glowatzki, E. and Fuchs, P. A. (2002). Transmitter release at the hair cell ribbon synapse. *Nat Neurosci*, 5(2):147–154.
- Goldwyn, J. H., Rubinstein, J. T., and Shea-Brown, E. (2012). A point process framework for modeling electrical stimulation of the auditory nerve. *J Neurophysiol*, 108(5):1430–1452.
- Gulledge, A. T., Dasari, S., Onoue, K., Stephens, E. K., Hasse, J. M., and Avesar, D. (2013). A sodium-pump-mediated afterhyperpolarization in pyramidal neurons. *J Neurosci*, 33(32):13025–13041.
- Hardie, N. A. and Shepherd, R. K. (1999). Sensorineural hearing loss during development: morphological and physiological response of the cochlea and auditory brainstem. *Hear Res*, 128(1-2):147–165.
- Hartmann, R., Topp, G., and Klinke, R. (1984). Discharge patterns of cat primary auditory fibers with electrical-stimulation of the cochlea. *Hear Res*, 13(1):47–62.
- Heffer, L. F. (2010). *High rate electrical stimulation of the auditory nerve: examining the effects of sensorineural hearing loss*. PhD thesis, The University of Melbourne, Melbourne, Victoria.
- Heffer, L. F., Sly, D. J., Fallon, J. B., White, M. W., Shepherd, R. K., and O’Leary, S. J. (2010). Examining the auditory nerve fiber response to high rate cochlear implant stimulation: chronic sensorineural hearing loss and facilitation. *J Neurophysiol*, 104(6):3124–3135.
- Heil, P., Neubauer, H., Irvine, D. R. F., and Brown, M. (2007). Spontaneous activity of auditory-nerve fibers: insights into stochastic processes at ribbon synapses. *J Neurosci*, 27(31):8457–8474.
- Hill, A. V. (1936). Excitation and accommodation in nerve. *Proc R Soc B*, 119(814):305–355.
- Hodgkin, A. L. (1938). The subthreshold potentials in a crustacean nerve fibre. *Proc R Soc B*, 126(842):87–121.
- Hodgkin, A. L. and Huxley, A. F. (1952). A quantitative description of membrane current and its application to conduction and excitation in nerve. *J Physiol*, 117(4):500–544.
- Holden, L. K., Skinner, M. W., Holden, T. A., and Demorest, M. E. (2002). Effects of stimulation rate with the Nucleus 24 ACE speech coding strategy. *Ear Hear*, 23(5):463–476.
- Hossain, W. A., Antic, S. D., Yang, Y., Rasband, M. N., and Morest, D. K. (2005). Where is the spike generator of the cochlear nerve? Voltage-gated sodium channels in the mouse cochlea. *J Neurosci*, 25(29):6857–6868.

- Howells, J., Trevillion, L., Bostock, H., and Burke, D. (2012). The voltage dependence of I_h in human myelinated axons. *J Physiol (Lond)*, 590(Pt 7):1625–1640.
- Imennov, N. S. and Rubinstein, J. T. (2009). Stochastic population model for electrical stimulation of the auditory nerve. *IEEE Trans Biomed Eng*, 56(10):2493–2501.
- Izhikevich, E. M. (2003). Simple model of spiking neurons. *IEEE Trans. Neural Netw.*, 14(6):1569–1572.
- Javel, E. and Viemeister, N. F. (2000). Stochastic properties of cat auditory nerve responses to electric and acoustic stimuli and application to intensity discrimination. *J Acoust Soc Am*, 107(2):908.
- June, L. and Young, E. D. (1993). Discharge-rate dependence of refractory behavior of cat auditory-nerve fibers. *Hear Res*, 69(1-2):151–162.
- Kandel, E. R., Schwartz, J., and Jessell, T. (2000). *Principles of neural science*. McGraw-Hill Medical, 4th edition.
- Katz, B. (1936). Multiple response to constant current in frog's medullated nerve. *J Physiol*, 88(2):239–255.
- Kiefer, J., von Ilberg, C., Rupprecht, V., Hubner-Egner, J., and Knecht, R. (2000). Optimized speech understanding with the continuous interleaved sampling speech coding strategy in patients with cochlear implants: effect of variations in stimulation rate and number of channels. *Ann Otol Rhinol Laryngol*, 109(11):1009–1020.
- Knight, B. W. (1972). Dynamics of encoding in a population of neurons. *The Journal of General Physiology*, 59(6):734–766.
- Lai, H. C. and Jan, L. Y. (2006). The distribution and targeting of neuronal voltage-gated ion channels. *Nat Rev Neurosci*, 7(7):548–562.
- Lapicque, L. (1907). Recherches quantitatives sur l'excitation électrique des nerfs traitée comme une polarisation. *J Physiol Pathol Gen*, 9:620–635.
- Litvak, L. M., Delgutte, B., and Eddington, D. K. (2001). Auditory nerve fiber responses to electric stimulation: modulated and unmodulated pulse trains. *J Acoust Soc Am*, 110(1):368–379.
- Litvak, L. M., Smith, Z. M., Delgutte, B., and Eddington, D. K. (2003). Desynchronization of electrically evoked auditory-nerve activity by high-frequency pulse trains of long duration. *J Acoust Soc Am*, 114(4 Pt 1):2066–2078.
- Liu, Q., Lee, E., and Davis, R. L. (2014a). Heterogeneous intrinsic excitability of murine spiral ganglion neurons is determined by Kv1 and HCN channels. *Neuroscience*, 257:96–110.

- Liu, Q., Manis, P. B., and Davis, R. L. (2014b). I_h and HCN channels in murine spiral ganglion neurons: tonotopic variation, local heterogeneity, and kinetic model. *J Assoc Res Otolaryngol*, 15(4):585–599.
- Loizou, P. C. (1998). Mimicking the human ear. *IEEE Signal Processing Magazine*, 15(5):101–130.
- Loizou, P. C., Poroy, O., and Dorman, M. (2000). The effect of parametric variations of cochlear implant processors on speech understanding. *J Acoust Soc Am*, 108(2):790–802.
- Lucas, K. (1910). Quantitative researches on the summation of inadequate stimuli in muscle and nerve, with observations on the time-factor in electric excitation. *J Physiol*, 39(6):461–475.
- Macherey, O., Carlyon, R. P., van Wieringen, A., Deeks, J. M., and Wouters, J. (2008). Higher sensitivity of human auditory nerve fibers to positive electrical currents. *J Assoc Res Otolaryngol*, 9(2):241–251.
- Madison, D. V. and Nicoll, R. A. (1984). Control of the repetitive discharge of rat CA1 pyramidal neurones in vitro. *J Physiol*, 354:319–331.
- Mark, K. E. and Miller, M. I. (1992). Bayesian model selection and minimum description length estimation of auditory-nerve discharge rates. *J Acoust Soc Am*, 91(2):989–1002.
- Matsuoka, A. J., Rubinstein, J. T., Abbas, P. J., and Miller, C. A. (2001). The effects of interpulse interval on stochastic properties of electrical stimulation: models and measurements. *IEEE Trans Biomed Eng*, 48(4):416–424.
- Merzenich, M. M. and White, M. W. (1977). Cochlear implants: the interface problem. In Hambrecht, F. T. and Reswick, J. B., editors, *Functional Electrical Stimulation: Applications in Neural Prostheses*, pages 321–340. Marcel Dekker, Inc., New York.
- Miller, C., Abbas, P. J., Nourski, K. V., Hu, N., and Robinson, B. K. (2003). Electrode configuration influences action potential initiation site and ensemble stochastic response properties. *Hear Res*, 175(1-2):200–214.
- Miller, C. A., Abbas, P. J., and Robinson, B. (2001). Response properties of the refractory auditory nerve fiber. *J Assoc Res Otolaryngol*, 2(3):216–232.
- Miller, C. A., Woo, J., Abbas, P. J., Hu, N., and Robinson, B. K. (2011). Neural masking by sub-threshold electric stimuli: animal and computer model results. *J Assoc Res Otolaryngol*, 12(2):219–232.
- Miller, M. I. (1985). Algorithms for removing recovery-related distortion from auditory-nerve discharge patterns. *J Acoust Soc Am*, 77(4):1452–1464.

- Miller, M. I. and Mark, K. E. (1992). A statistical study of cochlear nerve discharge patterns in response to complex speech stimuli. *J Acoust Soc Am*, 92(1):202–209.
- Mino, H., Rubinstein, J. T., Miller, C. A., and Abbas, P. J. (2004). Effects of electrode-to-fiber distance on temporal neural response with electrical stimulation. *IEEE Trans Biomed Eng*, 51(1):13–20.
- Mo, Z. L., Adamson, C. L., and Davis, R. L. (2002). Dendrotoxin-sensitive K⁺ currents contribute to accommodation in murine spiral ganglion neurons. *J Physiol*, 542(3):763–778.
- Negm, M. H. and Bruce, I. C. (2008). Effects of I_h and I_{KLT} on the response of the auditory nerve to electrical stimulation in a stochastic Hodgkin–Huxley model. *Proc 30th Annu Int Conf IEEE Eng Med Biol Soc*, 2008:5539–5542.
- Negm, M. H. and Bruce, I. C. (2014). The effects of HCN and KLT ion channels on adaptation and refractoriness in a stochastic auditory nerve model. *IEEE Trans Biomed Eng*, 61(11):2749–2759.
- Nernst, W. (1908). Zur theorie des elektrischen reizes. *Pfluger Arch*, 122(7-9):275–314.
- Nie, K., Barco, A., and Zeng, F. G. (2006). Spectral and temporal cues in cochlear implant speech perception. *Ear Hear*, 27(2):208–217.
- Phan, T. T., White, M. W., Finley, C. C., and Cartee, L. A. (1994). Neural membrane model responses to sinusoidal electrical stimuli. In Hochmair-Desoyer, I. J. and Hochmair, E. S., editors, *Advances in Cochlear Implants*, pages 342–347, Vienna, Austria. Manz.
- Plant, K., Holden, L., Skinner, M., Arcaroli, J., Whitford, L., Law, M.-A., and Nel, E. (2007). Clinical evaluation of higher stimulation rates in the nucleus research platform 8 system. *Ear Hear*, 28(3):381–393.
- Plant, K. L., Whitford, L. A., Psarros, C. E., and Vandali, A. E. (2002). Parameter selection and programming recommendations for the ACE and CIS speech-processing strategies in the Nucleus 24 cochlear implant system. *Cochlear Implants Int*, 3(2):104–125.
- Plourde, E., Delgutte, B., and Brown, E. N. (2011). A point process model for auditory neurons considering both their intrinsic dynamics and the spectrotemporal properties of an extrinsic signal. *IEEE Trans Biomed Eng*, 58(6):1507–1510.
- Prijs, V. F., Keijzer, J., Versnel, H., and Schoonhoven, R. (1993). Recovery characteristics of auditory nerve fibres in the normal and noise-damaged guinea pig cochlea. *Hear Res*, 71(1-2):190–201.
- Rasband, M. N. and Shrager, P. (2000). Ion channel sequestration in central nervous system axons. *J Physiol*, 525 Pt 1:63–73.

- Rattay, F. (2000). Basics of hearing theory and noise in cochlear implants. *Chaos Soliton Fract*, 11(12):1875–1884.
- Rattay, F. and Danner, S. M. (2014). Peak I of the human auditory brainstem response results from the somatic regions of type I spiral ganglion cells: evidence from computer modeling. *Hear Res*, 315:67–79.
- Rattay, F., Lutter, P., and Felix, H. (2001). A model of the electrically excited human cochlear neuron. *Hear Res*, 153(1-2):43–63.
- Rattay, F., Potrusil, T., Wenger, C., Wise, A. K., Glueckert, R., and Schrott-Fischer, A. (2013). Impact of morphometry, myelination and synaptic current strength on spike conduction in human and cat spiral ganglion neurons. *PLoS ONE*, 8(11):e79256.
- Reid, M. A., Flores-Otero, J., and Davis, R. L. (2004). Firing patterns of type II spiral ganglion neurons in vitro. *J Neurosci*, 24(3):733–742.
- Robinson, R. B. and Siegelbaum, S. A. (2003). Hyperpolarization-activated cation currents: from molecules to physiological function. *Annu Rev Physiol*, 65:453–480.
- Rothman, J. S. and Manis, P. B. (2003). Kinetic analyses of three distinct potassium conductances in ventral cochlear nucleus neurons. *J Neurophysiol*, 89(6):3083–3096.
- Rubinstein, J. T. (1995). Threshold fluctuations in an N sodium channel model of the node of Ranvier. *Biophys J*, 68(3):779–785.
- Safieddine, S., El-Amraoui, A., and Petit, C. (2012). The auditory hair cell ribbon synapse: from assembly to function. *Annu Rev Neurosci*, 35(1):509–528.
- Sigworth, F. J. (1981). Covariance of nonstationary sodium current fluctuations at the node of Ranvier. *Biophys J*, 34(1):111–133.
- Sly, D. J., Heffer, L. F., White, M. W., Shepherd, R. K., Birch, M. G. J., Minter, R. L., Nelson, N. E., Wise, A. K., and O’Leary, S. J. (2007). Deafness alters auditory nerve fibre responses to cochlear implant stimulation. *Eur J Neurosci*, 26(2):510–522.
- Smit, J. E., Hanekom, T., and Hanekom, J. J. (2008). Predicting action potential characteristics of human auditory nerve fibres through modification of the Hodgkin-Huxley equations. *S Afr J Sc.*, 104(7-8):284–292.
- Smit, J. E., Hanekom, T., van Wieringen, A., Wouters, J., and Hanekom, J. J. (2010). Threshold predictions of different pulse shapes using a human auditory nerve fibre model containing persistent sodium and slow potassium currents. *Hear Res*, 269(1-2):12–22.
- Solandt, D. Y. (1936). The measurement of “accommodation” in nerve. *Proc R Soc B*, 119(814):355–379.

- Tait, J. (1910). The relation between refractory phase and electrical change. *Exp Physiol*, 3(3):221–232.
- Trevino, A., Coleman, T. P., and Allen, J. (2010). A dynamical point process model of auditory nerve spiking in response to complex sounds. *J Comput Neurosci*, 29(1-2):193–201.
- van den Honert, C. and Kelsall, D. C. (2007). Focused intracochlear electric stimulation with phased array channels. *J Acoust Soc Am*, 121(6):3703–3716.
- Vandali, A. E., Whitford, L. A., Plant, K. L., and Clarke, G. M. (2000). Speech perception as a function of electrical stimulation rate: using the nucleus 24 cochlear implant system. *Ear Hear*, 21(6):608–624.
- Verschuur, C. A. (2005). Effect of stimulation rate on speech perception in adult users of the Med-El CIS speech processing strategy. *Int J Audiol*, 44(1):58–63.
- Verveen, A. A. (1961). *Fluctuation in excitability*. PhD thesis, Netherlands Central Institute for Brain Research, Amsterdam, Netherlands.
- Verveen, A. A. (1962). Axon diameter and fluctuation in excitability. *Acta Morphol Neerl Scand*, 5:79–85.
- Verveen, A. A. and Derksen, H. E. (1968). Fluctuation phenomena in nerve membrane. *Proc IEEE*, 56(6):906–916.
- Weber, B. P., Lai, W. K., Dillier, N., von Wallenberg, E. L., Killian, M. J. P., Pesch, J., Battmer, R. D., and Lenarz, T. (2007). Performance and preference for ACE stimulation rates obtained with nucleus RP 8 and freedom system. *Ear Hear*, 28(2):46S–48S.
- Webster, M. and Webster, D. B. (1981). Spiral ganglion neuron loss following organ of Corti loss: a quantitative study. *Brain Res*, 212(1):17–30.
- White, M. W. (1984). Psychophysical and neuropsychological considerations in the design of a cochlear prosthesis. *Audiol Ital*, 1:77–117.
- Wilson, B. S., Finley, C. C., Farmer, J. C., Lawson, D. T., Weber, B. A., Wolford, R. D., Kenan, P. D., White, M. W., Merzenich, M. M., and Schindler, R. A. (1988). Comparative studies of speech processing strategies for cochlear implants. *Laryngoscope*, 98(10):1069–1077.
- Wilson, B. S., Finley, C. C., Lawson, D. T., Wolford, R. D., and Zerbi, M. (1993). Design and evaluation of a continuous interleaved sampling (CIS) processing strategy for multichannel cochlear implants. *J Rehabil Res Dev*, 30(1):110–116.
- Woo, J., Miller, C. A., and Abbas, P. J. (2009a). Biophysical model of an auditory nerve fiber with a novel adaptation component. *IEEE Trans Biomed Eng*, 56(9):2177–2180.

- Woo, J., Miller, C. A., and Abbas, P. J. (2009b). Simulation of the electrically stimulated cochlear neuron: modeling adaptation to trains of electric pulses. *IEEE Trans Biomed Eng*, 56(5):1348–1359.
- Woo, J., Miller, C. A., and Abbas, P. J. (2010). The dependence of auditory nerve rate adaptation on electric stimulus parameters, electrode position, and fiber diameter: a computer model study. *J Assoc Res Otolaryngol*, 11(2):283–296.
- Yi, E., Roux, I., and Glowatzki, E. (2010). Dendritic HCN channels shape excitatory postsynaptic potentials at the inner hair cell afferent synapse in the mammalian cochlea. *J Neurophysiol*, 103(5):2532–2543.
- Zhang, F., Miller, C. A., Robinson, B. K., Abbas, P. J., and Hu, N. (2007). Changes across time in spike rate and spike amplitude of auditory nerve fibers stimulated by electric pulse trains. *J Assoc Res Otolaryngol*, 8(3):356–372.

Phenomenological Model of Auditory Nerve Fiber Responses to Cochlear Implant Stimulation: Subthreshold and Suprathreshold Influences

Abstract

Refractoriness is a common neural phenomenon associated with the auditory nerve fiber (ANF) spike-dependent response to cochlear implant (CI) stimulation. However, for high-rate pulse trains, a continual drop in spike rate over time is often observed that cannot be explained by refractoriness alone. This is typically assumed to be caused by spike-dependent neuronal adaptation, but mounting evidence suggests that subthreshold stimulus-response behaviors may also affect the ANF stimulus-response electrophysiology. In this study, along with refractoriness and spike rate adaptation, we explored two subthreshold mechanisms: facilitation and accommodation in which a non-spiking stimulus increases or decreases the subsequent neural excitability, respectively. Previously, no phenomenological model has combined all four of these stimulus-response behaviors: refractoriness, spike rate adaptation, facilitation and accommodation. Our study presents a stochastic integrate-and-fire model that simultaneously considers all four phenomena. Using parameters from fits to data in paired pulse experiments, we are able to model facilitation, accommodation and refractoriness. Recordings of pulse train responses shape how we model long-term accommodation and spike rate adaptation. Simulation results show that refractoriness and spike rate adaptation behave as expected. However, in response to pulse train stimulation at 1000 pulses/s and above, our model predicts that subthreshold accommodation is responsible for further dropping the spike rate over the duration of the stimulus, suggesting that spike rate adaptation alone may be insufficient to explain such reduced excitability. The proposed model with all four temporal mechanisms permits a systematic investigation of their contribution to ANF response properties under various stimulus conditions, which is often necessary to interpret published cat ANF data, given the large range in response rates.

3.1 Introduction

In a review by Boulet et al. (2016) (or Chap. 2), several stimulus-response behaviors (see Fig. 3.1) were identified as contributors to modulating auditory nerve fiber (ANF) spike rates being electrically stimulated by cochlear implants (CIs). Two of these phenomena are classified as spike-dependent (suprathreshold): refractoriness and spike rate adaptation. The remaining two are stimulus dependent (subthreshold): facilitation and accommodation. Through the lens of post-stimulus time histograms (PSTHs), their dynamic involvement in crafting the mean spike rate may not be easily disentangled. Whereas refractoriness depends on the time since the last spike and spike rate adaptation depends on the spike history, the effects of facilitation and accommodation should not be underestimated since they depend on stimulus parameters in addition to spike history. The aim of this study is to show how any combination of refractoriness, spike rate adaptation, facilitation, and accommodation can affect the ANF spike rate in response to pulse train stimulation. In

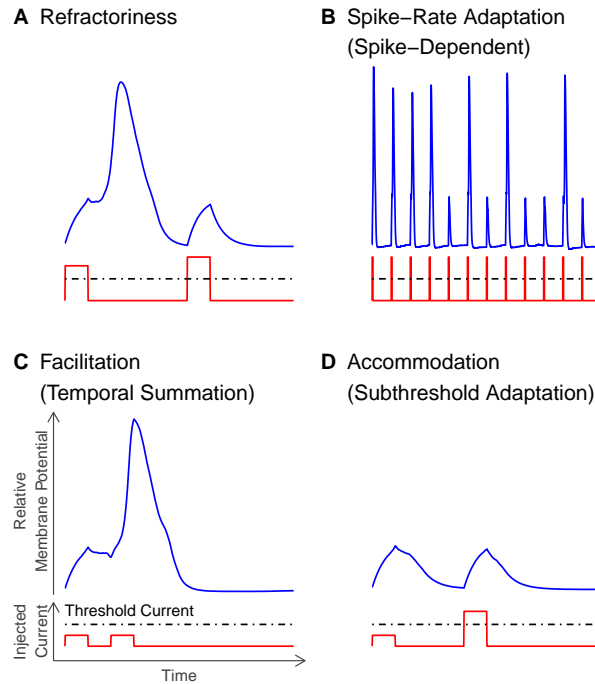


Figure 3.1 Stimulus-response phenomena represented by single-trial traces of the relative membrane potential. Responses to all phenomena shown (A–D) are subject to the stochastic nature of the ANF response and multiple responses to the same stimuli are required to determine the spike response statistics. **A** Refractoriness is observed as reduced excitability to the second pulse given a spike in response to the first pulse, whereas at longer inter-pulse intervals, a second spike is more probable. **B** In response to ongoing spiking due to pulse train stimulation, spike rate adaptation refers to the diminished spiking activity over longer timescales than refractoriness that is dependent on the spiking history, not just the time since the last spike. **C** Facilitation acts as membrane integration of two subthreshold pulses at small inter-pulse intervals to elicit a spike in response to the second pulse, whereas in the case of **D** accommodation, the states of some ion channels are responsible for reducing excitability after a subthreshold pulse such that a spike may not be generated in response to a following pulse above the resting threshold current. Responses (*blue line*) to monophasic current pulses (*red line*) were generated from an augmented Hodgkin–Huxley ANF membrane model (Negm and Bruce, 2014) with updated hyperpolarization-activated cyclic nucleotide-gated cation (HCN) kinetics (Liu et al., 2014). The *black dot-dashed line* shows the resting threshold current for the ANF model. This figure was adapted from Fig. 2 of Boulet et al. (2016) (or Fig. 2.2 in Chap. 2).

this study, we focus our exploration of the stimulus parameter space to stimulation rate and current amplitude.

The PSTH is a tool for observing an estimate of the firing rate over time. This measure can be processed over multiple neurons to obtain a population estimate, or in terms of one neuron’s response to multiple trials. In both cases, the stimulus is the same across multiple presentations. Figure 3.2 illustrates responses to pulse train stimulation at various current amplitudes and stimulation rates in the form of PSTHs. One common feature across all PSTHs is that the cat ANF eventually adapts to the pulse train by firing at a rate lower than the initial spike rate, and in some cases the ANF ceases to fire (see the *top and middle panels* of Figure 3.2D).

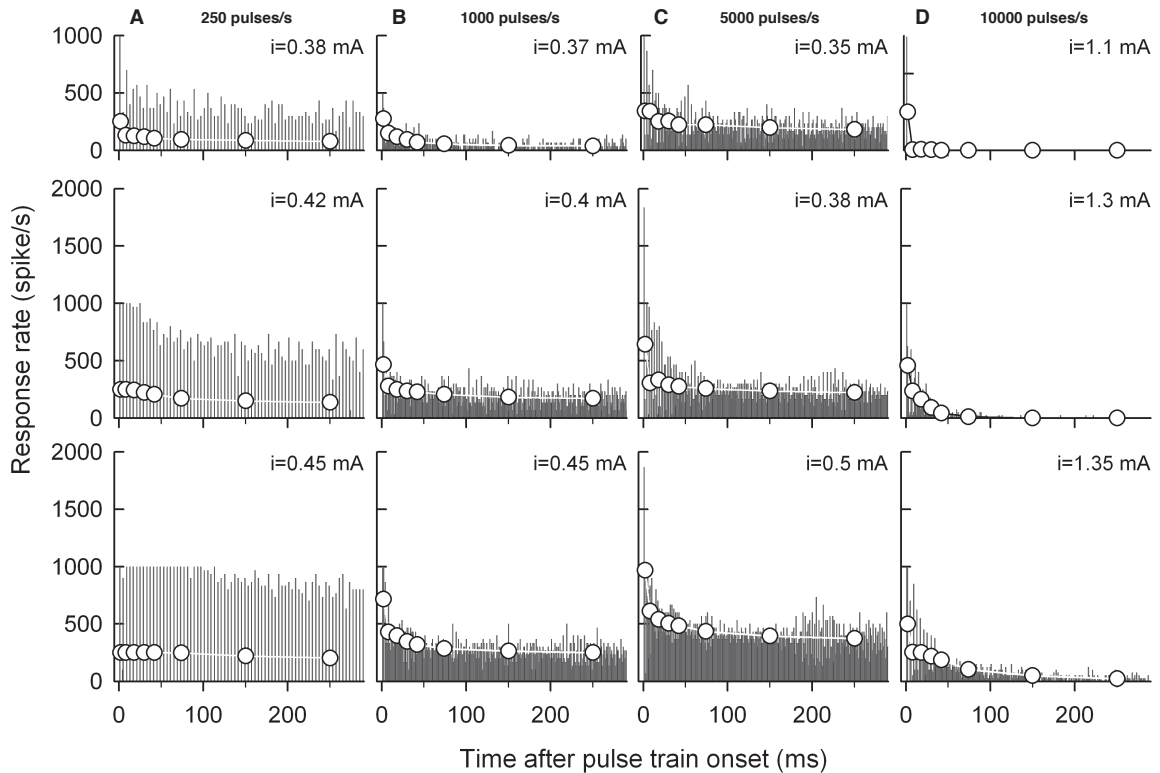


Figure 3.2 Cat ANF response rate as a function of the time since pulse train onset over a 300 ms interval. Column-wise subpanel layout indicate responses to stimulation at the rates of **A** 250 pulses/s, **B** 1000 pulses/s, **C** 5000 pulses/s, and **D** 10 000 pulses/s. Row-wise layout of the subpanels show an increasing biphasic pulse current level starting from the top panel to the bottom panel. Responses in panels **A**, **B**, and **C** were taken from a different ANF than those in panel **D**. Bars represent the response rate over 1 ms intervals and dots show the response rate over the progressively wider intervals (0–4, 4–12, 12–24, 24–36, 36–48, 48–100, 100–200, and 200–300 ms). This figure was adapted with kind permission of Springer Science & Business Media: Fig. 2 from Zhang et al. (2007), © 2007.

Throughout all panels of Fig. 3.2, we can identify instances of the four aforementioned phenomena and cases involving their combined interaction. Assuming that the absolute refractory period (ARP) of the ANF is approximately $332 \mu\text{s}$ (Miller et al., 2001), then refractoriness is clearly seen in the first 50 ms as an oscillatory response of the PSTH in the *bottom panel* of Fig. 3.2D, (*black bars*). This happens since the 1 ms bin widths are not synchronized to the post-spike ARP, thus alternating PSTH time bins count many more spikes than their neighbors. Refractoriness also limits the maximum firing rate in cases when the time between consecutive pulses is less than the absolute refractory period, thus removing any possibility of the ANF spiking to every pulse. Spike rate adaptation is responsible for a substantial portion of the slow drop in excitability (Heffer et al., 2010; Miller et al., 2011; Zhang et al., 2007). As facilitation (or *temporal summation*) increases the excitability of the neuron, its presence may be observed as the increase in spike rate from the 1000 pulses/s response to the 5000 pulses/s response despite the effects of refractoriness

(see Fig. 3.2B and C, *top* and *mid* panels). The 10 000 pulses/s cases respond with a reduction in excitability that eventually reaches a spike rate of approximately 0 spikes/s, which is substantially lower than the 5000 pulses/s cases. Since absolute refractoriness would only be responsible for suppressing twice as many spikes as the 5000 pulses/s response (given that the pulse rate is doubled), we would expect the same average responses in the 5000 pulses/s and 10 000 pulses/s cases. So, if refractoriness cannot explain this response difference then, perhaps accommodation or *subthreshold adaptation* is better suited to do so. In fact, since accommodation, like facilitation, regulates subthreshold excitability, but in contrast to facilitation reduces subthreshold excitability, accommodation may be overriding facilitation to produce a net in reduction subthreshold excitability. This occurs by exerting a pulse-dependent reduction in excitability such that subsequent responses do not generate a spike. Over sequential non-spiking responses, the effects of accommodation may accumulate (Negm and Bruce, 2014), further reducing subthreshold excitability until the neuron ceases to spike. This stranglehold on the ANF could, in theory, be undone by not delivering a pulse for a relatively longer time to allow the accumulation of accommodation to return to the resting level (Miller et al., 2011).

3.1.1 Single Pulse or Resting Response

An important characteristic of the ANF response is the inherent stochasticity generated by voltage-gated ion channel fluctuations. Verveen and Derksen (1968) first reported that resting membrane potential fluctuations of myelinated neurons had a $1/f$ spectrum with a Gaussian amplitude distribution. By transforming the membrane fluctuation amplitudes into the injected current amplitude, Verveen (1961) was able to express the probability of firing, or the firing efficiency (FE), as a function of the stimulation current I_{stim} according to

$$\text{FE}(I_{\text{stim}}) = \Phi\left(\frac{I_{\text{stim}} - \theta}{\sigma}\right), \quad (3.1)$$

parameterized by the threshold current θ and dynamic range, or noise amplitude σ (see Fig. 3.3), given the Gaussian cumulative distribution function

$$\Phi(x) = \frac{1}{\sqrt{2\pi}} \int_{-\infty}^x \exp\left(-\frac{z^2}{2}\right) dz. \quad (3.2)$$

The values of the threshold current and the dynamic range are determined empirically from the spiking responses to repeated presentations of a single pulse for a range of current pulse amplitudes. The neuron's dynamic range is typically reported as the relative spread (RS), a quantity that is scaled to the threshold current

$$\text{RS} = \frac{\sigma}{\theta}. \quad (3.3)$$

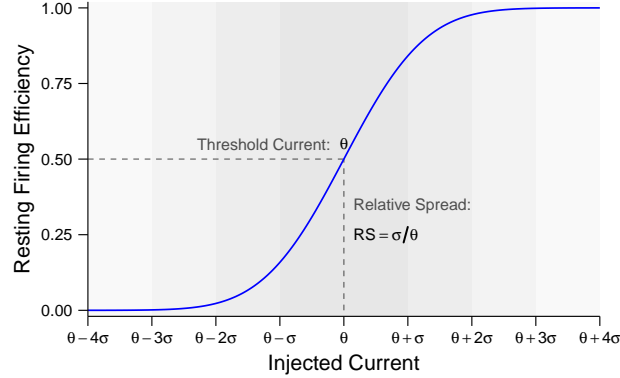


Figure 3.3 Single pulse or resting firing efficiency (FE) as a function of the injected current shown as a *blue line*. Single pulse threshold current (θ) and single pulse relative spread (RS) characterize the FE with an cumulative Gaussian distribution (Bruce et al., 1999b; Verveen, 1961). RS is a normalized measure of a neuron’s dynamic range given membrane fluctuations (Verveen, 1961; Verveen and Derksen, 1968).

Bruce et al. (1999b) developed a stochastic single pulse response model by approximating the stimulus response potential and the $1/f$ membrane noise (Verveen, 1961; Verveen and Derksen, 1968), centered at a threshold potential, which was constant over the pulse width. If the stimulus response potential V_{stim} crossed the ‘noisy’ threshold potential $V_{\text{thr}} + V_{\sigma}$ then, the model ANF fired. This resulted in a Bernoulli process where the probability of spiking was determined by a cumulative Gaussian distribution that was dependent on the stimulus response potential V_{stim} , the mean threshold potential V_{thr} and the standard deviation of the $1/f$ noise V_{σ} .

Hamacher (2004) and Fredelake and Hohmann (2012) expanded on this work by introducing the integrate-and-fire model (Gerstner and Kistler, 2002; Lapicque, 1907) to model the membrane potential. Unlike Bruce et al. (1999b), Hamacher (2004) and Fredelake and Hohmann (2012) added noise to the membrane potential instead of the threshold potential. This distinction is one of importance, which is utilized to distinguish the difference in underlying biophysical processes that may be categorized as *active*: related to ion channel mechanisms, from the *passive*: governed by the linear response of the membrane capacitance-resistance circuit. If we extend the Bruce et al. (1999b) model to include the integrate-and-fire model, V_{stim} is the result of the stimulus current I_{stim} convolved with the passive membrane impulse response $h_{\text{mem}}(t)$

$$h_{\text{mem}}(t) = \frac{1}{C_{\text{mem}}} \exp\left(-\frac{t}{\tau_{\text{mem}}}\right), \quad (3.4)$$

where $\tau_{\text{mem}} = R_{\text{mem}}C_{\text{mem}}$ are the membrane time constant and C_{mem} and R_{mem} is the membrane capacitance and resistance, respectively. Equivalently, the stimulus response potential may be solved by the differential equation

$$\begin{cases} V_{\text{stim}}(t) = 0 & \text{if } t - t_i^s < \Delta t_{\text{abs}} \\ \frac{d V_{\text{stim}}(t)}{d t} = -\frac{V_{\text{stim}}(t)}{\tau_{\text{mem}}} + \frac{I_{\text{stim}}(t)}{C_{\text{mem}}} & \text{otherwise} \end{cases} \quad (3.5)$$

where t_i^s is the time since the last spike, and given the resting initial condition $V_{\text{stim}}(0) = 0$ mV. This model of single pulse ANF response is accurate in determining the firing efficiency as a function of the stimulation current (Horne et al., 2016; Nourski et al., 2006). Going forward, we interpret responses to time-varying stimuli as temporal variations of the single pulse response, specifically as modifications to the resting threshold and resting RS.

3.1.2 Refractoriness

Probably the best characterized ANF stimulus-response phenomena is refractoriness. The reason is due to the simplicity of its operational definition, which states that refractoriness is a reduction in neural excitability following a spike and is dependent only on the time since the last spike. If a neuron fires, refractoriness is activated such the probability of firing immediately after that spike drops to zero during the absolute refractory period (ARP). This is followed by a period of reduced excitability known as the relative refractory period (RRP) over which the excitability of the neuron returns to the resting threshold. During the RRP, it is possible for the neuron to fire, given on average, a current pulse with amplitude greater than the resting threshold. Miller et al. (2001) showed that the refractory recovery could be determined by stimulating cat ANF with a pair of pulses separated by an interpulse interval (IPI, or masker-probe interval), given a spike in response to the first (or masker) pulse. Figure 3.4A, illustrates the ratio of the probe pulse threshold to the single pulse threshold (SPT) as a function of the IPI for individual neurons as *black dots*, the population mean as *white dots*, and the functional fit (equation shown) to all neurons as the *black line*. Although the absolute refractory period, reported as 332 μ s (Miller et al., 2001), was not shown in Fig. 3.4A, the time course of the relative refractoriness is apparent. Figure 3.4B shows the normalized noise level, as characterized by the RS value, increases post-spike, eventually returning to resting levels. Unlike the threshold, the relative spread data shows an intermediate period from 1 ms to at least 4 ms that is lower than the resting level.

The Bruce et al. (1999b) single pulse response model was extended with refractoriness (Bruce et al., 1999a) to explain the pulse train response. Bruce et al. (1999a) implemented refractoriness by increasing the threshold potential with the refractory potential V_{refr} , which is a function of the time since the last spike, similar to Miller et al. (2001). Changes in the relative spread over time were not modeled in the Bruce et al. (1999a) study. This model was accurate for predicting pulse train responses at moderately high firing efficiencies and up to 800 pulses/s. Given the relatively large ARP (0.7 ms) in the Bruce et al. (1999a)

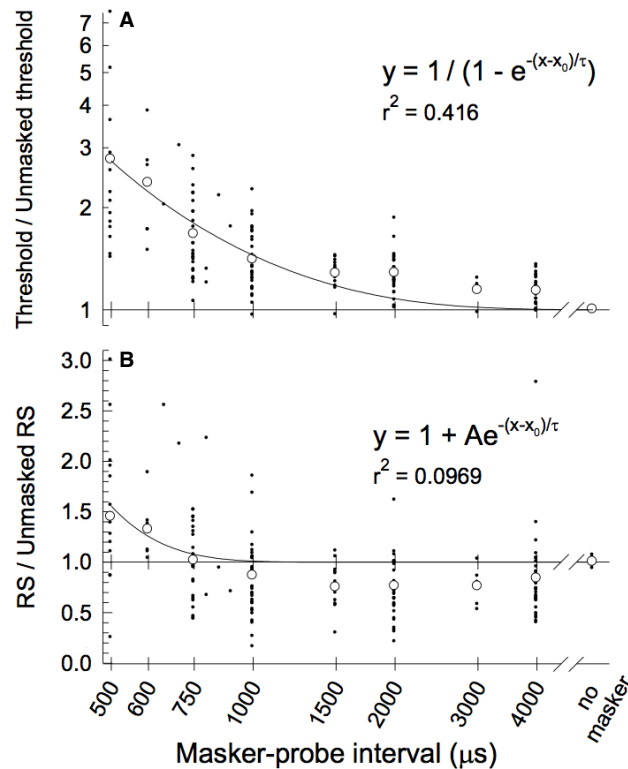


Figure 3.4 Refractory probe response threshold and RS ratio as a function of the interval between masker and probe pulses from cat ANF (Miller et al., 2001). Panel **A** shows the threshold (probe pulse threshold) / unmasked threshold (SPT), or $\theta_{\text{sup}}/\theta_{\text{SP}}$ and panel **B** similarly displays the RS / unmasked RS ($\text{RS}_{\text{sup}}/\text{RS}_{\text{SP}}$). Note that $\theta_{\text{sup}}/\theta_{\text{SP}}$ and IPI are scaled on a log-10 axis. The *open white dots* represent mean values of the ratios from responses by each neuron, which are shown as *black dots*. The *black curves* show the fits by the equations shown in each panel to the data points represented by the *black dots*. Panels **A** and **B** are reprinted with kind permission of Springer Science & Business Media: Fig. 7 from Miller et al. (2001), © 2001.

study, this model would have trouble accurately predicting responses to pulse rates over 1000 pulses/s. Since the Bruce et al. (1999a) model does not explicitly include subthreshold effects, responses to low FEs may not be accurate. Finally, since the longest pulse train duration examined by Bruce et al. (1999a) was 100 ms, the effects of spike rate adaptation, especially in response to higher pulse rates, may not have been captured given that the timescale of adaptation in ANFs can go beyond 100 ms (Zhang et al., 2007).

3.1.3 Spike Rate Adaptation

Spiking neurons pay a substantial metabolic cost to encode information about the environment (Laughlin, 2001). In many neurons, information about such a stimulus is encoded by a firing rate, which is bounded on average, by a non-spiking response and some maximum firing rate (Stemmler and Koch, 1999). Therefore, commonly-occurring events are typically

expressed by a low firing rate in an attempt to efficiently process stimuli whilst minimizing energy expenditure, leading to neuronal adaptation (Stemmler and Koch, 1999). In ANFs, neuronal adaptation may be implemented, in some form, by spike rate adaptation. A parsimonious example of how spike rate adaptation may operate in ANF was outlined by Nourski et al. (2006). The effect of spike rate adaptation on the threshold is a function of the instantaneous spiking such that it begins at a maximum value that is diminished by some fractional quantity after every spike, which is then followed by recovery over some time constant (Nourski et al., 2006). However, this approach does not directly increase the threshold, and we will address this in a later section.

3.1.4 Facilitation and Accommodation

Refractoriness and spike rate adaptation are suprathreshold behaviors, that is, they are spike-dependent phenomena. In contrast, facilitation and accommodation are stimulus-dependent such that non-spiking responses to previous stimuli can either increase excitability to the next pulse (facilitation) or decrease excitability to the next pulse (accommodation). Models of these subthreshold behaviors can be described either in a top-down fashion by characterizations of stimulus-response paradigms or in a bottom-up manner by the dynamics of voltage-gated ion channels and membrane capacitance and resistance.

Facilitation may be subdivided into *passive facilitation* and *active facilitation*. These distinctions are given based on the mechanisms that are responsible for their dynamics. Passive facilitation occurs due to the accumulation of responses (V_{stim}) of the passive membrane circuit composed of the membrane capacitance and resistance (see (3.5) and Lapicque, 1907) when stimulated with depolarizing current pulses. Active facilitation can be predicted by the stochastic activity of the Hodgkin and Huxley (1952) model. As the membrane potential nears the threshold potential, Na activation approaches a bifurcation point where a strong enough perturbation can induce a limit cycle oscillation, or action potential.

Figure 3.5 shows these concepts by comparing three different cases. Panel C of Fig. 3.5 shows a masker followed by probe pulse that causes changes to the relative membrane potential (Fig. 3.5A) and the percentage of open Na_v channels (Fig. 3.5B) over time. The *black, dot-dashed curves* are a demonstration of when the voltage-gated ion channels states are fixed to their resting levels at the beginning of the trial. As expected, this does not prompt a change in the percentage of open Na_v channels. Therefore, the increase in the relative membrane potential (Fig. 3.5A) in response to both the masker and the probe pulses is solely due to the passive effects of membrane resistance-capacitance circuit. Therefore, passive facilitation is the process of charge accumulation on the neural membrane over the duration of a given pulse (Lapicque, 1907). This can be augmented by active facilitation where relatively large fluctuations in sodium activation sustain the membrane potential at a higher amplitude until the next pulse. In Fig. 3.5A, *green curves* show cases in which the neuron spikes in response to the probe pulse whereas, the *magenta curves* represent

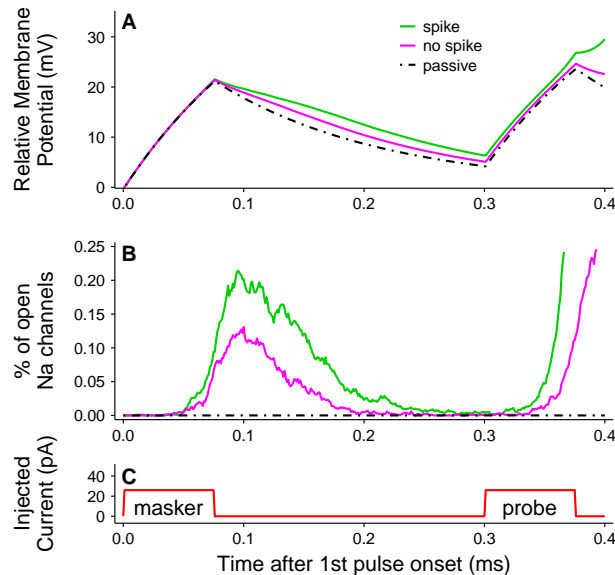


Figure 3.5 Contributions of passive and active facilitation. **A** The relative membrane potential and corresponding **B** percentage of open Na_v channels in response to **C** monophasic masker and probe pulses with 75 μ s/phase pulse durations and at current amplitudes less than the resting threshold current. These simulation results were averaged over 100 trials of the stochastic Hodgkin–Huxley model (Hodgkin and Huxley, 1952; Mino et al., 2002; Negm and Bruce, 2014) for three different cases. In panels **A** and **B**, *green curves* represent the average response for trials where the probe pulse generated a spike, *magenta curves* are for trials where no spike was generated, while the *black, dot-dashed curves* show the case where the ion channel states were frozen at resting levels. This figure was reprinted with kind permission of Springer Science & Business Media: Fig. 5 of Boulet et al. (2016), © 2016, or Fig. 2.5 in Chap. 2.

instances when the probe pulse did not generate an action potential. In both of these cases, the relative membrane potential is greater than when the ion channel states are fixed to resting levels. However, when the neuron spikes, the relative membrane potential is greater (*green curve*) than when it does not spike (*magenta curve*). Figure 3.5B reveals that the percentage of open Na_v channels is greater when the neuron spikes in response to the second pulse. More specifically, this relative increase in the percentage of open Na_v channels begins in response to the masker probe, which causes an increase in the relative membrane potential, thereby causing a slower decay. Finally, at the time when the probe pulse stimulates, the relative membrane potential is closer to threshold, causing the neuron to spike more easily, on average. Therefore, active facilitation is the mechanism by which increases in the percentage of open Na_v channels preconditions the membrane potential to spike to the next pulse. As the number of pulses increases over some interval, V_{stim} approaches the threshold potential, increasing the probability of the ANF firing. Once the ANF has spiked, the effect of passive facilitation ceases and may only begin after the absolute refractory period is over (see (3.5)).

Accommodation has been linked to the activity of hyperpolarization-activated ion channels in ANFs (Liu et al., 2014). A computational model by Negm and Bruce (2014) showed that in cases when a model ANF did not spike to a train of pulses, the hyperpolarization-

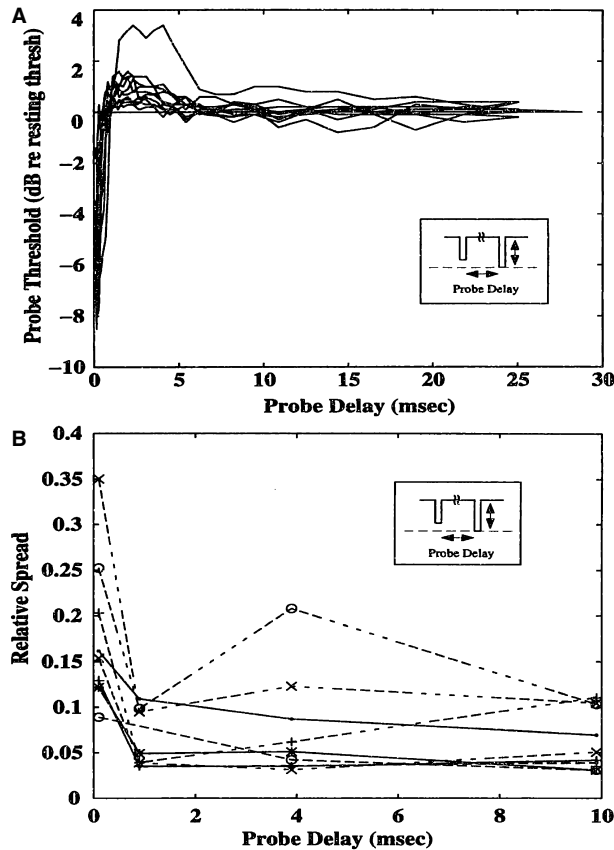


Figure 3.6 Data from cat ANF recordings illustrating the combined effects of facilitation and accommodation on the threshold and RS ratio in response to a subthreshold masker pulse, followed by a probe pulse. The masker pulse is set to levels of 2 to 0.5 dB below the single pulse threshold, while the level of the delayed probe is varied. Accommodation is seen at probe threshold values greater than 0 dB, whereas facilitation occurs below 0 dB. Panels A and B are used with permission from Fig. 3-2 and Fig. 3-9, respectively of Dynes (1996). © Massachusetts Institute of Technology.

activated channels were responsible for widening gap between the membrane potential and the threshold potential, thus reducing excitability of the ANF.

Our brief description of subthreshold response properties may not be complete since other ion channel types may also be involved. Therefore, it is convenient to discuss facilitation and accommodation as stimulus-response phenomena. Unfortunately, clear examples of these phenomena throughout CI research are rare despite the obvious applicability to CI stimulation. However, the work of Dynes (1996) and Cartee et al. (2000) has done exactly that. Although Cartee et al. (2000) employed the subthreshold paired pulse stimulation paradigm to find evidence of facilitation (of interpulse intervals in the range of 100 to 300 μ s), Dynes (1996) was the first to show the coexistence of facilitation and accommodation.

Both panels of Fig. 3.6 show changes in the probe threshold and RS relative to the resting threshold and RS, respectively, as a function of the interpulse interval. This was achieved by stimulating with a first pulse amplitude that was less than the SPT, then varying the

probe pulse amplitude and IPI (Dynes, 1996). Figure 3.6A shows the probe pulse elicits a decrease in the threshold or *facilitation* at IPIs less than approximately 1 ms whereas from 1 to 5 ms, the probe pulse promotes an increase in the threshold or *accommodation*, eventually returning to the resting threshold. Figure 3.6B shows an increase in subthreshold stochasticity (RS) for IPIs in the range of approximately 0 to 1 ms that returns to the single pulse relative spread at longer IPIs. In summary, Fig. 3.6 shows that changes to subthreshold excitability are a result of the combination of passive facilitation, active facilitation, and accommodation.

3.2 Methods

3.2.1 Dynamic Threshold Potential Model

In this section we present the framework in which refractoriness (r), spike rate adaptation (s), active facilitation (f), and accommodation (a) modulate single pulse ANF excitability in response to pulsatile stimuli and its spiking history. We build a phenomenological model that incorporates aspects of previous models of the single pulse response, refractoriness, and spike rate adaptation, while reformulating the subthreshold phenomena reported by Dynes (1996) into separate active facilitation and accommodation modules. An advantage of our model is that any combination of either refractoriness, spike rate adaptation, active facilitation, and accommodation can be applied to simulate sets of spike trains to test whether or not combinations of these phenomena can generate spike trains consistent with real ANF recordings.

Model Overview

A monophasic pulse train is composed of a series of rectangular waves, where each wave $\Pi(t)$ is defined as

$$\Pi(t) = \begin{cases} 1 & 0 \leq t < w \\ 0 & \text{otherwise} \end{cases} \quad (3.6)$$

where w is the pulse width. Pulse onset times are defined such that the onset time of the k^{th} pulse is written as t_k^p . The corresponding stimulation current pulse train is written as

$$I_{\text{stim}}(t) = \sum_{k=1}^m A_{\text{stim}} \Pi(t - t_k^p) \quad (3.7)$$

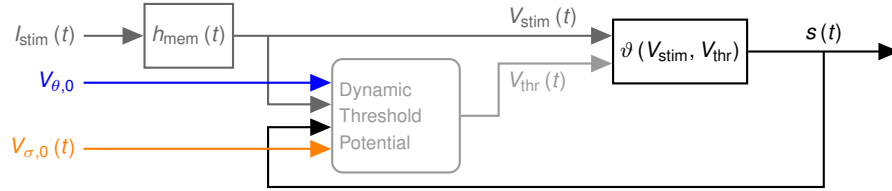


Figure 3.7 Diagram of phenomenological stimulus-response model. Inputs are shown on the left and outputs on the right. A diagram of the dynamic threshold potential model is shown in Fig. 3.8.

where A_{stim} is the current amplitude and m is the number of pulses. In this instance, we did not specify periodicity in the pulse train. However, pulse trains stimulating at frequency f , may be written as

$$I_{\text{stim}}(t) = \sum_{k=1}^m A_{\text{stim}} \Pi(t - k/f). \quad (3.8)$$

Since this model produces spikes and requires feedback of its spike history, it is useful to define how spikes are treated throughout the text. Spike times t_i^s are generated if at time t the simulation response potential $V_{\text{stim}}(t)$ exceeds some dynamic threshold value $V_{\text{thr}}(t)$ as outlined below

$$t_i^s = \vartheta(V_{\text{stim}}(t), V_{\text{thr}}(t)) \quad (3.9)$$

where the threshold function $\vartheta(x(t), y(t))$ is defined as

$$\vartheta(x(t), y(t)) = \begin{cases} t & \text{if } x(t) \geq y(t) \\ \emptyset & \text{otherwise} \end{cases}. \quad (3.10)$$

If the set of spike times is written as $\{t_i^s\}$, then the spike train $s(t)$ is represented as the sum of Dirac delta functions

$$s(t) = \sum_{i=1}^n \delta(t - t_i^s) \quad (3.11)$$

at those times, where n is the total number of spikes.

Figure 3.7 shows a diagrammatic overview of our phenomenological model. The model contains the three inputs: the current waveform I_{stim} , mean resting threshold potential (constant) $V_{\theta,0}$, and the resting threshold potential noise $V_{\sigma,0}(t)$ which is characterized by a time series with a $1/f$ frequency spectrum, mean 0, and standard deviation $V_{\sigma,0}$. The $1/f$ noise models ion channel fluctuations (Verveen and Derksen, 1968).

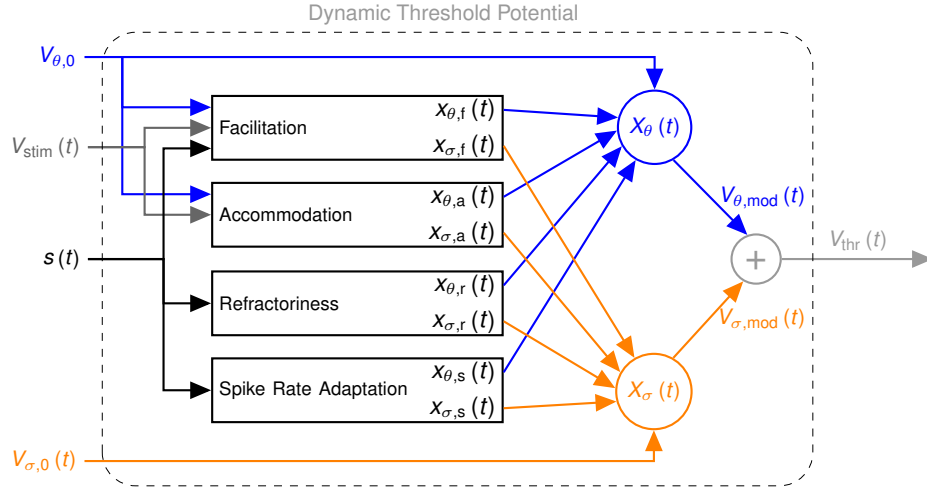


Figure 3.8 Diagram of the dynamic threshold potential model. Inputs are shown on the left and outputs on the right. Detailed descriptions of the components are given in the text.

We set the mean resting threshold potential to $V_{\theta,0} = 30$ mV, which is the relative membrane potential threshold value of the biophysical ANF model (Negm and Bruce, 2008). The relative spread of the Negm and Bruce (2008, 2014) model for a depolarizing phase leading biphasic pulse with a pulse duration of $100 \mu\text{s}/\text{phase}$ is approximately $RS_{SP} = 0.046$. The Negm and Bruce (2008) study did not explore values of RS at shorter pulse widths therefore, those values are unknown. We chose a value of $RS_{SP} = 0.05$ for use in our model. Since the relative spread is unitless, we can express the noisy resting threshold potential standard deviation as

$$V_{\sigma,0} = RS_{SP} V_{\theta,0} \quad (3.12)$$

where the pulse current amplitude equivalent is given by (3.3).

We define the stimulus response potential (here, the analog of the relative membrane potential) $V_{stim}(t)$ as the potential due the integration of the stimulation current $I_{stim}(t)$ through the parallel membrane capacitance C_{mem} and resistance R_{mem} circuit. Recall that (3.5) shows how to solve for $V_{stim}(t)$.

The central hypothesis of this paper is that subthreshold and suprathreshold effects can influence the excitability of the neuron. It then follows in the most literal sense, that dynamic changes in the threshold potential can be directly responsible for the neuron's ongoing ability to spike. For example, if we refer to (3.9) and (3.10), then is it clear that if $V_{thr}(t)$ decreases, then the neuron is more likely to spike, and the opposite is true if $V_{thr}(t)$ increases. How exactly $V_{thr}(t)$ changes over time is the focus of this section. Figure 3.8 lays out the internals of the *Dynamic Threshold Potential* module introduced in Fig. 3.7. We begin by following the Bruce et al. (1999a,b) model architecture where the dynamic membrane potential $V_{thr}(t)$ is just the sum of the modified threshold potential $V_{\theta,mod}(t)$

and the modified noise potential $V_{\sigma,\text{mod}}(t)$ given below

$$V_{\text{thr}}(t) = V_{\theta,\text{mod}}(t) + V_{\sigma,\text{mod}}(t) \quad (3.13)$$

where $V_{\theta,\text{mod}}(t)$ and $V_{\sigma,\text{mod}}(t)$ are modified versions of the constant single pulse threshold potential $V_{\theta,0}$ and the $1/f$ noise potential $V_{\sigma,0}(t)$

$$V_{\theta,\text{mod}}(t) = X_{\theta}(t) V_{\theta,0} \quad (3.14)$$

$$V_{\sigma,\text{mod}}(t) = X_{\sigma}(t) V_{\sigma,0}(t) \quad (3.15)$$

which have been multiplied respectively by the threshold and noise modifiers, $X_{\theta}(t)$ and $X_{\sigma}(t)$. In this context, modification refers to the influence exerted by each of the stimulus-response phenomena: refractoriness (r), spike rate adaptation (s), active facilitation (f), and accommodation (a). Next, we describe the combined effect of each phenomena to both the threshold modifier and noise modifier

$$X_{\theta}(t) = x_{\theta,f}(t) x_{\theta,a}(t) x_{\theta,r}(t) x_{\theta,s}(t) \quad (3.16)$$

$$X_{\sigma}(t) = x_{\sigma,f}(t) x_{\sigma,a}(t) x_{\sigma,r}(t) x_{\sigma,s}(t) \quad (3.17)$$

where the subscripts f, a, r, and s indicate the stimulus-response phenomena of interest. For instance, the active facilitation threshold modifier (or ratio) is written as $x_{\theta,f}(t)$. All of these stimulus-response-specific modifiers are ratio variables and are therefore dimensionless. The functional arrangement of (3.16) and (3.17) was introduced by Nourski et al. (2006) with refractoriness and spike rate adaptation. We extend this framework to include active facilitation and accommodation. Before going further it should be noted that for each stimulus-response behavior, we will characterize their noise contribution in terms of RS. Therefore, if we recall (3.12), we rescale to the noise ratio using the relation

$$x_{\sigma,f/a/r/s}(t) = x_{\text{RS},f/a/r/s}(t) x_{\theta,f/a/r/s}(t). \quad (3.18)$$

The remainder of this section will deal with each of the subthreshold and suprathreshold effects separately to show how they modify the dynamic threshold potential. Parameters for the model are summarized in Table 3.1.

Table 3.1 Summary of parameters for the phenomenological dynamic threshold potential model.

Parameter	Symbol	Value	Reference
<i>Single pulse response</i>			
Threshold current	θ_{SP}	≈ 50 pA	Negm and Bruce (2014), text
Relative spread	RS_{SP}	≈ 0.05	Negm and Bruce (2014), text
Threshold potential	$V_{\theta,0}$	≈ 30 mV	Negm and Bruce (2014), text
<i>Membrane</i>			
Resistance	R_{mem}	1.9535 G Ω	Negm and Bruce (2014)
Capacitance	C_{mem}	0.0714 pF	Negm and Bruce (2014)
Time constant	τ_{mem}	0.1395 ms	Negm and Bruce (2014)
<i>Refractoriness</i>			
Threshold absolute refractory period	Δt_{abs}	0.332 ms	Miller et al. (2001)
Threshold relative refractory period	τ_{rel}	0.411 ms	Miller et al. (2001)
Relative spread strength	$a_{RS,r}$	1	Fig. 7 of Miller et al. (2001)
Relative spread strength time constant	$\tau_{RS,r}$	0.2 ms	Fig. 7 of Miller et al. (2001)
<i>Spike rate adaptation</i>			
Threshold spike-dep. decrement	$p_{\theta,s}$	0.04	Nourski et al. (2006), text
Threshold recovery time constant	$\tau_{\theta,s}$	50 ms	Nourski et al. (2006), text
Relative spread spike-dep. decrement	$p_{RS,s}$	0.04	text
Relative spread recovery time constant	$\tau_{RS,s}$	50 ms	text
<i>Active facilitation</i>			
Threshold time constant	$\tau_{\theta,f}$	0.5 ms	Fig. 3-2 of Dynes (1996)
Relative spread time constant	$\tau_{RS,f}$	0.3 ms	Fig. 3-9 of Dynes (1996)
Threshold strength	$a_{\theta,f}$	-0.15 ms $^{-1}$	Fig. 3-2 of Dynes (1996), text
Relative spread strength	$a_{RS,f}$	0.75 ms $^{-1}$	Fig. 3-9 of Dynes (1996), text
<i>Accommodation</i>			
Threshold time constant (quick)	τ_{θ,a_q}	1.5 ms	Fig. 3-2 of Dynes (1996)
Relative spread time constant (quick)	τ_{RS,a_q}	0.3 ms	Fig. 3-9 of Dynes (1996)
Threshold strength (quick)	a_{θ,a_q}	0.5 ms $^{-1}$	Fig. 3-2 of Dynes (1996), text
Relative spread strength (quick)	a_{RS,a_q}	0.75 ms $^{-1}$	Fig. 3-9 of Dynes (1996), text
Threshold time constant (slow)	τ_{θ,a_s}	50 ms	text
Relative spread time constant (slow)	τ_{RS,a_s}	50 ms	text
Threshold strength (slow)	a_{θ,a_s}	0.01 ms $^{-1}$	text
Relative spread strength (slow)	a_{RS,a_s}	0 ms $^{-1}$	text

Refractoriness

Refractoriness is a function of the time since the last spike $\Delta t_i^s = t - t_i^s$, where t_i^s is the time of the last spike. It can be segmented into absolute and relative refractory periods

$$x_{\theta,r}(t) = \begin{cases} \infty & \text{if } \Delta t_i^s < \Delta t_{\text{abs}} \\ \frac{1}{1 - \exp\left(-\frac{\Delta t_i^s - \Delta t_{\text{abs}}}{\tau_{\text{rel}}}\right)} & \text{otherwise} \end{cases} \quad (3.19)$$

as evidenced by its effect on the threshold (Miller et al., 2001). The effect of refractoriness on the RS was also reported by Miller et al. (2001) as

$$x_{\text{RS},r}(t) = 1 + a_{\text{RS},r} \exp\left(-\frac{\Delta t_i^s - \Delta t_{\text{abs}}}{\tau_{\text{RS},r}}\right) \quad (3.20)$$

and shown as the fit to the data in Fig. 3.4B. Notice how that in Fig. 3.4A, the mean data points are above the curve of best fit for IPIs starting at 1.5 ms out to at least 4 ms. A similar issue affects the RS ratio where at an IPI of 1 ms, continuing on to at least 4 ms, the mean data points fall below the best-fitting curve. Therefore, better-fitting functions may be formulated such as (4.4) and (5.3), introduced by Negm and Bruce (2014) for the probe threshold ratio equation, to be used in this type of stimulus-response phenomenological model. However, in this study we used (3.19) and (3.20) given by Miller et al. (2001).

Spike Rate Adaptation

As Nourski et al. (2006) and § 3.1.3 point out, the effect of spike rate adaptation on the threshold $x_{\theta,s}(t)$, similarly to refractoriness, is a function of instantaneous spike timing. In contrast to our model, Nourski et al. (2006) models how spike rate adaptation decreases its effect on the dynamic threshold potential, which means that in their model, $x_{\theta,s}(t)$ is placed in the denominator of (3.16). However, since our model not only incorporates refractoriness and spike rate adaptation (Nourski et al., 2006) but also facilitation and accommodation, it simplifies the interpretation of the model behavior to have each phenomena contribute to the threshold on the same scale. To accomplish this, the effect of spike rate adaptation on the threshold (or the threshold ratio) is initialized at a value of $y_{\theta,s}(0) = 1$. Every time a spike occurs, the threshold ratio is incremented by a fractional quantity $p_{\theta,s}$, which reduces the excitability of the ANF. This can be written as

$$x_{\theta,s}(t) = p_{\theta,s} + x_{\theta,s}(t - \Delta t), \text{ if } t = t_i^s. \quad (3.21)$$

The recovery of adaptation occurs over the timescale $\tau_{\theta,s}$ and is governed by the linear differential equation, with fixed point 1 (indicating full recovery or maximum excitability):

$$\frac{d x_{\theta,s}(t)}{d t} = \frac{1}{\tau_{\theta,s}} [1 - x_{\theta,s}(t)]. \quad (3.22)$$

Our time constant is different than the 100 ms used by Nourski et al. (2006). We use a time constant of 50 ms, which is an average value (over the membrane potential range) of the time constant of the voltage-gated ion channel that can predict spike rate adaptation in auditory nerve fibers (Liu et al., 2014; Negm and Bruce, 2014). Consequently, to compensate for these different time constants, the spike-dependent fractional increase ($p_{\theta,s}$) was changed from 0.01 (Nourski et al., 2006) to 0.04. Unfortunately, to the best of our knowledge, the effect of spike rate adaptation on the relative spread is unknown. We chose to model it with the same equations as its effect on the threshold:

$$x_{RS,s}(t) = x_{\theta,s}(t). \quad (3.23)$$

However, in future iterations of the model the RS ratio variable may be explored. If these changes lead to more accurate pulse train responses, then perhaps this functional description of RS ratio could shed light on the biophysical mechanisms behind spike rate adaptation.

Facilitation and Accommodation

As Dynes (1996) and Cartee et al. (2000) have demonstrated, the effects of subthreshold excitability on the threshold can be described by varying the interpulse interval and the respective amplitude of paired pulses (see Fig. 3.6A). The short-term facilitation ratio reported by Cartee et al. (2000) could be predicted by single time constant exponential function such that at an IPI of 0 ms, the facilitation threshold ratio was between 0 and 1. As the IPI increases, the facilitation threshold ratio returns to a value of 1. Dynes (1996) observed that by extending the IPI range out to 25 ms, not only was facilitation found at the same time scale reported by Cartee et al. (2000), but accommodation was also seen in the range of approximately 1 to 5 ms. This motivated us to model the effects of active facilitation and accommodation ratio as individual exponential functions, each with unique time constants and coefficients. Specifically, the accommodation threshold ratio function would have a longer time constant than active facilitation and would be greater than the unity ratio for all IPI values.

Subthreshold masker train stimulation has shown that ANF excitability is reduced in response to subsequent probe train stimulation at timescales out to 100 ms (Miller et al., 2011). Experimental (Liu et al., 2014) and computational (Negm and Bruce, 2014) studies suggest that hyperpolarization-activated cyclic nucleotide-gated channels may be responsible for modulating subthreshold excitability. In order to reflect this, we modeled an additional relatively weak ‘slow’ accommodation component a_s , which is different than

the ‘quick’ accommodation a_q (Dynes, 1996).

The active facilitation ratio function relaxes towards 1 (from a value less than 1 at IPI = 0) with some time constant $\tau_{\theta,f}$. The value of accommodation at IPI = 0 should be greater than 1, followed by the decay back to 1 with time constant $\tau_{\theta,a_q} > \tau_{\theta,f}$ to ensure a combined subthreshold ratio greater than 1 at intermediate IPI values. In order to convert ratio functions to impulse responses, we simply subtract 1 from the ratio functions. This results in the separate impulse response functions for active facilitation and accommodation

$$h_{\theta,f/a_q/a_s}(t) = a_{\theta,f/a_q/a_s} \exp\left(-\frac{t}{\tau_{\theta,f/a_q/a_s}}\right). \quad (3.24)$$

A similar procedure can be applied to separate the effects of active facilitation and accommodation on the relative spread, assuming that Fig. 3.6B accurately represents their combined effects. Unfortunately, we are not aware of a method to decouple their separate activity since neither the effects of facilitation nor accommodation on the relative spread are known independently. To simplify the RS models of active facilitation and accommodation, we assume that they contribute equally to the RS ratio. Therefore, we can write the RS impulse functions as

$$h_{RS,f/a_q/a_s}(t) = a_{RS,f/a_q/a_s} \exp\left(-\frac{t}{\tau_{RS,f/a_q/a_s}}\right). \quad (3.25)$$

Sodium channel activation is the primary component of active facilitation (recall Fig. 3.5) and HCN channel activation and deactivation are the main known contributors to long-term accommodation (Boulet et al., 2016; Negm and Bruce, 2014, or see Chap. 2). These channel-regulated subthreshold processes operate at membrane potentials near the threshold potential. Therefore, we define a pulse-derived input to active facilitation and accommodation $z(t)$ that is scaled by the resting threshold potential $V_{\theta,0}$

$$z(t) = \frac{V_{stim}(t-w)}{V_{\theta,0}} \quad (3.26)$$

where $V_{stim}(t-w)$ is the stimulus response potential delayed by the pulse width w to ensure that active facilitation or accommodation begins no earlier than the offset of the depolarizing I_{stim} pulse. The effect of active facilitation on the threshold and RS are applied as

$$\begin{cases} y_{\theta/RS,f}(t) = 0 & \text{if } t = t_k^p + w \\ y_{\theta/RS,f}(t) = 0 & \text{if } \Delta t_i^s < \Delta t_{\text{abs}} \\ y_{\theta/RS,f}(t) = h_{\theta/RS,f}(t) * z(t) & \text{otherwise} \end{cases} \quad (3.27)$$

where Δt_i^s is the time since the last spike and $t_k^p + w$ is the pulse offset time. We reset the effect of active facilitation after a spike since sodium activation returns to resting levels over the duration of the absolute refractory period (Hodgkin and Huxley, 1952). Active facilitation was also reset at every pulse offset time ($t_k^p + w$) in order to approximate the total contribution to the sodium current whereby sodium activation is likely to be nullified by the accumulation of sodium inactivation over longer time periods (Hodgkin and Huxley, 1952). However, the effect of active facilitation, in that the threshold is lowered, may still span two pulses. If the first pulse does not respond with a spike, then at the offset of that pulse, active facilitation activates, causing V_{thr} to reduce, bringing it closer to V_{stim} . As V_{stim} accumulates or integrates over the duration of second current pulse, the probability of active facilitation-induced spiking increases.

The accumulation of accommodation on the threshold may be written as

$$y_{\theta/RS,a_q/a_s}(t) = h_{\theta/RS,a_q/a_s}(t) * z(t) \quad (3.28)$$

where $y_{\theta/RS,f/a_q/a_s}(t)$ represents the accumulation of facilitation or accommodation over several pulses. Given the specific form of the subthreshold impulse functions (3.24) and (3.25), we may transform the convolution $h_{\theta/RS,f/a_q/a_s}(t) * z(t)$ in (3.27) and (3.28) to the closed form differential equation

$$\frac{d y_{\theta/RS,f/a_q/a_s}(t)}{d t} = -\frac{1}{\tau_{\theta/RS,f/a_q/a_s}} y_{\theta/RS,f/a_q/a_s}(t) + a_{\theta/RS,f/a_q/a_s} z(t) \quad (3.29)$$

with initial conditions $y_{\theta/RS,f/a_q/a_s}(0) = 0$. A disadvantage of this method is that it cannot accept an impulse function of arbitrary shape. However, the speed of numerical simulation in the time domain is greatly increased since the computational complexity of numerical solutions of differential equations are $\mathcal{O}(n)$ compared to $\mathcal{O}(n^2)$ for numerical convolution. Finally, the threshold and RS ratios for active facilitation are just

$$x_{\theta,f}(t) = 1 + y_{\theta,f}(t) \quad (3.30)$$

$$x_{RS,f}(t) = 1 + y_{RS,f}(t) \quad (3.31)$$

whereas for accommodation, the quick, slow, and total contributions are

$$x_{\theta,a_q/a_s}(t) = 1 + y_{\theta,a_q/a_s}(t) \quad (3.32)$$

$$x_{\theta,a}(t) = 1 + y_{\theta,a_q}(t) + y_{\theta,a_s}(t) \quad (3.33)$$

$$x_{RS,a_q/a_s}(t) = 1 + y_{RS,a_q/a_s}(t) \quad (3.34)$$

$$x_{RS,a}(t) = 1 + y_{RS,a_q}(t) + y_{RS,a_s}(t) \quad (3.35)$$

where 1 is added to the pulse-dependent accumulation of the respective subthreshold processes.

3.2.2 Model Simulation

We simulated the phenomenological model by temporally discretizing it with a time step of $\Delta t = 1 \mu\text{s}$. Solving all of the model's differential equations was performed by explicit forward Euler numerical integration. The combinations of effects that were applied in the phenomenological model were, refractoriness (r: on), active facilitation (f: on/off), accommodation (a: on/off), and spike rate adaptation (s: on/off). Since refractoriness is a well-known phenomena in ANFs, all model variants included refractoriness. In all simulations, we allowed models to initialize over a 100 ms duration, with $I_{\text{stim}} = 0 \text{ pA}$.

As an example of the simulation of the phenomenological model with all effects turned on, Fig. 3.9 shows an overview of how important system variables change over time and crucially, in response to pulse trains and the self-generated spike train history.

3.2.3 Stimuli

Single Pulse Discharge Probability (FE) Versus Current Level

Monophasic single pulses were set to a duration of $50 \mu\text{s}$ and delivered at 25 current levels centered around a first-pass estimate of the single pulse threshold current. This set of stimuli was repeated for 10 000 trials, where each trial was simulated for 1 ms after the pulse onset.

Paired Pulses to Simulate Refractory, Facilitation, and Accommodation Effects

Monophasic paired pulse stimuli were created with an initial masker pulse, followed by a probe pulse, each with a pulse duration of $50 \mu\text{s}$. Masker and probe pulses were temporally separated by 60 various IPIs drawn from 20 exponentially-spaced IPIs from 0.15 to 10 ms and 40 linearly-spaced IPIs from 0.151 to 4 ms. The masker pulse current level was set to

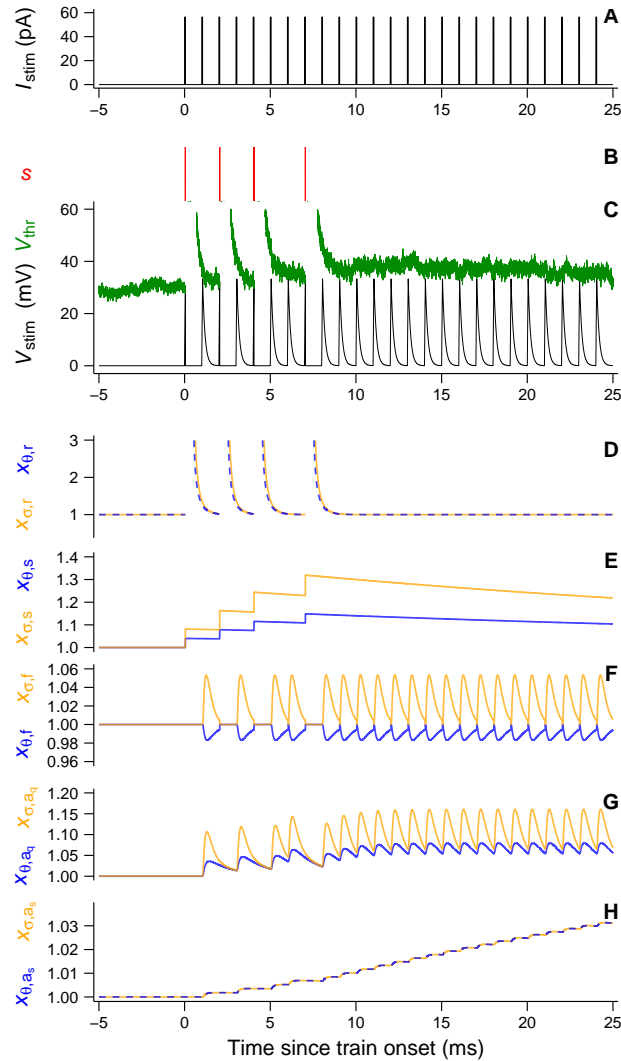


Figure 3.9 Overview of inputs to and phenomenological model system variables. **A** Stimulation current I_{stim} at a pulse level of $\theta_{\text{SP}}(1 + 2.5\text{RS}_{\text{SP}}) = 54.9$ pA and rate of 1000 pulses/s. **B** Spike train showing spike times (*red upright lines*) occurring from instances when **C** $V_{\text{stim}} \geq V_{\text{thr}}$ (*black line, green line*). The next five panels show the threshold ratio (*blue line*) and relative spread ratio (*orange line*) for **D** refractoriness: $x_{\theta,r}$, $x_{\text{RS},r}$; **E** spike rate adaptation: $x_{\theta,s}$, $x_{\text{RS},s}$; **F** active facilitation: $x_{\theta,f}$, $x_{\text{RS},f}$; **G** quick accommodation: x_{θ,a_q} , x_{RS,a_q} ; and **H** slow accommodation: x_{θ,a_s} , x_{RS,a_s} .

the 50 % single-pulse-equivalent FE. Probe pulses were then delivered at 80 linearly-spaced current levels ranging from 0 to 200 pA. Each of these stimuli were repeated for 1000 trials, where each stimulation lasted 1 ms past the onset time of the probe pulse.

Pulse Train Responses

Monophasic pulse train stimuli (with a 50 μs pulse duration) were delivered to the phenomenological model ANF at a number of different current levels and stimulation rates, each presented for 100 trials, over a stimulus duration of 300 ms. Pulse current levels were delivered at a value of $\theta_{\text{SP}} (1 + u\text{RS}_{\text{SP}})$ or $\theta_{\text{SP}} + u\sigma_{\text{SP}}$, where u varied from -10 to 15 by increments of 0.5 , totaling 51 different levels. For each of these current levels, a pulse train was delivered at the one of the 100, 250, 500, 800, 1000, 1250, 2500, 5000, or 10 000 pulses/s stimulation rates.

3.2.4 Data analysis

Single Pulse Stimuli

Single pulse responses were quantified by estimating θ_{SP} and RS_{SP} from the spike response data as a function of the stimulation current I_{stim} over 10 000 trials. Estimates of θ_{SP} and RS_{SP} were obtained by minimizing the sum of the squared residuals between the spike response data and (3.1). For binary data such as this case, where 0 represents no spike and 1 for a spike, the quality of the fit was reported by the R^2_{count} statistic (Long, 1997). The R^2_{count} statistic is just the proportion of correctly predicted binary values.

Paired Pulse Stimuli

Outcomes of paired pulse stimulation can be classified in a dichotomous fashion, depending on the response to the masker pulse, i.e., a suprathreshold or subthreshold conditioner. If a spike occurred in response to the masker pulse, then that trial was said to be a suprathreshold conditioner, indicating that there is a possibility that the neuron could be in a refractory state, depending on the IPI and probe pulse current level. Otherwise, when no spike was generated in response to the masker pulse, we classified that trial response as a subthreshold conditioner, which opened up the possibility for either facilitation or accommodation to determine the outcome of the probe response. For both suprathreshold and subthreshold conditioner cases and each IPI, the probe response threshold current (θ_{sup} , θ_{sub}) and relative spread (RS_{sup} , RS_{sub}) were evaluated using the same procedure as for the single pulse response. These quantities were then divided by their single pulse response companions to determine the suprathreshold and subthreshold conditioner ratio for the threshold current ($\theta_{\text{sup}}/\theta_{\text{SP}}$, $\theta_{\text{sub}}/\theta_{\text{SP}}$) and relative spread ($\text{RS}_{\text{sup}}/\text{RS}_{\text{SP}}$, $\text{RS}_{\text{sub}}/\text{RS}_{\text{SP}}$). Since refractoriness would have a major effect and spike rate adaptation would be negligible for just a pair of pulses in isolation, the suprathreshold conditioner ratio functions $\hat{\theta}_{\text{sup/SP}}(t)$ and $\widehat{\text{RS}}_{\text{sup/SP}}(t)$ were set to functions of the form given by (3.19) and (3.20), where t was evaluated at every IPI.

Subthreshold conditioner ratios are slightly more complicated due to the multiplicity of subthreshold processes and their interaction with each pulse $z(t)$. Our hypothesis is that passive facilitation (mem), active facilitation (f), and accommodation (a_q and a_s) should contribute to the subthreshold conditioner ratios. With these considerations, the subthreshold conditioner ratio functions $\hat{\theta}_{\text{sub/SP}}(t)$ and $\widehat{\text{RS}}_{\text{sub/SP}}(t)$ were set to linear combinations of the form given by (3.4), (3.24), and (3.25), where t was evaluated at every IPI.

We then fit the paired pulse response probe ratios: $\theta_{\text{sup}}/\theta_{\text{SP}}$ (IPI) to $\hat{\theta}_{\text{sup/SP}}(t)$, $\theta_{\text{sub}}/\theta_{\text{SP}}$ (IPI) to $\hat{\theta}_{\text{sub/SP}}(t)$, $\text{RS}_{\text{sup}}/\text{RS}_{\text{SP}}$ (IPI) to $\widehat{\text{RS}}_{\text{sup/SP}}(t)$, and finally $\text{RS}_{\text{sub}}/\text{RS}_{\text{SP}}$ (IPI) to $\widehat{\text{RS}}_{\text{sub/SP}}(t)$. The fitting procedure was performed by a constrained nonlinear optimization routine (MATLAB 2015b and Optimization Toolbox, The MathWorks, Inc., Natick, Massachusetts, United States). The quality of the fit was reported by the coefficient of determination R^2 . Fits were tested against the null hypothesis, being the single pulse response ratio (1), by computing the F -statistic (not reported). Any corresponding p -value less than 0.001 indicates that the suprathreshold or subthreshold conditioner ratio fit was better than the single pulse response ratio fit.

Pulse Train Stimuli

Pulse train responses were quantified by PSTHs as an estimate of the spike or response rate. Post-stimulus time histograms were evaluated for two sets of time bins. The first binning procedure was simply to divide the time axis into 1 ms bins (Zhang et al., 2007). The second binning method was used to look at longer-term trends by binning spike counts with the increasingly wider intervals 0–4, 4–12, 12–24, 24–36, 36–48, 48–100, 100–200, and 200–300 ms (Zhang et al., 2007). The response rate $\rho(t)$ was computed as

$$\rho(t) = \frac{1}{\Delta T_{\text{bin}} N_{\text{trials}}} \sum_{n=1}^{N_{\text{trials}}} \int_{t-\frac{\Delta T_{\text{bin}}}{2}}^{t+\frac{\Delta T_{\text{bin}}}{2}} s(t) dt \quad (3.36)$$

for both 1 ms and wide bin intervals, where $s(t)$ is the spike train, ΔT_{bin} is the bin interval, and N_{trials} is the number of trials. From the response rate, we calculated the normalized spike rate decrement (NSRD, Zhang et al., 2007) which is a measure between 0 and 1 that quantifies the degree of adaptation, where 0 indicated no adaptation and 1 represents complete adaptation (a non-spiking long-term response). The spike rate decrement is simply the difference between the onset spike rate (0 to 12 ms) and the final spike rate (200 to 300 ms). Finally, the NSRD is just the spike rate decrement divided by the onset rate.

3.3 Results

3.3.1 Single Pulse Response

Single pulse responses refer to the response of the resting ANF model to one pulse and thus should not be influenced by the effects of active facilitation, accommodation, or spike rate adaptation. However, over the course of the 100 ms initialization of each model with no current injection, the noisy membrane potential may freely fluctuate. This effect randomizes the initial value of the dynamic threshold potential which may then influence the excitability of the ANF as a single pulse is applied. Therefore, in order to ascertain the stability of the single pulse response, we determined estimates of the single pulse threshold and relative spread, θ_{SP} and RS_{SP} .

Figure 3.10 shows the firing efficiency as a function of the stimulation current for each of the model combinations. The proportion of spiking responses drawn as *symbols* appears to fit well to (3.1) shown by the *curves*. Table 3.2 shows that this is the case by reporting the R^2_{count} value for each model along with θ_{SP} and RS_{SP} . Since the R^2_{count} statistic is the proportion of correctly predicted binary values, the larger the RS_{SP} is, the lower R^2_{count} will be due to maximum variance in the proportion of correctly predicted binary values around θ_{SP} . However, Fig. 3.10 shows the proportion of spiking responses fitted to (3.1), which appears to be near perfect when quantified by the coefficient of determination R^2 . Values of the single pulse threshold and relative spread among all models are very close to each other, indicating that there is no effect of active facilitation, accommodation, or spike rate adaptation on the single pulse response.

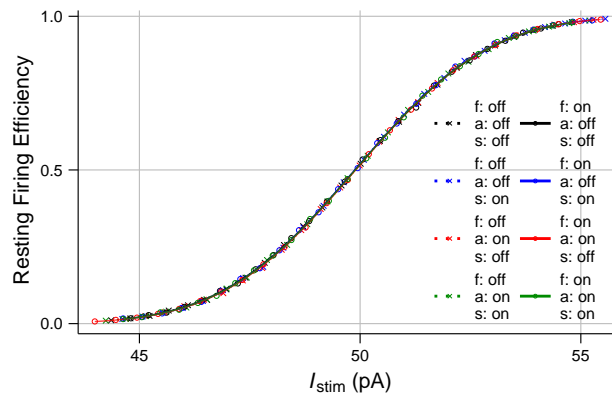


Figure 3.10 Single pulse response or resting response represented as the proportion of spiking responses to the number of trials (*colored symbols*) plotted against the fit to (3.1) (*colored curves*). Results for all models are shown: active facilitation (f), accommodation (a), and spike rate adaptation (s).

Table 3.2 Parameters and quality of fit quantified by R_{count}^2 and R^2 of the single pulse response data to (3.1).

Model			Quantity			
f	a	s	θ_{SP} (pA)	RS_{SP}	R_{count}^2	R^2
off	off	off	49.89	0.0484	0.825	1.000
off	off	on	49.88	0.0478	0.834	1.000
off	on	off	49.89	0.0477	0.829	1.000
off	on	on	49.89	0.0480	0.834	1.000
on	off	off	49.88	0.0484	0.813	1.000
on	off	on	49.88	0.0479	0.829	1.000
on	on	off	49.90	0.0479	0.841	1.000
on	on	on	49.89	0.0481	0.822	1.000

3.3.2 Paired Pulse Response

The paired pulse response may be expressed as a ratio, or a quantity normalized by its corresponding resting level, as a function of the interpulse interval. The paired pulse response may further be classified into cases when the masker (or first) pulse elicited a spike or not. We refer to cases when the masker pulse did not generate a spike as a subthreshold conditioner. Conversely, a suprathreshold conditioner indicates that the ANF spiked in response to the masker pulse. The paired pulse response quantities of interest are the probe current threshold ratio and the probe relative spread ratio. More specifically, we define four quantities: the subthreshold probe current threshold ratio $\theta_{\text{sub}}/\theta_{\text{SP}}$, the suprathreshold probe current threshold ratio $\theta_{\text{sup}}/\theta_{\text{SP}}$, the subthreshold probe relative spread ratio $\text{RS}_{\text{sub}}/\text{RS}_{\text{SP}}$, and lastly the suprathreshold probe relative spread ratio $\text{RS}_{\text{sup}}/\text{RS}_{\text{SP}}$.

In Fig. 3.11 we report on all four of these ratios. Figure 3.11A shows that the majority of changes to the subthreshold conditioner threshold ratio can be attributed to passive facilitation. This can be seen by contrasting the two subpanels that show model versions with active facilitation turned off and on, since $\theta_{\text{sub}}/\theta_{\text{SP}}$ shows a relatively small difference in the range of values below 1. Since all models contain passive facilitation, any difference in the data points and curves in Fig. 3.11A can be attributed to active facilitation and/or accommodation. If we refer to Fig. 3.12A, which shows a zoomed-in section of Fig. 3.11A near the intercept, although the difference is small, we can see that models with active facilitation turned on (f:off, compared to f:on) have a lower subthreshold conditioner threshold ratio intercept $\hat{\theta}_{\text{sub}/\text{SP}}(0)$, as expected since any facilitation should reduce the threshold. Conversely, we can see that model versions with accommodation turned on (*black and blue* compared to *red and green*) show an increase in $\hat{\theta}_{\text{sub}/\text{SP}}(0)$. This effect continues for all IPIs ($\max\{\hat{\theta}_{\text{sub}/\text{SP}}(t)\}$), as shown in Fig. 3.11A and is maximized in the range of 0.5 to 2 ms as displayed in Fig. 3.12B. In contrast, models without accommodation only return to unity threshold ratio asymptotically below 1. Since this response is to

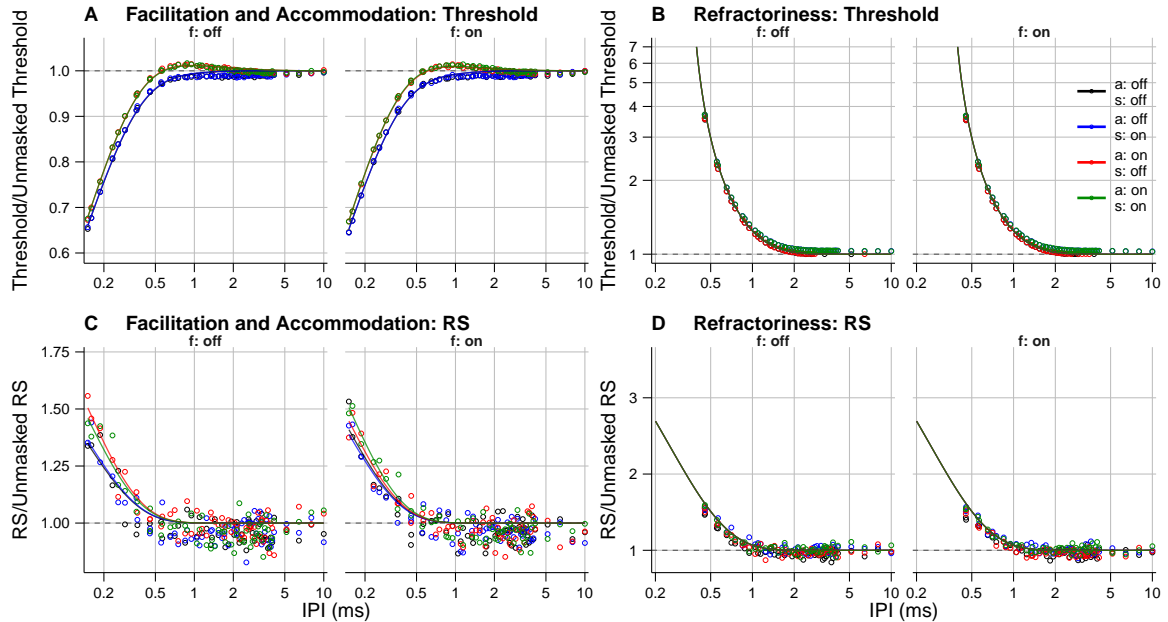


Figure 3.11 Responses of a paired pulse paradigm for the subthreshold conditioner response: facilitation and accommodation, and the suprathreshold conditioner response: refractoriness. The masker pulse was delivered at the single pulse threshold current level. The *open circles* represent the subthreshold or suprathreshold conditioner ratios, whereas the *curves* show the subthreshold or suprathreshold conditioner functions, which the ratios were fit to. The *dashed line* represents the single pulse threshold or RS. **A** Subthreshold conditioner threshold ratio, **B** suprathreshold conditioner threshold ratio, **C** subthreshold conditioner relative spread ratio, and **D** suprathreshold conditioner relative spread ratio.

a pair of pulses only, spike rate adaptation does not influence the threshold since the data points and curves overlap regardless of whether spike rate adaptation is off or on. From this perspective, i.e. from Fig. 3.12, the effects of active facilitation (f: off/on) and accommodation (a: off/on) on the subthreshold conditioner threshold ratio are visible. Active facilitation reduces the threshold, whereas accommodation increases it.

We can similarly conclude that in cases with only active facilitation turned on *or* accommodation turned on, that the subthreshold conditioner relative spread ratio is larger than when they are off, or when only passive facilitation is on (see Fig. 3.11C). These effects are additive in that the subthreshold conditioner relative spread ratio is greater when both active facilitation *and* accommodation are turned on than when only one of them is turned on. The notion that passive facilitation (mem), active facilitation (f), and accommodation (a) impose additive effects on the subthreshold conditioner ratios is therefore confirmed. Table 3.3 reports the quality of fits ($\hat{\theta}_{\text{sub/SP}}$ and $\widehat{RS}_{\text{sub/SP}}$), to the data ($\theta_{\text{sub}}/\theta_{\text{SP}}$ and $RS_{\text{sub}}/RS_{\text{SP}}$) with the coefficient of determination and the rejection of paired pulse response being represented by the single pulse response, for all model combinations.

The suprathreshold conditioner responses (threshold and relative spread) are simpler in that refractoriness alone should contribute for the case of two pulses in isolation. In reality, these responses see small increases due to the effect of spike rate adaptation, or

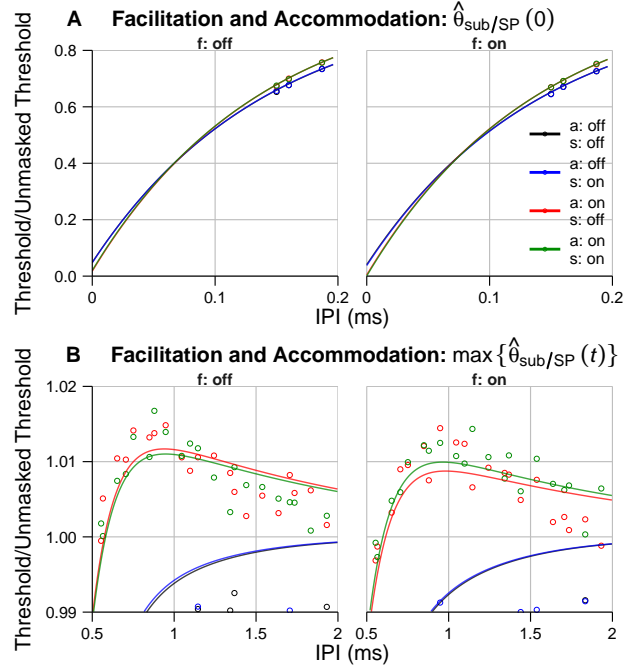


Figure 3.12 Zoomed-in sections of Fig. 3.11A. Neighborhoods of the **A** subthreshold conditioner threshold ratio intercept ($\hat{\theta}_{\text{sub/SP}}(0)$) and **B** subthreshold conditioner threshold ratio maximum ($\max\{\hat{\theta}_{\text{sub/SP}}(t)\}$) for each model combination.

Table 3.3 Quality of fit quantified by R^2 of the probe response threshold data to the corresponding curves, as a function of the IPI, shown in Fig. 3.11. All models are significant compared to the single pulse threshold and relative spread ($p < 0.001$).

Model			Subthreshold		Suprathreshold	
f	a	s	θ	RS	θ	RS
off	off	off	0.996	0.771	0.999	0.912
off	off	on	0.995	0.780	0.999	0.894
off	on	off	0.997	0.851	0.999	0.912
off	on	on	0.996	0.821	0.999	0.894
on	off	off	0.996	0.816	0.999	0.872
on	off	on	0.996	0.833	0.999	0.901
on	on	off	0.997	0.812	0.999	0.909
on	on	on	0.998	0.882	0.999	0.919

cases with s: on compared to s: off (see Fig. 3.11B and D *blue and green circles*, relative to *black and red circles*). However, Table 3.3 reports that the suprathreshold conditioner threshold and relative spread are well-fit by only considering the effect of refractoriness.

3.3.3 Pulse Train Response

The four stimulus-response phenomena contribute differentially to shaping the spike rate in response to pulse train stimulation. After every spike, the ANF model immediately enters the absolute refractory period, which renders it unable to spike until the ARP has ended. Therefore, absolute refractoriness alone sets the upper limit equally on both the onset spike rate (0–12 ms) and final spike rate (200–300 ms). This means that long-term reductions in ANF excitability cannot be due to refractoriness. Active facilitation, in our model, cannot accumulate beyond two pulses and therefore can only contribute to increasing short-term subthreshold excitability. In contrast, our model states that accommodation may accumulate as long as current pulses are injected (see Fig. 3.9G and H), effectively reducing the ongoing subthreshold excitability. Spike rate adaptation also reduces the long-term excitability, however this occurs in response to spiking (see to Fig. 3.9E).

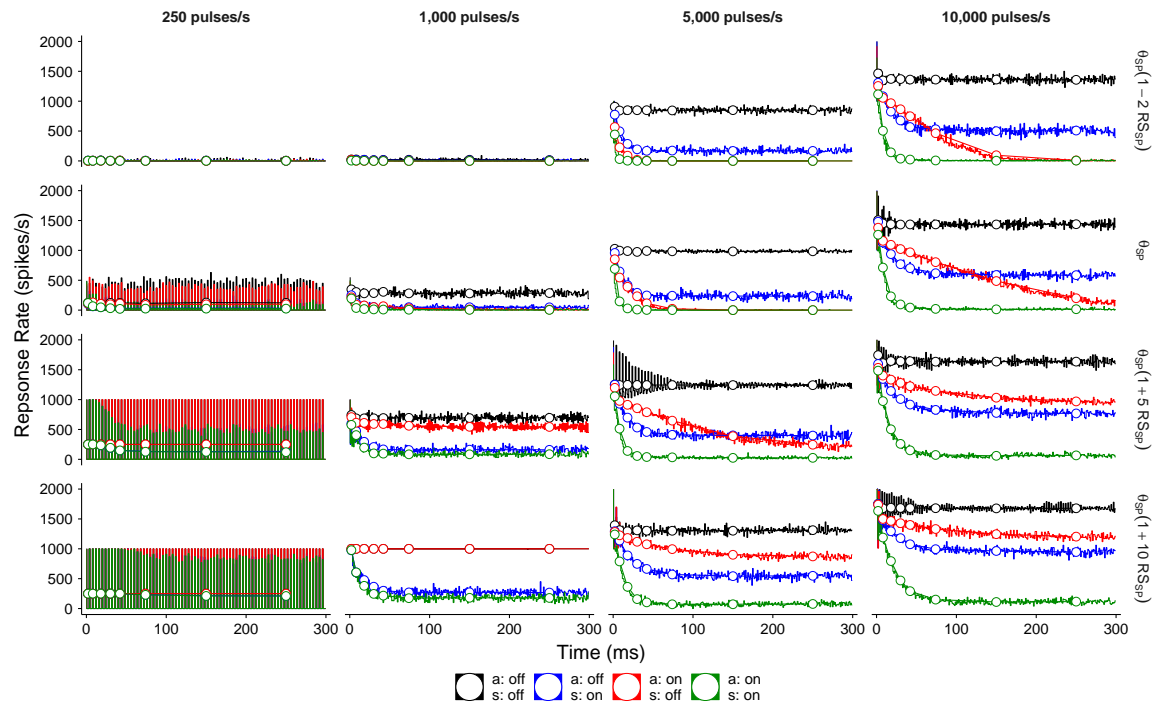


Figure 3.13 Response rates (or spike rates) of four different phenomenological model versions to pulse train stimulation with 250, 1000, 5000, and 10 000 pulses/s rates and $\theta_{SP}(1 + uRS_{SP})$ current levels, where $u = \{-2, 0, 5, 10\}$. Response rates were calculated with two sets of bins: 1 ms (*thin lines*) and increasing-width (*thick lines with white dots*). In all model versions, refractoriness and active facilitation are turned on; only accommodation and spike rate adaptation are varied to produce the 4 model versions shown each with a different color (a: off, s: off as *black*; a: off, s: on as *blue*; a: on, s: off as *red*; and a: on, s: on as *green*).

Therefore, accommodation and spike rate adaptation are the only stimulus-response processes that can produce spike rate decrements over the time scales of 10 to 100 ms. To address this, in Fig. 3.13 we focus on accommodation and spike rate adaptation, by turning them on or off and limit refractoriness and facilitation to both be on. Accom-

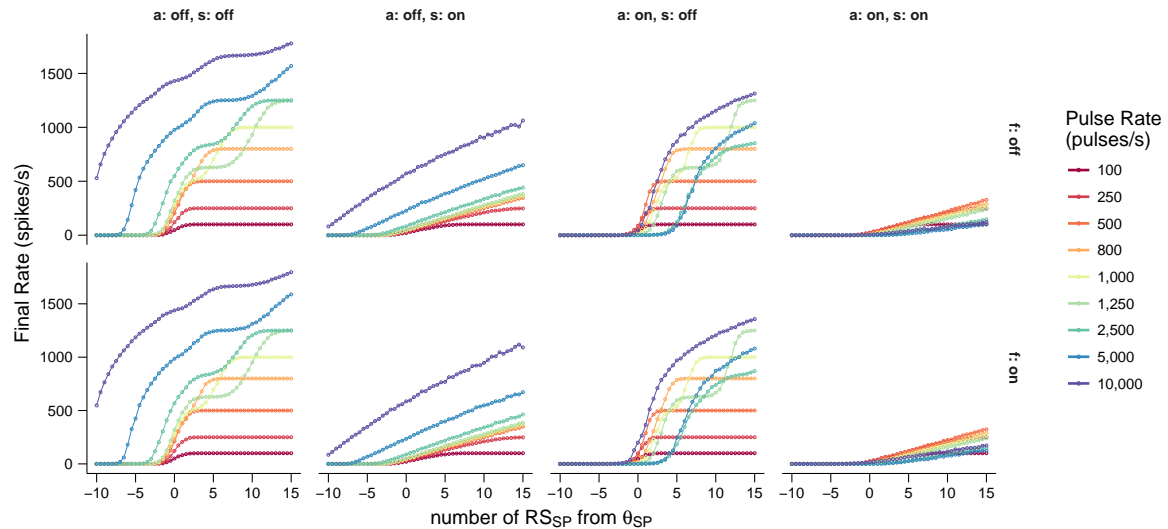


Figure 3.14 Final response rate as a function of the number of RS_{SP} away from θ_{SP} , or u (recall the $\theta_{SP}(1 + uRS_{SP})$ current levels). The final response rate was evaluated over the 200–300 ms interval. All four models shown in Fig. 3.13 are presented here plus those same models with active facilitation enabled, for a total of eight models. Each color represents a different stimulation rate, presented in the legend.

modulation can only accumulate over pulses, but not spikes, which limits the amount of reduction in excitability that can effectively be produced in a rapidly firing neuron. Across the 5000 pulses/s and 10 000 pulses/s stimulation rates, the model versions with accommodation turned on and spike rate adaptation turned off (*red line*) shows an ongoing decrease in response rate over the entire pulse train interval compared to the case with both accommodation and spike rate adaptation turned off (*black line*). This suggests that as the pulse rate increases, the effect of accommodation undergoes greater accumulation, resulting in reduced response rates. However, at high current levels and high pulse rates, accommodation is unable to strongly reduce the spike rate (in Fig. 3.13, *red line*, refer to the bottom panel of 5000 pulses/s and both the middle and bottom panels of 10 000 pulses/s). In contrast, spike rate adaptation reduces neuronal excitability in response to all current levels and pulse rates (*blue line*). Figure 3.13 illustrates that together, accommodation and spike rate adaptation (*green line*) drive the ANF towards non-spiking activity with increasing pulse rates. The final response rate increases with pulse current level, consistent with the data (Fig. 3.2).

In Fig. 3.14, we report the final response rate (over the 200–300 ms interval) in terms of the pulse train current level. Responses to each stimulation rate are plotted as a unique color, with each model variant shown in a separate panel. Spike rate adaptation perhaps imposes the most drastic change on the final response rate in that it broadens the dynamic range, at least for rates lower than 250 pulses/s, and it increases the spiking threshold for all pulse rates. It is also clear that accommodation increases the firing threshold for stimulation rates greater and including 2500 pulses/s. Any effects of active facilitation on the final response rate are not readily apparent. This is not surprising given that active

facilitation was not a major factor in predicting the paired pulse response, as we discovered in Fig. 3.12A–B, and since active facilitation does not accumulate beyond one IPI (recall (3.27)).

The Adaptation Continuum in ANFs: The Effect of Accommodation and Spike Rate Adaptation on the Normalized Spike Rate Decrement (NSRD)

Evidence from single neuron recordings suggest, that although refractoriness places a limit on the maximum spike rate, accommodation and spike rate adaptation are responsible for reducing the spike rate over longer time scales than refractoriness (Zhang et al., 2007). Evidence from ANF models suggests that HCN channels are responsible for producing spike rate adaptation that covaries with accommodation (Negm and Bruce, 2014). We simulated versions of the phenomenological model in which we simultaneously covaried the amount of spike rate adaptation and accommodation over a range of values. The strength of accommodation (quick and slow) and spike rate adaptation for threshold (a_{θ,a_q} , $2a_{\theta,a_s}$, and $p_{\theta,s}$) and relative spread (a_{RS,a_q} and $p_{RS,s}$) were varied as a percentage of those values (found in Table 3.1) in increments of 10 %. These models also incorporated refractoriness and active facilitation, as earlier.

Spike rate adaptation should only vary with the onset response rate. Since spike rate adaptation cannot occur when a neuron does not fire, accommodation is the process that then limits the steady-state firing rate. This implies that only together can accommodation and spike rate adaptation drive the neuron to the lowest spike rates, which impacts the steady-state, or final spike rate. The combined effect of accommodation and spike rate adaptation naturally increases the normalized spike rate decrement (NSRD, the difference between the onset and final spike rates, normalized by the onset rate), thereby classifying the neuron as a strong adapter. Furthermore, accommodation is dependent on the IPI or pulse rate, therefore we should expect variation in the NSRD as a function of the pulse train rate.

The exact mixture of accommodation and spike rate adaptation may be able to explain the NSRD versus onset rate plots (Zhang et al., 2007). First, these plots show that the proportion of strong adapters ($\text{NSRD} \geq 0.9$) increases with the pulse rate. Second, they show that the slope of NSRD versus onset rate begins as approximately flat and becomes progressively more negative with increasing pulse rate. Figure 3.15 also shows the proportion of strongly adapting model versions ($\text{NSRD} \geq 0.75$, as in Negm and Bruce, 2014). Additionally, Fig. 3.15 shows that the slope of NSRD versus onset increasingly becomes more negative with pulse rate, which is due primarily to the slow component of accommodation. Figure 3.15 shows that increasing the strength of subthreshold and suprathreshold adaptation produces an increase in NSRD, as expected. A more nuanced effect is that the combination of several strengths of adaptation produces variability in the NSRD. This may help explain a similar experimental result (see Fig. 5 of Zhang et al., 2007), implying that heterogeneity in the cell-to-cell strengths of accommodation and spike rate adaptation could explain a wide range in NSRD observed in the animal data.

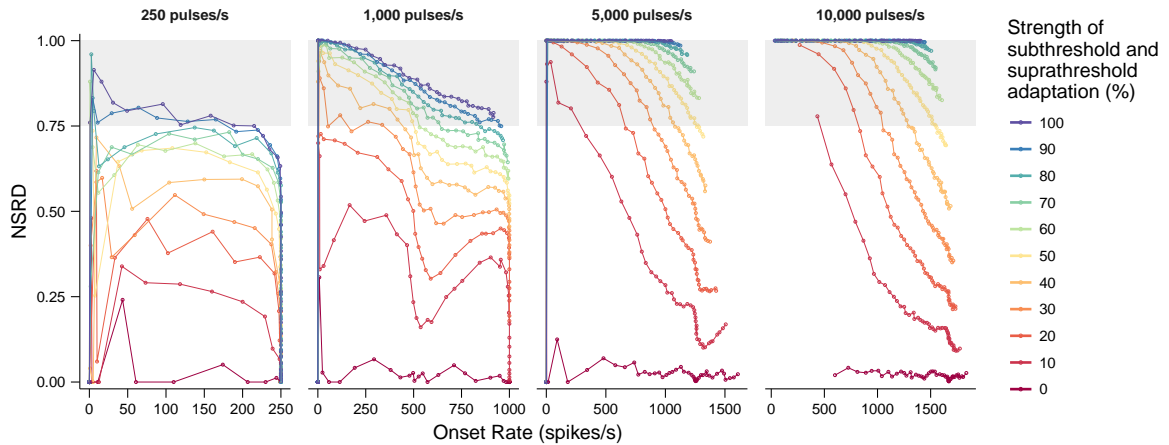


Figure 3.15 NSRD versus onset rate in response to pulse train stimulation at the rates of 250, 1000, 5000, and 10 000 pulses/s. Strength of subthreshold and suprathreshold adaptation ranging from 0 % (no adaptation) to 100 % (strong adaptation) is displayed with a variety of colors (see legend). Responses to increasing pulse current level flow from low to high onset rate.

3.4 Discussion

Our dynamic threshold potential model, which incorporates refractoriness, spike rate adaptation, facilitation, and accommodation can explain response rate profiles on the order of 10 to 100 ms (Heffer et al., 2010; Miller et al., 2011; Zhang et al., 2007) to pulse train stimulation delivered at a wide range of pulse rates. Accommodation works synergistically with spike rate adaptation to more rapidly reduce spiking levels at moderate-to-high pulse train rates. Previous models have not considered accommodation to explain this data. The model of Bruce et al. (1999a), which only included refractoriness, accurately simulated pulse train responses up to 800 pulses/s, but not higher. Goldwyn et al. (2012) included refractoriness and facilitation in a point-process model ANF, but could not predict the relatively higher level of irregularity in the response rate that would be associated with accommodation (Sly et al., 2007), nor could it predict greater levels of adaptation seen in response to higher pulse rates (Zhang et al., 2007). Given variable-amplitude pulse train input with the aim of predicting the probability of firing, (Campbell et al., 2012) built a computational stimulus-response model of ANF that included the effects of refractoriness, spike rate adaptation, and accommodation. Their model could accurately predict responses to pulse rate of up to pulses/s, but not higher. Unsurprisingly, accommodation is directly applicable since it is pulse-rate-dependent therefore, its effects grow as pulse rates increase. Our model was capable of estimating responses to pulse rates up to 5000 to 10 000 pulses/s. This is of particular importance to CI stimulation strategies whose effective stimulation rates are in this range (Boulet et al., 2016, or see Chap. 2).

To the best of our knowledge, our model is the first to implement the individual effects of passive and active facilitation. Passive facilitation imposes a relatively high floor on the long-term (or final) response rate in response to 5000 to 10 000 pulses/s pulse rates and

active facilitation just boosts this phenomenon (see Fig. 3.14). While active facilitation is primarily a function of residual sodium activation near the threshold potential between pulses, passive facilitation relies on membrane capacitance, membrane resistance (or leakage conductance), and electrode-to-neuron distance or geometry. Our model mimicked responses to intracellular injection by using membrane capacitance and resistance values from a patch of ANF node of Ranvier as well as resting threshold potential and intracellular resting threshold current. Predicting more accurate CI responses may benefit from considering extracellular parameters such as extracellular resting threshold current as well as the different membrane capacitance and resistance values at individual nodes of Ranvier. This translates to multiple possibilities for how extracellular passive facilitation would affect neural excitability. Along those lines, if we consider different spike initiation nodes, then active facilitation, accommodation, refractoriness, and spike rate adaptation would also have behave differently since it is well known that ion channel type distribution is not uniform along the length of the ANF (see Boulet et al., 2016; Davis and Crozier, 2015, and references therein, or Chap. 2). Accounting for responses from a full ANF model requires an intractable number of parameters which is not best suited for a phenomenological ANF responses to a CI, but rather a multicompartmental biophysical model. Therefore, for our phenomenological ANF model we deemed it was more appropriate to enforce a parsimonious model description while attempting to maintain accuracy of the ANF responses.

Our phenomenological model could not accurately reproduce the complete loss of long-term excitability in response to 10 000 pulses/s stimulation near resting threshold current levels reported by Zhang et al. (2007) (and shown in Fig. 3.2D). However, the ANF that was exposed to 10 000 pulses/s stimulation was different than the ANF that responded to the 250, 1000, and 5000 pulses/s stimulation rates. Additionally, Zhang et al. (2007) delivered 10 000 pulses/s trains of 20 μ s/phase biphasic pulses compared to the 250, 1000, and 5000 pulses/s trains of 40 μ s/phase biphasic pulses, whereas our 250, 1000, and 5000 pulses/s trains were composed of longer 40 μ s/phase monophasic pulses. These shortened pulse durations leave less time for the membrane potential to be near threshold and therefore reduce the amount of active facilitation, which may help explain why our model pulse train responses exhibit a slightly higher final rate than those recorded by Zhang et al. (2007) for the 10 000 pulses/s stimulation. Figure 3.15 also suggests that a large range of NSRD is possible depending on the pulse current level and strength of subthreshold and suprathreshold adaptation.

There is potential for further refinement of the interaction between pulses and the subthreshold phenomena of active facilitation and accommodation. As it stands, the subthreshold mechanisms are delivered by a delayed and normalized quantity of the stimulus response potential $V_{stim}(t)$. The delay was introduced as a means of forcing the activation of active facilitation and accommodation no earlier than at the offset of the depolarizing phase of V_{stim} , thereby influencing the subthreshold excitability of the ANF in response to the next pulse. Normalization was performed by dividing $V_{stim}(t - w)$ by $V_{\theta,0}$ which allowed the effects of active facilitation and accommodation to be relative to $V_{\theta,0}$. Our

model is based on responses to monophasic pulses. Further research is required to ascertain the effects of active facilitation and accommodation in response to the hyperpolarizing phases of biphasic pulses before they are used in a computational model of this sort. It will be important to generalize the model to explain single pulse and pulse train responses to multiple pulse shapes including 1) biphasic pulses with and without interphase gaps and 2) different pulse widths, since this directly impacts the effects of facilitation and accommodation. Once more light has been shed on these effects, one starting point would be to use separate stimulus filters for the positive and negative phases (Goldwyn et al., 2012) of the current pulse train in order to more accurately model the subthreshold contribution to biphasic stimulation. A single pulse response model developed by Horne et al. (2016) may be another way of including those effects in our model. Important aspects of our phenomenological dynamic threshold potential model outside of the predicting ANF responses to CI stimulation, are the simplicity, expandability, and applicability of the model. For example, other stimulus-response phenomena can be inserted in the model. Our model can easily be used as a research tool to investigate separate mechanisms that contribute to responses to CI stimulation. This is in contrast to other phenomenological-biophysical hybrid models that in which mechanisms not easily interchangeable. It will be interesting to test the responses of our model to amplitude-modulated pulse trains, responsible for encoding slow changes in the amplitude of the acoustic signal (Wilson et al., 1988), that are typically delivered to ANFs in standard CIs. The model is also efficient enough for real-time processing, which could be used in refining cochlear implant stimulation.

3.5 Conclusions

We have proposed a phenomenological model of how ANFs may respond to CI stimulation, given their time-varying subthreshold and suprathreshold effects. Our model predicts responses to paired pulse stimulation and constant current level pulse trains, as reported by various experiments using single fiber recordings in cats. Amplitude variation of the pulse train over time may lead to dynamic shifts: from a primarily subthreshold processing regime where accommodation governs the reduction of the ANF responses, to one that is dominated by spike rate adaptation. As we have shown, this has implications for online changes to the steady-state threshold and dynamic range, depending on whether accommodation or spike rate adaptation is active in responding to pulse train stimulation.

References

Boulet, J., White, M. W., and Bruce, I. C. (2016). Temporal considerations for stimulating spiral ganglion neurons with cochlear implants. *J Assoc Res Otolaryngol*, 17(1):1–17.

- Bruce, I. C., Irlicht, L. S., White, M. W., O’Leary, S. J., Dynes, S., Javel, E., and Clark, G. M. (1999a). A stochastic model of the electrically stimulated auditory nerve: pulse-train response. *IEEE Trans Biomed Eng*, 46(6):630–637.
- Bruce, I. C., White, M. W., Irlicht, L. S., O’Leary, S. J., Dynes, S., Javel, E., and Clark, G. M. (1999b). A stochastic model of the electrically stimulated auditory nerve: single-pulse response. *IEEE Trans Biomed Eng*, 46(6):617–629.
- Campbell, L. J., Sly, D. J., and O’Leary, S. J. (2012). Prediction and control of neural responses to pulsatile electrical stimulation. *J Neural Eng*, 9(2):026023.
- Cartee, L. A., van den Honert, C., Finley, C. C., and Miller, R. L. (2000). Evaluation of a model of the cochlear neural membrane. I. physiological measurement of membrane characteristics in response to intrameatal electrical stimulation. *Hear Res*, 146(1-2):143–152.
- Davis, R. L. and Crozier, R. A. (2015). Dynamic firing properties of type I spiral ganglion neurons. *Cell Tissue Res*, 361(1):115–127.
- Dynes, S. B. C. (1996). *Discharge characteristics of auditory nerve fibers for pulsatile electrical stimuli*. PhD thesis, Massachusetts Institute of Technology, Cambridge, Massachusetts.
- Fredelake, S. and Hohmann, V. (2012). Factors affecting predicted speech intelligibility with cochlear implants in an auditory model for electrical stimulation. *Hear Res*, 287(1-2):76–90.
- Gerstner, W. and Kistler, W. M. (2002). *Spiking Neuron Models*. Single Neurons, Populations, Plasticity. Cambridge University Press.
- Goldwyn, J. H., Rubinstein, J. T., and Shea-Brown, E. (2012). A point process framework for modeling electrical stimulation of the auditory nerve. *J Neurophysiol*, 108(5):1430–1452.
- Hamacher, V. (2004). *Signalverarbeitungsmodelle des elektrisch stimulierten Gehörs*. PhD thesis, Verlag Mainz, Aachen.
- Heffer, L. F., Sly, D. J., Fallon, J. B., White, M. W., Shepherd, R. K., and O’Leary, S. J. (2010). Examining the auditory nerve fiber response to high rate cochlear implant stimulation: chronic sensorineural hearing loss and facilitation. *J Neurophysiol*, 104(6):3124–3135.
- Hodgkin, A. L. and Huxley, A. F. (1952). A quantitative description of membrane current and its application to conduction and excitation in nerve. *J Physiol*, 117(4):500–544.
- Horne, C. D. F., Sumner, C. J., and Seeber, B. U. (2016). A Phenomenological Model of the Electrically Stimulated Auditory Nerve Fiber: Temporal and Biphasic Response Properties. *Front Comput Neurosci*, 10(9):5–17.

- Lapicque, L. (1907). Recherches quantitatives sur l'excitation électrique des nerfs traitée comme une polarisation. *J Physiol Pathol Gen*, 9:620–635.
- Laughlin, S. B. (2001). Energy as a constraint on the coding and processing of sensory information. *Curr Opin Neurobiol*, 11(4):475–480.
- Liu, Q., Manis, P. B., and Davis, R. L. (2014). I_h and HCN channels in murine spiral ganglion neurons: tonotopic variation, local heterogeneity, and kinetic model. *J Assoc Res Otolaryngol*, 15(4):585–599.
- Long, J. S. (1997). *Regression models for categorical and limited dependent variables*. SAGE Publications, Inc.
- Miller, C. A., Abbas, P. J., and Robinson, B. (2001). Response properties of the refractory auditory nerve fiber. *J Assoc Res Otolaryngol*, 2(3):216–232.
- Miller, C. A., Woo, J., Abbas, P. J., Hu, N., and Robinson, B. K. (2011). Neural masking by sub-threshold electric stimuli: animal and computer model results. *J Assoc Res Otolaryngol*, 12(2):219–232.
- Mino, H., Rubinstein, J. T., and White, J. A. (2002). Comparison of algorithms for the simulation of action potentials with stochastic sodium channels. *Ann Biomed Eng*, 30(4):578–587.
- Negm, M. H. and Bruce, I. C. (2008). Effects of I_h and I_{KLT} on the response of the auditory nerve to electrical stimulation in a stochastic Hodgkin–Huxley model. *Proc 30th Annu Int Conf IEEE Eng Med Biol Soc*, 2008:5539–5542.
- Negm, M. H. and Bruce, I. C. (2014). The effects of HCN and KLT ion channels on adaptation and refractoriness in a stochastic auditory nerve model. *IEEE Trans Biomed Eng*, 61(11):2749–2759.
- Nourski, K. V., Abbas, P. J., and Miller, C. A. (2006). Effects of remaining hair cells on cochlear implant function. Technical Report 15, University of Iowa, Iowa City.
- Sly, D. J., Heffer, L. F., White, M. W., Shepherd, R. K., Birch, M. G. J., Minter, R. L., Nelson, N. E., Wise, A. K., and O'Leary, S. J. (2007). Deafness alters auditory nerve fibre responses to cochlear implant stimulation. *Eur J Neurosci*, 26(2):510–522.
- Stemmler, M. and Koch, C. (1999). How voltage-dependent conductances can adapt to maximize the information encoded by neuronal firing rate. *Nat Neurosci*, 2(6):521–527.
- Verveen, A. A. (1961). *Fluctuation in excitability*. PhD thesis, Netherlands Central Institute for Brain Research, Amsterdam, Netherlands.
- Verveen, A. A. and Derksen, H. E. (1968). Fluctuation phenomena in nerve membrane. *Proc IEEE*, 56(6):906–916.

Wilson, B. S., Finley, C. C., Farmer, J. C., Lawson, D. T., Weber, B. A., Wolford, R. D., Kenan, P. D., White, M. W., Merzenich, M. M., and Schindler, R. A. (1988). Comparative studies of speech processing strategies for cochlear implants. *Laryngoscope*, 98(10):1069–1077.

Zhang, F., Miller, C. A., Robinson, B. K., Abbas, P. J., and Hu, N. (2007). Changes across time in spike rate and spike amplitude of auditory nerve fibers stimulated by electric pulse trains. *J Assoc Res Otolaryngol*, 8(3):356–372.

Predictions of the Contribution of Hyperpolarization-Activated
Cyclic Nucleotide-Gated Cation Half-Maximal Activation Potential
Heterogeneity to Variability in Intrinsic Adaptation of Spiral
Ganglion Neurons

Abstract

Spiral ganglion neurons (SGNs) exhibit a wide range in their strength of intrinsic adaptation on a timescale of 10s to 100s of milliseconds to electrical stimulation from a cochlear implant (CI). The purpose of this study was to determine how much of that variability could be caused by the heterogeneity in half-maximal activation potentials of hyperpolarization-activated cyclic nucleotide-gated cation (HCN) channels, which are known to produce intrinsic adaptation. We developed a computational membrane model of feline Type I SGN based on the Hodgkin–Huxley model plus HCN and low-threshold potassium (KLT) conductances in which we varied the half-maximal activation potential of the HCN channel and simulated the SGN’s response to pulse train and paired-pulse stimulation. Physiologically-plausible variation of HCN half-maximal activation potentials could indeed determine the range of adaptation on the timescale of 10s to 100s of milliseconds and recovery from adaptation seen in the physiological data while maintaining refractoriness within physiological bounds. This computational model demonstrates that HCN channels play an important role in regulating the degree of adaptation in response to pulse train stimulation and therefore contribute to variable constraints on acoustic information coding by CIs. This finding has broad implications for CI stimulation paradigms in that cell-to-cell variation of HCN channel properties are likely to significantly alter SGN excitability and therefore auditory perception.

4.1 Introduction

Spiral ganglion neurons (SGNs) function to relay auditory information from the inner hair cells (IHC) of the cochlea to the cochlear nucleus in the auditory brainstem. If IHCs are damaged or dead, cochlear implants (CIs) provide a prosthetic solution for delivering a functional sense of hearing to individuals by electrically stimulating SGNs with patterned pulses. Studies such as the work by Arora et al. (2009) have demonstrated that speech perception is not necessarily improved by increasing the stimulation rate above 900 pulses/s per electrode. Adaptation may be partially responsible for the variability in speech perception by diminishing the SGN response for high-rate stimulation. A computational model that can accurately describe how SGNs respond to electrical stimulation may provide an important tool for understanding the underlying electrophysiology of the SGN and for developing CI stimulation paradigms that take into account the operating limits and spatio-temporal interactions of SGNs (Boulet et al., 2016; Miller et al., 2003, or Chap. 2).

Adaptation can be observed in post-stimulus time histograms (PSTHs) as an ongoing decay in a neuron’s firing rate. In SGN responses to CI stimulation, this phenomenon typically occurs on the order of 10 to 100 ms or more and is prevalent for a wide range of stimulation pulse rates and current levels (Heffer et al., 2010; Litvak et al., 2003; Miller et al., 2011; Zhang et al., 2007). In particular, Zhang et al. (2007) found a range of adaptation

strengths in response to stimulating SGNs with high-rate pulse trains. Another study by Miller et al. (2011) showed that SGNs slowly recovered on a timescale of 10 to 100 ms after adapting to trains of high-rate stimulation. It is notable that this adaptation appears to consist of both suprathreshold adaptation, i.e., spike-dependent spike-rate adaptation, and accommodation, i.e., a subthreshold stimulus-dependent drop in excitability (Boulet et al., 2016; Miller et al., 2011; Negm and Bruce, 2014).

Since the Hodgkin–Huxley model (Hodgkin and Huxley, 1952) does not predict spike rate adaptation, Woo et al. (2009a,b, 2010) proposed a Hodgkin–Huxley model augmented with a spike-dependent extracellular potassium accumulation mechanism that is endogenous to leech central nervous system (Baylor and Nicholls, 1969). This model was extended by Miller et al. (2011) to explain accommodation (subthreshold adaptation) by including low-threshold potassium (KLT) channels characterized by 2-state-activation. Unfortunately, the adjustment of the nodal KLT channel densities responsible for producing realistically strong adaptation led to unrealistically long absolute refractory period (ARP) durations (Miller et al., 2011).

However, Type I SGNs are endowed with a remarkable diversity of voltage-gated ion channel types that allow for various modes of excitation, including adaptation/accommodation to constant current injection (see Table 1 and Fig. 3 of Davis and Crozier, 2015). Of these many channel types, the hyperpolarization-activated cyclic nucleotide-gated cation (HCN) channel has been characterized as being partially open at rest and has gating dynamics with time constants in the range of 10s to 100s of milliseconds at mammalian body temperature (Benarroch, 2013; Biel et al., 2009; Howells et al., 2012; Robinson and Siegelbaum, 2003). These characteristics led Negm and Bruce (2008, 2014) to propose an alternative SGN model for CI stimulation that was capable of producing spike rate adaptation and accommodation while also generating accurate ARP values. In their model, Negm and Bruce (2008, 2014) added HCN channels (Huganard and McCormick, 1992; Rothman and Manis, 2003b) and KLT channels with activation and partial inactivation particles (Rothman and Manis, 2003a) found in murine ventral cochlear nucleus (VCN) neurons to the standard Hodgkin–Huxley model. Despite varying HCN and KLT channel densities, the model could only produce no adaptation or strong adaptation, not the continuum of strengths of adaptation that is observed experimentally.

HCN channel subunits are prevalent in neurons of the lower auditory system where they function by activating under membrane hyperpolarization, a restoring force towards its depolarized reversal potential and deactivating under membrane depolarization, thus regulating the effective resting membrane potential (RMP) (Cao and Oertel, 2011; Kim and Holt, 2013; Liu et al., 2014a,b; Rothman and Manis, 2003a; Rusznák and Szűcs, 2008). The half-maximal activation potential ($V_{1/2}$) is a parameter involved in determining a channel's voltage-dependent gating and has known heterogeneity in HCN channels. In guinea pig SGN, $V_{1/2}$ was reported as -104 mV in the afferent dendrites (Yi et al., 2010) and -101 mV at the soma (Chen, 1997). The $V_{1/2}$ values reported in murinae expressed the wide range of -115 to -87 mV in the apex and -110 to -92 mV in the middle and base of the cochlea (Liu et al., 2014b, see Table 2), whereas cell-to-cell variation within a cochlear region showed

a similar range (-122 to -78 mV) (Mo and Davis, 1997). Finally, in neonatal mice, the half-maximal activation potential was reported in the range of -106 to -91 mV (Kim and Holt, 2013).

In this study, we sought to test the hypothesis that varying the half-maximal activation potential of the HCN model taken from murine VCN (Rothman and Manis, 2003b) or a newer HCN model obtained from basal SGN (Liu et al., 2014b) impacts the strength of spike rate adaptation and accommodation in a membrane model of Type I SGN. We also tested how changing the HCN $V_{1/2}$ affected refractoriness and verified to ensure that properties of the neuron's refractoriness stayed within experimentally-observed bounds.

4.2 Methods

4.2.1 Membrane Model

We modeled the membrane potential (V_m) of a single node of Ranvier for a Type I SGN in the same fashion as Negm and Bruce (2008, 2014). This model builds on the Hodgkin-Huxley-type (Hodgkin and Huxley, 1952) Na_v and K_v channels that were modified for $37^\circ C$ (Mino et al., 2002), plus additional ionic currents described below, a leakage current I_{leak} , and the injected stimulation current I_{inj} . In total, the four ionic currents were characterized by the fast sodium (I_{Na}) (Mino et al., 2004, 2002), delayed-rectifier potassium (I_K) (Mino et al., 2004, 2002), low-threshold potassium (I_{KLT}) (Rothman and Manis, 2003a), and either one of two hyperpolarization-activated currents: $I_{h,r}$ (Rothman and Manis, 2003b) or $I_{h,(q,s)}$ (Liu et al., 2014b). The I_h currents were modeled from HCN channels, where $I_{h,r}$ refers to the current generated by the HCN(r) channel model. Governed by the HCN(q,s) channel model, $I_{h,(q,s)}$ contains two currents that operate independently at separate time scales and activations. The dual nature of the HCN(q,s) channel model is likely the result of HCN1 and HCN4 subunit expression in heteromeric channels or a mix of homomeric channels in one SGN (Liu et al., 2014b; Yi et al., 2010). The reversal potential of the leakage current was configured to ensure a baseline resting membrane potential of -78 mV across all model variants. The dynamics of the membrane potential V_m obey the first-order differential equation

$$C_m \frac{dV_m}{dt} + I_{Na} + I_K + I_{KLT} + I_h + I_{leak} = I_{inj} \quad (4.1)$$

where C_m is the membrane capacitance. Experimentally-derived single-channel conductance values for the I_{KLT} and I_h currents, temperature scaling coefficients, as well as nodal densities for the corresponding channels are unknown. These values used in our study were chosen based on the modeling studies performed by Negm and Bruce (2008, 2014). In their SGN membrane model, Negm and Bruce (2014) showed that KLT and HCN channels can

Table 4.1 SGN node of Ranvier membrane model parameters.

Parameter	Symbol	Value	Reference
Nodal capacitance	C_m	0.0714 pF	Bruce (2006)
Nodal resistance	R_m	1953.49 M Ω	Bruce (2006)
Na reversal potential	E_{Na}	66 mV	Mino et al. (2002)
K reversal potential	E_K	-88 mV	Mino et al. (2002)
HCN(r) reversal potential	$E_{h,r}$	-43 mV	Rothman and Manis (2003b)
HCN(q,s) reversal potential	$E_{h,(q,s)}$	-41 mV	Liu et al. (2014b)
Resting membrane potential	V_{rest}	-78 mV	Mino et al. (2002)
Na _v conductance	γ_{Na}	25.69 pS	Mino et al. (2002)
K _v conductance	γ_K	50.0 pS	Mino et al. (2004)
KLT conductance	γ_{KLT}	13.0 pS	Negm and Bruce (2014); text
HCN conductance	γ_h	13.0 pS	Negm and Bruce (2014); text
Max# Na _v channels	N_{Na}^{max}	1000	Mino et al. (2002)
Max# K _v channels	N_K^{max}	166	Negm and Bruce (2014); text
Max# KLT channels	N_{KLT}^{max}	166	Negm and Bruce (2014); text
Max# HCN(r) channels	$N_{h,r}^{max}$	100	Negm and Bruce (2014); text
Max# HCN(q) channels	$N_{h,q}^{max}$	$p_q N_{h,r}^{max}$	Liu et al. (2014b)
Max# HCN(s) channels	$N_{h,s}^{max}$	$p_s N_{h,r}^{max}$	Liu et al. (2014b)
Proportion HCN(q) channels	p_q	0.4471	Liu et al. (2014b)
Proportion HCN(s) channels	p_s	$1-p_q$	Liu et al. (2014b)
KLT thermal coefficient	$Q_{10,KLT}$	3.0	Negm and Bruce (2014); text
HCN thermal coefficient	$Q_{10,h}$	3.3	Negm and Bruce (2014); text
HCN(r) $V_{1/2}$ stan. dev.	σ_r	6.37 mV	Liu et al. (2014b); text
HCN(q) $V_{1/2}$ stan. dev.	σ_q	3.20 mV	Liu et al. (2014b)
HCN(s) $V_{1/2}$ stan. dev.	σ_s	6.37 mV	Liu et al. (2014b); text

induce spike rate adaptation and significantly change the degree of refractoriness compared to the Hodgkin–Huxley (HH) model. However, the degree of spike rate adaptation and refractoriness was largely insensitive to the number of KLT and HCN channels (Negm and Bruce, 2014). For membrane model parameter values, refer to Table 4.1. We simulated six different models of which the first was the Hodgkin–Huxley model 1) HH and the remaining five were HH models augmented with ionic currents and are denoted by their channel type: 2) +HCN(r), 3) +HCN(q,s), 4) +KLT, 5) +HCN(r)+KLT, and 6) +HCN(q,s)+KLT.

The effect of voltage-gated ion channel stochasticity on the membrane potential is inversely related to the neuron’s diameter (Verveen, 1962; Verveen and Derksen, 1968) and since Type I SGN axons are relatively small, the fluctuations contribute to the total membrane response in a significant way (Imenov and Rubinstein, 2009; Rubinstein, 1995). The effects of single-cell stochasticity also provide better predictions of some psychophysical phenomena (Bruce et al., 1999a). Therefore, it is important to accurately model the stochastic nature of voltage-gated ion channels since the resulting membrane fluctuations are one of the main sources of spike timing variability (Schneidman et al., 1998). Voltage-gated

ion channel states were simulated with a version of Gillespie’s Direct Method (Gillespie, 1977) for Markov chains (MC) which is an efficient and exact algorithm known as the channel number tracking procedure (Mino et al., 2002). Under certain conditions diffusion approximation (DA) techniques can be faster and scale at no cost for an arbitrary number of channels, but they may provide inaccurate results (Pezo et al., 2014). We used the MC algorithm to simulate channel states since the relatively small number of HCN and KLT channels, their slow kinetics, along with the simulation of membrane model (4.1) solved by the explicit Euler method for a $1 \mu\text{s}$ time step were not well suited for the DA approach. All channel models were first initialized at resting membrane potential in order to randomize channel states over a period long enough (300 ms, see Fig. 4.1B) to capture the kinetics of even the slowest model. Next, the membrane model was initialized for 300 ms with $I_{\text{inj}} = 0 \text{ pA}$, allowing the membrane potential to fluctuate naturally prior to the membrane model being exposed to stimulation paradigms.

4.2.2 Modifications to Kinetic HCN Channel Models

In this study, we varied the half-maximal activation potential ($V_{1/2}$) of the two HCN kinetic models to determine the operational range of the channel in terms of its ability to slowly modulate the voltage response of the neural membrane. The half-maximal activation potential is the voltage at which the activation function is equal to 0.5 (see Fig. 4.1A). Following the Negm and Bruce (2014) study, we first adjusted the HCN(r) model to account for the difference in the resting membrane potential of the VCN cell model of (Rothman and Manis, 2003b) and that of the SGN cell model. Since the HCN(q,s) model was already characterized from murine SGN we made the assumption that the resting membrane potential is similar between murine and feline SGNs. Figure 4.1 shows the activation functions and time constants (as a function of the relative transmembrane potential $V = V_m - V_{\text{rest}}$) at their mean $V_{1/2}$ HCN models (bold curves).

The basal cochlear HCN(q,s) channel model contains two parallel conductances that operate at distinct timescales. The ‘quick’ q particle’s $V_{1/2}$ standard deviation is 3.20 mV (Liu et al., 2014b). The activation of the ‘slow’ s particle (s_∞) is described by two Boltzmann equations and is characterized by the $V_{1/2}$ standard deviations: 4.34 mV and 8.40 mV (Liu et al., 2014b). In order to simplify shifts in s_∞ and τ_s without distorting the shape of the functions, we shifted both of the s particle’s components by integer multiples of the mean value, 6.37 mV. As for the HCN(r) channel description, we chose to shift its activation function r_∞ and time constant τ_r by the same value (6.37 mV) in order to simplify the comparison of the relative effects of HCN channel type.

A range of $V_{1/2}$ shifts were systematically applied to the HCN kinetic models. These shifts were defined as $cV_{1/2}$ standard deviations, where c is an integer. We decided to explore shifts over $\pm 4 V_{1/2}$ standard deviations, because of some uncertainty as to the direct applicability of the $V_{1/2}$ statistics from cultured, neonatal, murine SGNs to our model of *in vivo* responses of adult, feline SGNs, as well as uncertainty about the resting membrane

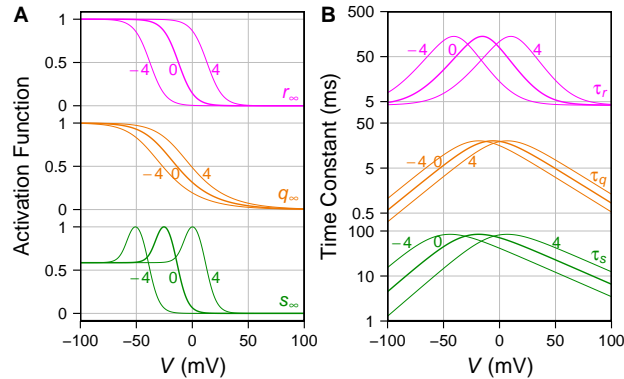


Figure 4.1 **A** Activation functions and **B** time constants for the HCN(r) and HCN(q,s) channel models as a function of the relative membrane potential V . Several curves are shown for each HCN model, including one *bold line* that represents the non-shifted model and *two thinner lines* that indicate the minimum and maximum of the explored ranges. Numbers shown beside the curves indicate how many $V_{1/2}$ standard deviations the functions have been shifted by. Refer to (4.8), (4.9), and (4.12)–(4.17) for more details.

potential of murine SGNs. Figure 4.1 shows the shifts applied to both the activation functions and the time constants as a function of the relative membrane potential (which is the membrane potential relative to the resting membrane potential). The activation function of each particle is shown in Fig. 4.1A and is shifted by specific integer multiples (shown beside the curves) of the $V_{1/2}$ standard deviation. Figure 4.1B shows the time constant, shifted by the same values as the activation function. The HCN(r) and HCN(q,s) model functions were shifted by $-4, -3, -2, -1, 0, 1, 2, 3,$ and 4 standard deviations of $V_{1/2}$. When referring to a model variant with shifted kinetics, such as +HCN(q,s)+KLT that has its HCN(q,s) kinetics shifted by $cV_{1/2}$ standard deviations, we will use this convention throughout: +HCN(q,s,c)+KLT.

4.2.3 Stimuli

In our simulation study, the pulse amplitude of the adaptation, masker-probe train recovery, and refractoriness stimulation paradigms was quantified in terms of the firing efficiencies (FEs) specific to each neuron model. For a single trial, single pulse response, the matter of whether a neuron fires or not is one that can only have a binary outcome. In that respect, the FE corresponds to the probability that the neuron will spike due to being driven by a single pulse at a specific current level. A firing efficiency of 50 % corresponds to the average single pulse threshold current. The stimulation parameters varied somewhat across the studies from which the data were taken to evaluate the modeling results. In order to reduce the number of simulations required, we have chosen a consistent set of stimulation parameters that are close to, but do not all exactly match, the parameters used in the experimental studies.

A 200 ms train of high-rate pulses was initially used by Miller et al. (2011) as a forward

masker to determine its effect on the subsequent neural recovery in response to a 250 ms low-frequency probe pulse train. Two types of stimuli trains were generated: 1) probe-alone and 2) masker-probe, where the probe-alone case represented the masker-free control condition. In our case, each masker and probe train lasted for 300 ms, held a fixed pulse current level, and directly followed each other. For the probe-alone train, the masker train was delivered at $I_{inj} = 0$ pA. In our simulations, the masker-probe train began with a masker train and was delivered at a variety of first-pulse FEs (1, 10, 20, 50, 80, 99, 99.99, and 99.9999 %) and pulse rates (200, 800, 2000, and 5000 pulses/s) (Miller et al., 2008, 2011; Negm and Bruce, 2008, 2014; Zhang et al., 2007). The high FEs, i.e., 99.99 and 99.9999 % were chosen to emulate the highest current levels of Miller et al. (2011), which respectively were approximately 0.9 dB and 1.3 dB greater than the lowest current level to elicit at least one spike in response to the masker pulse train interval. In all cases, the probe train was delivered at the single pulse threshold current level and 100 pulses/s (Miller et al., 2011). Each pulse was a biphasic, symmetric, charge balanced, depolarizing-phase-leading pulse that lasted 50 μ s/phase without an interphase gap (Negm and Bruce, 2014). The stimuli for studying onset adaptation were just the initial masker portion of the masker-probe pulse trains, without the probe.

In order to determine the refractory behavior we adopted a paired-pulse paradigm (Cartee et al., 2006, 2000; Dynes, 1996; Miller et al., 2001) that was designed to establish the current amplitude of a second pulse required to elicit a spike, given that the neuron always spiked in response to the first pulse. More specifically, the pulses were separated in time by an interpulse interval (IPI) (Cartee et al., 2006, 2000; Dynes, 1996; Miller et al., 2001; Negm and Bruce, 2014). The first pulse I_{inj} amplitude was set to a value equivalent to an FE of 99.9 %, where only cases that elicited a spike in response to the first pulse were collected. The second pulse was separated from the first pulse by a range of IPIs, each with various current levels to determine the operational range of FEs as a function of the IPI. Similarly to Miller et al. (2001), each pulse was monophasic, but with a 50 μ s duration.

4.2.4 Analysis

Since our model neurons are stochastic, their probability of firing for any given stimulation current level can, on average, be predicted by a Gaussian cumulative distribution function (Φ), as a function of the injected current (I_{inj}) (Bruce et al., 1999b; Verveen and Derksen, 1968). This is known as the firing efficiency

$$FE(I_{inj}) = \Phi\left(\frac{I_{inj} - \theta}{\sigma}\right) \quad (4.2)$$

where θ is the threshold current and σ determines the dynamic range. Typically, the neuron's dynamic range is reported in a normalized fashion as the relative spread, or $RS = \sigma/\theta$ (Verveen and Derksen, 1968). Since the threshold current and relative spread are sensitive to the exact mixture of voltage-gated ion channels, they help define a stimulus

current scale that is calibrated to each model neuron variant. For each such model neuron variant, we estimated its single pulse threshold (θ_{SP}) and single pulse relative spread (RS_{SP}). This was done by fitting the outcomes of 1000 simulation trials across a range of injected current levels to (4.2), where the current waveforms consisted of 50 μ s duration monophasic and biphasic pulses. Due to the discrete, binary nature of whether a neuron spikes or not, the quality of all fits (4.2) to the spike data were evaluated by the R_{count}^2 measure (Long, 1997).

Post-stimulus time histograms were calculated over 500 simulation trials for the masker-probe train responses and for the adaptation responses. The response rate (or spike rate), captured by the PSTHs was computed as the number of spike occurrences within a given time bin, divided by the bin interval and the number of trials. PSTHs were evaluated for narrow bins of 1 ms and a wide interval axis where the bins are 0–4, 4–12, 12–24, 24–36, 36–48, 48–100, 100–200, and 200–300 ms, as in Zhang et al. (2007). Several features were extracted from the response rate as a function of time: 1) onset rate, 2) normalized spike rate decrement (NSRD), 3) adaptation time constant (τ_{adapt}), 4) probe response recovery ratio (PRRR), and 5) the mean response rate to the masker. The onset rate is just the response rate over the 0–12 ms interval (Zhang et al., 2007). The NSRD is the spike rate decrement divided by the onset rate where the spike rate decrement is the onset rate subtracted by the final rate (or the rate corresponding to the 200–300 ms bin) (Zhang et al., 2007). One adaptation time constant τ_{adapt} was extracted by fitting the PSTH simulation results to $s(t)$, a decaying exponential function

$$s(t) = A_{ss} + A_{dec} \exp\left(-\frac{t}{\tau_{adapt}}\right) \quad (4.3)$$

where A_{ss} and A_{dec} are estimates of the steady-state rate and the spike rate decrement, respectively. Whereas Zhang et al. (2007) tested decaying exponential fits with both one and two time constants, we found that one time constant was sufficient, as reported by an R^2 value. Note that τ_{adapt} refers to the overall time-course of the drop in spike rate and is influenced by refractoriness, facilitation, and accommodation (subthreshold adaptation) in addition to spike-dependent spike rate adaptation (Boulet et al., 2016, or Chap. 2). The PRRR is the ratio of probe response spikes in the masker-probe condition to the probe-alone condition (Miller et al., 2011). Finally, the mean response rate to the masker was calculated simply as the time-averaged response rate over the entire masker train interval of 300 ms.

In the refractory function analysis, we calculated the ratio of the masked (second) pulse threshold (θ_{ref}) to the unmasked or single pulse threshold (θ_{SP}) as a function of the interpulse interval. The number of trials varied as a function of the interpulse interval such that at the minimum IPI there were 500, whereas at the maximum IPI there were 100. This procedure was carried out to obtain a better estimate of the absolute refractory period. Miller et al. (2001) found that a significant proportion of SGNs exhibited an extended relative refractory period in their refractory threshold ratio data. In order to address this need to capture more than one time scale in the refractory response, we adopted the approach introduced by Negm and Bruce (2014) that generalized the refractory threshold ratio function to two

time constants

$$\frac{\theta_{\text{ref}}}{\theta_{\text{SP}}} = \frac{\sum_{i=1}^2 A_i}{\sum_{i=1}^2 A_i \left[1 - \exp\left(-\frac{\text{IPI} - \Delta t_{\text{abs}}}{\tau_i}\right) \right]} \quad (4.4)$$

where Δt_{abs} is the ARP, $\tau_{\text{rel},1}$ and $\tau_{\text{rel},2}$ are the relative refractory period (RRP) time constants, and A_1 and A_2 are the corresponding strengths.

4.2.5 Spike Detection

The detection of spikes by comparing the relative membrane potential to a sufficiently elevated fixed relative membrane potential crossing level of say 100 mV may be adequate in response to single pulse stimulation. In multi-compartmental models of a full neuron, any impulse that propagates to the end of the axon is recognized as a spike and thus spike detection is a trivial task. However, high-rate (short IPI) and large-amplitude (beyond the neuron's dynamic range) multiple stimuli present unique challenges for spike detection for non-spatially distributed neural models.

Passive charging of the membrane potential in response to large-amplitude pulses may visually appear to be artifacts, yet may still cross an arbitrary threshold, resulting in the false classification of spiking. This scenario is common with refractory stimuli in response to the second (or probe) pulse (refer to the Amplitude / Unmasked amplitude or bottom panel of Fig. 7 in Miller et al., 2001) due to the depletion of open sodium channels in response to a spike driven by the first (or masker) pulse. At the onset of the second pulse, few sodium channels are ready for voltage-dependent activation which results in a major capacitive current (thus, large passive charging, or fixed-point dynamics) and a minor sodium current. In contrast, if the sodium current participates in a positive feedback loop with the membrane potential, a limit cycle forms (Guevara, 2003), which is the hallmark of Hodgkin–Huxley action potential (AP) generation. Thus, the sodium activation may result in a relatively long-lasting, self-sustaining event known as a spike (or AP), or may create a passive response that is pulse-width-dependent in duration.

Therefore, we hypothesized that spikes could be accurately predicted by some value of λ , the sodium conduction duration, defined as the period of time for which the proportion of open sodium channels is greater than 0. Where $N_{m_3h_1}(t)$ is the number of Na channels in the open or conducting state (m_3h_1 , in the Hodgkin–Huxley channel formalism) at time t , we can write the set of λ s occurring over the interval $0 \leq t \leq T_{\text{stim}}$ as

$$\{\lambda\} \triangleq \text{duration} \left(\frac{N_{m_3h_1}(t)}{N_{\text{Na}}^{\text{max}}} > 0 \right) \quad (4.5)$$

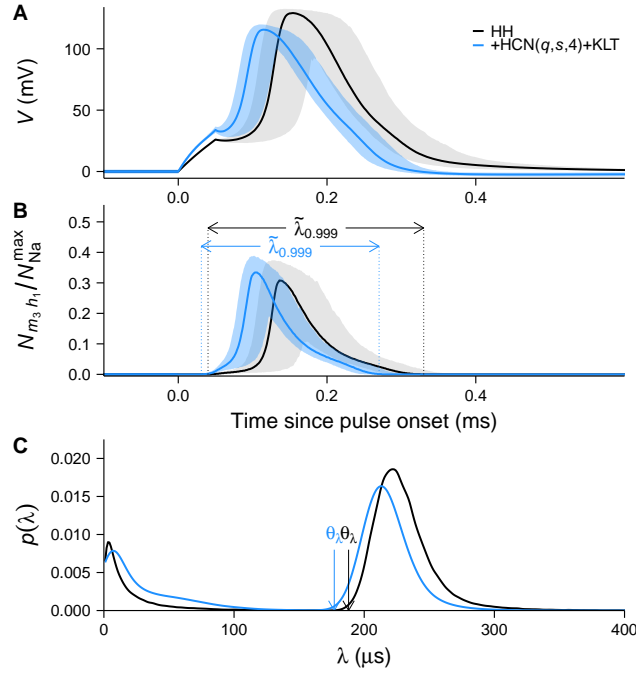


Figure 4.2 Determination of a spiking threshold based on the sodium conductance duration λ . The HH model is shown in black, the +HCN($q,s,4$)+KLT model is shown in light blue. Data from panels A and B represent 1000 independent responses to a 50 μs monophasic single pulse delivered at a current level equivalent to a FE of 99.9%. In panels A and B data on the ordinate axes have been summarized by median values (*solid line*) and the lower 2.5 and upper 97.5 percentiles (*shaded area*). A Relative membrane potential (V). B Proportion of open sodium ion channels ($N_{m_3 h_1} / N_{Na}^{max}$). $\tilde{\lambda}_{0.999}$ denotes the median sodium conductance duration, or the median duration over which $N_{m_3 h_1} / N_{Na}^{max} > 0$ given a stimulus FE of 99.9%. C Empirical probability density of λ marginalized over all stimulus current levels. Values to the left of θ_λ represent sodium conductances that are either failed action potentials or short-lived sodium fluctuations whereas the distribution that lies to the right of θ_λ represents values of λ which were sufficient to generate a spike. Thus, the threshold θ_λ is said to be the minimum value of λ required to generate an action potential.

and where T_{stim} is the stimulus interval. Figure 4.2B shows examples of the sodium conductance duration λ for the HH and +HCN($q,s,4$)+KLT model variants. In this scenario, when stimulated with a 50 μs monophasic single pulse set to a FE of 99.9%, the +HCN($q,s,4$)+KLT model achieves a lower median value of λ . When stimulated over a wide range of current levels, Fig. 4.2C shows that a bimodal distribution of λ emerges, suggesting that a threshold θ_λ can be determined such that values which are greater may be classified as action potentials instead of smaller sodium fluctuations.

In order to determine θ_λ , we first stimulated the neuron with independent single pulses at 200 linearly-spaced current levels spanning the range 0 to 150 pA. Each stimulus was presented for a total of 1000 trials per current level. For every trial, the maximum λ was collected. The set of all λ s, $\{\lambda\}$ was then aggregated over all current levels and trials. Next, we clustered $\{\lambda\}$ into two groups: $\{\lambda_1\}$ containing small values and $\{\lambda_2\}$ composed of all values greater than those in $\{\lambda_1\}$. This was performed by a method known as Jenks natural breaks optimization (Jenks, 1967), which is equivalent to k -means clustering for

1-dimensional data. Following this, θ_λ was defined as a value in $\{\lambda_2\}$ equal to the 0.1 percentile of $\{\lambda_2\}$. This step was performed to minimize false spike detection due to possible crossover of the tails of the λ_1 and λ_2 distributions since those distributions were not known a priori. For all single pulse, adaptation, masker-probe train, and refractory simulations, action potentials were identified if $\lambda \geq \theta_\lambda$.

4.3 Results

4.3.1 Single Pulse

Simulation results shown in Fig. 4.3 establish the monophasic and biphasic single pulse statistics for all neuron model variants as a function of the shift in HCN half-maximal activation potential (Fig. 4.3A sodium conductance duration threshold, Fig. 4.3B AP threshold current, and Fig. 4.3C relative spread). Results for the HH and +KLT models appear constant as a function of c since no HCN channels are included in those models. However, all models that do contain HCN display a decreasing θ_λ as a function of c . This is due to 1) an increased total resting membrane conductance and 2) an increased rate of repolarization produced by HCN deactivation following depolarization.

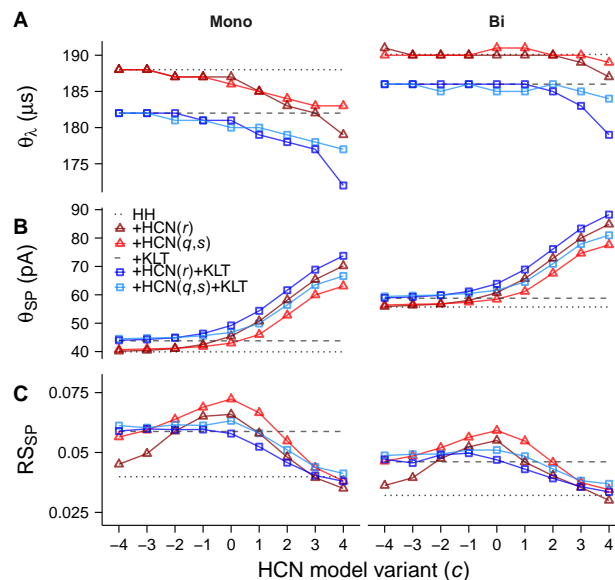


Figure 4.3 Monophasic and biphasic single pulse **A** sodium conductance duration threshold (θ_λ), **B** AP threshold current (θ_{SP}), and **C** relative spread (RS_{SP}) as a function of the HCN $V_{1/2}$ shift parameter c .

Due to the increased total resting membrane conductance, the single pulse threshold currents increase with respect to c for models with HCN channels. Just as previously

reported (Liu et al., 2014a; Negm and Bruce, 2008, 2014), KLT shows an increase of θ_{SP} relative to HH in the +KLT model and an additive effect to θ_{SP} in models with HCN. Whereas Negm and Bruce (2014) used a threshold-crossing value of 80 mV relative to rest, we used θ_{λ} to detect action potentials. For the models HH, +HCN($r,0$), +KLT, and +HCN($r,0$)+KLT models, Negm and Bruce (2014) reported the respective biphasic single pulse thresholds 54.29, 59.68, 57.36, and 62.70 pA in contrast to our values: 55.70, 60.74, 58.80, and 63.88 pA.

For both monophasic and biphasic stimulation, the +KLT model shows a greater relative spread than the HH model, indicating a greater dynamic range in response to single pulses, consistent with Negm and Bruce (2008). The +HCN(r) and +HCN(q,s) models maximize the RS_{SP} at $c = 0$. In contrast, the +HCN(r)+KLT and +HCN(q,s)+KLT models show a constant RS_{SP} for $c \leq 0$ approximately equal to the +KLT model, whereas for $c > 0$, RS_{SP} tends towards the HH model value. The quality of fits to (4.2) was quantified by R_{count}^2 with the +HCN($q,s,0$) model responding to monophasic stimulation having the lowest value $R_{count}^2 = 0.823$ and the +HCN($r,4$)+KLT model in response to biphasic pulses having the highest $R_{count}^2 = 0.925$.

4.3.2 Adaptation

Changes in the excitability of feline SGNs driven by ongoing electrical pulsatile stimulation come in a few forms that often overlap temporally (for a review, refer to Boulet et al., 2016, or Chap. 2). Examples of the decay in the response rate are illustrated by the *white line-dot curves* in Fig. 4.4. Here, feline SGNs respond to the various stimulation rates, and each to a variety of pulse current levels. This phenomenon is typically referred to as having arisen due to *spike rate adaptation*, which has a spike-dependent nature. Upon closer examination, Fig. 4.4C (middle row) shows that a neuron firing in response to a 5000 pulses/s pulse train also shows the effects of *refractoriness*, which can be observed by the oscillatory response of the *bars*. An increase in the spike rate produced by *facilitation* is also apparent when comparing Fig. 4.4C to Fig. 4.4A, B, and D. Finally, clear evidence of *accommodation*, or subthreshold adaptation is apparent in Fig. 4.4D during the interval in which the SGN is not spiking. However, the question remains as to what is the primary biophysical contributor to reducing electrical excitability in SGNs.

Changing the HCN half-maximal activation potential affects the pulse train response in terms of varying neuronal excitability, or the strength of adaptation. Figure 4.5 clearly demonstrates this point for pulse train stimulation with amplitude $FE = 80\%$ and rate of 2000 pulses/s for models +HCN(r) and +HCN(q,s), where the strength of adaptation increases as a function of c .

Figure 4.6 shows the PSTH responses for the six membrane models over the 20, 50, and 80 % FEs and all stimulation rates. The +HCN($r,3$), +HCN($q,s,4$), +HCN($r,3$)+KLT, and +HCN($q,s,4$)+KLT kinetic variants in Fig. 4.6 are the strongest-adapting models with HCN channels (see Fig. 4.7B, NSRD). Overall, the PSTHs display a relatively high onset rate that is followed by a gradual drop down to a lower steady-state response rate. On aggregate,

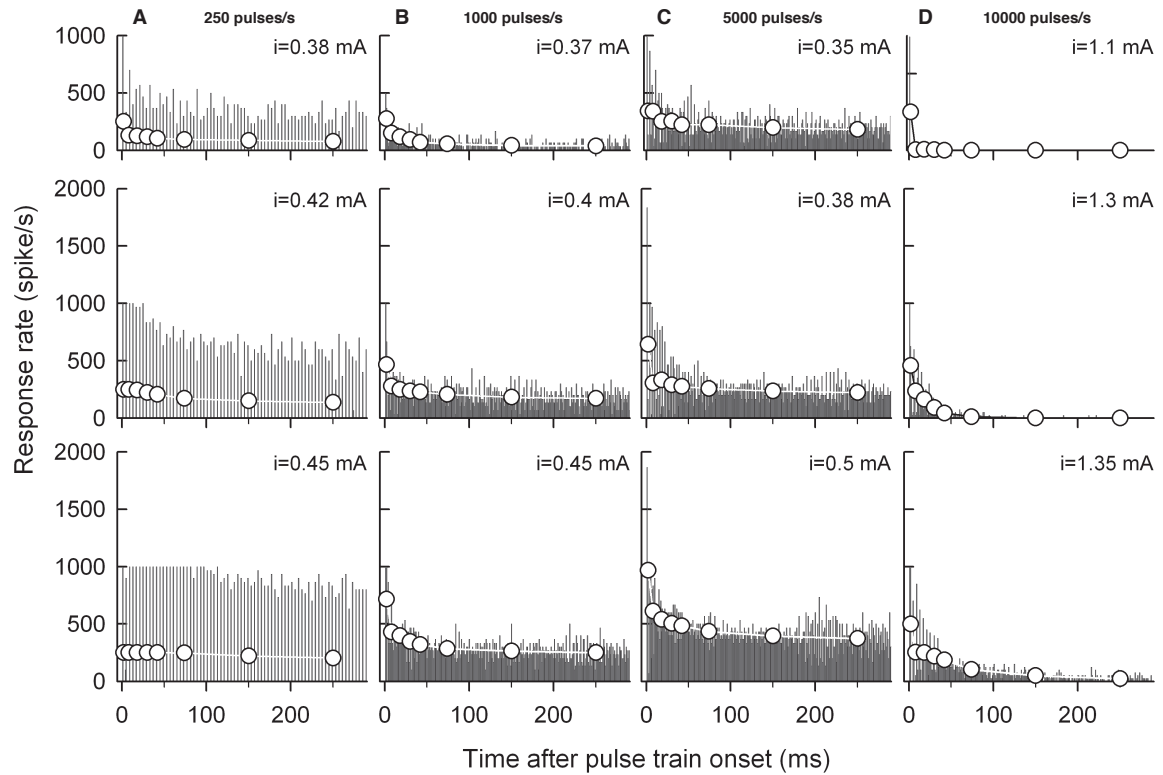


Figure 4.4 Feline SGN response rate as a function of the time since pulse train onset over a 300 ms interval. Subpanels with columnar arrangement indicate responses to stimulation at the rates of **A** 250 pulses/s, **B** 1000 pulses/s, **C** 5000 pulses/s, and **D** 10 000 pulses/s. Row-wise layout of the subpanels show an increasing biphasic pulse current level starting from the top panel to the bottom panel. Responses in panels **A**, **B**, and **C** were taken from a different SGN than those in panel **D**. Bars represent the response rate over 1 ms intervals and dots show the response rate over the progressively wider intervals (0–4, 4–12, 12–24, 24–36, 36–48, 48–100, 100–200, and 200–300 ms). This figure was adapted with kind permission of Springer Science & Business Media: Fig. 2 from Zhang et al. (2007), © 2007.

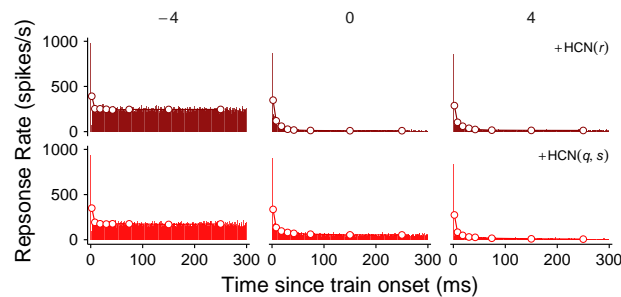


Figure 4.5 PSTH responses to pulse train stimulation over a 300 ms interval at an FE of 80 % and rate of 2000 pulses/s for models +HCN(r) and +HCN(q, s) showing various strengths of adaptation as a function of the HCN $V_{1/2}$ shift parameter c . Bars and dots represent the same intervals as in Fig. 4.4.

both onset and final spike rates are higher as a function of the firing efficiency. However, the final spike rates are not linearly predicted by pulse rate, which can be seen by the

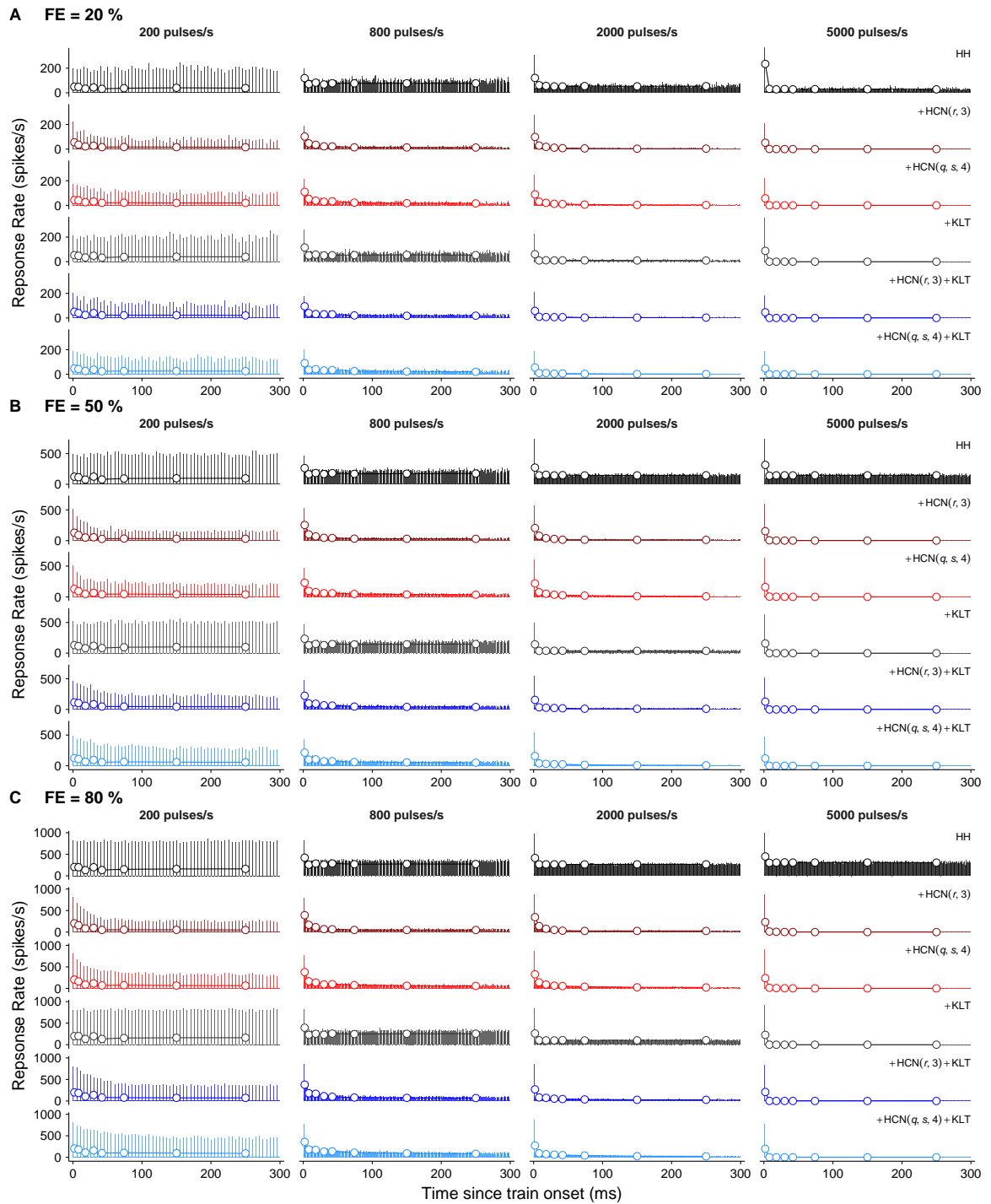


Figure 4.6 PSTH or response rate for the strongest-adapting SGN membrane models over a 300 ms interval where c was set to give strong adaptation in the model versions containing HCN channels. Panels represent responses to individual FEs: **A** 20 %, **B** 50 %, and **C** 80 %. Row subpanels indicate membrane model and column subpanels represent stimulation rate. *Bars and dots* represent the same intervals as in Figs. 4.4 and 4.5.

wide-bin dots. Across all models and firing efficiencies, the final spike rate is maximized at 800 pulses/s and decreases in response to greater stimulation rates with the exception of the HH model. The drop in the response rate for the HH model at stimulation rates including and above 800 pulses/s occurs immediately after 1 ms and thus is not representative of adaptation but rather refractoriness. The +KLT model behaves similarly to the HH model at the 200 pulses/s and 800 pulses/s stimulation rates. However, at 2000 pulses/s the response rate is lower, and at 5000 pulses/s the neuron does not respond except to the first pulse, indicating accommodation (subthreshold adaptation). Models containing HCN channels respond similarly to the +KLT model in terms of onset and final response rates but appear to display adaptation behavior across a broad set of stimulation rates exhibited by the relatively slower decay in the PSTH. Overall, wide bin response rates were well predicted by (4.3) since the worst fit was model variant +HCN($r,-4$)+KLT ($R^2 = 0.819$) and the best fit was model variant +HCN($r,3$) ($R^2 = 0.980$).

Figure 4.7 contains simulation results that summarize the pulse train responses over the range of HCN half-maximal activation potentials (varied by c , the integer multiples of HCN $V_{1/2}$ standard deviations). Figure 4.7 also shows our simulation results and experimental results from Zhang et al. (2007) of the normalized spike rate decrement (NSRD) versus the onset response rate. Figure 4.7A shows the onset rate, Fig. 4.7B displays the normalized spike rate decrement (NSRD), and Fig. 4.7C reports the adaptation time constant (τ_{adapt}). Simulation results in Fig. 4.7A, B, and C (onset rate, NSRD, and adaptation time constant) were averaged over all FEs (1, 10, 20, 50, 80, 99, 99.99, and 99.9999 %) and the pulse rates (200, 800, 2000, and 5000 pulses/s). ‘Strong-adapters’ were defined as the neurons with NSRD greater than 0.75, just as in Negm and Bruce (2014), and can be seen in the light grey zone (in Fig. 4.7B). Out of all membrane models and their respectively shifted $V_{1/2}$ HCN variants, the following are classified as strong-adapters: +HCN($r,1$), +HCN($r,2$), +HCN($r,3$), +HCN($r,4$), +HCN($q,s,4$), +HCN($r,2$)+KLT, +HCN($r,3$)+KLT, +HCN($r,4$)+KLT, and +HCN($q,s,4$)+KLT. Notably absent from the list of strongly-adapting neurons are the HH and +KLT models, indicating that HCN channels are required to produce strong adaptation.

All models containing the KLT channels have a distinctly lower onset response rate in Fig. 4.7A than those without, and thus KLT appears to be a strong regulator of the onset response rate. Since the onset response rate is calculated over 0–12 ms and the drop in the firing rate occurs 1 ms after the onset of the pulse train (see Fig. 4.6), this could be related to processes other than spike rate adaptation, such as refractoriness. However, as seen in Fig. 4.6 the HH and +KLT models have a relatively high final response rate, with the HH response being the highest. This may help explain the disparity in the NSRD between the HH and KLT-containing models. Models with HCN but without KLT channels cover a wide set of onset response rates ranging from approximately 190 to 310 spikes/s near the HH response. Onset response rates of the HCN models that are near the HH response can be explained by the HCN channels being closed at (and somewhat below) the RMP, specifically the r_{∞} and the slow s_{∞} component (see Fig. 4.1A). In terms of the positively-shifted $V_{1/2}$ HCN model variants, the r and s particles are at least half open at the resting membrane potential and are in a position to strongly restore the membrane potential towards E_h . For

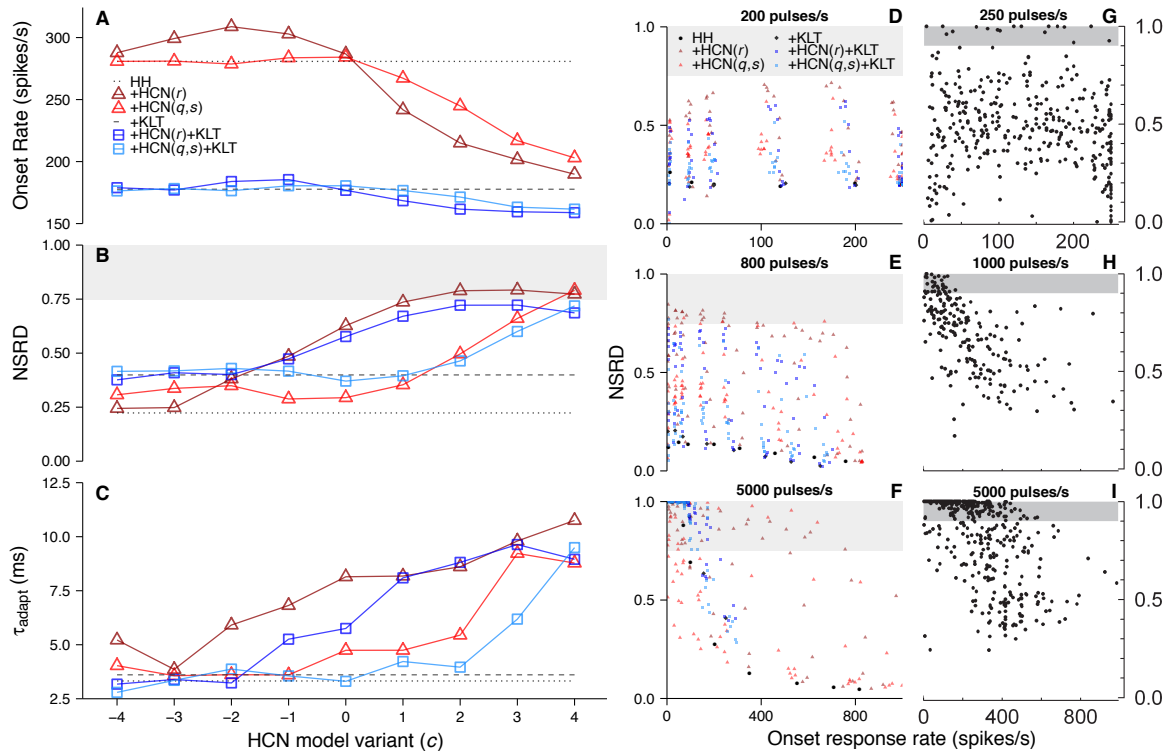


Figure 4.7 Summary of the pulse train response statistics. Pulse train responses for all SGN model variants given by **A** onset rate, **B** NSRD, and **C** τ_{adapt} , as a function of the HCN $V_{1/2}$ shift parameter c . Simulation results shown in panels **A**, **B**, and **C** were averaged over all FEs (1, 10, 20, 50, 80, 99, 99.99, and 99.9999 %) and all pulse rates (200, 800, 2000, and 5000 pulses/s). SGN model simulation results for NSRD as a function of the onset response rate in response to pulse train stimulation at the **D** 200 pulses/s, **E** 800 pulses/s, and **F** 5000 pulses/s rates. Panels **D**, **E**, and **F** contain simulation results across all HCN $V_{1/2}$ levels (-4 to 4) and FEs (1, 10, 20, 50, 80, 99, 99.99, and 99.9999 %). The remaining panels correspond to the same NSRD versus onset response rate simulation plots, but for feline SGN recordings (Zhang et al., 2007) responding to **G** 250 pulses/s, **H** 1000 pulses/s, and **I** 5000 pulses/s pulse train stimulation. Note that the span of the onset response rate in panels **D** and **G** is 0 to 250 spikes/s whereas in panels **E**, **F**, **H**, and **I** it is 0 to 1000 spikes/s. Panels **G**, **H**, and **I** were adapted with kind permission of Springer Science & Business Media: Fig. 5, panels **B**, **E**, and **G** from Zhang et al. (2007), © 2007.

example, the s particle of the +HCN($q,s,4$) model undergoes maximum activation near the resting membrane potential. This leads to maximizing the NSRD, produced by a maximal contribution to the ionic current I_h in cases of hyperpolarization and towards V_{rest} for cases of depolarization. However, the main differential activity between the HCN(r) and HCN(q,s) channels is the ‘quick’ q particle remaining partially open for all explored values of c . In terms of the negatively-shifted model variants, this provides a higher baseline NSRD for the +HCN(q,s) compared to the +HCN(r) model variants.

The relatively short adaptation time constants (τ_{adapt}) of the HH and +KLT models seen in Fig. 4.7C can be clearly interpreted from the PSTHs of those models in Fig. 4.6 that show a sharp decrease in the spike rate following the onset response for stimulation rates above 200 pulses/s. In the same manner, compared to the weakly adapting models, the strongly

adapting models clearly boast larger adaptation time constants, which are in the range of 8.5–11 ms. In summary, the shifted $V_{1/2}$ HCN value appears to be the main modulator of the adaptation time constant.

The next portions of Fig. 4.7 plot the NSRD against the onset response rate. We provide our simulation results over all model variants and FEs where Fig. 4.7D, E, and F correspond to the respective stimulation rates: 200, 800, and 5000 pulses/s. The remaining panels, namely Fig. 4.7G, H, and I show experimental data from feline SGN (Zhang et al., 2007) that responded to 250, 1000, and 5000 pulses/s pulse train stimulation. The proportion of strong adapters increases with the pulse rate for both our simulation results and those of Zhang et al. (2007). The fact that the NSRD is dependent on pulse rate indicates that accommodation is largely responsible for the occurrence of strongly-adapting neurons. The reasoning is that spike rate adaptation should only be dependent on the onset spike rate, not the spike rate decrement, nor the pulse rate. Therefore, if spike rate adaptation were the only contribution to the spike rate, NSRD would not be a function of pulse rate. If spike rate adaptation were the only process responsible for reducing the response rate, all points in Fig. 4.7D–I would lie on a line with positive slope extending from the bottom-left to the top-right corners, suggesting that an increase in onset response rate produces a proportional decrement in activity. Instead, we observe a negative relationship between NSRD and the onset response rate that grows stronger with increasing pulse rate, further suggesting that accommodation is at play. It is also worth noting a small discrepancy in NSRD between model simulations in response to a 200 pulses/s stimulation (Fig. 4.7D) and data from experiment in response to a 250 pulses/s pulse train (Fig. 4.7I). Specifically, a subset of fibers in the data appear to be strong adapters, whereas the model simulations do not produce strong adapters at this low pulse rate. The strong adapters appear to be independent of the onset response rate, shown in Fig. 4.7I, suggesting that the response of this small subset of neurons may have been subject to fluctuations in excitability in addition to those that are present in our model.

4.3.3 Recovery from Masker Train

Just as we have seen in § 4.3.2, spike rates eventually adapt to a constant steady-state in response to a fixed stimulation rate and current level. Figure 4.8 shows data from Miller et al. (2011) where low-rate probe train responses of feline SGNs undergo an initial period of reduced excitability after stimulation from either suprathreshold (Fig. 4.8A and B) or subthreshold (Fig. 4.8D) high-rate masker trains. Likewise, we investigated how the masker response history that was driven by a high-rate pulse train contributed to the dynamics of the low-rate probe response. Figure 4.9 shows the masker and probe response to pulse trains for the same set of model variants as in Fig. 4.6, but for the A 1 %, B 50 %, C 99.99 %, and D 99.9999 % FEs at the 5000 pulses/s masker pulse train rate.

Given that the current level was set to a FE = 50 % (or the single pulse threshold) in the probe-alone condition (i.e., when there was no masker train), we expected a constant

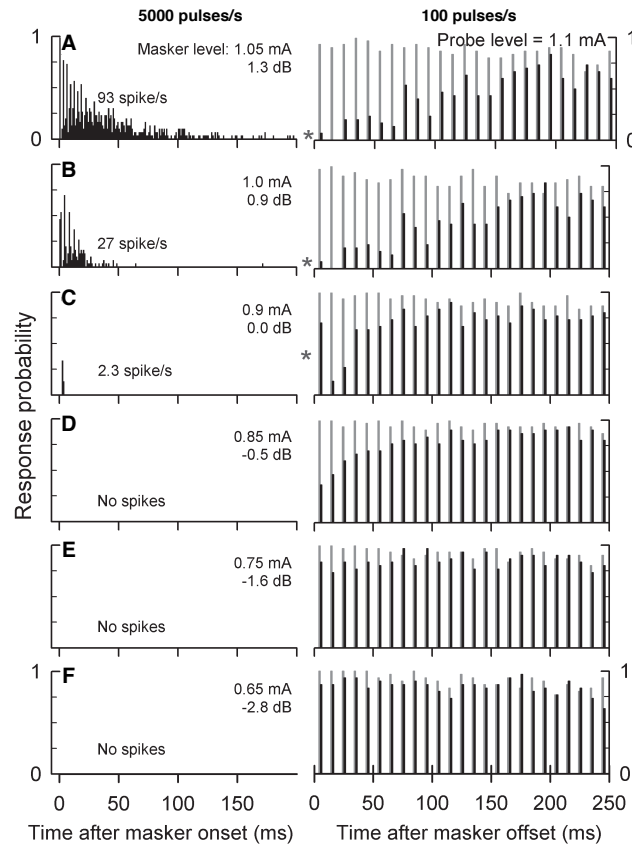


Figure 4.8 Feline SGN masker-probe pulse train responses in terms of response probability (= normalized response rate assuming a maximum of one spike per pulse). Masker train responses are shown in the left subpanels and the following probe train responses are shown in the companion right subpanels. This figure shows cases with masker followed by probe train responses (*black bars*) and probe train alone responses (*grey bars*). All probe train responses are shown with *thicker bars* are for visual aid only and were calculated over 1 ms intervals. All masker trains were delivered at rate of 5000 pulses/s over a 200 ms interval. Every probe train was delivered at 100 pulses/s for 250 ms with a pulse current level approximately equivalent to the SPT. Going from top to bottom, subpanels **A**, **B**, **C**, **D**, **E**, and **F** portray responses to decreasing masker pulse levels (shown). Asterisks correspond to cases when the first probe response was greater than the second. All panels were adapted with kind permission of Springer Science & Business Media: Fig. 1 from Miller et al. (2011), © 2011.

response rate similarly to the results of Miller et al. (2011), represented by the *grey bars* in Fig. 4.8. This would equate to approximately 500 spikes/s within a 1 ms time bin in response to each pulse in the probe train. Over the entire stimulus duration, this produces an average response rate of 50 spikes/s. Figure 4.9 (*thick, lightly-colored bars*) shows that this was indeed the case and was largely independent of the model. The reasons for this behavior can be summarized by the following points: 1) there was no masker stimulus that could pre-condition the probe response and 2) the probe train IPI had a relatively large value of 10 ms (minimizing probe train pulse interactions). The exception to this constant response rate was for the +HCN(*r*,3), +HCN(*q*,*s*,4) and to a lesser extent, the

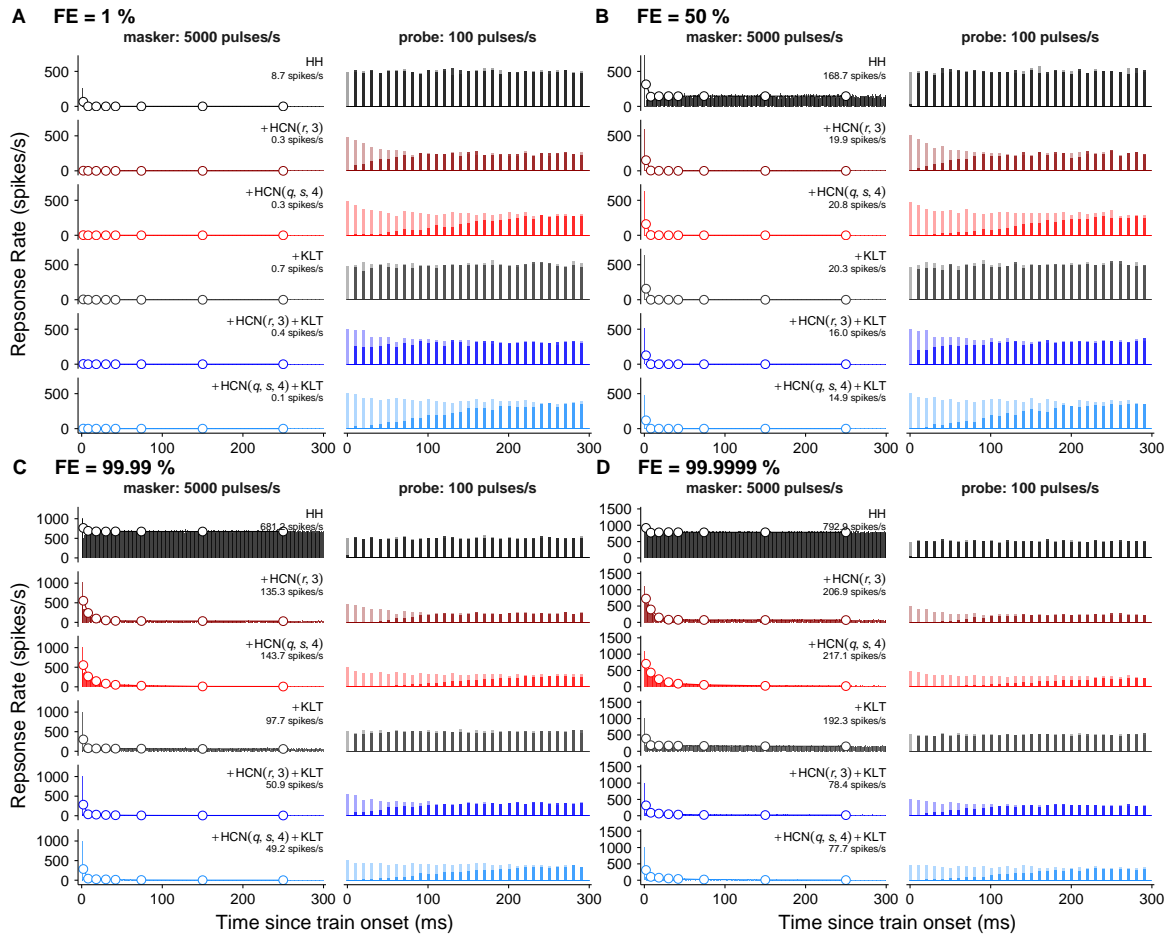


Figure 4.9 PSTH or response rate for the strongest-adapting SGN membrane models simulated over a 300 ms interval in response to a 5000 pulses/s masker train followed immediately by a 100 pulses/s probe train. *Dark-colored bars* represent responses to the condition with a masker train (masker-probe), whereas *lighter-colored bars* indicate that no masker train stimulated the neuron (probe-alone). Panels represent masker train responses to different FEs: **A** 1%, **B** 50%, **C** 99.99%, and **D** 99.9999%. All *bars* represent the response rate over 1 ms intervals and *dots* show the response rate over wider intervals (Zhang et al., 2007). Note that the *thicker bars* shown in the probe response panels are for visual aid only and were calculated over 1 ms intervals. The spike rates reported in each masker subpanel were calculated over the 0–300 ms interval.

+HCN($r,3$)+KLT, +HCN($q,s,4$)+KLT models where the probe-alone response displayed adaptation.

In contrast to the probe-alone response, in the masker-probe condition we do not expect a flat probe train response due to the pre-conditioning imposed by the masker train on the membrane potential. Figure 4.9 superimposes the results of the masker-probe train response (*thin dark bars, followed by thick dark bars*) over the probe-alone response. Each model's gross probe recovery pattern in the masker-probe condition was such that a gradual increase in the response was observed. This pattern was consistent for masker train pulse current levels that were either greater or less than θ_{SP} , similarly to the experimental

results reported by Miller et al. (2011). The only difference between the masker-probe and probe-alone conditions for models HH and +KLT were the weak first probe pulse responses. However, all +HCN model variants shown in Fig. 4.9, namely, +HCN($r,3$), +HCN($q,s,4$), +HCN($r,3$)+KLT, and +HCN($q,s,4$)+KLT displayed a longer probe recovery time course than the HH and +KLT models. In particular, model variants +HCN($q,s,4$) and +HCN($q,s,4$)+KLT had the slowest masker-probe recovery.

Simulation results in Fig. 4.10 show the effect of the HCN $V_{1/2}$ shift (c) on the probe response recovery ratio (PRRR). Figure 4.10 also shows the PRRR versus the mean response rate to the masker for our simulation results (Fig. 4.10B and D) and experimental results (Fig. 4.10D and E) from Miller et al. (2011). Similarly to the results in Fig. 4.7A, B, and C, the PRRR shown in Fig. 4.10A has also been averaged over all FEs (1, 10, 20, 50, 80, 99, 99.99, and 99.9999 %) and the 200, 800, 2000, and 5000 pulses/s stimulation rates. As shown in Fig. 4.10, the PRRR appears to decrease as a function of the HCN $V_{1/2}$. Comparing this finding to the one in Fig. 4.7B, this translates to strongly-adapting neurons exhibiting a relatively low PRRR, given their differing activation characteristics relative to the weakly-adapting HCN variants, which show near complete recovery in their probe response. Figure 4.10 shows that the negatively-shifted HCN model variants have a similarly large PRRR to the HH model of just under 1. Overall, the +HCN model variants show a relatively large PRRR range, with model variants containing the HCN(q,s) channel having the largest range, specifically +HCN($q,s,4$) achieving an average PRRR of less than 0.7.

The channel mechanisms that can explain the change in NSRD as a function of c , may also be used to understand the occurrence of values of PRRR near 1 at smaller values of c . That is, that HCN will not contribute to the total membrane conductance with such $V_{1/2}$ shifts (see Fig. 4.1). Therefore, the r and s channel particles cannot contribute to the afterhyperpolarization phase, nor can they regulate the resting membrane potential. These channel particles are responsible for reducing excitability on the timescale of approximately 100 ms which may partially explain the probe recovery in response to pulse train stimulation at 100 pulses/s, in contrast to the quicker-responding q particle (see τ_q in Fig. 4.1).

There are similar trends in the PRRR versus the mean response rate to the masker as a function of the pulse rate. That is, whereas the 5000 pulses/s case (Fig. 4.10B and D) shows a shallow negative slope, the slower pulse rates (Fig. 4.10C: 200 pulses/s; Fig. 4.10E: 250 pulses/s) express a steeper one. However, we cannot explain as great of a range in the PRRR when comparing our simulation results to the experimental results of Miller et al. (2011). Particularly, the recovery of the response to the 100 pulses/s probe train is poor (low PRRR) in a subset of neurons when preconditioned with a 5000 pulses/s masker train. This phenomena was conserved for the entire range of mean response rates to the masker (see Fig. 4.10D) whereas the simulation results of any model SGNs could not produce this activity (see Fig. 4.10C). This behavior may indicate a low absolute PRRR in a subset of neurons. This could correspond to a subset of neurons that were subject to fluctuations in excitability in addition to those that are present in our model, such as was the case for Fig. 4.7. Alternatively, given that we used a probe train interval of 300 ms that is somewhat longer than the probe train interval of 250 ms used by Miller et al. (2011), our model SGN

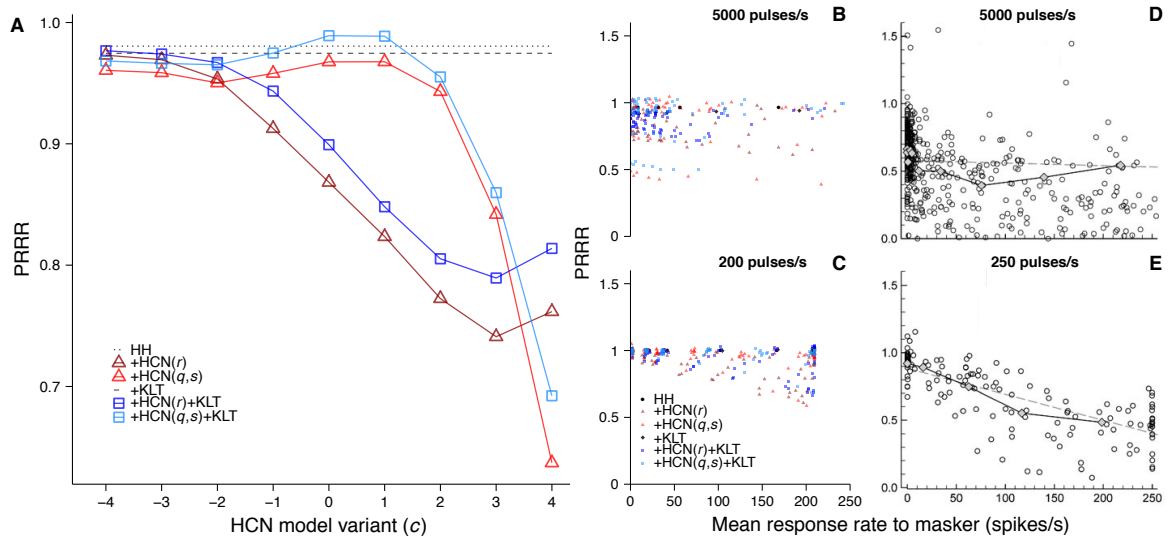


Figure 4.10 Summary of the probe response recovery ratio (PRRR). SGN model simulation results show the effect of **A** the HCN $V_{1/2}$ shift parameter c on the PRRR. Simulation results in panel **A** were averaged over all FEs (1, 10, 20, 50, 80, 99, 99.99, and 99.9999 %) and the 200, 800, 2000, and 5000 pulses/s rates. SGN model simulation results for PRRR as a function of the mean response rate to the masker for the masker pulse train rates of **B** 5000 pulses/s and **C** 200 pulses/s. Here, the mean response rate to the masker was calculated over the entire 0–300 ms masker train interval. Panels **B** and **C** contain simulation results across all HCN $V_{1/2}$ levels (–4 to 4) and FEs (1, 10, 20, 50, 80, 99, 99.99, and 99.9999 %). The remaining panels correspond to the same PRRR versus mean response rate to the masker simulation results plot, but for feline SGN recordings responding to **D** 5000 pulses/s and **E** 250 pulses/s masker-probe pulse train stimulation, where the mean response rate to the masker was calculated over the entire 0–200 ms masker train interval. Panels **D** and **E** were adapted with kind permission of Springer Science & Business Media: Fig. 3, panels **D** and **E** from Miller et al. (2011), © 2011.

may have been capable of more recovery, thus increasing the PRRR.

4.3.4 Refractoriness

Figure 4.11 shows the threshold recovery data as a function of the IPI for our simulation results and those from experimental feline SGN recordings Miller et al. (2001). Figure 4.11A presents the threshold recovery ratio for the strongest-adapting model variants. The corresponding parameter estimates have been extracted from the fit to (4.4) and are given in Table 4.2. By comparing HH, +HCN($r,3$), and +HCN($q,s,4$) to +KLT, +HCN($r,3$)+KLT, and +HCN($q,s,4$)+KLT in Fig. 4.11, KLT appears to be responsible for increasing the ARP (Δt_{abs}) and the RRP time course. Table 4.2 lists the values of Δt_{abs} and the larger of the two time constants $\tau_{\text{rel},2}$ where the effect of KLT appears to be an additive one.

In contrast, the presence of KLT reduces $\tau_{\text{rel},1}$. Nevertheless, the addition of KLT to any model cannot produce a sufficiently long relative refractory period as observed by Miller et al. (2001) (see Fig. 4.11B) where the effects of relative refractoriness persist until

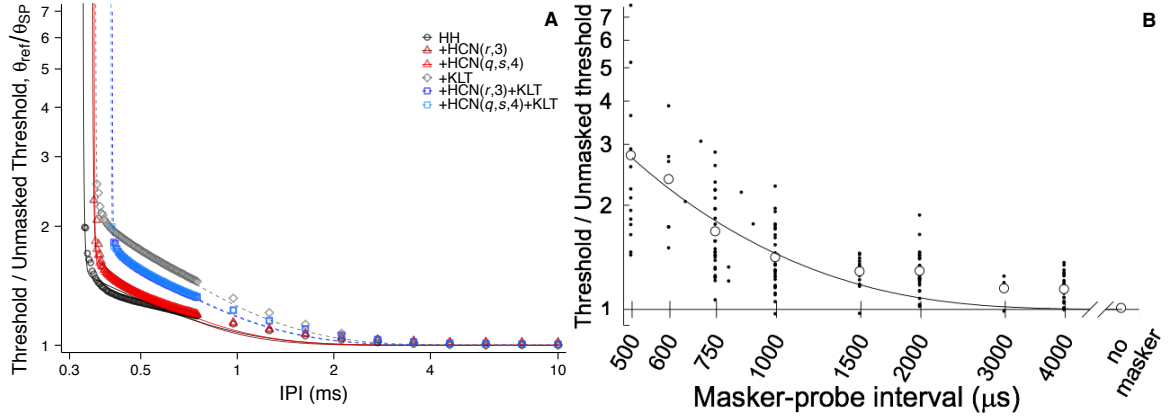


Figure 4.11 Refractory threshold ratio as a function of the interval between pulses. **A** Threshold / unmasked threshold (θ_{ref}/θ_{SP}) vs. interpulse interval (IPI) for the strongest-adapting SGN membrane models. Note that θ_{ref}/θ_{SP} and IPI are scaled on a log-10 axis. **B** Threshold / unmasked threshold as a function of the masker-probe interval (or IPI) from feline SGN (Miller et al., 2001). Panel **B** reprinted with kind permission of Springer Science & Business Media: Fig. 7 from Miller et al. (2001), © 2001.

at least 4 ms in a sizable subset of fibers. Negm and Bruce (2014) reported similar ARP findings. While our ARP values are slightly different than those of Negm and Bruce (2014) and Miller et al. (2001), we can attribute this to several factors. One reason could be due to the ability of our spike detection algorithm to discriminate spikes when the sodium conductance duration is greater than θ_λ even if $V(t)$ is less than an arbitrary spike detection threshold, especially for small IPIs (e.g., response to the second pulse for the refractory simulation). Another reason may be due to stimulus-dependent refractoriness (Morse et al., 2015). Whereas Negm and Bruce (2014) used biphasic pulses with 75 μ s duration and 75 μ s interphase gap, we stimulated with 50 μ s duration monophasic pulses to be more consistent with the Miller et al. (2001) stimulation paradigm. Finally, unlike the extracellular stimulation used by Miller et al. (2001), we used a single-node SGN model with ‘intracellular’ stimulation. With the exception of the +KLT model, all models shown in Table 4.2 exhibit a greater effect of the short time constant $\tau_{rel,1}$ on the RRP ($A_1 > A_2$).

Table 4.2 Refractory recovery function parameter estimates for strongest-adapting model variants.

Model	A_1	A_2	Δt_{abs} (ms)	$\tau_{rel,1}$ (μ s)	$\tau_{rel,2}$ (ms)	R^2
HH	2.05	1.05	0.329	4.90	0.46	0.935
+HCN(r,3)	1.81	1.21	0.353	3.41	0.35	0.927
+HCN(q,s,4)	1.94	1.17	0.357	2.10	0.42	0.971
+KLT	1.40	1.64	0.360	2.71	0.64	0.969
+HCN(r,3)+KLT	1.74	1.28	0.407	1.79	0.58	0.991
+HCN(q,s,4)+KLT	1.75	1.31	0.403	1.98	0.60	0.995

The effect of HCN on the refractory response of the membrane models becomes more apparent in Fig. 4.12 as the ARP is plotted against the HCN $V_{1/2}$ shift c . The Δt_{abs} is

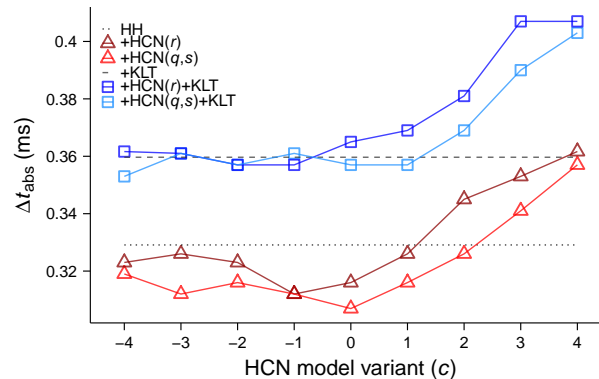


Figure 4.12 Absolute refractory period vs. the HCN $V_{1/2}$ shift parameter c for each of the membrane models.

approximately constant for values of $c < 0$. However, beyond that, Δt_{abs} increases as a function of c . The additive effect of KLT is invariant for all values of c when comparing +HCN(r) and +HCN(q,s) to +HCN(r)+KLT and +HCN(q,s)+KLT.

4.4 Discussion

Woo et al. (2009a,b, 2010) demonstrated spike rate adaptation in model SGNs by incorporating an extracellular potassium accumulation phenomena, native to leech central nervous system (Baylor and Nicholls, 1969), into a Hodgkin–Huxley model. Miller et al. (2011) showed that the addition of a KLT channel in concert with the K^+ accumulation mechanism was capable of explaining accommodation (or subthreshold adaptation) in response to pulse train stimulation. They also proposed variation in axonal diameter as a potential factor in determining the degree of SGN adaptation (Woo et al., 2010). However, the relatively large ARP values reported by Miller et al. (2011) were not representative of the ARP values collected experimentally from feline SGNs (Miller et al., 2001). This suggests that alternative mechanisms may be necessary to holistically explain the SGN response to high-rate electrical stimulation.

Our study has established that HCN channels may be responsible for strong adaptation in response to pulsatile stimulation through the combination of both spike rate adaptation and the buildup of accommodation that is observed in SGNs. For strongly-adapting SGN models, all of which contain HCN channels, we have shown that the time course over which adaptation acts (8.5–11 ms) qualitatively agrees with the mean rapid adaptation time constant values in feline SGNs (8.2–11.8 ms) (Zhang et al., 2007) across a range pulse train rates (250, 1000, and 5000 pulses/s). Although a greater number of the +HCN(r) than the +HCN(q,s) model variants exhibit strong adaptation, the +HCN(q,s) model has benefits of 1) having the largest range in PRRR which is similar to the results found by Miller et al.

(2011) and 2) the HCN(q,s) channel model is representative of channels found in the SGN (Liu et al., 2014b). Additionally, the +HCN(q,s) model variants display less adaptation to the low-frequency probe-alone pulse train than +HCN(r) model variants (recall Fig. 4.9). We have also ascertained that HCN may contribute towards determining the absolute refractory period in SGNs.

Our simulation results are dependent on the configuration of the HCN channel activation characteristics (Chen, 1997; Kim and Holt, 2013; Liu et al., 2014b; Mo and Davis, 1997; Yi et al., 2010). We chose to extend the ranges of HCN $V_{1/2}$ values explored to double the ranges estimated by Liu et al. (2014b) in neonatal murinae, i.e., ± 4 standard deviations rather than ± 2 standard deviations around the mean. This wider range was motivated by the lack of knowledge about the precise range of values for feline SGNs and possible differences in the RMP of murinae and adult feline SGNs. However, we found that a change of around 4 standard deviations in HCN $V_{1/2}$ was sufficient to almost completely account for the variability in degree of spike rate adaptation, accommodation, and refractoriness observed in response to CI stimulation (see Figs. 4.7B and 4.10A). For the older HCN(r) model, the range of values over which the model changed from being non-adapting to strongly-adapting was centered around the mean HCN $V_{1/2}$, i.e., for shift values of c between approximately -2 and $+2$. For the newer HCN(q,s) channel model, the effective range for c to modulate the strength of adaptation was between $+1$ and $+4$, suggesting that the mean HCN $V_{1/2}$ for adult feline SGNs may be at more positive values than was estimated for neonatal murinae by Liu et al. (2014b). It has been noted by Davis and Crozier (2015) that adult SGNs have the capability to regulate their strength of adaptation, so the difference in the range of effective $V_{1/2}$ in our +HCN(q,s) model of adult feline SGNs compared to the range measured by Liu et al. (2014b) may be due to both species and age differences.

Shifting the value of $V_{1/2}$ of a channel model changes the operating range as a function of the membrane potential of that channel (Krouchev et al., 2015). This can amount to a voltage-dependent ‘thresholding’ effect on the channel’s activity and as such, we deemed that it was an appropriate HCN model parameter to vary as a first step towards explaining the variability of SGN excitability. Other channel parameters can play a role in regulating channel activity other than $V_{1/2}$ such as the slope factor, reversal potential, activation minimum, and activation maximum. These values may be explored in future studies to further fine-tune the SGN response, given supporting experimental evidence of the variation in these parameters.

Together with the refractory behavior reported by Negm and Bruce (2014), our results have shown that KLT can increase the ARP and RRP time constants within physiological bounds, compared to the HH model. However, despite the qualitative increase in the RRP time constant, our models cannot predict the extended relative refractoriness observed in a subset of SGNs, as previously reported (Botros and Psarros, 2010; Cartee et al., 2000; Cohen, 2009; Miller et al., 2001). We kept the same Na_v and K_v ion channels used in the alternative model of Woo and colleagues (Miller et al., 2011; Woo et al., 2009a,b, 2010) in order to directly compare our results with theirs, with the only difference being in the adaptation mechanisms. However, the model’s AP duration is somewhat shorter than

value of $330 \mu\text{s}$ recently estimated for adult SGNs (Rattay and Danner, 2014). This possible inaccuracy, along with the discrepancy in refractory properties for some SGNs, suggests that further refinement of the types and characteristics of ion channels included in our SGN model is warranted. A number of different Na_v and K_v channel descriptions have been explored in previous SGN models (see O'Brien and Rubinstein, 2016, for a recent review), but none of these models have incorporated HCN channels. The emerging extended relative refractoriness shown in models with KLT is motivation for experimentally determining the channel's kinetics and the possible nodal and juxtapanodal distribution (Lai and Jan, 2006; Rasband and Shrager, 2000) that are specific to feline SGN. Exploring different channel types and configurations found in SGNs such as different Na_v , high-threshold K, and other K channels (recall Davis and Crozier, 2015) should be a step in a positive direction, as our study has shown that more accurate characterizations of HCN channels endogenous to SGNs can better explain *in vivo* responses to CI stimulation on the order of 10 to 100 ms. These different channels may shed light on the differences in action potential duration and refractoriness, as well as the very slow ($> 1 \text{ s}$) adaptation observed in some SGNs (Litvak et al., 2003). However, as we have seen in this study, there is significant scope for heterogeneity of channel properties alone to account for variability in stimulus-response statistics.

4.5 Conclusions

In our study we have shown that heterogeneity in the half-maximal activation potential of HCN channels can explain the variability of adaptation in SGNs responding to pulsatile CI stimulation while maintaining a physiologically-realistic absolute refractory period. A better understanding of the mechanisms behind intrinsic adaptation of SGNs is important for determining how different SGNs in the auditory nerve might respond differently to the same electrical stimulus. In addition, the degree of adaptation may also vary with the site of action potential initiation, because of differential expression of ion channel types at different locations along the neuron. Finally, a more accurate computational model of SGNs that can incorporate the range of adaptation strengths observed *in vivo* should provide an invaluable tool for evaluating CI stimulating strategies in present clinical use, as well as for the development of novel stimulation approaches.

4.6 Appendix

For the equations that model the current and channel kinetics of the Na_v , K_v , and KLT channels, please refer to the appendix in Negm and Bruce (2014). Here, we supply the equations describing the voltage-gated activity of the $\text{HCN}(r)$ and $\text{HCN}(q,s)$ channel models,

shifted by $cV_{1/2}$ standard deviations as functions of the relative membrane potential (σ_x , where x is the channel particle).

4.6.1 HCN(r) Channel Model

The ionic current follows

$$I_{h,r}(t) = \gamma_h N_{r_1}(t) [V_m(t) - E_{h,r}] \quad (4.6)$$

where $N_{r_1}(t)$ is the number of channels in the fully-open, conducting state governed by the kinetic Markov chain state transition diagram



where transition rates α_r and β_r , calculated by (4.19) and (4.20), are dependent on the relative membrane potential and are functions of the activation function (r_∞) and time constant (τ_r) below

$$r_\infty(V) = \frac{1}{1 + 5.879 \exp[(V - c\sigma_r)/7]} \quad (4.8)$$

$$\tau_r(V) = 4.17 + \frac{758.8 \exp[(V - c\sigma_r)/14]}{1 + 9.199 \exp[13(V - c\sigma_r)/84]} \quad (4.9)$$

4.6.2 HCN(q,s) Channel Model

The ionic current follows

$$I_{h,(q,s)}(t) = \gamma_h [N_{q_2}(t) + N_{s_1}(t)] [V_m(t) - E_{h,(q,s)}] \quad (4.10)$$

where $N_{q_2}(t)$ and $N_{s_1}(t)$ are the number of channels in the fully-open, conducting states governed by the parallel kinetic Markov chain state transition diagram



where transition rates α_q , β_q , α_s , β_s , calculated by (4.19) and (4.20), are dependent on the relative membrane potential and are functions of the activation functions (q_∞ , s_∞) and time

constants (τ_q , τ_s) below

$$q_\infty(V) = \frac{1}{(1 + 9.104 \exp[(V - c\sigma_q)/12.36])^{1/2}} \quad (4.12)$$

$$s_{A,\infty}(V) = \frac{0.6628}{1 + 17.09 \exp[(V - c\sigma_s)/4.883]} \quad (4.13)$$

$$s_{B,\infty}(V) = \frac{1 - 0.6628}{1 + 3648 \exp[(V - c\sigma_s)/3.927]} \quad (4.14)$$

$$s_\infty(V) = \frac{s_{A,\infty}(V) - s_{B,\infty}(V)}{0.5551729} \quad (4.15)$$

$$\tau_q(V) = \frac{60.98 \exp[(V - c\sigma_q)/21.48]}{1 + 2.107 \exp[(V - c\sigma_q)/12.19]} \quad (4.16)$$

$$\tau_s(V) = \frac{632.3 \exp[(V - c\sigma_s)/20.23]}{1 + 7.925 \exp[(V - c\sigma_s)/13.44]} \quad (4.17)$$

4.6.3 Neuron-Specific Channel Modifications

The original channel time constants for KLT: τ_w and τ_z (Rothman and Manis, 2003a) and HCN: τ_r (Rothman and Manis, 2003b); τ_q and τ_s (Liu et al., 2014b) were divided by their respective thermal scaling coefficients k_w , k_z , k_r , k_q , and k_s to adjust the temperature to 37 °C where

$$k_x = Q_{10,x}^{(T-T_0)/10} \quad (4.18)$$

and x is the channel particle and $Q_{10,x}$ (see Table 4.1 for channel-specific values) represents the rate gain for two temperature-dependent biological processes separated by 10 °C (Cartee, 2000). T_0 represents the original temperature whereas T is the current temperature. The transition rates were then computed as

$$\alpha_x(V) = x_\infty(V) / \tau_x(V) \quad (4.19)$$

$$\beta_x(V) = [1 - x_\infty(V)] / \tau_x(V) \quad (4.20)$$

with the steady-state activation functions (x_∞) and time constants (τ_x).

References

- Arora, K., Dawson, P., Dowell, R., and Vandali, A. (2009). Electrical stimulation rate effects on speech perception in cochlear implants. *Int J Audiol*, 48(8):561–567.
- Baylor, D. A. and Nicholls, J. G. (1969). Changes in extracellular potassium concentration produced by neuronal activity in the central nervous system of the leech. *J Physiol*, 203(3):555–569.
- Benarroch, E. E. (2013). HCN channels: function and clinical implications. *Neurology*, 80(3):304–310.
- Biel, M., Wahl-Schott, C., Michalakis, S., and Zong, X. (2009). Hyperpolarization-activated cation channels: from genes to function. *Physiol Rev*, 89(3):847–885.
- Botros, A. and Psarros, C. (2010). Neural response telemetry reconsidered: II. the influence of neural population on the ECAP recovery function and refractoriness. *Ear Hear*, 31(3):380–391.
- Boulet, J., White, M. W., and Bruce, I. C. (2016). Temporal considerations for stimulating spiral ganglion neurons with cochlear implants. *J Assoc Res Otolaryngol*, 17(1):1–17.
- Bruce, I. C. (2006). Implementation issues in approximate methods for stochastic Hodgkin–Huxley models. *Ann Biomed Eng*, 35(2):315–318.
- Bruce, I. C., White, M. W., Irlicht, L. S., O’Leary, S. J., and Clark, G. M. (1999a). The effects of stochastic neural activity in a model predicting intensity perception with cochlear implants: low-rate stimulation. *IEEE Trans Biomed Eng*, 46(12):1393–1404.
- Bruce, I. C., White, M. W., Irlicht, L. S., O’Leary, S. J., Dynes, S., Javel, E., and Clark, G. M. (1999b). A stochastic model of the electrically stimulated auditory nerve: single-pulse response. *IEEE Trans Biomed Eng*, 46(6):617–629.
- Cao, X. J. and Oertel, D. (2011). The magnitudes of hyperpolarization-activated and low-voltage-activated potassium currents co-vary in neurons of the ventral cochlear nucleus. *J Neurophysiol*, 106(2):630–640.
- Cartee, L. A. (2000). Evaluation of a model of the cochlear neural membrane. II: comparison of model and physiological measures of membrane properties measured in response to intrameatal electrical stimulation. *Hear Res*, 146(1-2):153–166.
- Cartee, L. A., Miller, C. A., and van den Honert, C. (2006). Spiral ganglion cell site of excitation I: comparison of scala tympani and intrameatal electrode responses. *Hear Res*, 215(1-2):10–21.

- Cartee, L. A., van den Honert, C., Finley, C. C., and Miller, R. L. (2000). Evaluation of a model of the cochlear neural membrane. I. physiological measurement of membrane characteristics in response to intrameatal electrical stimulation. *Hear Res*, 146(1-2):143–152.
- Chen, C. (1997). Hyperpolarization-activated current (I_h) in primary auditory neurons. *Hear Res*, 110(1-2):179–190.
- Cohen, L. T. (2009). Practical model description of peripheral neural excitation in cochlear implant recipients: 5. refractory recovery and facilitation. *Hear Res*, 248(1-2):1–14.
- Davis, R. L. and Crozier, R. A. (2015). Dynamic firing properties of type I spiral ganglion neurons. *Cell Tissue Res*, 361(1):115–127.
- Dynes, S. B. C. (1996). *Discharge characteristics of auditory nerve fibers for pulsatile electrical stimuli*. PhD thesis, Massachusetts Institute of Technology, Cambridge, Massachusetts.
- Gillespie, D. T. (1977). Exact stochastic simulation of coupled chemical reactions. *J. Phys. Chem.*, 81(25):2340–2361.
- Guevara, M. R. (2003). Bifurcations involving fixed points and limit cycles in biological systems. In Beuter, A., Glass, L., Mackey, M. C., and Titcombe, M. S., editors, *Nonlinear Dynamics in Physiology and Medicine*, pages 41–85. Springer New York, New York, NY.
- Heffer, L. F., Sly, D. J., Fallon, J. B., White, M. W., Shepherd, R. K., and O’Leary, S. J. (2010). Examining the auditory nerve fiber response to high rate cochlear implant stimulation: chronic sensorineural hearing loss and facilitation. *J Neurophysiol*, 104(6):3124–3135.
- Hodgkin, A. L. and Huxley, A. F. (1952). A quantitative description of membrane current and its application to conduction and excitation in nerve. *J Physiol*, 117(4):500–544.
- Howells, J., Trevillion, L., Bostock, H., and Burke, D. (2012). The voltage dependence of I_h in human myelinated axons. *J Physiol (Lond)*, 590(Pt 7):1625–1640.
- Huganard, J. R. and McCormick, D. A. (1992). Simulation of the currents involved in rhythmic oscillations in thalamic relay neurons. *J Neurophysiol*, 68(4):1373–1383.
- Imennov, N. S. and Rubinstein, J. T. (2009). Stochastic population model for electrical stimulation of the auditory nerve. *IEEE Trans Biomed Eng*, 56(10):2493–2501.
- Jenks, G. F. (1967). The data model concept in statistical mapping. In Frenzel, K., editor, *International yearbook of cartography*, pages 186–190. George Philip & Son.
- Kim, Y.-H. and Holt, J. R. (2013). Functional contributions of HCN channels in the primary auditory neurons of the mouse inner ear. *The Journal of General Physiology*, 142(3):207–223.

- Krouchev, N. I., Rattay, F., Sawan, M., and Vinet, A. (2015). From squid to mammals with the HH model through the Na_v channels' half-activation-voltage parameter. *PLoS ONE*, 10(12):e0143570–31.
- Lai, H. C. and Jan, L. Y. (2006). The distribution and targeting of neuronal voltage-gated ion channels. *Nat Rev Neurosci*, 7(7):548–562.
- Litvak, L. M., Smith, Z. M., Delgutte, B., and Eddington, D. K. (2003). Desynchronization of electrically evoked auditory-nerve activity by high-frequency pulse trains of long duration. *J Acoust Soc Am*, 114(4 Pt 1):2066–2078.
- Liu, Q., Lee, E., and Davis, R. L. (2014a). Heterogeneous intrinsic excitability of murine spiral ganglion neurons is determined by Kv1 and HCN channels. *Neuroscience*, 257:96–110.
- Liu, Q., Manis, P. B., and Davis, R. L. (2014b). I_h and HCN channels in murine spiral ganglion neurons: tonotopic variation, local heterogeneity, and kinetic model. *J Assoc Res Otolaryngol*, 15(4):585–599.
- Long, J. S. (1997). *Regression models for categorical and limited dependent variables*. SAGE Publications, Inc.
- Miller, C., Abbas, P. J., Nourski, K. V., Hu, N., and Robinson, B. K. (2003). Electrode configuration influences action potential initiation site and ensemble stochastic response properties. *Hear Res*, 175(1-2):200–214.
- Miller, C. A., Abbas, P. J., and Robinson, B. (2001). Response properties of the refractory auditory nerve fiber. *J Assoc Res Otolaryngol*, 2(3):216–232.
- Miller, C. A., Hu, N., Zhang, F., Robinson, B. K., and Abbas, P. J. (2008). Changes across time in the temporal responses of auditory nerve fibers stimulated by electric pulse trains. *J Assoc Res Otolaryngol*, 9(1):122–137.
- Miller, C. A., Woo, J., Abbas, P. J., Hu, N., and Robinson, B. K. (2011). Neural masking by sub-threshold electric stimuli: animal and computer model results. *J Assoc Res Otolaryngol*, 12(2):219–232.
- Mino, H., Rubinstein, J. T., Miller, C. A., and Abbas, P. J. (2004). Effects of electrode-to-fiber distance on temporal neural response with electrical stimulation. *IEEE Trans Biomed Eng*, 51(1):13–20.
- Mino, H., Rubinstein, J. T., and White, J. A. (2002). Comparison of algorithms for the simulation of action potentials with stochastic sodium channels. *Ann Biomed Eng*, 30(4):578–587.
- Mo, Z. L. and Davis, R. L. (1997). Heterogeneous voltage dependence of inward rectifier currents in spiral ganglion neurons. *J Neurophysiol*, 78(6):3019–3027.

- Morse, R. P., Allingham, D., and Stocks, N. G. (2015). Stimulus-dependent refractoriness in the Frankenhaeuser–Huxley model. *J Theo Biol*, 382(C):397–404.
- Negm, M. H. and Bruce, I. C. (2008). Effects of I_h and I_{KLT} on the response of the auditory nerve to electrical stimulation in a stochastic Hodgkin–Huxley model. *Proc 30th Annu Int Conf IEEE Eng Med Biol Soc*, 2008:5539–5542.
- Negm, M. H. and Bruce, I. C. (2014). The effects of HCN and KLT ion channels on adaptation and refractoriness in a stochastic auditory nerve model. *IEEE Trans Biomed Eng*, 61(11):2749–2759.
- O’Brien, G. E. and Rubinstein, J. T. (2016). The development of biophysical models of the electrically stimulated auditory nerve: Single-node and cable models. *Network*, pages 1–22.
- Pezo, D., Soudry, D., and Orío, P. (2014). Diffusion approximation-based simulation of stochastic ion channels: which method to use? *Front Comput Neurosci*, 8.
- Rasband, M. N. and Shrager, P. (2000). Ion channel sequestration in central nervous system axons. *J Physiol*, 525 Pt 1:63–73.
- Rattay, F. and Danner, S. M. (2014). Peak I of the human auditory brainstem response results from the somatic regions of type I spiral ganglion cells: evidence from computer modeling. *Hear Res*, 315:67–79.
- Robinson, R. B. and Siegelbaum, S. A. (2003). Hyperpolarization-activated cation currents: from molecules to physiological function. *Annu Rev Physiol*, 65:453–480.
- Rothman, J. S. and Manis, P. B. (2003a). Kinetic analyses of three distinct potassium conductances in ventral cochlear nucleus neurons. *J Neurophysiol*, 89(6):3083–3096.
- Rothman, J. S. and Manis, P. B. (2003b). The roles potassium currents play in regulating the electrical activity of ventral cochlear nucleus neurons. *J Neurophysiol*, 89(6):3097–3113.
- Rubinstein, J. T. (1995). Threshold fluctuations in an N sodium channel model of the node of Ranvier. *Biophys J*, 68(3):779–785.
- Rusznák, Z. and Szűcs, G. (2008). Spiral ganglion neurones: an overview of morphology, firing behaviour, ionic channels and function. *Pflugers Arch - Eur J Physiol*, 457(6):1303–1325.
- Schneidman, E., Freedman, B., and Segev, I. (1998). Ion channel stochasticity may be critical in determining the reliability and precision of spike timing. *Neural Comput*, 10(7):1679–1703.
- Verveen, A. A. (1962). Axon diameter and fluctuation in excitability. *Acta Morphol Neerl Scand*, 5:79–85.

- Verveen, A. A. and Derksen, H. E. (1968). Fluctuation phenomena in nerve membrane. *Proc IEEE*, 56(6):906–916.
- Woo, J., Miller, C. A., and Abbas, P. J. (2009a). Biophysical model of an auditory nerve fiber with a novel adaptation component. *IEEE Trans Biomed Eng*, 56(9):2177–2180.
- Woo, J., Miller, C. A., and Abbas, P. J. (2009b). Simulation of the electrically stimulated cochlear neuron: modeling adaptation to trains of electric pulses. *IEEE Trans Biomed Eng*, 56(5):1348–1359.
- Woo, J., Miller, C. A., and Abbas, P. J. (2010). The dependence of auditory nerve rate adaptation on electric stimulus parameters, electrode position, and fiber diameter: a computer model study. *J Assoc Res Otolaryngol*, 11(2):283–296.
- Yi, E., Roux, I., and Glowatzki, E. (2010). Dendritic HCN channels shape excitatory postsynaptic potentials at the inner hair cell afferent synapse in the mammalian cochlea. *J Neurophysiol*, 103(5):2532–2543.
- Zhang, F., Miller, C. A., Robinson, B. K., Abbas, P. J., and Hu, N. (2007). Changes across time in spike rate and spike amplitude of auditory nerve fibers stimulated by electric pulse trains. *J Assoc Res Otolaryngol*, 8(3):356–372.

Spike Initiation at Different Nodes of Ranvier in Spiral Ganglion
Neurons: Spatio-Temporal Responses to Cochlear Implant
Stimulation

Abstract

Several recent histological and electrophysiological experiments involving spiral ganglion neurons (SGNs) have located voltage-gated ion channels at specific nodes of Ranvier and have characterized the kinetics of those channels. Out of these histological studies, several possible ion channel type distributions along the SGN were pointed out. In terms of the electrophysiological experiments, hyperpolarization-activated cyclic nucleotide-gated (HCN) channels were located at certain nodes of Ranvier in SGNs of murinae. These channels operate at timescales that may explain the slow drop in excitability observed in response to *in vivo* pulse train stimulation in cats. Therefore, uncertainty remains as to what the distribution and kinetics of HCN channels may be in cats. Understanding the functions of these channels should provide new insights into how these cells respond to cochlear implant (CI) stimulation. We simulated the responses of several possible multicompartmental SGN models, each with unique node of Ranvier ion channel configurations, to determine the effect of different voltage-gated ion channels on the spatio-temporal patterns in response to different patterns of electrical stimulation. We evaluated responses from single pulse, paired pulse, pulse train, and masker-probe train stimulation, since those stimulation paradigms have been shown to be reliable methods for quantifying the effects of various electrical stimulus-response temporal phenomena in SGNs (see Chap. 2, or Boulet et al., 2016, and references therein). With the single pulse response, we can determine a baseline threshold and dynamic range for a given SGN model, which may be used to calibrate the current pulse amplitudes for the remaining stimulation paradigms. The responses to paired pulse stimuli are useful for characterizing refractoriness, facilitation, and short-term accommodation. Pulse train and masker-probe train responses inform us about the neuron's refractoriness and facilitation, as well as the relatively slower processes on timescales of tens to hundreds of milliseconds such as long-term accommodation and spike rate adaptation. In addition to estimating several temporal response characteristics of model SGNs, we also investigated the spike initiation profile along the length of the cell. Depending on which node of Ranvier initiated the action potential, we could expect different temporal responses given the systematic differences in the ion channel type and the number of channels from node-to-node. On top of the spike rate adaptation and accommodation generated by the HCN model shown in Chap. 4, we also show that each SGN model version and different electrode placements produce unique spatial spiking recruitment profiles. These combined temporal and spatial response characteristics of model SGNs provide a more accurate comprehension on how mammalian SGNs may process stimulation delivered by CIs. This information should be valuable for developing new perspectives on how to overcome limitations of contemporary CI stimulation strategies arising from the CI-SGN interface.

5.1 Introduction

The electrical activity that forms the interface between a cochlear implant (CI) and spiral ganglion neurons (SGNs), in terms of the stimulus and the corresponding response, can be influenced by spatial and temporal factors. The approach taken in Chap. 4 where we focused on the single node of Ranvier biophysical model response, only allowed for the investigation of the temporal stimulus-response phenomena. Even then, single node models cannot produce the higher levels of facilitation that are predicted by a full cell SGN model (Cartee, 2000) or SGN responses in cats (Cartee et al., 2000; Dynes, 1996). In this chapter, we consider the electrical spatio-temporal responses of SGNs to CIs by determining the responses of multicompartmental SGN models to extracellular stimulation.

Since CI electrodes reside in the extracellular space of SGNs, the current delivered by those electrodes spreads out spatially and the current amplitude attenuates with distance (see Fig. 2.1). For a temperature-adjusted Hodgkin–Huxley axon SGN model, this causes a distribution of spike initiation nodes, typically centered at the node that is closest to the stimulating electrode (Mino et al., 2004). This distribution of spike initiation nodes may be altered by the nonuniform morphology of the SGN (peripheral process, soma, and central axon) as well as the nonuniform ion channel density and different ion channel types across the different nodes of Ranvier.

When Type I spiral ganglion neurons were extracellularly stimulated with pulse train stimulation in cats (Heffer et al., 2010; Miller et al., 2011; Zhang et al., 2007), steady-state spike rates dropped relative to the onset spike rate over the course of 10s to 100s of milliseconds. In contrast, channels of the classical Hodgkin–Huxley model (Hodgkin and Huxley, 1952), the fast sodium (Na_v) and delayed-rectifier (K_v), when are adjusted for mammalian body temperature, can predict refractoriness but cannot predict the drop in neural excitability observed by Zhang et al. (2007), Heffer et al. (2010), and Miller et al. (2011). In a different multicompartmental SGN model with the addition of post-spike external potassium ion concentration accumulation (Woo et al., 2009a, 2010), it was shown that spike rate reductions could be generated on similar timescales to those of Zhang et al. (2007), Heffer et al. (2010), and Miller et al. (2011).

In contrast to the mechanisms introduced in the model by Woo et al. (2009a, 2010) that are not known to be endogenous to mammalian SGNs, our explanation for changes to firing patterns in the feline SGN relies solely on the variable distribution of multiple types of voltage-gated ion channels found along the various nodes of Ranvier of the SGN. Fortunately, some of these channel types are known to be responsible for reducing excitability at the appropriate timescales. At the first peripheral node and at nodes flanking the soma, $\text{Na}_v1.6$ channels were found at elevated densities (Hossain et al., 2005). The authors suggest that this particular placement of the higher density $\text{Na}_v1.6$ channels throughout the SGN could be responsible for fast spike generation and for helping conduction of action potentials across the soma. Hyperpolarization-activated cyclic nucleotide-gated (HCN) channels were found on rat SGNs at the same nodes as the high density $\text{Na}_v1.6$ channels, i.e., the first peripheral node and nodes flanking the soma (Yi et al., 2010). Low-threshold

potassium (KLT) channels are also known to colocalize with HCN1 channel subunits in principal cells of the ventral cochlear nucleus (Cao and Oertel, 2011; Oertel et al., 2008) and have also been found on SGN axons that synapse onto cells in the ventral cochlear nucleus (Bortone et al., 2006).

By comparing responses between intracellular and extracellular current injection, we aim to determine what components of the published stimulus-response data are due to temporal phenomena, spatial effects, or a combination of both. The temporal phenomena we are referring to have been mentioned in the previous chapters, namely as refractoriness, facilitation, accommodation, and spike rate adaptation. Some spatial effects include the site of stimulation and the spike initiation node. The spike initiation node is interesting since SGN geometry is not uniform and contains different voltage-gate ion channel types.

5.2 Methods

5.2.1 Multicompartmental SGN Model

As shown in Fig. 5.1, the general morphology of the feline SGN used in this study is a bipolar neuron composed of a peripheral axon with four nodes of Ranvier, a soma, and a central axon expressing twenty-three nodes of Ranvier. The soma and all internodes are myelinated. To account for the inherent spatial extension of the neuron we discretize it into multiple compartments (k), each represented by individual transmembrane isopotentials V_m^k . The resulting multicompartmental model contains one compartment per node of Ranvier, 9 compartments per internode and 9 compartments for the soma. The SGN geometry and passive electrical parameters given in Table 5.1 in the Appendix are based on the values of Woo et al. (2010). Other SGN parameters are listed in Table 5.2 for channel density values and Table 5.3 for values relevant to the nodes of Ranvier, both in the Appendix.

Ionic Currents and Channel Distribution

Recent evidence suggests that the distribution of voltage-gated ion channel types at the nodes along the SGN is nonuniform. Fast sodium and delayed-rectifier potassium channels (Hodgkin and Huxley, 1952) are characteristically found at all nodes along the SGN. High densities of the $\text{Na}_v1.6$ subunit were observed at the first peripheral node (p1) and nodes flanking the soma (p4 and c1) (Hossain et al., 2005). Taken together, this configuration describes the ion channel distribution for the HH SGN model. Hyperpolarization-activated cyclic nucleotide-gated (HCN) channels which are responsible for the I_h current, were present at nodes p1, p4, and c1 in rats (Yi et al., 2010). Specifically, subunits HCN1 and HCN4 were found at these nodes. We define this distribution of HCN channels, combined

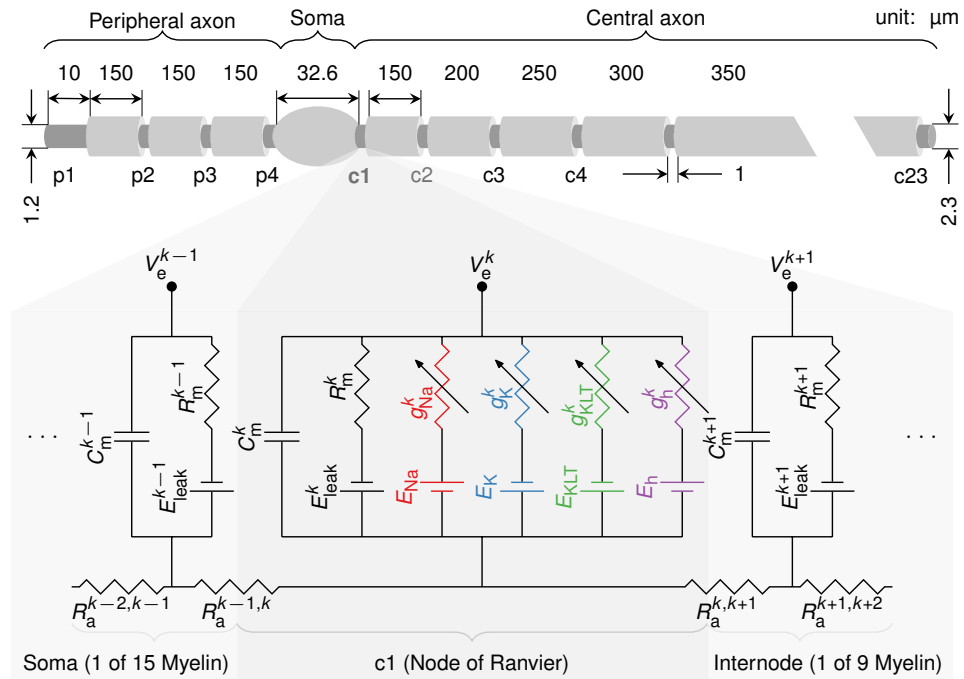


Figure 5.1 Morphology of the Type I SGN in cat, based on Woo et al. (2010), and the corresponding circuit model. The upper portion of the figure shows the SGN geometry. The peripheral nodes of Ranvier are denoted by p1–p4 whereas the central nodes are called c1–c23. All internodes between nodes c5–c23 are the same length. The lower part of the figure shows a portion of the circuit model at node c1 and the surrounding internodes. Starting at the left is a compartment of the soma, followed by the nodal compartment including all ion channels and finally, to the right, is one internodal compartment. Refer to Table 5.1 in the Appendix for a complete set of parameters of the neuronal geometry.

with the HH model, as the +HCN SGN model. Lastly, low-threshold potassium (KLT) channels were found on axons of SGNs projecting to cells of the ventral cochlear nucleus (Bortone et al., 2006). This supports our last model configuration, model +HCN+KLT, which is model +HCN SGN model, but with additional KLT channels distributed at all nodes. The kinetics of the Na and K channels were previously adjusted for 37 °C (Mino et al., 2002). The KLT channel model was introduced by Rothman and Manis (2003), then used by Negm and Bruce (2008) and Negm and Bruce (2014) in a single node of Ranvier membrane model with kinetics adjusted to 37 °C (see § 4.6 and Cartee, 2000). The HCN channel model was introduced in Chap. 4 as HCN(q, s) (Liu et al., 2014). Similarly, the HCN channel model was adjusted for a mammalian temperature (see § 4.6 and Cartee, 2000). We used two different variants of the HCN(q, s) model in order to simulate moderate and strong adaptation to pulse train stimulation. Referring to Chap. 4, we denote HCN($q, s, 2$) as HCN(moderate), and HCN($q, s, 4$) as HCN(strong) where the moderate and strong versions refer to channels that produce those respective levels of adaptation in a single node model. In total, we tested the five multicompartmental SGN models: HH, +HCN(moderate), +HCN(strong), +HCN(moderate)+KLT, +HCN(strong)+KLT.

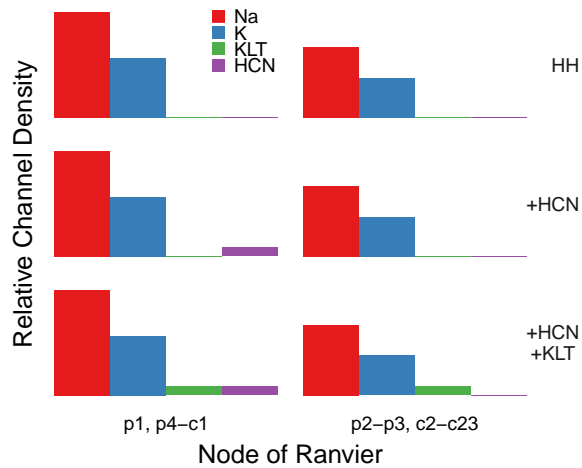


Figure 5.2 Na, K, KLT, and HCN ion channel densities at each node of Ranvier for three model configurations: HH, +HCN, and +HCN+KLT. Refer to Table 5.2 in the Appendix for exact values.

5.2.2 Stimuli

Increasing the electrode-to-neuron distance leads to spike initiation across a larger number of different nodes due to the broader spread of excitation (Mino et al., 2004). This result was obtained from a simulation study by using a myelinated cat SGN axon with homogeneous properties, including identical ion channel numbers and types at every node. This study differs from ours in that we model a more realistic cat SGN in terms of morphology, which includes both peripheral and central axons, connected by a soma (Woo et al., 2010), and ion channel type distribution as a function of the different nodes of Ranvier and the channel numbers at those nodes. Therefore, the potential for a differential spike initiation node depending on electrode placement is greater in our study and may potentially impact features of the temporal spiking patterns.

In order to address these concerns, all stimulation was delivered with a monopolar electrode either intracellularly or at one of the two extracellular distances z_{ex} from the neuron: 1225 μm or 2500 μm . The electrode-to-neuron distance z_d^k is the Euclidean distance from the electrode to the k^{th} neuronal compartment. In contrast, when mentioning ‘distance’ by itself, we are referring to a unique case of the electrode-to-neuron distance, which we define as the distance from the stimulating electrode to the nearest node of Ranvier. In this study, we stimulated near the four nodes, two at the peripheral process: p1 and p2, and two more at the central axon: c1 and c5. For example, referring to the orientation of the model neuron in Fig. 5.1, placement of an electrode at 2500 μm c1, refers to placing an electrode directly above or below (or more generally, as any distance orthogonal to the length-wise axis of the neuron) node c1 at a distance of 2500 μm . Polarity of the stimulation was chosen to be a cathodic-leading pulse since simulation studies have shown that cat SGNs have lower current thresholds for spiking compared to human SGNs where anodic-leading stimulation produces lower thresholds (Rattay et al., 2001). Pulse shapes were chosen for consistency across a set of simulation and experimental studies (Miller et al., 2001a, 2008,

2011; Woo et al., 2010; Zhang et al., 2007) as rectangular pulses with 40 μ s/phase duration and with no interphase gap.

Single Pulse Discharge Probability (FE) Versus Current Level

Monophasic and biphasic single pulses were delivered at 25 current levels centered around a first-pass estimate of the single pulse threshold current. This set of stimuli was repeated for 1000 trials, where each trial was simulated for 1.5 ms beyond the pulse onset.

Paired Pulses to Simulate Refractory Effects

Monophasic and biphasic paired pulse stimuli were created with an initial masker pulse, followed by a probe pulse. Masker and probe pulses were temporally separated by 120 various interpulse intervals (IPIs) drawn from 20 exponentially-spaced IPIs from 0.25 to 10 ms and 20 linearly-spaced IPIs from 0.251 to 2 ms. The masker pulse current level was set to a current amplitude of $\theta_{SP}(1 + 3RS_{SP})$, which is equivalent to FE = 97.7 %. Probe pulses were then delivered at 21 linearly-spaced current levels ranging from a first-pass estimate of the model's dynamic range over the FE interval between 0.1 and 99.9 %. Each of these paired pulse stimuli were repeated for 100 trials, given that a spike was elicited in response to the masker pulse, where each stimulus lasted 1.5 ms longer than the onset time of the probe pulse.

Paired Pulses to Simulate Facilitation and Accommodation Effects

Monophasic and biphasic paired pulse stimuli were created with an initial masker pulse, followed by a probe pulse. Masker and probe pulses were temporally separated by 40 various IPIs drawn from 20 exponentially-spaced IPIs from 0.15 to 10 ms and 20 linearly-spaced IPIs from 0.151 to 2 ms. The masker pulse current level was set to one of the 10, 30, and 50 % single-pulse-equivalent FEs. Probe pulses were then delivered at 21 linearly-spaced current levels ranging from a first-pass estimate of the model's dynamic range spanning the FEs from 0.1 to 99.9 %. Each of these paired pulse stimuli were repeated for 100 trials, given no spike occurred in response to the masker pulse, where each stimulus lasted 1.5 ms longer than the onset time of the probe pulse.

Pulse Train and Masker-Probe Train Responses

Pulse train and masker-probe train stimulation was approached in a similar fashion that was previously described in § 4.2.3, except for a few differences. Responses to both monophasic and biphasic pulse trains were simulated. Pulse train and masker train stimulation was

delivered at 1, 10, 20, 50, 80, 90, 99, 99.99, and 99.9999 % FEs and 250, 1000, and 5000 pulses/s rates. Following the masker train, the probe train was always injected at an FE of 50 % and the relatively slow rate of 100 pulses/s.

5.2.3 Computer Simulation and Analysis

We used a simulation time step of $\Delta t = 2.5 \mu\text{s}$ to solve the cable equation (5.14), given in the Appendix. Since all voltage-gated ion channels are stochastic (Imennov and Rubinstein, 2009; Miller et al., 2011; Mino et al., 2004, 2002; Negm and Bruce, 2008, 2014; Rattay et al., 2001, 2013; Woo et al., 2009a,b, 2010), we followed two steps for every trial simulation in order to randomize their states, according to their kinetics. The first step was to initialize ion channels over a period of 300 ms while holding the relative transmembrane potential $V^k = 0 \text{ mV}$. The second step was to allow the membrane potential to fluctuate freely, again over a period of 300 ms in response to $I_{\text{in}} = 0 \text{ pA}$ or $I_{\text{ex}} = 0 \text{ mA}$.

Spike Detection: When and Where?

As discussed in § 4.2.5, spike detection is not trivial in response to interpulse intervals on the order of the action potential duration when using a fixed membrane potential crossing level. However, the problem of accurately detecting spikes is conceptually easier in a multicompartmental model, compared to a non-spatially distributed model, since a spike may be defined as a ‘propagated disturbance’. Still, there is ambiguity in defining what this disturbance is. In the bottom panel of Fig. 7 of Miller et al. (2001a), the action potential maximum (APmax) increases as a function of the interpulse interval. This means that if the neuron spiked, then the next spike, in response to the next pulse, will eventually return to the resting action potential maximum. Miller et al. (2001a) shows that this return to the resting APmax occurs somewhere between an IPI of 4 to 10 ms. Even for a propagating action potential in response to a single pulse, APmax may not be constant across all nodes. The reasoning behind this is, since there is variability in the number of sodium channels across nodes within a cell, then the resulting current responsible for spike generation would also be variable from node-to-node. These matters suggest that, even for a multicompartmental neuronal model, using a fixed membrane potential crossing level to detect if an action potential has propagated may not be sufficient. Therefore, to address these issues, we used the same general spike detection algorithm introduced in § 4.2.5, which is based on determining the minimum sodium channel opening duration θ_λ required to generate an action potential. In order to apply the single node spike detection algorithm to a multicompartmental model we contributed multiple amendments. For every model (HH, +HCN(moderate), +HCN(strong), +HCN(moderate)+KLT, +HCN(strong)+KLT) we collected the sodium channel opening duration λ in response to a single pulse ranging 200 different current pulse amplitudes, 100 trials, sites of stimulation (p1, p2, c1, and c5),

and the three electrode distances (extracellular: 1225 μm and 2500 μm , and intracellular). Therefore, for every model version, a set of sodium channel opening durations $\{\lambda\}$ was aggregated over all current pulse amplitudes, trials, sites of stimulation, electrode distance, and lastly, and all nodes of Ranvier. From here, the sodium channel opening duration threshold θ_λ was determined for each SGN model version as demonstrated in § 4.2.5 and Fig. 4.2.

Once θ_λ is known, for any given simulation trial, we can then tag the i^{th} time at which $\lambda \geq \theta_\lambda$ as the time of spike propagation $t_i^{s,n}$ at node of Ranvier n . As the action potential propagates outwardly in both directions toward nodes p1 and c23, we can then collect $t_i^{s,n}$ for all nodes. A spike is deemed to have successfully propagated if the action potential reached node c17 (c16 was used by Woo et al., 2010). The idea behind this is that information is being transmitted to central auditory neural structures, which is the primary function of Type I SGNs. Once spike i has propagated to node c17, we can then observe the spike propagation times over all nodes $\{t_i^{s,n}\}$. The spike initiation time t_i^{Sinit} is just the earliest of those times, or

$$t_i^{\text{Sinit}} \triangleq \min_n \{t_i^{s,n}\} \quad (5.1)$$

and spike initiation node n_i^{Sinit} is defined as the node at which t_i^{Sinit} occurs, or

$$n_i^{\text{Sinit}} \triangleq \arg \min_n \{t_i^{s,n}\}. \quad (5.2)$$

We then repeat this process for all spike propagations.

Single Pulse Stimuli

We fit the single pulse firing efficiency (FE) to the cumulative Gaussian distribution as previously introduced in (3.1) and (4.2), which is a function of the injected current amplitude (I_{ex} or I_{in} , only). From this, we can estimate the single pulse threshold current θ_{SP} and single pulse relative spread RS_{SP} (3.3). We evaluate the quality of the fits to the single pulse response data by the R_{count}^2 measure (Long, 1997). Refer to § 3.2.4 and 4.2.4 for more details on this analysis. These statistics, θ_{SP} , RS_{SP} , and R_{count}^2 were calculated for the 5 models \times 3 distances \times 4 sites \times 2 pulse shapes.

As we explained in § 5.2.3, spikes may not necessarily be initiated at the node of Ranvier closest to the stimulating electrode. There is more potential for this to occur with extracellular current injection (Javel and Shepherd, 2000; Miller et al., 2004; Mino et al., 2004), compared to intracellular stimulation due to a wider current spread. Biphasic pulses may also broaden the locus of the spike initiation node along the length of the SGN with respect to the site of stimulation. Compared with a monophasic pulse, the anodic phase of a biphasic pulse on average effectively increases the single pulse threshold (Gorman and

Mortimer, 1983; Miller et al., 2001b; Shepherd and Javel, 1999) by cancelling a proportion of the spikes that are undergoing initiation near the stimulating electrode. However, nodes of Ranvier that are more distal to the stimulating electrode may still initiate a spike given a large enough current injection. Therefore, in order to assess the spread of excitation along the SGN, we tabulated the probability of spiking as a rectangular array in terms of the spike initiation site and site of stimulation. Probability of spiking was defined as the fraction of spiking responses to both spiking and non-spiking responses. This process was repeated for a range of single pulse FEs centered around θ_{SP} and scaled to RS_{SP} . We also provided a summary of the probability of spiking as a function of the spike initiation site and site of stimulation as a correlation in terms of Spearman's ρ (or Spearman's rank correlation coefficient). With this measure we attempted to answer the question of whether the site of stimulation correlated with spike initiation site. A Spearman's ρ value of 1 indicates a perfect correlation, or that action potentials are always initiated at the site of stimulation. A value of -1 refers to the spike initiation node being completely anti-correlated to the site of stimulation.

Paired Pulse Stimuli for Refractoriness

Following Negm and Bruce (2014), we fit the refractory paired pulse responses, that is, the ratio of the probe threshold to the single pulse threshold $\theta_{ref}(IPI)/\theta_{SP}$, as a function of the IPI to (4.4), or

$$\hat{\theta}_{ref/SP}(IPI) = \frac{\sum_{i=1}^2 A_i}{\sum_{i=1}^2 A_i \left[1 - \exp\left(-\frac{IPI - \Delta t_{abs}}{\tau_{rel,i}}\right) \right]}. \quad (5.3)$$

Refer to § 4.2.4 for further details on this analysis. The coefficients A_1 and A_2 , relative refractory period (RRP) time constants $\tau_{rel,1}$ and $\tau_{rel,2}$, the absolute refractory period (ARP) Δt_{abs} , and the corresponding quality of the fits R^2 to (5.3) were calculated for the 5 models \times 3 distances \times 4 sites \times 2 pulse shapes. However, in this chapter we only report Δt_{abs} and R^2 .

Paired Pulse Stimuli for Facilitation and Accommodation

The paired pulse response analysis introduced in § 3.2.4 was designed to separate the effects of passive facilitation (mem), active facilitation (f), and accommodation (a: quick or short-term a_q and slow or long-term a_s). There are several more factors that contribute to facilitation and accommodation in our biophysical multicompartmental. The typical response to the first pulse in paired pulse stimulation is that the spike did not propagate

beyond node c17. This could be the result of either a failed spike initiation or a failed spike propagation. Therefore, either only local circuits are activated in a subthreshold manner (failed spike initiation), or a that a node initiated a spike, followed by several other activated nodes in which significant axial current flowed to neighboring compartments but did not propagate beyond c17. In either case, what this means is that there is an effect of spatial activation due to a subthreshold preconditioning pulse. Passive facilitation should also be influenced by the electrode-to-neuron distance. Hence, a linear combination of multiple node-centric facilitation and accommodation models becomes intractable. Instead, we choose to describe how all of these effects contribute to the subthreshold excitability in the range of 0 to 10 ms as one facilitation (fac) and one accommodation (acc) component

$$\hat{\theta}_{\text{sub/SP}}(\text{IPI}) = 1 + a_{\text{fac}} \exp\left(-\frac{\text{IPI}}{\tau_{\text{fac}}}\right) + a_{\text{acc}} \exp\left(-\frac{\text{IPI}}{\tau_{\text{acc}}}\right) \quad (5.4)$$

where τ_{fac} and τ_{acc} are the facilitation and accommodation time constants, and $a_{\text{fac}} \leq 0$ and $a_{\text{acc}} \geq 0$ are the corresponding coefficients. Just as we have done with the refractory paired pulse responses, we fit $\theta_{\text{sub}}(\text{IPI})/\theta_{\text{SP}}$ to (5.4). All coefficients and time constants in (5.4), and quality of the fits R^2 to (5.4) were calculated for the 5 models \times 3 distances \times 4 sites \times 2 pulse shapes \times 3 masker pulse FEs.

Pulse Train Stimuli

Most of the measures for quantifying the pulse train response were previously introduced in § 3.2.4 and § 4.2.4. Post-stimulus time histograms (PSTHs) were evaluated by (3.36) to estimate the firing rate. PSTHs were counted according to two time axes: 1) containing all 1 ms bins, and 2) a variable-width bin axis defined by the intervals 0–4, 4–12, 12–24, 24–36, 36–48, 48–100, 100–200, and 200–300 ms (Zhang et al., 2007). The normalized spike rate decrement (NSRD), was calculated as the difference between the response rate during 0–12 ms (or onset rate) and 200–300 ms (final rate), then divided by the response rate during the 0–12 ms interval (Zhang et al., 2007). Two time constants of adaptation $\tau_{\text{adapt},1}$ and $\tau_{\text{adapt},2}$ were estimated by fitting the wide-bin PSTH responses to

$$s(t) = A_{\text{ss}} + A_{\text{dec},1} \exp\left(-\frac{t}{\tau_{\text{adapt},1}}\right) + A_{\text{dec},2} \exp\left(-\frac{t}{\tau_{\text{adapt},2}}\right) \quad (5.5)$$

where t was evaluated at the center of the wide-bin intervals (Zhang et al., 2007). All coefficients and time constants ($\tau_{\text{adapt},1}$ and $\tau_{\text{adapt},2}$) in (5.5), quality of the fits R^2 to (5.5), onset rate, and NSRD were calculated for the 5 models \times 3 distances \times 4 sites \times 2 pulse shapes \times 3 stimulation rates \times 9 pulse FEs. Lastly, spatial SGN activation was estimated as in § 5.2.3, except we used pulse train responses in the final interval of 200–300 ms. Specifically, we calculated the 1) probability of spiking as a function of the spike initiation node and site of stimulation and the 2) spatial correlation (Spearman's ρ) between the spike initiation

node and site of stimulation.

Masker-Probe Train Stimuli

Responses to masker pulse trains were treated just as pulse train responses were treated in § 5.2.3. All analysis for responses to masker-probe train stimulation used in this chapter is identical to that introduced in § 4.2.4. Post-stimulus time histograms were estimated for probe train responses using 1 ms bins (Miller et al., 2011). The probe response recovery ratio (PRRR) was calculated as the ratio of the number of spikes in response to probe train stimulation with previous masker train stimulation to without previous masker train stimulation (Miller et al., 2011). The PRRR was calculated for the 5 models \times 3 distances \times 4 sites \times 2 pulse shapes \times 3 stimulation rates \times 9 pulse FEs.

5.3 Results

The difference in the effect of the two extracellular stimulation distances z_{ex} (1225 μm and 2500 μm) on all results was relatively small except for θ_{sp} , as expected. Therefore, to encourage brevity in reporting the results section, we will not present cases with stimulation from the 1225 μm distance.

If we consider the quality of all fits to data as previously described by R_{count}^2 or R^2 , then the single pulse response has 120 cases (5 models \times 3 distances \times 4 sites \times 2 pulse shapes), the refractory response also has 120 cases (5 models \times 3 distances \times 4 sites \times 2 pulse shapes), the subthreshold conditioner response has 360 cases (5 models \times 3 distances \times 4 sites \times 2 pulse shapes \times 3 masker pulse FEs), and the pulse train response has 3240 cases (5 models \times 3 distances \times 4 sites \times 2 pulse shapes \times 3 stimulation rates \times 9 pulse FEs). Clearly, there are many responses to each stimulation type. Therefore, we summarized the quality of fit over all cases per stimulation type by the value of R_{count}^2 or R^2 at the 25 % quantile of the R_{count}^2 or R^2 empirical distribution (75 % of the quality of fits are greater than this value). This descriptive statistic was chosen since the minimum or maximum values do not accurately characterize the spread of the R_{count}^2 or R^2 values and the 25 % quantile is a more conservative measure than the median.

5.3.1 Single Pulse Response

The single pulse responses were fitted to the cumulative Gaussian distribution function ((3.1) or (4.2)). Over all model versions, sites of stimulation, pulse shapes, and stimulation distances, 75 % of the corresponding R_{count}^2 values were greater than 0.856, indicating that of most model versions and stimulation cases were well-fit. Figure 5.3 reports the single

pulse threshold θ_{SP} . Extracellular stimulation obviously caused higher θ_{SP} values than intracellular stimulation. As expected, biphasic stimulation resulted in greater single pulse thresholds than monophasic stimulation. Responses to intracellular stimulation generated single pulse threshold values on the order of approximately 40 pA to 85 pA, which were reported in § 4.3.1 and by Negm and Bruce (2008, 2014) for single node of Ranvier SGN models (using a pulse width of 50 μ s/phase to 100 μ s/phase, compared to our 40 μ s/phase pulse width). These same studies showed that HCN and KLT can individually increase the single pulse threshold. Since the HCN(strong) channel is fully open at rest, whereas the HCN(moderate) channel is only partially open (see Fig. 4.1A, s_{∞} where HCN(strong) is the HCN($q,s,4$) model and HCN(moderate) is the HCN($q,s,2$) model), model versions with HCN(strong) have the lowest resting input resistance and therefore, the highest θ_{SP} values. This result is consistent with the single node model results in Fig. 4.3A.

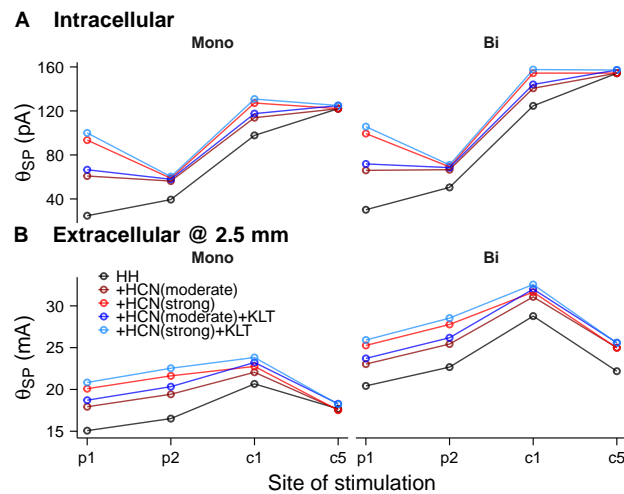


Figure 5.3 Single pulse threshold θ_{SP} for each SGN model version (HH, +HCN(moderate), +HCN(strong), +HCN(moderate)+KLT, +HCN(strong)+KLT), site of stimulation (p1, p2, c1, and c5), and pulse shape (monophasic and biphasic). Panels show the response to **A** intracellular stimulation and **B** extracellular stimulation at a distance of 2500 μ m.

Figure 5.4 reports the single pulse relative spread RS_{SP} . In response to intracellular stimulation, RS_{SP} covered the range of approximately 0.025 to 0.055, which is a similar range shown in § 4.3.1 reported to be within 0.03 to 0.07. The smaller values of RS_{SP} in this study compared to those reported in § 4.3.1 are likely due to the shorter pulse width (40 μ s/phase compared to 50 μ s/phase). This is consistent with RS_{SP} increasing as a function of the pulse width (Negm and Bruce, 2008). Relatively speaking, RS_{SP} decreased in response to extracellular stimulation. The larger extent of current spread from extracellular stimulation promotes a broader extent of local node-to-node current flow. Thus, the lowered single pulse relative spread values in response to extracellular stimulation may be a consequence of an average of the increased local current flow. The HH model shows an exception to this in response to extracellular biphasic stimulation near c5. As we will discover in Fig. 5.5, when responding to extracellular biphasic stimulation at c5, the HH model initiates spiking

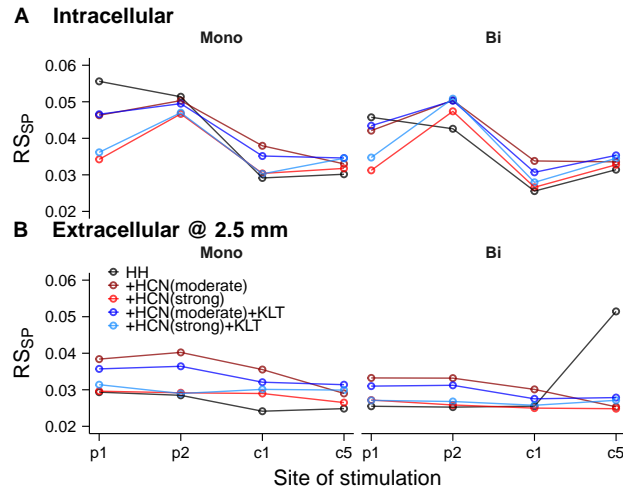


Figure 5.4 Single pulse relative spread RS_{SP} for each SGN model version (HH, +HCN(moderate), +HCN(strong), +HCN(moderate)+KLT, +HCN(strong)+KLT), site of stimulation (p1, p2, c1, and c5), and pulse shape (monophasic and biphasic). Panels show the response to **A** intracellular stimulation and **B** extracellular stimulation at a distance of 2500 μm .

only at nodes p1 and p3. Spiral ganglion neuron model versions with HCN(moderate) channels (HCN($q,s,2$) channel) have a greater single pulse relative spread than model versions with the HCN(strong) channels (HCN($q,s,4$) channel). This result is in agreement with Fig. 4.3C that shows that the RS_{SP} is maximized for single node of Ranvier SGN models with the HCN(q,s,c) channel model at $c = 0$, then monotonically decreases from that point. The stochasticity defined by RS_{SP} occurs in response to the timescale of a single pulse width, which coincides with the time constant of the quick component of the HCN(q,s,c) channel model (refer to Fig. 4.1B, τ_q).

Figure 5.5 shows the probability of spiking at nodes p1–c6 (the spike initiation node) in response to the site of stimulation for all model versions, monophasic and biphasic pulses, 25.05, 50, and 74.95 % FEs, and two different distances including intracellular stimulation (Fig. 5.5A) and extracellular stimulation at a distance of 2500 μm (Fig. 5.5B). A perfect spatial response would look like a probability of spiking equal to 1, being initiated at the site of stimulation. This means that we would expect red squares at the coordinates (p1,p1), (p2,p2), (c1,c1), and (c5,c5). Instead, all SGN models initiate some spikes at nodes that are different from where they are stimulated. This is most obvious for the HH model since even p1 initiates spikes when stimulated at c1, which is the case for both intracellular stimulation and extracellular stimulation (monophasic, at a distance of 2500 μm). This suggests that HCN channels encourage a higher spike initiation node specificity. The next largest differences are related to the pulse shape and the stimulation distance. Biphasic pulses activate a broader set of nodes, compared to the monophasic pulses. Even more so, due to current spread, extracellular stimulation allows spike initiation at an even wider range of nodes, compared to intracellular stimulation.

To summarize Fig. 5.5, we report Spearman's ρ , or the SGN's spatial activation corre-

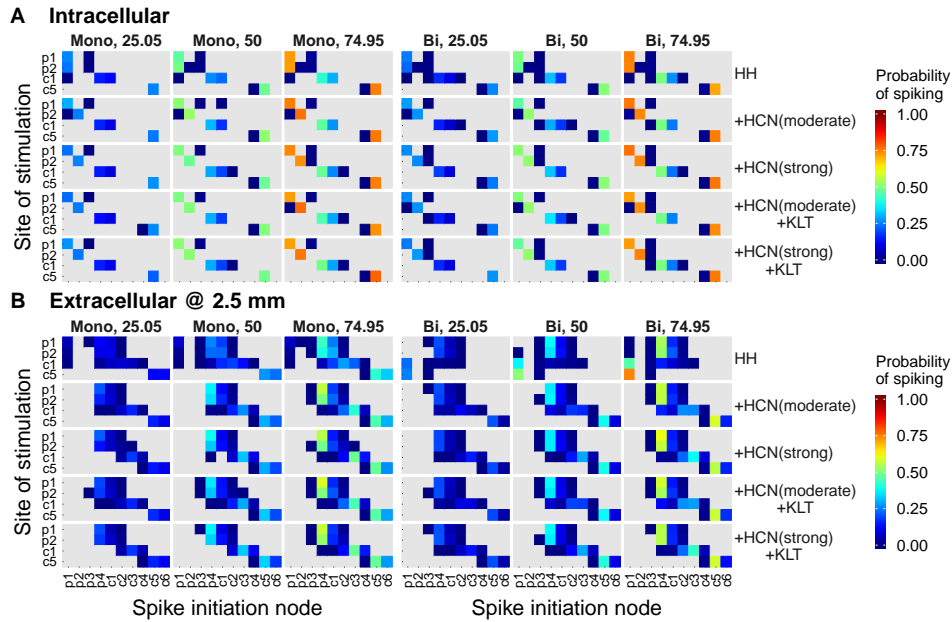


Figure 5.5 Probability of spiking as a function of the spike initiation node (p1–c6 shown) and the site of stimulation (p1, p2, c1, and c5), represented by the colorbar on the right, for each SGN model version (HH, +HCN(moderate), +HCN(strong), +HCN(moderate)+KLT, +HCN(strong)+KLT). *Light grey squares* indicate that spikes were not initiated at that node. Panels show the response to **A** intracellular stimulation and **B** extracellular stimulation at a distance of 2500 μm . Responses to monophasic and biphasic single pulses at the 25.05, 50, and 74.95 % FEs are shown in the subpanels.

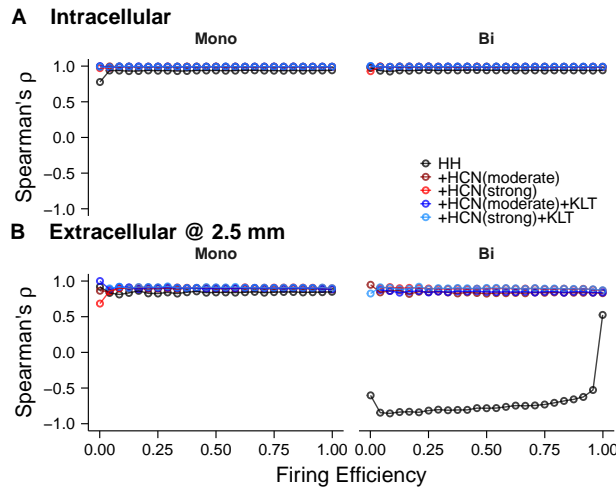


Figure 5.6 Spatial correlation (Spearman's ρ) between site of stimulation and spike initiation node as a function of the firing efficiency (FE) in response to monophasic and biphasic single pulses for each SGN model version (HH, +HCN(moderate), +HCN(strong), +HCN(moderate)+KLT, +HCN(strong)+KLT). Panels show the response to **A** intracellular stimulation and **B** extracellular stimulation at a distance of 2500 μm .

lation as a function of the firing efficiency in Fig. 5.6. The HH model shows the biggest difference in Spearman's ρ , compared to all other models. The HH model in response to ex-

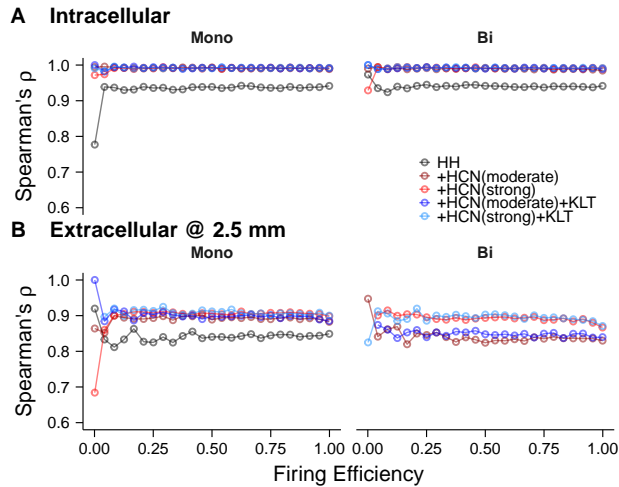


Figure 5.7 A zoomed-in version of Fig. 5.6 for Spearman's ρ from 0.6 to 1.

tracellular biphasic stimulation at a distance of 2500 μm has a negative value of Spearman's ρ over most firing efficiencies, which translates to the spike initiation node being anti-correlated with the site of stimulation. In other words, extracellular biphasic stimulation at a distance of 2500 μm of the HH model will result in spike initiation at a distant node with high probability. All models with HCN show a very high correlation between the site of stimulation and the spike initiation node, resulting in a value of Spearman's ρ close to 1. However, at the scale shown in Fig. 5.6, it is difficult to observe any other differences. Therefore, we present Fig. 5.7, which is a zoomed-in version of Fig. 5.6. There does not appear to be any effect of KLT channels on Spearman's ρ when added to the +HCN models. The only difference in the effect of the model version on the spatial activation correlation, again is in response to extracellular biphasic stimulation at a distance of 2500 μm , where models with the HCN(strong) channels have the highest Spearman's ρ values. Within our stimulation parameter space, biphasic extracellular stimulation poses the greatest challenge to the SGN in terms of initiating spiking nearest to the site of stimulation. We have also previously mentioned that HCN channels appear have the effect of increasing the probability of spike initiation at the node closest to the site of stimulation. Therefore, the question remains as to why models with the HCN(strong) channels initiate spikes more often at the nodes that are near the site of stimulation than models with the HCN(moderate) channels. This effect may be related to the slow component of the HCN(strong) model being fully open at rest, whereas the HCN(moderate) model is only partially open (see Fig. 3.1A, s_{∞} where HCN(strong) is the HCN($q,s,4$) model and HCN(moderate) is the HCN($q,s,2$) model).

5.3.2 Refractory Paired Pulse Response

Figure 5.8 shows the probe threshold ratio for refractory paired pulse responses and their fits to (5.3). Over all model versions, sites of stimulation, pulse shapes, and stimulation

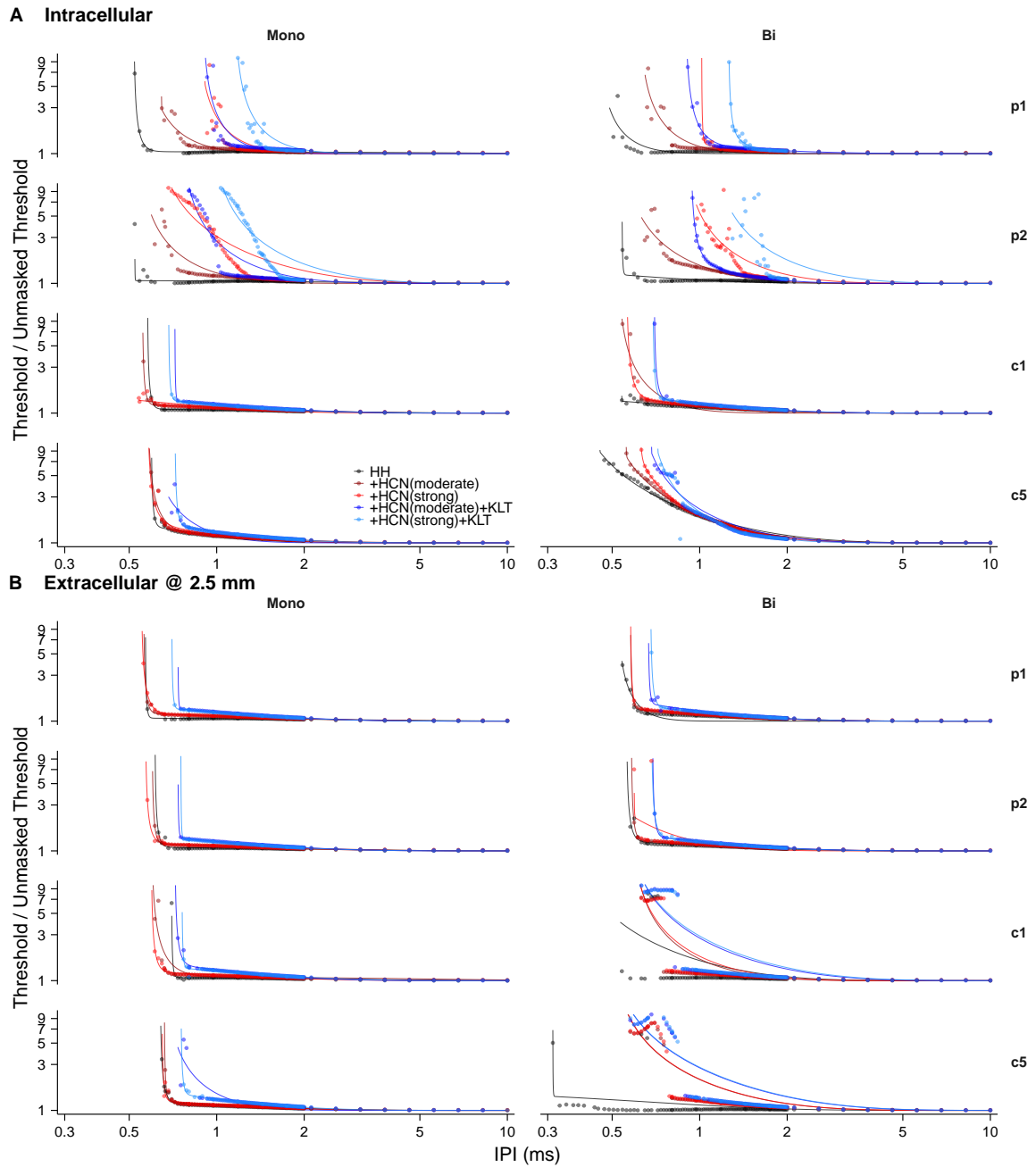


Figure 5.8 Ratio of the refractory probe threshold and single pulse threshold (refractory threshold / unmasked threshold) displayed as *dots* and refractory recovery function shown as *curves* as a function of the interpulse interval for each SGN model version (HH, +HCN(moderate), +HCN(strong), +HCN(moderate)+KLT, +HCN(strong)+KLT). Panels show the response to **A** intracellular stimulation and **B** extracellular stimulation at a distance of 2500 μm . Each panel contains subpanels showing refractory responses to the different sites of stimulation (p1, p2, c1, and c5) as *rows* and the corresponding monophasic and biphasic responses as *columns*.

distances, 75 % of the corresponding R^2 values were greater than 0.779. Models with KLT

have greater Δt_{abs} and relative refractory period time constants than models without the KLT channels, consistent with Fig. 4.11. Responses to intracellular stimulation have larger relative refractory period time constants compared to cases with extracellular stimulation. Responses to intracellular stimulation at p1 and p2 show a wider variation across model versions compared to stimulation at c1 and c5. This may be due to the greater variety in ion channel type distribution at the peripheral nodes compared to at the central nodes. Model versions with the HCN(strong) channels have a larger Δt_{abs} compared to model versions with HCN(moderate) channels in response to extracellular stimulation at nodes p1 and p2. This result is in agreement with Fig. 4.12. The HH model exhibits obviously smaller absolute refractory periods and smaller relative refractory period time constants than all other SGN model versions for certain stimulation cases that include monophasic and biphasic intracellular stimulation at p1 and p2, and in particular, biphasic intracellular at 2500 μm from c5. This type of probe threshold ratio pattern may be a symptom of the spiking probe response being initiated at a more distant node than the first spike, in such a way that refractory properties are minimized.

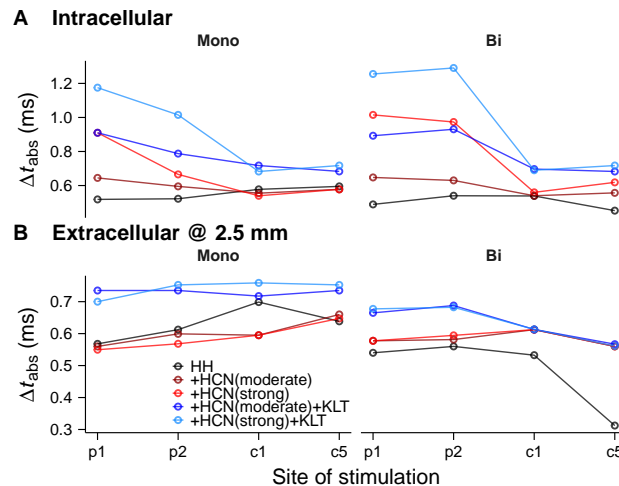


Figure 5.9 Estimates of the absolute refractory period Δt_{abs} for each SGN model version (HH, +HCN(moderate), +HCN(strong), +HCN(moderate)+KLT, +HCN(strong)+KLT) and site of stimulation (p1, p2, c1, and c5) in response to monophasic and biphasic stimulation. Panels show the response to **A** intracellular stimulation and **B** extracellular stimulation at a distance of 2500 μm .

Next, in Fig. 5.9 we summarize the absolute refractory period Δt_{abs} , which was provided by fitting the ratio of the refractory probe threshold and single pulse threshold to (5.3), presented in Fig. 5.8. Figure 5.9 confirms that model versions with KLT channels have a longer absolute refractory period than model versions without KLT and model versions with HCN(strong) channels have a greater Δt_{abs} than models with the HCN(moderate) channels. Intracellular stimulation produces absolute refractory periods in the range of approximately 0.55 to 1.25 ms, while extracellular stimulation produce values in a lower range of about 0.3 to 0.75 ms. The range of Δt_{abs} values in response to extracellular stimulation are closer to the range reported by Miller et al. (2001a) in which cat SGNs were also stimulated

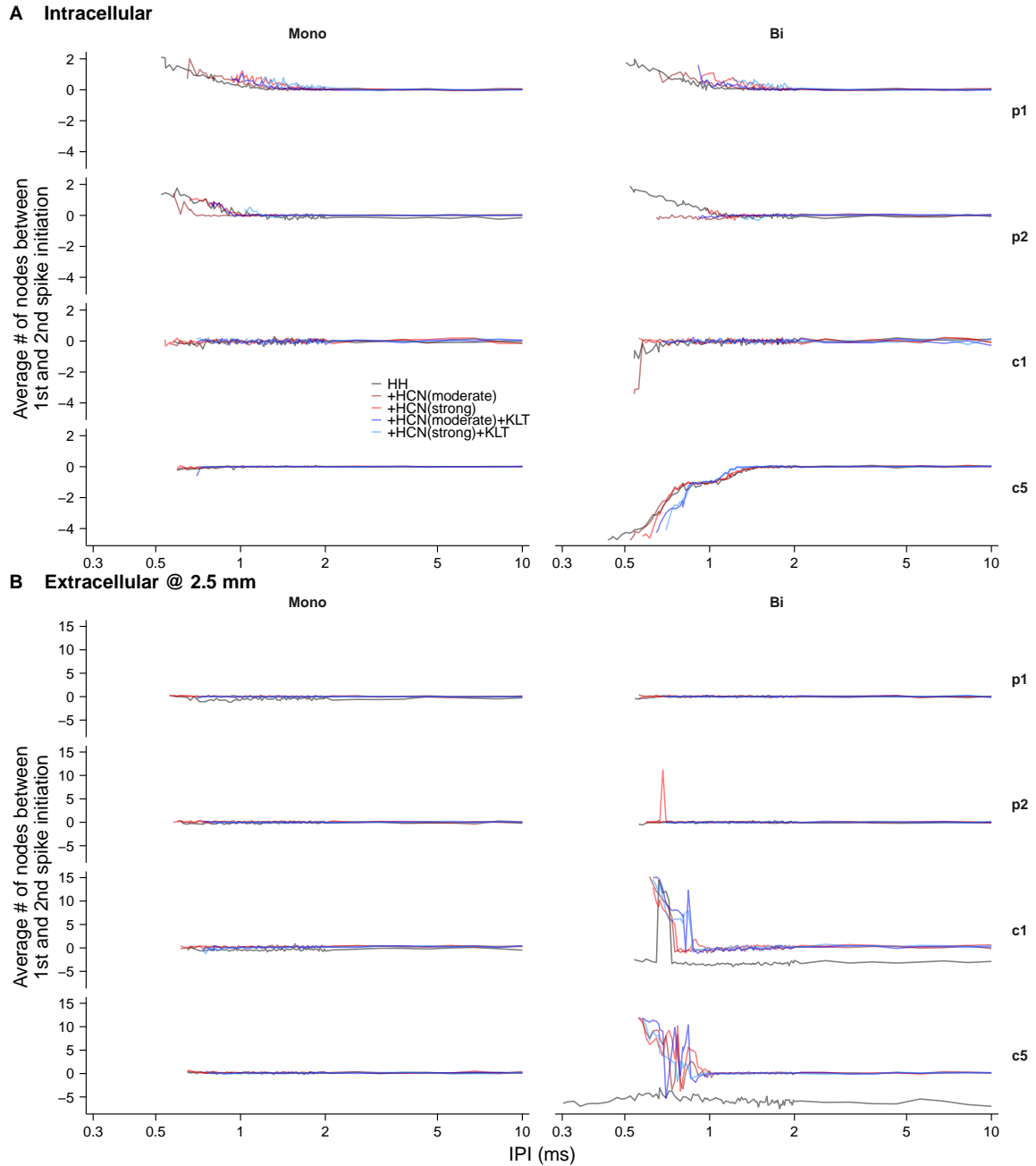


Figure 5.10 Average number of nodes between first and second spike initiation for the refractory paired pulse response shown as *connected lines* as a function of the interpulse interval for each SGN model version (HH, +HCN(moderate), +HCN(strong), +HCN(moderate)+KLT, +HCN(strong)+KLT). The value at each IPI corresponds to the average number of nodes of Ranvier between both spikes near the probe threshold (calculated over 100 trials). Values greater than 0 indicate a relatively central activation, whereas values less than 0 correspond to a relatively peripheral spike initiation. Panels show the response to **A** intracellular stimulation and **B** extracellular stimulation at a distance of 2500 μm . Each panel contains subpanels showing refractory responses to the different sites of stimulation (p1, p2, c1, and c5) as *rows* and the corresponding monophasic and biphasic responses as *columns*.

extracellularly. The difference in ranges of the Δt_{abs} values in response to intracellular and extracellular stimulation may be due to different spike initiation nodes for the first and second spikes.

In Fig. 5.10, we present the average number of nodes between the first and second spike initiation as a function of the IPI near the probe pulse threshold. If the nodal difference between first and second spike initiation is positive, then the second spike was initiated at a more central node than the first spike, otherwise it was initiated more peripherally than the first. Most model versions in response to any type of stimulation appear to have a stable spike initiation node as the IPI increases (the average number of nodes between first and second spike initiation tends to 0 with increasing IPI). The HH model has two exceptions to this when it is extracellularly stimulated with biphasic pulses near nodes c1 and c5, which show an almost constant difference for all IPIs (recall Fig. 5.5). Other cases show stable spike initiation nodes for both spikes across all IPIs or as the IPI increases. Over the relative refractory period, some models and stimulation conditions show a tendency to initiate a second spike that is either more peripheral or more central than the first, which on average returns to the first spike initiation node with increasing IPI. In response to intracellular monophasic and biphasic stimulation near nodes p1 and p2, most models show more central activation for the second spike. In contrast, for biphasic intracellular stimulation at c1 and c5, most models show that the second spike occurs at a node that is more peripheral than the first spike. Biphasic extracellular stimulation at 2500 μm from c5 also shows preferential activation at nodes that are more central than the first spike.

5.3.3 Subthreshold Paired Pulse Response (Facilitation and Accommodation)

By fitting subthreshold conditioner responses to (5.4), we found that over all model versions, sites of stimulation, pulse shapes, stimulation distances, and masker pulse FEs, 75 % of the corresponding R^2 values were greater than 0.916. For responses to extracellular stimulation, we expect a spatially broader subthreshold depolarization. This effect should promote a greater number of nodes to produce facilitation, resulting in more total facilitation. Figure 5.11 shows the paired pulse response to a subthreshold conditioner pulse (FE = 30 %; FE = 10 % and FE = 50 % not shown) in terms of the probe threshold ratio and as a function of the interpulse interval. Values of the threshold ratio that are less than 1 indicate facilitation, otherwise accommodation is present. Since facilitation and short-term accommodation act as opposing forces in this framework (5.4), increases in one phenomena will produce decreases in the other.

Figure 5.11 shows that responses to extracellular stimulation from a distance of 2500 μm exhibit more facilitation than responses to intracellular stimulation, as expected. Responses to biphasic stimulation show less facilitation, as expected since the anodic phase (second phase) of the pulse reduces excitability. Models with HCN channels produce more accommodation than the HH model. Model versions with the HCN(strong) channel produce more

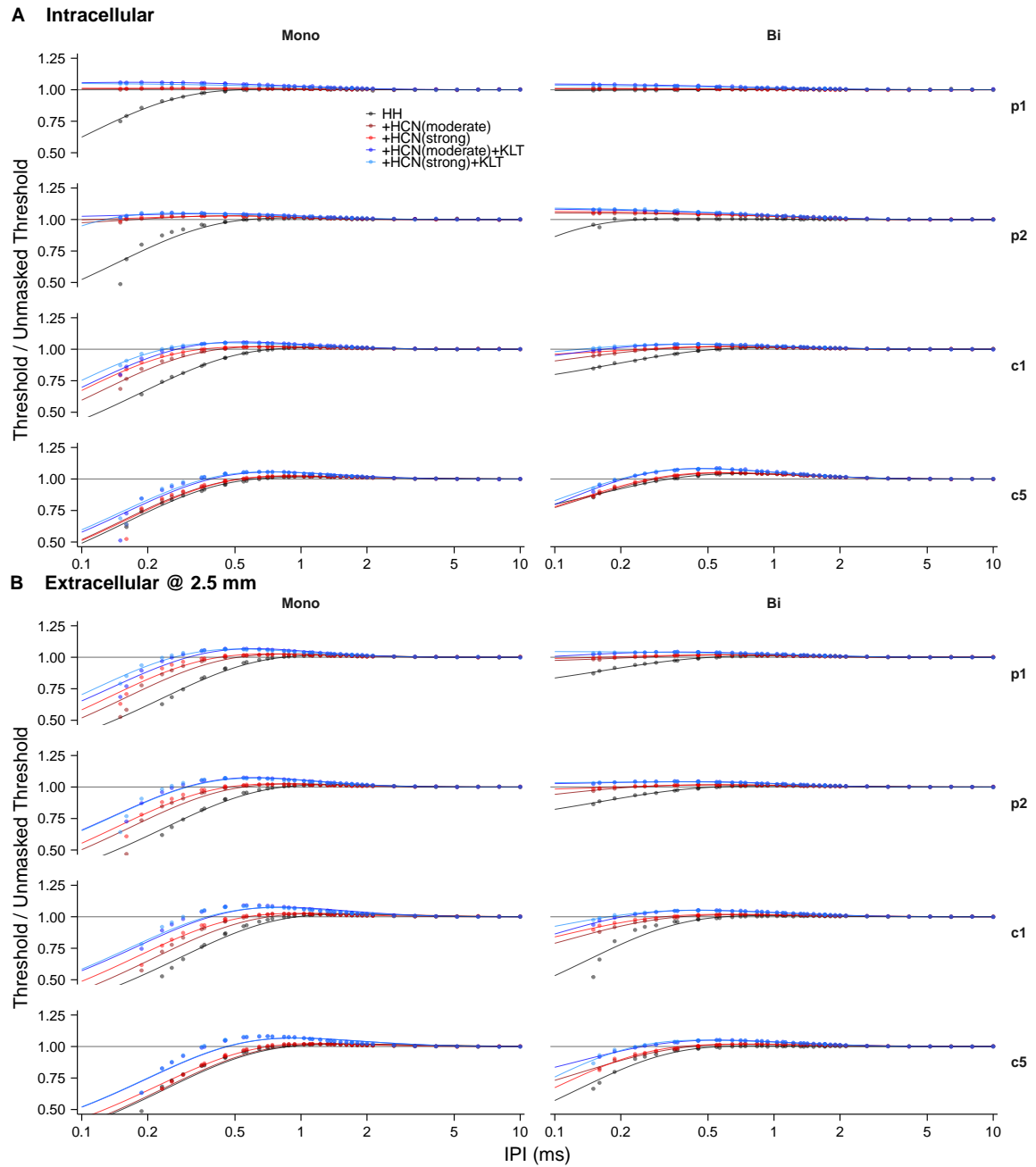


Figure 5.11 Ratio of probe threshold and single pulse threshold (threshold / unmasked threshold), given a masker pulse amplitude equivalent to an FE = 30 %, displayed as *dots* and subthreshold conditioner function shown as *curves* as a function of the interpulse interval for each SGN model version (HH, +HCN(moderate), +HCN(strong), +HCN(moderate)+KLT, +HCN(strong)+KLT). Panels show the response to **A** intracellular stimulation and **B** extracellular stimulation at a distance of 2500 μm . Each panel contains subpanels showing subthreshold conditioner responses to the different sites of stimulation (p1, p2, c1, and c5) as *rows* and the corresponding monophasic and biphasic responses as *columns*.

short-term accommodation than models with the HCN(moderate) channel. KLT channels further increase the level of short-term accommodation. Finally, responses to stimulation that target more central nodes show more facilitation (or less short-term accommodation) since the central nodes (except for c1) do not have HCN channels, which as we have seen, increase the amount of short-term accommodation. In summary, results from Fig. 5.11 are consistent with results from Fig. 3.11 and (see Fig. 3-2 of Dynes, 1996, or Fig. 2.3C and Fig. 3.6A in previous chapters) in that facilitation is present at IPIs less than approximately 0.5 ms and accommodation occurs at IPIs between 0.5 and 1 ms for models with HCN channels or models with HCN and KLT channels.

5.3.4 Pulse Train Response

Over all model versions, sites of stimulation, pulse shapes, stimulation distances, FEs, and stimulation rates, 75 % of the corresponding R^2 values were greater than 0.940 for pulse train responses fitted to (5.5). We only present responses to biphasic stimulation in this section.

Figure 5.12 shows the response rate (or spike rate) of the SGN model versions in response to 300 ms of extracellular biphasic pulse train stimulation at 2500 μm from p1 at the rates of 250, 1000, and 5000 pulses/s. Panels of Fig. 5.12 show the response to the increasing pulse current amplitudes A: FE = 20 %, B: FE = 50 %, and C: FE = 80 %. Similarly to Fig. 4.6, which shows biphasic pulse train responses of single node of Ranvier SGN models containing HCN channels parameterized to produce strong adaptation, response rates in Fig. 5.12 show relatively slow adaptation with continued spiking for the 250 to 1000 pulses/s pulse train, and the 5000 pulses/s responses exhibit a seemingly quicker drop in excitability immediately followed by a steady-state where the SGN effectively ceases to spike. The progressive drop in excitability with increasing pulse rate points to long-term accommodation being the key temporal stimulus-response phenomena. The HH model shows no such reduction of the steady-state response rate as a function of the pulse rate and instead, shows the inverse relationship. This behavior is consistent with Fig. 5.11B, which shows that in response to biphasic extracellular stimulation near p1, the HH model produces facilitation in the range of IPIs from 0.15 ms to approximately 1 ms that translates to pulse rates of within the range of 1000 to 5000 pulses/s.

Next, in Fig. 5.13 and Fig. 5.14 we evaluate the different spatial activation profiles of the SGN models for the final response rate (over the 200 to 300 ms interval). Here, we used the same approach that was introduced for the single pulse response (refer to § 5.2.3) and presented by Figs. 5.5–5.7. Figure 5.13 shows the probability of spiking at spike initiation nodes p1–c6, in response to pulse trains at the FE = 99.99 % current level with the 250, 1000, and 5000 pulses/s rates and the usual sites of stimulation. As with the single pulse response, in the last 100 ms of pulse train stimulation the probability of spike initiation extends to a wider set of nodes for extracellular compared to intracellular stimulation. It is also apparent that models with HCN channels initiate spikes at nodes that are closer to the

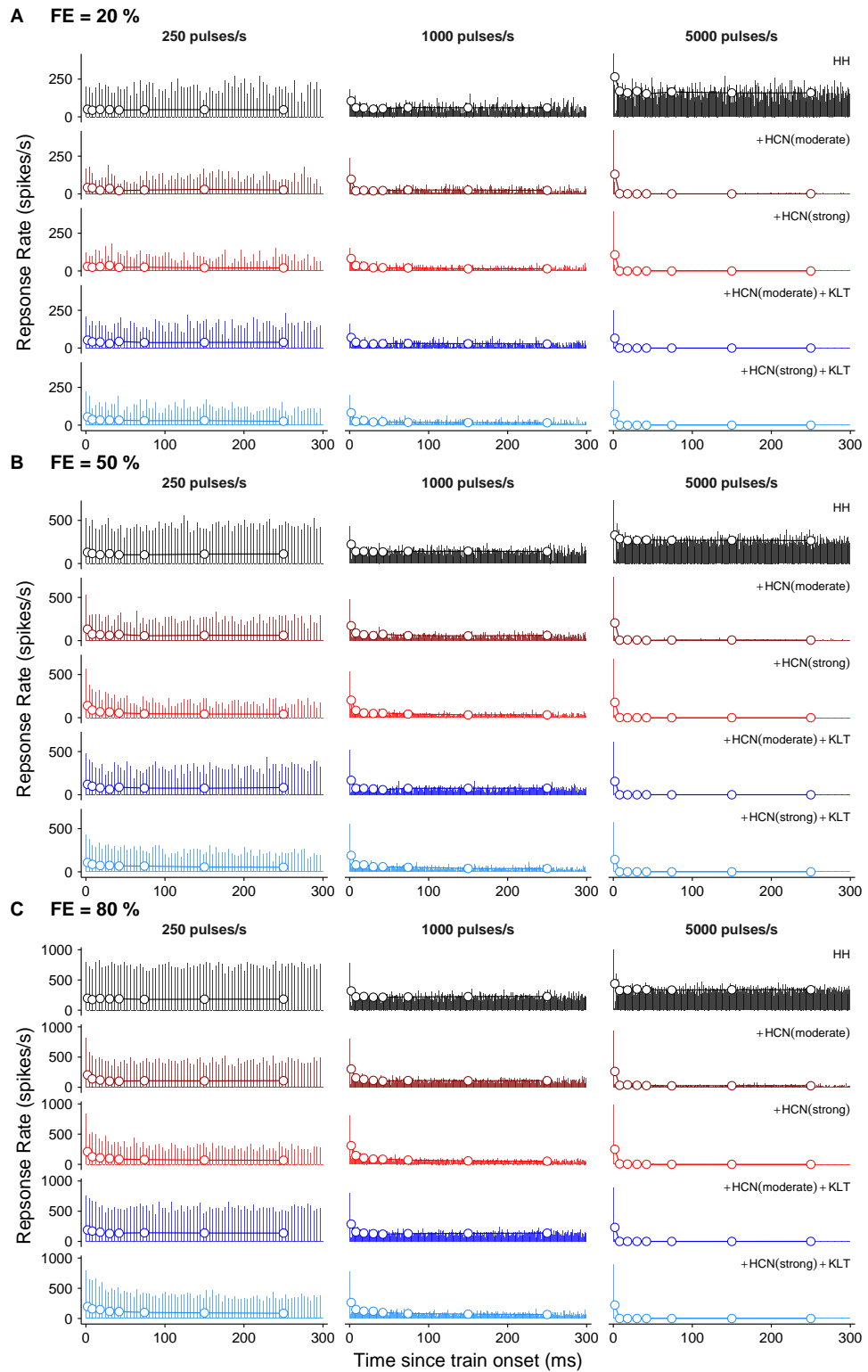


Figure 5.12 Post-stimulus time histograms (PSTHs) in response to 300 ms of ongoing biphasic pulse train stimulation at the rates of 250, 1000, and 5000 pulses/s at site of stimulation p1 and extracellular distance 2500 μm for each SGN model version (HH, +HCN(moderate), +HCN(strong), +HCN(moderate)+KLT, +HCN(strong)+KLT).

Figure 5.12 (continued) The response rate is shown by using two different bin widths. The first, uses time bins of 1 ms shown in *bars* and the second, uses wider bins centered at 2, 8, 18, 30, 42, 74, 150, and 250 ms (Zhang et al., 2007) and is displayed by *open circles, connected by lines*. Panels indicate different current pulse amplitudes **A** FE = 20 %, **B** FE = 50 %, and **C** FE = 80 %.

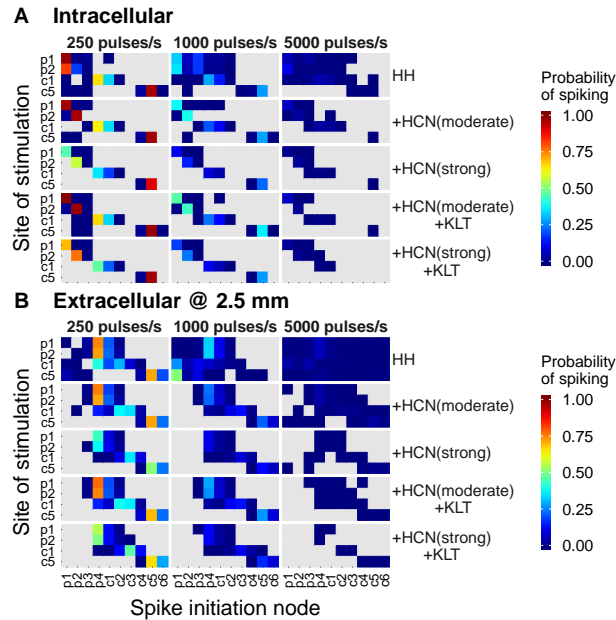


Figure 5.13 Probability of spiking as a function of the spike initiation node (p1–c6 shown) and the site of stimulation (p1, p2, c1, and c5), represented by the colorbar on the right, for each SGN model version (HH, +HCN(moderate), +HCN(strong), +HCN(moderate)+KLT, +HCN(strong)+KLT) in response to the final 100 ms of a 300 ms biphasic pulse train with a current amplitude of FE = 99.99 %. Panels show the response to **A** intracellular stimulation and **B** extracellular stimulation at a distance of 2500 μm . Subpanels show responses to pulse trains at the rates of 250, 1000, and 5000 pulses/s.

site of stimulation, consistent with the single pulse response.

It is difficult to draw any other conclusions from Fig. 5.13, such as the effects of KLT, the strength of the HCN model, or pulse rate on the preferential spike initiation nodes for the SGN model versions. Those queries are settled in Fig. 5.14 by showing Spearman's ρ plotted against the firing efficiency. The spatial spiking correlations in Fig. 5.14 assert the findings summarized in Fig. 5.6 and Fig. 5.7, which reveal that KLT does not have a substantially visible effect on the spatial pattern of spike initiation and that the HCN(strong) channel promotes a stronger spatial correlation than does the HCN(moderate) channel. There is an exception to these observations in Fig. 5.13B where the 5000 pulses/s pulse train condition shows that only the HH and the +HCN(moderate) models respond to a wide range of FEs, due to being the models that produce the lowest amount of adaptation and are therefore still spiking throughout the final 100 ms of stimulation.

Our next analysis is aimed at differentiating between long-term accommodation and spike rate adaptation found in responses to pulse trains. The same procedure was presented

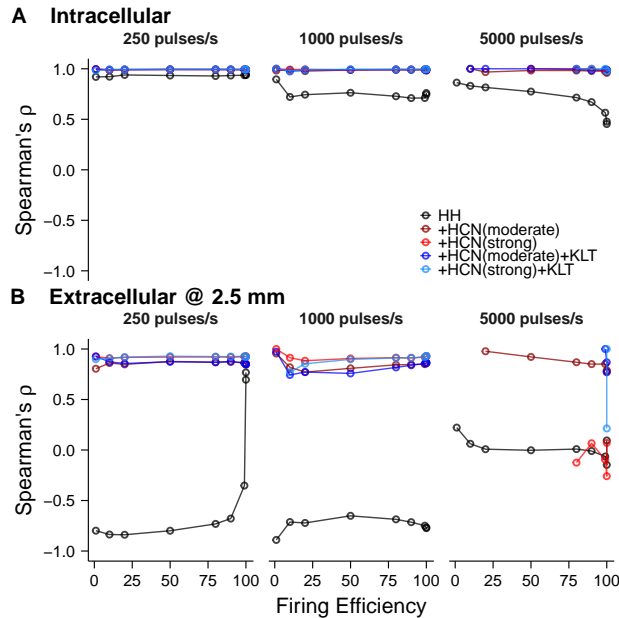


Figure 5.14 Spatial correlation (Spearman's ρ) between site of stimulation and spike initiation node as a function of the pulse train firing efficiency (FE) in response to the final 100 ms of a 300 ms biphasic pulse train for each SGN model version (HH, +HCN(moderate), +HCN(strong), +HCN(moderate)+KLT, +HCN(strong)+KLT). Panels show the response to **A** intracellular stimulation and **B** extracellular stimulation at a distance of 2500 μm . Subpanels show responses to pulse trains at the rates of 250, 1000, and 5000 pulses/s.

in Fig. 4.7D–F where it was found that responses to the single node of Ranvier model with HCN channels produced increasing levels of adaptation, or higher values of NSRD, to pulse train stimulation with increasing pulse rate. Those same SGN models, with HCN channels calibrated to produce strong adaptation, also generated a decrease in NSRD as a function of increasing onset response rate (over the 0 to 12 ms interval). These two relationships, argued for spike rate adaptation being involved with the ongoing reduction in the response rate, but that long-term accommodation would proportionally increase its impact on reducing the spike rate with increases in the rate of pulse train stimulation. Figure 5.15 presents the NSRD versus onset response rate plots of the published data from cats (Zhang et al., 2007) in panel A, followed by our simulation results of the different SGN models in response to intracellular stimulation in panel B and extracellular stimulation in panel C. The responses to intracellular stimulation largely reproduce the behavior exhibited in Fig. 4.7D–F. This suggests the adaptation produced from multicompartmental SGN models with HCN channels responding to intracellular pulse trains (Fig. 5.15B) do not add much more in terms of explaining the NSRD from Zhang et al. (2007) than that which is already explained by the single node of Ranvier models in Chap. 4. However, Fig. 5.15C shows that extracellular stimulation produces a higher proportion of model responses classified as strong adapters (NSRD ≥ 0.75) than responses to intracellular injection. Over all models, the extracellular NSRD versus onset rate responses match more closely with the data from Zhang et al. (2007), which itself was produced by injecting current into the

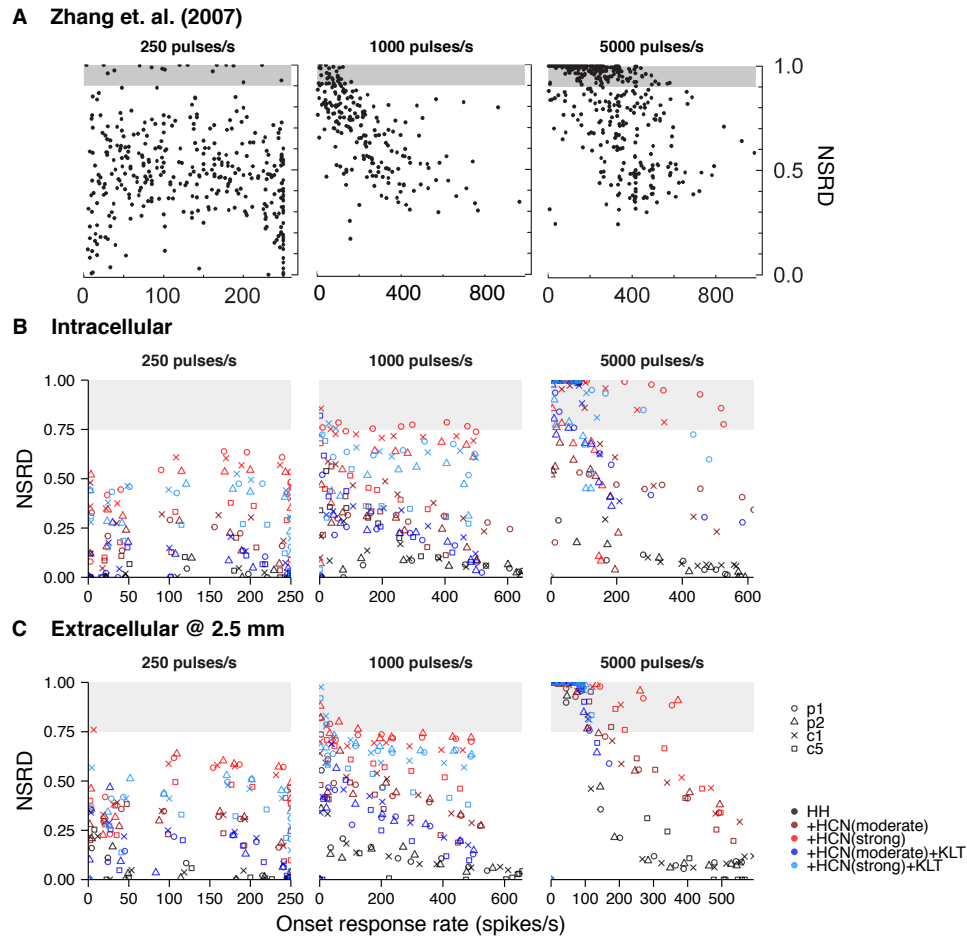


Figure 5.15 Normalized spike rate decrement (NSRD) as a function of the onset response rate (over the 0 to 12 ms interval) in response to biphasic pulse trains of various current amplitudes (1, 10, 20, 50, 80, 90, 99, 99.99, and 99.9999 % FEs; *not labeled*). Subpanels show responses to pulse trains at the rates of 250, 1000, and 5000 pulses/s. Panel **A** shows responses from cat SGNs (Zhang et al., 2007). The two bottom panels (**B**, **C**) show our simulation results for each SGN model version (HH, +HCN(moderate), +HCN(strong), +HCN(moderate)+KLT, +HCN(strong)+KLT) represented by *color* and site of stimulation (p1, p2, c1, and c5) represented by different *symbols*. These panels show the response to **B** intracellular stimulation and **C** extracellular stimulation at a distance of 2500 μm . Panel **A** was adapted with kind permission of Springer Science & Business Media: Fig. 5, panels **B**, **E**, and **G** from Zhang et al. (2007), © 2007.

extracellular space of cat SGNs. This suggests that variability in the spike initiation node could provide a mechanism for finding nodes that are more likely to adapt to pulse train stimulation.

We have maintained that adaptation to pulse trains can occur on the timescales of approximately 10s to 100s of milliseconds (see Chap. 2, or Boulet et al., 2016, and references therein). This is useful for helping to distinguish the relatively immediate effect that refractoriness has on dropping the response rate, beginning from train onset. Figure 5.16 presents estimates of the two adaptation time constants versus the onset response rate and

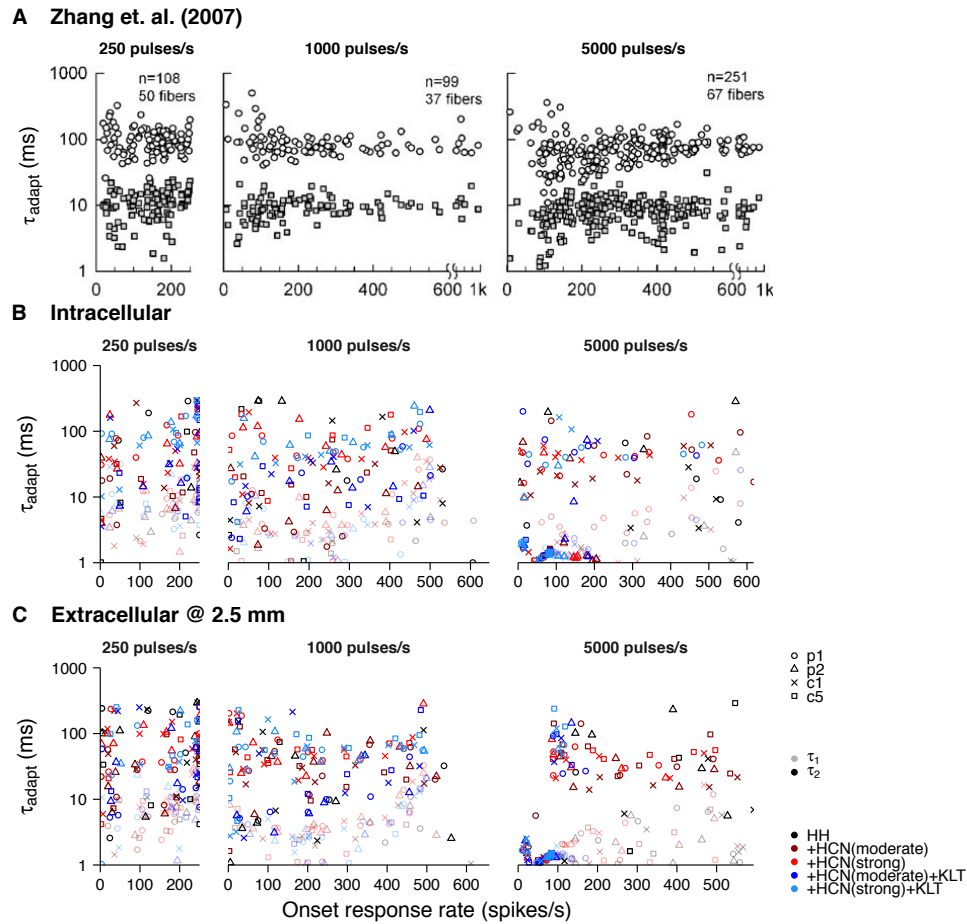


Figure 5.16 Adaptation time constants $\tau_{\text{adapt},1}$ and $\tau_{\text{adapt},2}$ as a function of the onset response rate. (over the 0 to 12 ms interval) in response to biphasic pulse trains of various current amplitudes (1, 10, 20, 50, 80, 90, 99, 99.99, and 99.9999 % FEs, *not labeled*). Subpanels show responses to pulse trains at the rates of 250, 1000, and 5000 pulses/s. Panel **A** shows responses from cat SGNs (Zhang et al., 2007). The two bottom panels (**B**, **C**) show our simulation results for each SGN model version (HH, +HCN(moderate), +HCN(strong), +HCN(moderate)+KLT, +HCN(strong)+KLT) represented by *color* and site of stimulation (p1, p2, c1, and c5) represented by different *symbols*. Time constants are represented by two different *shades*: $\tau_{\text{adapt},1}$ (*light*) and $\tau_{\text{adapt},2}$ (*dark*). These panels show the response to **B** intracellular stimulation and **C** extracellular stimulation at a distance of 2500 μm . Panel **A** was adapted with kind permission of Springer Science & Business Media: Fig. 7, top panels from Zhang et al. (2007), © 2007.

is organized similarly to Figure 5.15 in that data from Zhang et al. (2007) is presented in panel A whereas results from our simulations of our SGN models are shown in panels B and C in response to intracellular stimulation and extracellular stimulation, respectively. The time constants were extracted by fitting the wide-binned response rates to (5.5). The shortest of the two time constants $\tau_{\text{adapt},1}$ is presented by symbols with a lighter shade of the same color that also represents the longer time constant $\tau_{\text{adapt},2}$. The short and long time constants produced by simulations of the SGN models do not appear to cluster as tightly into two groups as the data shown from Zhang et al. (2007) in Fig. 5.16A, although

the extracellular simulations may exhibit some more signs of clustering compared to the intracellular simulations. However, most SGN models with HCN or KLT channels, or both, do in fact produce adaptation on the order of 10 to 100 ms in response to all FEs, pulse rates, and sites of stimulation. There are notable exceptions where the longest time constants are approximately 1 ms in response to the 5000 pulses/s. The majority of these are produced with SGN models containing KLT channels. These models are the same ones that are very strong adapters (see *blue and light blue symbols* in the 5000 pulses/s subpanels of Fig. 5.15B–C). Relatively fewer time constants are shown for the HH model (*black symbols*) since the ones that are not visible are less than 1 ms. This suggests that the reduction in excitability produced by the HH model are largely governed by process that are not spike rate adaptation or long-term accommodation.

5.3.5 Masker-Probe Train Response

In Fig. 5.17 we present simulation results of a stimulus-response paradigm introduced by Miller et al. (2011) which can be described by one of two cases. Common to both stimulation types are a probe train delivered at a rate of 100 pulses/s with a current level of FE = 50 %. All simulation results presented in this section were in response to biphasic stimulation only. What distinguishes both cases is that in one, a masker train is delivered to the SGN (*darker shade*) prior to the probe train, in contrast to no masker train (*lighter shade*), of no current injection for the same 300 ms duration. This approach allows for investigating the effects of recovery from adaptation. The results from Fig. 4.9 show that the stronger the adaptation is in response to the masker train produced by HCN channels, the longer the probe recovery time will be, thus lowering the total recovery in terms of the number of spikes generated in response to the probe train. Figure 5.17 shows spike rates in response to biphasic extracellular stimulation near node p1 delivered with a 5000 pulses/s masker train stimulation for the different FEs shown in panels A–D. The recovery shown in Fig. 5.17 is in agreement with that presented in Fig. 4.9 where models with HCN have the greatest effect on reducing the recovery from adaptation in response to relatively low and high masker train current levels. Combined with the subthreshold paired pulse response (from Fig. 5.11) and pulse train response, this result reinforces the idea that KLT is not active in reducing SGN excitability on the timescale of 10s to 100s of milliseconds, but rather on the order of 1 ms.

We summarize the recovery from adaptation in Fig. 5.18 with the probe response recovery ratio (PRRR) versus the mean response rate to the masker train. The PRRR is defined as the ratio of the number of spikes in response to the unmasked probe train to the masked probe train. Figure 5.18A shows responses from cat SGNs (Miller et al., 2011), panel B shows the simulation results of the different SGN models in response to biphasic intracellular stimulation, whereas panel C presents the corresponding responses to extracellular stimulation at a distance of 2500 μm . The trend that the PRRR decreases with the mean response to the masker train is consistent with those found by Miller et al.

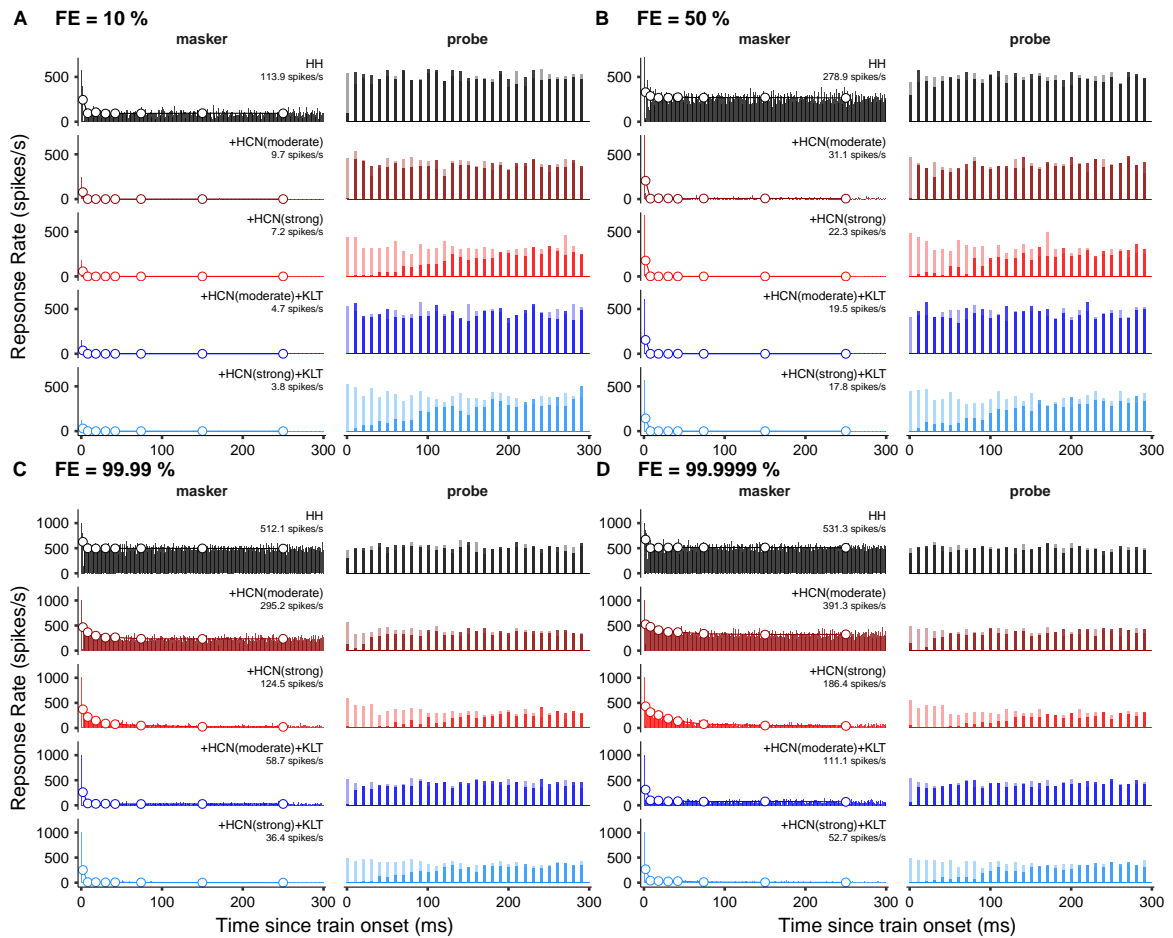


Figure 5.17 Post-stimulus time histograms (PSTHs) in response to 300 ms of ongoing 5000 pulses/s biphasic masker train stimulation followed by 300 ms of ongoing 100 pulses/s, FE = 50 % biphasic probe train stimulation at site of stimulation p1 and extracellular distance 2500 μm for each SGN model version (HH, +HCN(moderate), +HCN(strong), +HCN(moderate)+KLT, +HCN(strong)+KLT). Cases in which no masker train stimulated the model SGNs are shown *shaded as a lighter color*. The masker train response rate is shown by using two different bin widths. The first, uses time bins of 1 ms shown in *bars* and the second, uses wider bins centered at 2, 8, 18, 30, 42, 74, 150, and 250 ms (Zhang et al., 2007) and is displayed by *open circles, connected by lines*. Panels indicate different probe pulse current amplitudes **A** FE = 10 %, **B** FE = 50 %, **C** FE = 99.99 %, and **D** FE = 99.9999 %.

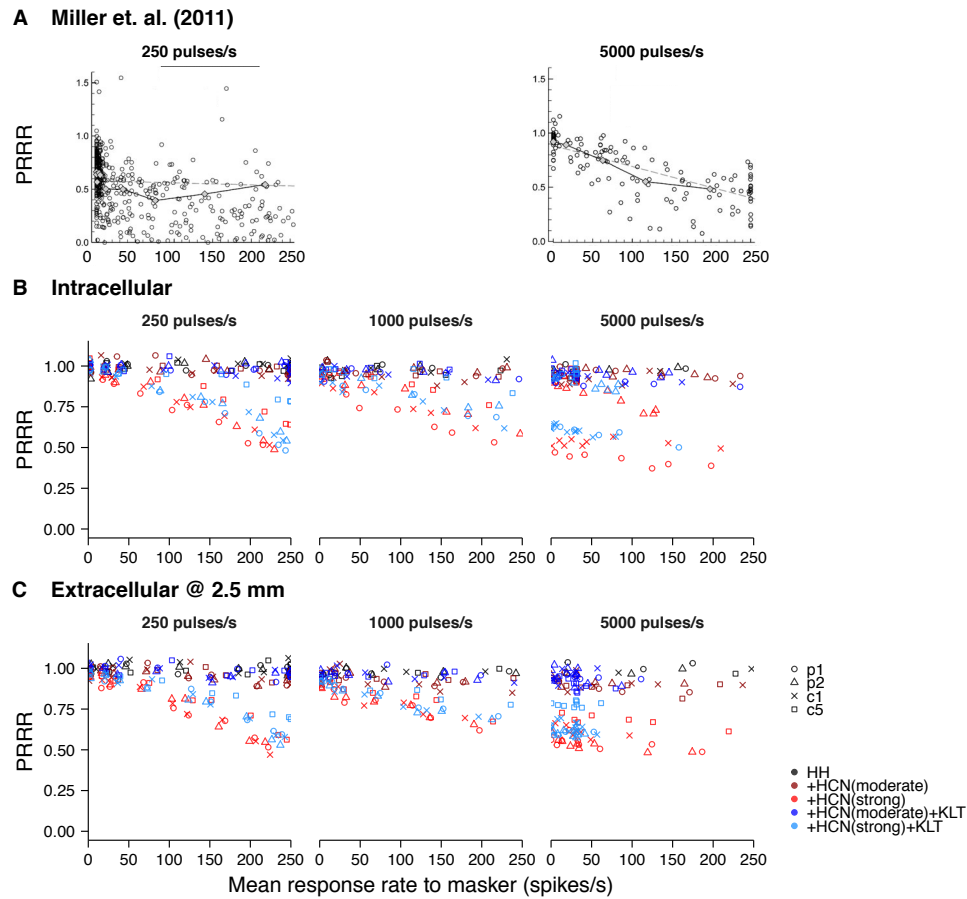


Figure 5.18 Probe response recovery ratio (PRRR) as a function of the mean response rate to the masker train (over the 0 to 300 ms interval) in response to biphasic masker pulse trains of various current amplitudes (1, 10, 20, 50, 80, 90, 99, 99.99, and 99.9999 % FEs; *not labeled*). Subpanels show the PRRR in response to masker trains at the rates of 250, 1000, and 5000 pulses/s. Panel **A** shows responses from cat SGNs (Miller et al., 2011), where the 1000 pulses/s was not reported. The two bottom panels (**B**, **C**) show our simulation results for each SGN model version (HH, +HCN(moderate), +HCN(strong), +HCN(moderate)+KLT, +HCN(strong)+KLT) represented by *color* and site of stimulation (p1, p2, c1, and c5) represented by different *symbols*. These panels show the response to **B** intracellular stimulation and **C** extracellular stimulation at a distance of 2500 μm . Panel **A** was adapted with kind permission of Springer Science & Business Media: Fig. 3, panels **D** and **E** from Miller et al. (2011), © 2011.

(2011). However, the variability in our simulation results of the PRRR spans just below 0.5 up to 1, whereas the data in Fig. 5.18A extends from 0 to beyond 1. Also, the effect of the different model versions observed in Fig. 5.17 generalizes to the different stimulus parameters (intracellular versus extracellular stimulation, site of stimulation, pulse rate, and FE). Models containing HCN channels that are parameterized to give stronger adaptation than HCN(strong) may produce lower values of PRRR.

5.4 Discussion

Using a multicompartmental model of an entire SGN introduces substantial differences in terms of the responses to either intracellular or extracellular stimulation compared to a single node model. For any given site of stimulation, there is variability in the spike initiation node—more so for extracellular stimulation than for intracellular stimulation. The single pulse results confirm this and also predict differences in threshold and RS based on the site of stimulation.

Spikes in response to a probe pulse following a masker pulse that initiates a spike are always caught in the wake of that first propagated action potential. Therefore the probe responses that are essentially trapped in the absolute and relative refractory period are not just a function of the local channel kinetics, but also of those at nodes in the neighborhood (for a general review see Bucher and Goaillard, 2011, and references therein). In order to bypass a local node that is in a state of absolute refractoriness, the SGN may initiate a second spike at another more distant node that is in a relative refractory state. If not, it risks initiating a second spike that fails to propagate to the end of the neuron. Assuming uniform neural structures, a different second spike initiation node from the first is not possible (although this can still occur in a model with stochastic channel kinetics) since more distant nodes would only enter relative refractoriness at a later time than the node that initiated the spike in response to the first pulse. However, changes in diameter along the length of the SGN (refer to Table 5.2) translates to node-by-node differences in ionic conductances, leading to changes in action potential shapes, and therefore refractory properties vary along the SGN. Further, differently distributed channel types such as HCN and KLT channels may give SGNs more scope to engage in recruiting different nodes for action potential initiation than only near the first spike. Figures 5.8 and 5.10 show that different sites of stimulation, stimulation phases, and whether the pulses are injected intracellularly or extracellularly, can promote either relatively more peripheral or central activation in response the second pulse. Intracellular injection at the peripheral nodes lead to a higher probability of initiating second spikes more centrally than the first. This does the SGN model no favors in terms of reducing the absolute refractory period, at least in response to stimulation at sites near p1 and p2. In contrast, biphasic extracellular stimulation at sites close to nodes c1 and c5 results in causing the second spike to initiate at relatively more peripheral nodes more often than not. Of course, in both cases the stability of the second spike initiation node returns to normal once relative refractoriness has ended (see Fig. 5.10).

From our analysis, it is difficult to conclude which nodes are influencing the excitability of the probe pulse response in the case of a subthreshold masker, since the response to the masker pulse always results in no spike. As expected, more facilitation was observed across all models in response to extracellular stimulation. There are clearly greater levels of short-term accommodation in response to biphasic stimulation as well as for models with the HCN(strong) and KLT channels. Still, KLT has a relatively stronger short-term accommodation effect, compared to HCN, as seen in the paired pulse paradigm. Interestingly, the HH model produced accommodation in the approximate range of IPIs from 0.3 ms out

to 2 ms in response to biphasic intracellular stimulation near c5. This accommodation may be caused by sodium inactivation, which was the case in frog nerves in response to slow ramp pulses (Frankenhaeuser and Vallbo, 1965).

Determining the precise spatio-temporal relationship for spiking responses to pulse trains in SGNs is substantially more challenging than for refractory responses to paired pulse stimulation. The reasoning is that the initial conditions for the next spike are constantly changing based on the suprathreshold stimulus-response effects such as spike time and spatial history (cumulative), various subthreshold effects including different ion channel states across all nodes of Ranvier, and changes to the membrane potential across the SGN. Despite these highly nonlinear stimulus-response features, the spike initiation node profile (see Fig. 5.13) for the steady-state responses (over the 200–300 ms pulse train interval) mirrors the single pulse response case (refer to Fig. 5.5) in terms of the different SGN models, site of stimulation, stimulation phase, and intracellular versus extracellular stimulation. However, as the pulse rate increases, the spatial spiking distribution widens to include more initiation nodes. These extra degrees of freedom are therefore increasingly utilized in order to overcome restrictions brought about by the abundance of temporal interactions (refractoriness) as a function of the pulse rate. As a corollary, responses to the 5000 pulses/s probe train are likely to show less spike initiation node variability than the 250 pulses/s pulse train response. This helps predict how the probe response recovery ratio (PRRR) of the multicompartmental model in response to intracellular and extracellular stimulation (Fig. 5.18B–C) is very similar to the single node response (refer to Fig. 4.10B–C). In summary, spiking responses to trains delivered at low pulse rates do not initiate at relatively more distant nodes. Just as we reported in Chap. 4, stronger adaptation was observed in models that initiated spikes at nodes with HCN channels. Responses to pulse trains delivered at the sites of stimulation p1 and c1 for models +HCN(moderate), +HCN(strong), +HCN(moderate)+KLT +HCN(strong)+KLT exhibited higher NSRD values.

5.5 Conclusions and Future Directions

Developing more effective methods by which cochlear implants can deliver electrical stimulation to spiral ganglion neurons is important for a multitude of reasons. The main goal is to accurately mimic the rich complexity of temporal information being transmitted through the inner hair cell-SGN synapse in a healthy system. However, CIs are limited by the poor spatial resolution of the electrode-neuron interface. To gain a better wholistic understanding of this, future work should focus on integrating our SGN models containing HCN and KLT channels with other aspects of the CI-SGN geometry such as the cochlear geometry (Frijns et al., 2000) and multiple electrodes (electrode array), as well as multipolar electrodes. Another limitation of our study is that we only observed responses of full SGN models, thus not capturing the effects of SGN pathologies that require CI implantation. Several animal studies show that following inner hair cell loss there is progressive degeneration of the SGN

beginning at the afferent terminal or the peripheral end of the SGN (see § 3.2 of Zeng et al., 2004, and references therein). Still, our results show definite implications for deafferented SGNs since c1 may be part of the neuron that remains in tact. Given degeneration of the peripheral process, and that SGN models with HCN channels show that c1 is a robust spike initiation node, c1 may be the primary spike initiation node. Given this, spikes initiated at c1 can expect to produce responses with high temporal precision (refractoriness), and varied strengths of spike rate adaptation and accommodation, depending on the mixture of HCN subunits at that node (recall Chap. 4), which dictate how strongly the responses adapt. Whereas the extent of our spatio-temporal analysis of the SGN focused on the spike initiation node, future work would benefit from determining the spatio-temporal relationships between channel activity and the membrane responses.

5.6 Appendix

5.6.1 Multicompartmental SGN Model

The membrane capacitance C_m^k , membrane resistance R_m^k , and ion channel number $N_m^{\max,k}$ (where m is the ion channel species) for the nodes are functions of the surface area A^k of the cylindrical compartment, given by the following

$$C_m^k = A^k C_m \quad (5.6)$$

$$R_m^k = \frac{R_m}{A^k} \quad (5.7)$$

$$N_m^{\max,k} = \text{nint} \left(A^k \rho_m^k \right) \quad (5.8)$$

$$(5.9)$$

where k denotes the compartment and Δx^k is its length, ρ_m^k is the ion channel density, and $\text{nint}()$ refers to the nearest integer. The unmyelinated compartments, which include the internodal and somatic compartments, have their own capacitance and resistance values (Woo et al., 2010) and with cylindrical symmetry, they are computed by

$$C_m^k = \frac{2\pi \varepsilon_0 \varepsilon_r \Delta x^k}{\ln(D^k/d^k)} \quad (5.10)$$

$$R_m^k = \frac{\rho_m (D^k - d^k)}{2\pi d^k \Delta x^k} \quad (5.11)$$

where d^k is the diameter of the node or soma, D^k is the outer diameter of the myelin. The

compartmental axial resistance R_a^k for a cylindrical compartment is

$$R_a^k = \frac{4r_a \Delta x^k}{\pi(d^k)^2} \quad (5.12)$$

where r_a is the axial resistivity. Then the inter-compartmental axial resistance $R_a^{k,k+1}$ is the axial resistance between adjacent compartments k and $k + 1$. Therefore, it is computed by

$$R_a^{k,k+1} = \frac{1}{2} (R_a^k + R_a^{k+1}). \quad (5.13)$$

For a complete information on these parameters, refer to Table 5.1 and Table 5.2.

5.6.2 Transmembrane Potential

In order to model the propagation of action potentials along the SGN, we solved the biophysical cable equation using the time-staggered Crank–Nicolson scheme (§ 4.2.3.1 of Carnevale and Hines, 2010) and (§ 14.3.6 of Mascagni and Sherman, 1998). We applied second order accurate sealed-end boundary conditions (Niebur and Niebur, 1991), which essentially states that the ends of the neuron have infinite axial resistance and there is no change in the membrane potential. The transmembrane potential $V_{m,j+1/2}^k$ at compartment k and mid point time $j + 1/2$ (half-way between time j and $j + 1$) for the cable equation is given by

$$\begin{aligned} & - \left(\frac{V_{m,j+1/2}^{k+1} - V_{m,j+1/2}^k}{R_a^{k,k+1}} - \frac{V_{m,j+1/2}^k - V_{m,j+1/2}^{k-1}}{R_a^{k-1,k}} \right) \\ & + C_m^k \frac{V_{m,j+1/2}^k - V_{m,j}^k}{\Delta t/2} + \frac{V_{m,j+1/2}^k - E_{\text{leak}}^k}{R_m^k} + I_{\text{ion},j+1/2}^k \\ & = \frac{V_{\text{ex},j+1}^{k+1} - V_{\text{ex},j+1/2}^k}{R_a^{k,k+1}} - \frac{V_{\text{ex},j+1/2}^k - V_{\text{ex},j+1/2}^{k-1}}{R_a^{k-1,k}} + I_{\text{in},j+1/2}^{k=n_{\text{stim}}} \end{aligned} \quad (5.14)$$

where $V_{\text{ex},j+1/2}^k$ is the extracellular potential at compartment k and time $j + 1/2$, and $I_{\text{in},j+1/2}^{k=n_{\text{stim}}}$ is the intracellular injected current at nodal compartment n_{stim} and time $j + 1/2$.

First, we solve (5.14) for the spatial component of $V_{m,j+1/2}^k$ for all compartments $k \in [1, K]$, where K is the number of compartments, using the tridiagonal matrix algorithm (see § 2.4 of Press et al., 2007). Next we advance the solution of (5.14) in time by two separate steps. The first step is to update the system to the mid-point time by solving the backward Euler scheme. The number of channels in the open, or conducting state $N_{m,j+1/2}^k$ is updated by the channel number tracking algorithm (Chow and White, 1996; Gillespie, 1977; Mino

Table 5.1 Multicompartmental model parameters (Woo et al., 2010) for compartment k . All of the listed units are self consistent for simulation of the cable equation (5.14) with μA , mV , and ms .

Parameter	Symbol	Value	Units	Compartment k
<i>Node of Ranvier</i>				
Nodal diameter	d^k	1.2	μm	p1–p4
		2.3	μm	c1–c23
Nodal length	Δx^k	1	μm	all, except p1
		10	μm	p1
<i>Internode</i>				
Unmyelinated fiber maximum diameter	d_{soma}	19.45	μm	soma
Myelinated outer fiber diameter	D^k	$d + 1$	μm	p1–c22, soma
Internodal length	Δx^k	150	μm	p1–p3, c1
		200	μm	c2
		250	μm	c3
		300	μm	c4
		350	μm	c5–c22
Permittivity of free space	ϵ_0	8.854×10^{-12}	$\mu\text{F } \mu\text{m}^{-1}$	soma
Myelin dielectric constant	ϵ_r	1.27	–	all
Internodal resistivity	ρ_m	29.26×10^9	$\text{k}\Omega \mu\text{m}$	all
<i>Intracellular</i>				
Axial resistivity	r_a	6.378×10^3	$\text{k}\Omega \mu\text{m}$	all
<i>Extracellular</i>				
Extracellular resistivity	ρ_{ex}	3×10^3	$\text{k}\Omega \mu\text{m}$	all

Table 5.2 SGN node of Ranvier ion channel densities (μm^{-2}). Channel numbers are obtained by multiplying channel densities by nodal surface area (see (5.8)). All models refers to HH, +HCN, and +HCN+KLT.

Channel m	Model	Node n	Density ρ_m^k	Reference
Na_v	all	all, except p1, p4, c1	80.0	Woo et al. (2010)
	all	p1, p4, c1	1.5×80.0	Woo et al. (2010), Hossain et al. (2005)
K_v	all	all, except p1, p4, c1	45.0	Woo et al. (2010)
	all	p1, p4, c1	1.5×45.0	Woo et al. (2010), Hossain et al. (2005)
KLT	HH, +HCN	all	0.0	Hodgkin and Huxley (1952)
	+HCN+KLT	all	10.0	Bortone et al. (2006)
HCN	HH	all	0.0	Hodgkin and Huxley (1952)
	+HCN, +HCN+KLT	p1, p4, c1	10.0	Yi et al. (2010)

et al., 2002) for each channel type, on the time-staggered grid from time $j - 1/2$ to $j + 1/2$ at the relative transmembrane potential ($V_j^k = V_{m,j}^k - V_{\text{rest}}$). Then, the ionic current $I_{\text{ion},j+1/2}^k$ is computed by

$$I_{\text{ion},j+1/2}^k = \begin{cases} \sum_m \gamma_m N_{m,j+1/2}^k (V_{m,j+1/2}^k - E_m) & \text{if } k \text{ is a node } n \\ 0 & \text{otherwise} \end{cases} \quad (5.15)$$

where m refers to the open or conducting states (m_3h_1 , n_4 , w_4z_1 , q_2 , and s_1) of the corresponding the ion channel types Na, K, KLT, and both quick and slow HCN components, h_q and h_s , at node k . Next, the extracellular potential $V_{\text{ex},j+1/2}^k$ is calculated by applying the known injected current into a saline solution with constant resistivity ρ_{ex}

$$V_{\text{ex},j+1/2}^k = \frac{\rho_{\text{ex}}}{4\pi z_d^k} I_{\text{ex},j+1/2}^{k=n_{\text{stim}}} \quad (5.16)$$

at an electrode-to-neuron distance z_d^k from neuronal compartment k . Once (5.14) has been solved, the transmembrane potential is now known at the mid-point, then the second step is to advance the system in time by another $\Delta t/2$ using the relationship between the backward Euler and Crank–Nicolson schemes (Carnevale and Hines, 2010) given by

$$V_{m,j+1}^k = 2V_{m,j+1/2}^k - V_{m,j}^k. \quad (5.17)$$

5.6.3 Ionic Currents and Channel Distribution

Current generated by the voltage-gated ion channels are given by the following set of equations.

$$I_{\text{Na},j}^k = \gamma_{\text{Na}} N_{m_3h_1,j}^k (V_{m,j}^k - E_{\text{Na}}) \quad (5.18)$$

$$I_{\text{K},j}^k = \gamma_{\text{K}} N_{n_4,j}^k (V_{m,j}^k - E_{\text{K}}) \quad (5.19)$$

$$I_{\text{KLT},j}^k = \gamma_{\text{KLT}} N_{w_4z_1,j}^k (V_{m,j}^k - E_{\text{KLT}}) \quad (5.20)$$

$$I_{h_q,j}^k = \gamma_h N_{q_2,j}^k (V_{m,j}^k - E_h) \quad (5.21)$$

$$I_{h_s,j}^k = \gamma_h N_{s_1,j}^k (V_{m,j}^k - E_h) \quad (5.22)$$

The leakage current in terms of the absolute transmembrane potential $V_{m,j}^k$ at time j is given by

$$I_{\text{leak},j}^k = g_{\text{leak}}^k [V_{m,j}^k - (E_{\text{leak}}^k - V_{\text{rest}})] \quad (5.23)$$

where $g_{\text{leak}}^k = 1/R_m^k$. The leakage current is set-up in a way such that the leakage potential, E_{leak}^k , is specified to preserve a constant transmembrane resting potential (Negm, 2008; Negm and Bruce, 2008, 2014) given by

$$E_{\text{leak}}^k = R_m \left[V_{\text{rest}} \left(g_{\text{Na},\infty}^k + g_{\text{K},\infty}^k + g_{\text{KLT},\infty}^k + g_{\text{h}_q,\infty}^k + g_{\text{h}_s,\infty}^k + g_{\text{leak}}^k \right) - \left(g_{\text{Na},\infty}^k E_{\text{Na}} + g_{\text{K},\infty}^k E_{\text{K}} + g_{\text{KLT},\infty}^k E_{\text{KLT}} + g_{\text{h}_q,\infty}^k E_{\text{h}} + g_{\text{h}_s,\infty}^k E_{\text{h}} \right) \right] \quad (5.24)$$

where the steady-state conductances are given by

$$g_{\text{Na},\infty}^k = \gamma_{\text{Na}} N_{\text{Na}}^{\text{max},k} m_{\infty}^3 h_{\infty} \quad (5.25)$$

$$g_{\text{K},\infty}^k = \gamma_{\text{K}} N_{\text{K}}^{\text{max},k} n_{\infty}^4 \quad (5.26)$$

$$g_{\text{KLT},\infty}^k = \gamma_{\text{KLT}} N_{\text{KLT}}^{\text{max},k} w_{\infty}^4 z_{\infty} \quad (5.27)$$

$$g_{\text{h}_q,\infty}^k = \gamma_{\text{h}} N_{\text{h}_q}^{\text{max},k} q_{\infty}^2 \quad (5.28)$$

$$g_{\text{h}_s,\infty}^k = \gamma_{\text{h}} N_{\text{h}_s}^{\text{max},k} s_{\infty} \quad (5.29)$$

$$(5.30)$$

and we evaluate the steady-state of the channel particles at the resting relative membrane potential $x_{\infty}(V^k = 0 \text{ mV})$.

Table 5.3 SGN node of Ranvier parameters. All of the listed units are self consistent for simulation of (5.14) with μA , mV , and ms .

Parameter	Symbol	Quantity	Reference
Specific nodal resistance	R_m	$166.2 \times 10^6 \text{ k}\Omega \mu\text{m}^2$	Woo et al. (2010)
Specific nodal capacitance	C_m	$0.5125 \times 10^{-9} \mu\text{F} \mu\text{m}^{-2}$	Woo et al. (2010)
Na reversal potential	E_{Na}	66 mV	Mino et al. (2002)
K reversal potential	E_{K}	-88 mV	Mino et al. (2002)
HCN(q,s) reversal potential	E_{h}	-41 mV	Liu et al. (2014)
Resting membrane potential	V_{rest}	-78 mV	Mino et al. (2002)
Na_v channel conductance	γ_{Na}	25.69 pS	Mino et al. (2002)
K_v channel conductance	γ_{K}	50.0 pS	Mino et al. (2004)
KLT channel conductance	γ_{KLT}	13.0 pS	Negm and Bruce (2014)
HCN channel conductance	γ_{h}	13.0 pS	Negm and Bruce (2014)
KLT thermal coefficient	$Q_{10,\text{KLT}}$	3.0	Negm and Bruce (2014)
HCN thermal coefficient	$Q_{10,\text{h}}$	3.3	Negm and Bruce (2014)

References

- Bortone, D. S., Mitchell, K., and Manis, P. B. (2006). Developmental time course of potassium channel expression in the rat cochlear nucleus. *Hear Res*, 211(1-2):114–125.
- Boulet, J., White, M. W., and Bruce, I. C. (2016). Temporal considerations for stimulating spiral ganglion neurons with cochlear implants. *J Assoc Res Otolaryngol*, 17(1):1–17.
- Bucher, D. and Goaillard, J.-M. (2011). Beyond faithful conduction: short-term dynamics, neuromodulation, and long-term regulation of spike propagation in the axon. *Prog. Neurobiol.*, 94(4):307–346.
- Cao, X. J. and Oertel, D. (2011). The magnitudes of hyperpolarization-activated and low-voltage-activated potassium currents co-vary in neurons of the ventral cochlear nucleus. *J Neurophysiol*, 106(2):630–640.
- Carnevale, N. T. and Hines, M. L. (2010). *The NEURON Book*. Cambridge University Press, Cambridge.
- Cartee, L. A. (2000). Evaluation of a model of the cochlear neural membrane. II: comparison of model and physiological measures of membrane properties measured in response to intrameatal electrical stimulation. *Hear Res*, 146(1-2):153–166.
- Cartee, L. A., van den Honert, C., Finley, C. C., and Miller, R. L. (2000). Evaluation of a model of the cochlear neural membrane. I. physiological measurement of membrane characteristics in response to intrameatal electrical stimulation. *Hear Res*, 146(1-2):143–152.
- Chow, C. C. and White, J. A. (1996). Spontaneous action potentials due to channel fluctuations. *Biophys J*, 71(6):3013–3021.
- Dynes, S. B. C. (1996). *Discharge characteristics of auditory nerve fibers for pulsatile electrical stimuli*. PhD thesis, Massachusetts Institute of Technology, Cambridge, Massachusetts.
- Frankenhaeuser, B. and Vallbo, A. B. (1965). Accommodation in myelinated nerve fibres of *Xenopus laevis* as computed on the basis of voltage clamp data. *Acta Physiol. Scand.*, 63(1-2):1–20.
- Frijns, J. H. M., Briaire, J. J., and Schoonhoven, R. (2000). Integrated use of volume conduction and neural models to simulate the response to cochlear implants. *Simulation Practice and Theory*, 8(1-2):75–97.
- Gillespie, D. T. (1977). Exact stochastic simulation of coupled chemical reactions. *J. Phys. Chem.*, 81(25):2340–2361.

- Gorman, P. H. and Mortimer, J. T. (1983). The effect of stimulus parameters on the recruitment characteristics of direct nerve stimulation. *IEEE Trans Biomed Eng*, 30(7):407–414.
- Heffer, L. F., Sly, D. J., Fallon, J. B., White, M. W., Shepherd, R. K., and O’Leary, S. J. (2010). Examining the auditory nerve fiber response to high rate cochlear implant stimulation: chronic sensorineural hearing loss and facilitation. *J Neurophysiol*, 104(6):3124–3135.
- Hodgkin, A. L. and Huxley, A. F. (1952). A quantitative description of membrane current and its application to conduction and excitation in nerve. *J Physiol*, 117(4):500–544.
- Hossain, W. A., Antic, S. D., Yang, Y., Rasband, M. N., and Morest, D. K. (2005). Where is the spike generator of the cochlear nerve? Voltage-gated sodium channels in the mouse cochlea. *J Neurosci*, 25(29):6857–6868.
- Imennov, N. S. and Rubinstein, J. T. (2009). Stochastic population model for electrical stimulation of the auditory nerve. *IEEE Trans Biomed Eng*, 56(10):2493–2501.
- Javel, E. and Shepherd, R. K. (2000). Electrical stimulation of the auditory nerve: III. response initiation sites and temporal fine structure. *Hear Res*, 140(1-2):45–76.
- Liu, Q., Manis, P. B., and Davis, R. L. (2014). I_h and HCN channels in murine spiral ganglion neurons: tonotopic variation, local heterogeneity, and kinetic model. *J Assoc Res Otolaryngol*, 15(4):585–599.
- Long, J. S. (1997). *Regression models for categorical and limited dependent variables*. SAGE Publications, Inc.
- Mascagni, M. V. and Sherman, A. S. (1998). Numerical methods for neuronal modeling. In *Methods in Neuronal Modeling: From Ions to Networks*. MIT Press/Bradford Books, Cambridge, MA.
- Miller, C. A., Abbas, P. J., Hay-McCutcheon, M. J., Robinson, B. K., Nourski, K. V., and Jeng, F.-C. (2004). Intracochlear and extracochlear ECAPs suggest antidromic action potentials. *Hear Res*, 198(1-2):75–86.
- Miller, C. A., Abbas, P. J., and Robinson, B. (2001a). Response properties of the refractory auditory nerve fiber. *J Assoc Res Otolaryngol*, 2(3):216–232.
- Miller, C. A., Hu, N., Zhang, F., Robinson, B. K., and Abbas, P. J. (2008). Changes across time in the temporal responses of auditory nerve fibers stimulated by electric pulse trains. *J Assoc Res Otolaryngol*, 9(1):122–137.
- Miller, C. A., Robinson, B. K., Rubinstein, J. T., Abbas, P. J., and Runge-Samuelson, C. L. (2001b). Auditory nerve responses to monophasic and biphasic electric stimuli. *Hear Res*, 151(1-2):79–94.

- Miller, C. A., Woo, J., Abbas, P. J., Hu, N., and Robinson, B. K. (2011). Neural masking by sub-threshold electric stimuli: animal and computer model results. *J Assoc Res Otolaryngol*, 12(2):219–232.
- Mino, H., Rubinstein, J. T., Miller, C. A., and Abbas, P. J. (2004). Effects of electrode-to-fiber distance on temporal neural response with electrical stimulation. *IEEE Trans Biomed Eng*, 51(1):13–20.
- Mino, H., Rubinstein, J. T., and White, J. A. (2002). Comparison of algorithms for the simulation of action potentials with stochastic sodium channels. *Ann Biomed Eng*, 30(4):578–587.
- Negm, M. H. (2008). *An Improved Stochastic Hodgkin–Huxley Based Model of a Node of Ranvier for Cochlear Implant Stimulation*. Master’s thesis, McMaster University.
- Negm, M. H. and Bruce, I. C. (2008). Effects of I_h and I_{KLT} on the response of the auditory nerve to electrical stimulation in a stochastic Hodgkin–Huxley model. *Proc 30th Annu Int Conf IEEE Eng Med Biol Soc*, 2008:5539–5542.
- Negm, M. H. and Bruce, I. C. (2014). The effects of HCN and KLT ion channels on adaptation and refractoriness in a stochastic auditory nerve model. *IEEE Trans Biomed Eng*, 61(11):2749–2759.
- Niebur, E. and Niebur, D. (1991). Numerical implementation of sealed-end boundary conditions in cable theory. *IEEE Trans Biomed Eng*, 38(12):1266–1271.
- Oertel, D., Shatadal, S., and Cao, X. J. (2008). In the ventral cochlear nucleus Kv1.1 and subunits of HCN1 are colocalized at surfaces of neurons that have low-voltage-activated and hyperpolarization-activated conductances. *Neuroscience*, 154(1):77–86.
- Press, W. H., Teukolsky, S., Vetterling, W., and Flannery, B. (2007). *Numerical Recipes 3rd Edition*. The Art of Scientific Computing. Cambridge University Press.
- Rattay, F., Lutter, P., and Felix, H. (2001). A model of the electrically excited human cochlear neuron. *Hear Res*, 153(1-2):43–63.
- Rattay, F., Potrusil, T., Wenger, C., Wise, A. K., Glueckert, R., and Schrott-Fischer, A. (2013). Impact of morphometry, myelination and synaptic current strength on spike conduction in human and cat spiral ganglion neurons. *PLoS ONE*, 8(11):e79256.
- Rothman, J. S. and Manis, P. B. (2003). Kinetic analyses of three distinct potassium conductances in ventral cochlear nucleus neurons. *J Neurophysiol*, 89(6):3083–3096.
- Shepherd, R. K. and Javel, E. (1999). Electrical stimulation of the auditory nerve: II. Effect of stimulus waveshape on single fibre response properties. *Hear Res*, 130(1-2):171–188.

- Woo, J., Miller, C. A., and Abbas, P. J. (2009a). Biophysical model of an auditory nerve fiber with a novel adaptation component. *IEEE Trans Biomed Eng*, 56(9):2177–2180.
- Woo, J., Miller, C. A., and Abbas, P. J. (2009b). Simulation of the electrically stimulated cochlear neuron: modeling adaptation to trains of electric pulses. *IEEE Trans Biomed Eng*, 56(5):1348–1359.
- Woo, J., Miller, C. A., and Abbas, P. J. (2010). The dependence of auditory nerve rate adaptation on electric stimulus parameters, electrode position, and fiber diameter: a computer model study. *J Assoc Res Otolaryngol*, 11(2):283–296.
- Yi, E., Roux, I., and Glowatzki, E. (2010). Dendritic HCN channels shape excitatory postsynaptic potentials at the inner hair cell afferent synapse in the mammalian cochlea. *J Neurophysiol*, 103(5):2532–2543.
- Zeng, F.-G., Popper, A. N., and Fay, R. R. (2004). *Cochlear Implants: Auditory Prostheses and Electric Hearing*. Springer Science & Business Media.
- Zhang, F., Miller, C. A., Robinson, B. K., Abbas, P. J., and Hu, N. (2007). Changes across time in spike rate and spike amplitude of auditory nerve fibers stimulated by electric pulse trains. *J Assoc Res Otolaryngol*, 8(3):356–372.

CHAPTER **6**

Conclusions and Future Directions

6.1 Summary of Conclusions

The primary goal of this thesis was to ascertain the mechanisms responsible for the progressive loss of spiral ganglion neuron excitability in response to sustained pulse train stimulation, which is typically delivered by CIs to SGNs. This brand of reduction in excitability generally exhibits accompanied increases in the strength of adaptation with pulse rate, yet occurs on the same timescale of 10s to 100s of milliseconds regardless of the pulse rate.

Initially (in Chap. 2 or Boulet et al., 2016), we considered the timescales and the sub-threshold and suprathreshold excitability regimes of four temporal stimulus-response phenomena including refractoriness, facilitation, accommodation, and spike rate adaptation, and how they may differentially affect the spike rate in response to pulse train stimulation. In Chap. 3, we developed a phenomenological model of responses to CI stimulation that included those four temporal stimulus-response processes. Here, we showed that accommodation and spike rate adaptation worked in tandem to reduce SGN excitability as a function of the spike rate. This means that the strength of adaptation to pulse train stimulation increased with increasing pulse rate, as was shown in recordings of the cat auditory nerve (Zhang et al., 2007).

In Chap. 4, we built on this finding to show that adaptation to pulse trains and the subsequent recovery of model node of Ranvier SGN responses could be predicted by HCN channels that were parameterized to produce moderate to strong adaptation by varying the HCN half-maximal activation potential. Confirming the findings of Chap. 3 and Zhang et al. (2007), we showed that accommodation and spike rate adaptation were the temporal stimulus-response phenomena that drove this effect. Finally, in Chap. 5 we simulated responses to different multicompartmental SGN models. We showed that models with HCN channels initiated responses in a more spatially focused pattern such that they were more likely to initiate spikes at nodes of Ranvier that were closer to the placement of the electrode, both for intracellular and extracellular stimulation. This effect was strong in HCN models with half-activation potentials that produced stronger adaptation. Models with only HCN channels or both HCN and low-threshold potassium (KLT) channels suppressed facilitation, which is generated by passive membrane properties and sodium channel activation in response to paired pulse stimulation. Models with KLT channels showed stronger short-term accommodation, while over longer periods of pulse train stimulation the accumulation of accommodation produced by HCN channels was capable of reducing SGN excitability as a function of the pulse rate.

6.2 Implications for Cochlear Implant Stimulation Strategies

We have shown that reduced excitability to pulse train stimulation can be predicted by HCN channel activation properties whether or not the response is subthreshold or suprathreshold

in nature (accommodation or spike rate adaptation). As we have demonstrated in Chap. 4, these SGN models require relatively long periods until they have fully recovered from intrinsic adaptation. Future CI stimulation paradigms may wish to limit the pulse rate for electrodes that stimulate areas of the cochlea that contain strongly-adapting neurons by considering the tonotopic gradient of HCN channels (Liu et al., 2014) or target spike initiation at nodes of Ranvier that are not subject to strong adaptation.

6.3 Future Directions

Our work adds to the numerous computational modeling and simulation studies that have matured our understanding of SGN mechanisms by also attempting to realize increasingly accurate responses to CI stimulation. We focused our efforts on developing the interaction of several temporal stimulus-response phenomena and refining temporal neural mechanisms endogenous to mammalian SGNs. However, many improvements can be made on our studies.

For instance, our dynamic threshold potential model introduced in Chap. 3 was developed in a modular fashion such that future iterations may extend the model with extra stimulus-response phenomena or reparameterize the existing ones. Other pulse shapes including biphasic pulses may also be used in our model, however more data is required in order to establish the effects of those pulse shapes on the stimulus-response phenomena (Takanen et al., 2016). Since detailed biophysical cable models typically require setting many parameter values, either finding the optimal set of those values can be intractable, or the target behavior of the models may be described by multiple sets of different parameters (Marder and Taylor, 2011). We overcame this issue by constraining our selection of ion channel types to a few of those that are native to mammalian SGNs. Yet, future studies would benefit from determining if other endogenous ion channel species (Davis and Crozier, 2015; Kim and Rutherford, 2016) could contribute to improving the accuracy of SGN responses to several CI stimulation types. This step is a necessary one since to this day, there is no mammalian species-specific biophysical model that can simultaneously predict all types of observed responses to various CI stimulation paradigms (O'Brien and Rubinstein, 2016), although we believe that the addition of HCN and KLT channels bring our model closer to this goal than many other previous attempts.

In Chap. 5, we used monopolar stimulation that was placed perpendicular to the SGN lengthwise axis since 1) the extent of our interest in spatial stimulus-response properties were limited to the nodal spiking patterns and 2) full models of the cochlea have complicated geometries requiring finite element methods that are generally not easily sharable or available to the academic community (Hanekom and Hanekom, 2016; Kalkman et al., 2016). Increasing the accuracy of spatial response models of SGNs also comes with considerable computational demands. Thus, combining our detailed stochastic channel models with realistic cochlear geometry would require substantial supercomputing facili-

ties. Furthermore, actual stimulation from CIs may not be delivered over the lengthwise axis of the SGN depending on electrode placement (Cartee et al., 2006) and current spread from individual electrodes and current interaction from multiple electrodes may yield significantly different activation patterns throughout the length of the SGN. Accurate models of cochlear geometry are ideal candidates to carry out these investigations since powerful three dimensional models of the cochlea allow for volume conduction and can simulate electrical field distributions (Hanekom and Hanekom, 2016; Kalkman et al., 2016). Our hope is that future studies led by groups that already have access to accurate electrode geometry, electrode placement, electrode polarity, multiple electrodes (electrode array), and accurate cochlear geometry (Hanekom and Hanekom, 2016; Kalkman et al., 2016), will update their models to incorporate the temporal accuracy of the neural models we developed in Chaps. 4 and 5. The merger of accurate neural models and cochlear geometry will serve as valuable tools for validating human electrically evoked compound action potential (ECAP) recordings. Such an advancement will pave the way for personalized cochlear stimulation strategies that may lead to improved hearing for any individual with a CI.

References

- Boulet, J., White, M. W., and Bruce, I. C. (2016). Temporal considerations for stimulating spiral ganglion neurons with cochlear implants. *J Assoc Res Otolaryngol*, 17(1):1–17.
- Cartee, L. A., Miller, C. A., and van den Honert, C. (2006). Spiral ganglion cell site of excitation I: comparison of scala tympani and intrameatal electrode responses. *Hear Res*, 215(1-2):10–21.
- Davis, R. L. and Crozier, R. A. (2015). Dynamic firing properties of type I spiral ganglion neurons. *Cell Tissue Res*, 361(1):115–127.
- Hanekom, T. and Hanekom, J. J. (2016). Three-dimensional models of cochlear implants: A review of their development and how they could support management and maintenance of cochlear implant performance. *Network*, pages 1–40.
- Kalkman, R. K., Briaire, J. J., and Frijns, J. H. M. (2016). Stimulation strategies and electrode design in computational models of the electrically stimulated cochlea: An overview of existing literature. *Network*, pages 1–28.
- Kim, K. X. and Rutherford, M. A. (2016). Maturation of Nav and Kv Channel Topographies in the Auditory Nerve Spike Initiator before and after Developmental Onset of Hearing Function. *J Neurosci*, 36(7):2111–2118.

- Liu, Q., Manis, P. B., and Davis, R. L. (2014). I_h and HCN channels in murine spiral ganglion neurons: tonotopic variation, local heterogeneity, and kinetic model. *J Assoc Res Otolaryngol*, 15(4):585–599.
- Marder, E. and Taylor, A. L. (2011). Multiple models to capture the variability in biological neurons and networks. *Nat Neurosci*, 14(2):133–138.
- O’Brien, G. E. and Rubinstein, J. T. (2016). The development of biophysical models of the electrically stimulated auditory nerve: Single-node and cable models. *Network*, pages 1–22.
- Takanen, M., Bruce, I. C., and Seeber, B. U. (2016). Phenomenological modelling of electrically stimulated auditory nerve fibers: A review. *Network*, pages 1–29.
- Zhang, F., Miller, C. A., Robinson, B. K., Abbas, P. J., and Hu, N. (2007). Changes across time in spike rate and spike amplitude of auditory nerve fibers stimulated by electric pulse trains. *J Assoc Res Otolaryngol*, 8(3):356–372.